AFRL-AFOSR-UK-TR-2023-0012

Ultrafast Machining of High Temperature Superconductor Nanostructures for Novel Mesoscale Physics

O'Neill, William
THE CHANCELLOR, MASTER AND SCHOLARS OF THE UNIVERISTY OF CAMBRIDGE
THE OLD SCHOOLS
CAMBRIDGE, , CB2 1TN
GB

10/18/2022
Final Technical Report

Air Force Research Laboratory
Air Force Office of Scientific Research
European Office of Aerospace Research and Development
Unit 4515 Box 14, APO AE 09421

REPORT DOCUMENTATION PAGE

PLEASE DO NOT RETURN YOUR FORM TO THE ABOVE ORGANIZATION.

1. REPORT DATE	2. REPORT TYPE	3. DATES COVERED	
20221018	Final	START DATE 20160930	END DATE 20190929

4. TITLE AND SUBTITLE
Ultrafast Machining of High Temperature Superconductor Nanostructures for Novel Mesoscale Physics

5a. CONTRACT NUMBER	5b. GRANT NUMBER	5c. PROGRAM ELEMENT NUMBER
	FA9550-16-1-0455	
5d. PROJECT NUMBER	**5e. TASK NUMBER**	**5f. WORK UNIT NUMBER**

6. AUTHOR(S)
William O'Neill

7. PERFORMING ORGANIZATION NAME(S) AND ADDRESS(ES)
THE CHANCELLOR, MASTER AND SCHOLARS OF THE UNIVERISTY OF CAMBRIDGE
THE OLD SCHOOLS
CAMBRIDGE CB2 1TN
GB

8. PERFORMING ORGANIZATION REPORT NUMBER

9. SPONSORING/MONITORING AGENCY NAME(S) AND ADDRESS(ES)	10. SPONSOR/MONITOR'S ACRONYM(S)	11. SPONSOR/MONITOR'S REPORT NUMBER(S)
EOARD UNIT 4515 APO AE 09421-4515	AFRL/AFOSR IOE	AFRL-AFOSR-UK-TR-2023-0012

12. DISTRIBUTION/AVAILABILITY STATEMENT
A Distribution Unlimited: PB Public Release

13. SUPPLEMENTARY NOTES

14. ABSTRACT
The high temperature superconductor YBa2Cu3O7-x (YBCO), with its critical temperature above the boiling point of liquid nitrogen, promised to make the use of superconductors in industrial applications affordable. When focussing on electrical applications such as antennas and sensors, patterning of the superconducting thin films is a necessity. Among the different patterning techniques, including lithography, mechanical scribing, and focussed ion beam, laser machining of YBCO has been continuously studied since 1988 due to its design flexibility and the absence of chemicals. One thing that is still not adequately understood is the nature of laser induced damage on YBCO, and to what proportion it affects the superconducting properties of YBCO, and its relation to feature size. In this work, the physical and electrical damage induced by an ultrashort pulse laser was investigated by scanning electron microscope (SEM) characterization and transport measurements over a range of stepwise machined YBCO microbridges. Assuming the damage is limited to the machined edge, an electrical machining limit of 550 nm was determined for a femtosecond laser (1030 nm, 350 fs). Additionally, Raman spectroscopy was used to identify spectral changes caused by degradation. While transport and Raman measurements are commonly used separately to evaluate YBCO, our approach links both techniques as a new method for quick measurements during the laser processing to identify thermal damage. The Ba/Cu2 Raman ratio was compared to the change in critical current density of thin films and bridges. After evaluating the machining limitations, the femtosecond laser was also used to create centimetre-scale
superconducting microwave emitters. To finalise this work, a setup to laser machine YBCO, while in its superconducting state, has been developed. Although it was possible to machine bridges at 77 K, current injection during the processing was not achieved due to time
constraints and difficulties with the cryogenic setup. However, the groundwork has been laid for laser processing of YBCO while superconducting to create bridges with controlled critical current.

15. SUBJECT TERMS

16. SECURITY CLASSIFICATION OF:			17. LIMITATION OF ABSTRACT	18. NUMBER OF PAGES
a. REPORT U	b. ABSTRACT U	c. THIS PAGE U	SAR	178

19a. NAME OF RESPONSIBLE PERSON	19b. PHONE NUMBER *(Include area code)*
JASON FOLEY	555-555-5555

EPSRC Centre for Doctoral Training in Ultra Precision Engineering

Ultrafast Machining of High Temperature Superconducting Nanostructures for Novel Mesoscale Physics

Katjana Lange

Corpus Christi College

Institute for Manufacturing,

Department of Engineering,

University of Cambridge

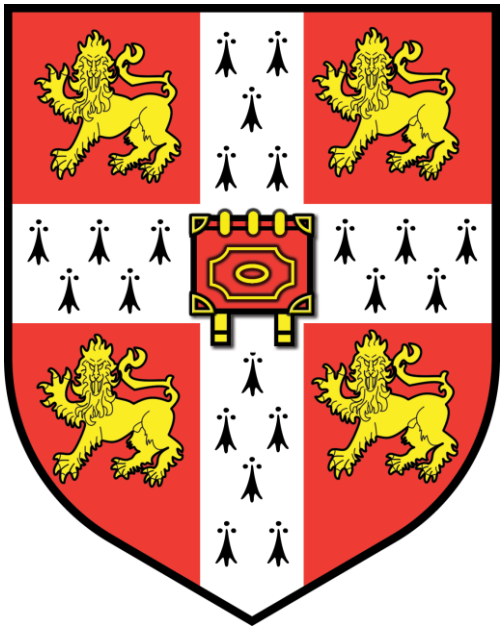

August 2020

This thesis is submitted for the degree of Doctor of Philosophy

Meiner Familie gewidmet.

Vielen Dank für die Geduld, Unterstützung und Liebe.

Ohne euch hätte ich es niemals soweit geschafft.

Declaration

This thesis is the result of my own work and includes nothing which is the outcome of work done in collaboration except as declared in the preface and specified in the text. It is not substantially the same as any that I have submitted, or, is being concurrently submitted for a degree or diploma or other qualification at the University of Cambridge or any other University or similar institution. I further state that no substantial part of my thesis has already been submitted, or, is being concurrently submitted for any such degree, diploma or other qualification at the University of Cambridge or any other University or similar institution. The length of this dissertation is under 65,000 words and 150 figures, and thus not exceeding the prescribed word limit for the Department of Engineering Degree Committee.

Katjana Lange

August 2020

Abstract

The high temperature superconductor $YBa_2Cu_3O_{7-x}$ (YBCO), with its critical temperature above the boiling point of liquid nitrogen, promised to make the use of superconductors in industrial applications affordable. When focussing on electrical applications such as antennas and sensors, patterning of the superconducting thin films is a necessity. Among the different patterning techniques, including lithography, mechanical scribing, and focussed ion beam, laser machining of YBCO has been continuously studied since 1988 due to its design flexibility and the absence of chemicals. One thing that is still not adequately understood is the nature of laser induced damage on YBCO, and to what proportion it affects the superconducting properties of YBCO, and its relation to feature size. In this work, the physical and electrical damage induced by an ultrashort pulse laser was investigated by scanning electron microscope (SEM) characterization and transport measurements over a range of step-wise machined YBCO microbridges. Assuming the damage is limited to the machined edge, an electrical machining limit of 550 nm was determined for a femtosecond laser (1030 nm, 350 fs). Additionally, Raman spectroscopy was used to identify spectral changes caused by degradation. While transport and Raman measurements are commonly used separately to evaluate YBCO, our approach links both techniques as a new method for quick measurements during the laser processing to identify thermal damage. The Ba/Cu2 Raman ratio was compared to the change in critical current density of thin films and bridges. After evaluating the machining limitations, the femtosecond laser was also used to create centimetre-scale superconducting microwave emitters. To finalise this work, a setup to laser machine YBCO, while in its superconducting state, has been developed. Although it was possible to machine bridges at 77 K, current injection during the processing was not achieved due to time constraints and difficulties with the cryogenic setup. However, the groundwork has been laid for laser processing of YBCO while superconducting to create bridges with controlled critical current.

Keywords: Femtosecond laser; micro machining; $YBa_2Cu_3O_{7-x}$ thin films; heat treatments; transport measurements; Raman spectroscopy

Acknowledgements

First, I would like to thank my supervisor Dr Martin Sparkes. He definitely whipped me into shape and was there to save the day before things crashed and burnt. I also would like to thank Prof Bill O'Neill for giving me the chance to join the CIP and IfM family in the first place. Thank you both for all your guidance, advice and experiences along the way. Special thanks also go to the US Air Force Laboratory for sponsoring this work which would not have happened without. Thank you, Dr Timothy Haugan, for supporting this project and providing expert insight in the world of superconductors and Dr Tom Bullard.

Speaking of CIP and IfM family, thank you all for making me feel welcome and always being to helpful. Thanks to:

- Dr Francisco Orozco for helping me with Talisker dramas and moving gas bottles. I know you secretly looked forward to it!
- Chris Wright for allowing me to use his programmes and knowledge and the planking session. It was always fun to talk to you.
- Dr Jason Ten and Franco Ussi for introducing me to 'animal food' during long working days. (And, of course, for helping out fixing the Satsuma laser.)
- Dr Andrew Cockburn, Dr Andy Payne and Dr Krste Pangovski. It would never get boring in the CIP with you.
- Dr Yoanna Shams for providing useful tips and tricks on how to cope with the thesis.
- Pete Atkin for helping me keeping the Satsuma and Talisker laser in check and for letting me pick your brain on laser science and the laughter and entertainment. (You still have a weird relationship to Jack though and I will probably never forget your collage.)
- I would also like to thank Dr Daniel Gortat, Dr Adam Bennet, Georgios Kokkinos, Henry de Fossard, Jack (John) Cook, Dr Laurent Michaux, Sam Brown and Dr Alex Diaz. Every one of you has helped me out with various laser problems along the way!

A very special thanks goes to the ultraprecisely cool group with James Ryley, Lily Delimata, Nadeem Gabbani, Will Fowler and later Diego Punin. I was quite anxious

after leaving Germany for the first time but you have made me feel welcome from the first day! James and Will, we managed one lab assignment after the other and you would patiently explain all these strange optical words to me that I had to add to my vocabulary. Nadeem, you are such an amazing and passionate person. You were always up for a chat (or for being bullied by Lily). Lily, you are so much fun. I wish my brain would be as fast as yours in firing back jokes and counter arguments. While my brain was still searching for a good comeback, you had already delivered three. I cannot wait and see what you will be up to in the future. And Diego, thank you for your wisdom and also for showing me some cool dance moves. You are really a great personality and I am happy to have gotten to know you.

Apart from the craziness happening in the labs, I would like to thank Sophie Gough, Alice Gregory, and Alison Martin who organised everything and were always there to help! I am absolutely amazed by their efficiency and guidance. It is nothing I have ever seen before. Thank you so, so much! On the technical side, I want to thank Chris Summerfield. Thank you for all the interesting discussions about design ideas like how to fill liquid nitrogen on an optical table next to a laser. A special thank you also goes to Dr Hsin-Ling Liang for helping me with measurements very last minute.

Outside the IfM, I would like to thank Dr Bence Börcsök for patiently taking time to explain superconductivity to me and helping me analyse my machining results regarding edge damage. I also had a lot of help from Dr John Bulmer, Dr John Durrell and John Feighan. Thank you to Dr John Bulmer to make this PhD possible in the first place and helping me getting into this project. Another thank you to Dr John Durrell for taking this time answering even most basic superconductivity questions and helping me with my confusion from time to time. And last but not least, thank you John Feighan! I did not know how much fun late night PhD work could be, when you have cool people around. Through the desperation of the sample holder breaking again and again, and plenty of soldering fails, it was always so much fun to talk to you! I really cannot thank you enough for all your time and efforts! (And sorry for all my dance talk!)

My life in Cambridge did not just happen in the lab. Outside the IfM, I was lucky to meet some extraordinary people such as CUDT and a special part of the team: the chicken group. Through CUDT I got to know Marta Tomaselli who is an amazing person and has become one of my best friends! Thank you for being there for me all

this time as friend, housemate, and co-captain. Outside the Cambridge university life, I would like to thank Rita Carvalho and Julius Knetter. I have learnt a lot from you which has expanded my horizon and given me courage in all sorts of situations. You might not even be aware how much I learnt from you.

A huge thank you also to my family. I have decided to study for a very long time and they have been very patient and supportive. Thank you for teaching me so many things since the moment I was born. I love you all very much.

Last but not least, I would like to thank my fiancé Sammy Mahdi. I definitely did not expect to meet my future husband in the IfM. Especially not in the dungeon called 'CIP'. You have supported me in so many ways from helping out with my experiments to emotional support and I am very thankful.

Glossary of abbreviations

AFM	Atomic force microscope
EDX	Energy-dispersive X-ray spectroscopy
FCL	Fault current limiter
FEM	Finite element methods
FIB	Focused ion beam
F_{th}	Ablation threshold
HAZ	Heat affected zone
H_c	Critical magnetic field
HTS	High temperature superconductor
I_c	Critical current
J_c	Critical current density
LN	Liquid nitrogen
LTS	Low temperature superconductor/ conventional superconductor
MMR	Material removal rate
PMT	Photo multiplier tube
SEM	Scanning electron microscope
T_c	Critical temperature
XRD	X-ray diffraction
YBCO	Yttrium barium copper oxide ($YBa_2Cu_3O_{7-x}$)

List of Figures

List of Tables

Table of Contents

1 Introduction

1.1 Background

High temperature superconductors (HTS) are unique materials which exhibit zero electrical resistance and exclusion of magnetic flux lines once cooled down below a critical temperature (T_c). In contrast to conventional low temperature superconductors (LTS), HTS, and in particular YBCO, have a critical temperature above the boiling point of liquid nitrogen (77 K) making them commercially attractive and affordable to run. Hence, since their discovery, HTS have been used in an increasing number of various small- and large-scale applications to make use of their advantageous properties [1], [2], [3]. The best-known small-scale application is the superconducting quantum interference (SQUID) magnetometer, which is sensitive enough to measure the magnetic fields generated by the heart and brain. Large-scale HTS applications include superconducting power transmission cables and magnets for magnetic resonance imaging (MRI) and Maglev trains [4], [5], where the HTS is used as a coated conductor.

This research is focussed on small-scale applications, specifically on repeatable processing of superconducting prototype devices [6]. Using HTS, it is possible to make devices smaller without reducing their performance or quality, which is not possible with devices made of normal metals due to their finite conductivity [1]. Using smaller devices can significantly decrease the amount of material needed, in turn reducing their costs. Additionally, by machining micro and nano structures into HTS the performance of those small-scale applications can be improved [7].

However, processing HTS is challenging due to the material's delicacy. The superconducting properties are easily affected by heat, oxygen loss, chemical exposure and irradiation damage. Furthermore, process induced degradation becomes even more crucial with decreasing feature sizes which means while smaller features are desired as they enhance the performance of HTS, it is also harder to process them while maintaining the superconductivity [8], [9], [10], [11]. This difficulty means common micro and nano processing techniques such as focused ion beam (FIB), (electron beam) lithography, and laser cutting (> fs) are limited in their performance when machining HTS, figure 1.

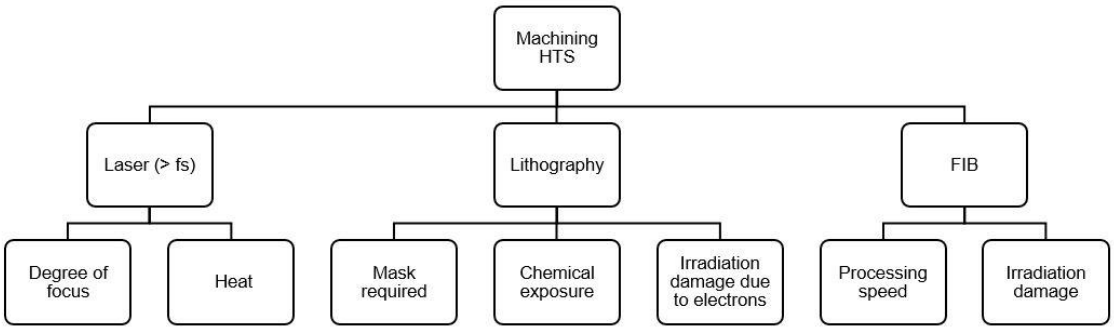

Figure 1: Process limitations for HTS depending on common machining techniques.

To make HTS more attractive and feasible for industrial applications, a processing technique is needed that offers rapid, chemical free, cold, and flexible machining. One such processing technique is ultrafast laser machining.

1.2 Research question

The main research question for this project is as follows:

Is ultrafast laser machining a suitable solution to produce nano/mesoscale patterns on the high temperature superconductor YBCO?

This research question will be further split into different research objectives after the literature review in which the current state of the art for YBCO processing is investigated and research gaps identified.

1.3 Overview of this thesis

Since this thesis investigates the ultrafast machining possibilities of YBCO, both the literature of the tool and the material need to be reviewed. Starting with laser processing in general, the basics such as light propagation and laser-matter interactions are covered in chapter 2. The different machining phenomena for ultrafast lasers are then explained in more detail. An introduction to the theory of superconductivity, with the main focus on HTS and YBCO, follows in chapter 3. This chapter also includes the state of the art of past and current laser machining experiments on YBCO to highlight research gaps. Chapter 4 describes the measurement capabilities of Raman spectroscopy on YBCO, as this work also focuses on the use of Raman spectroscopy to identify processing damages in a cost-effective and non-contact way. This chapter also marks the end of the literature review after which the initial research question is refined to more detailed research objectives based on identified research gaps and new possibilities.

The subsequent chapters are split into different experimental sections. Chapter 5 describes the sample preparation and briefly explains the different tools and techniques used. In chapter 6 different steps to laser machine YBCO bridges are described, starting with simple laser parameter optimization, followed by machining of initial trenches in YBCO thin films and finally moving to machining complete YBCO microbridges. To characterise the machined bridges, current vs voltage (IV) characteristics are measured. The results are then compared with other patterning techniques (lithography, FIB) and process limitations investigated. The theoretical machining limit is calculated by assessing the edge damage caused by laser machining. This chapter finishes with a review of the complete device manufactured for the US Air Force Laboratories.

Chapter 7 describes the possibilities of applying Raman spectroscopy as a method for quick measurements after laser processing of YBCO micron bridges to identify heat damage. A link between changes in the Raman spectra and transport measurements of YBCO thin films is investigated and analysed. After characterising Raman measurement parameters, repeated heat treatments at 300 °C in air are conducted while sequentially measuring the critical current density and Raman spectra as a reference. These results are then further used to assess laser machined samples.

The experimental section finishes with chapter 8 which explores the possibility of laser machining YBCO in its superconducting state at temperatures below T_c. With this, it would be possible to tailor the I_c of each bridge. The design of a prototype for a cryogenic setup is described in which samples are cooled with liquid nitrogen (LN) during the laser machining. The setup needs to endure temperature shocks and measure deformations for a feedback loop to compensate for any resulting offsets during the laser machining. Lastly, YBCO bridges are machined in the cryogenic setup validating the proof of concept.

To end the thesis, in Chapter 9 a summary of the research outcomes is given along with suggestions for future work.

1.4 Publications resulting from this work

K. Lange, M. Sparkes, J. Bulmer, J.P.F. Feighan, W. O'Neill and T.J. Haugan, *Analysing Laser Machined YBCO Microbridges Using Raman Spectroscopy and Transport Measurements Aiming to Investigate Process Induced Degradation*, Lasers in Engineering, 2020

2 Laser patterning – subtractive manufacture

Superconducting devices are promising for many electrical applications due to their unique properties. Such devices can be downsized without a loss in performance and their use in novel technologies, such as THz emitters and quantum computing, are being explored with an increasing interest [12], [13], [14]. What all these devices have in common is the need for the superconductor to be patterned on a micron-/nanometre scale. Machining superconductors, such as YBCO, is challenging due to their sensitive nature. They are easily influenced by different factors such as heat [15], atomic disorders/impurities via electron and ion irradiation [11], [16], humidity [9], [17] [18], and chemical exposure [19]. These processing limitations are problematic for the different machining methods currently used to machine HTS, table 1.

Table 1: Summary of the machining results and their limitations.

Processing Technique	**Results**	**Limitations**
Photolithography [20], [21]	~ 4 µm bridge width	Chemical exposure, undercuts
Electron beam lithography [22], [23]	40 nm wire width	Chemical exposure, electron irradiation
Ga^+ FIB [24], [25]	30 nm to 50 nm bridge width	Ion irradiation due to 'heavy' Ga^+ ions, low through-put
Helium FIB [20]	~ nm tunnel barrier	Low through-put
Nanosecond laser [7]	5 µm trench width	Heat effects
Ultrafast laser [14]	816 nm constriction width	Not known

Out of these machining techniques, ultrafast laser machining appears the most promising. It is a non-contact method (so avoiding any contamination of the sample) and offers a high degree of flexibility regarding the individual design [26]. The limitations of ultrafast machining on superconductors have rarely been studied and not much is known besides its negligible thermal influence. As this thesis aims to investigate these machining limits, a background on laser machining, focused on ultrafast lasers, is provided in this chapter.

2.1 Light propagation

The laser-matter interaction depends on a number of different factors. These include laser parameters such as the wavelength λ, the intensity, polarisation, angle of incidence and pulse duration τ and material characteristics such as microstructure, chemical composition and optical properties [26]. In this section, the optical properties of materials and how they affect the machining process are explained before discussing further complex laser-matter interactions.

When electromagnetic radiation (e.g. laser light) strikes a material surface, mainly two basic phenomena are observed: reflection R and transmission T. At a closer look, the intensity of the transmitted radiation is weakened by scattering events S and absorption A leading to the following energy budget, equation (1) and figure 2 [27].

$$1 = R + T + A + S \tag{1}$$

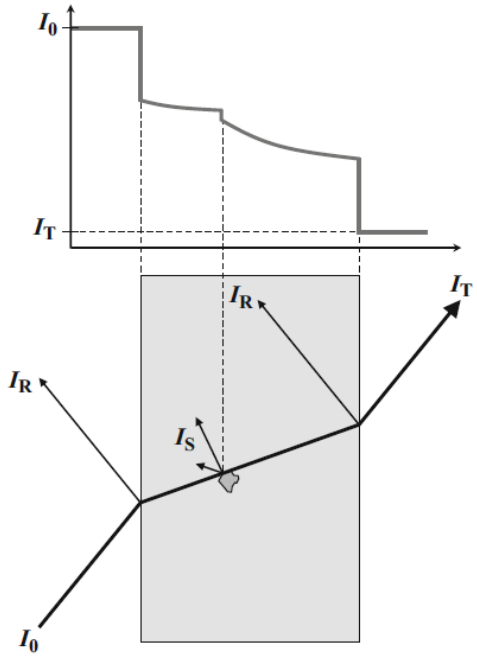

Figure 2: Mitigation of light throughout an optical material. When light strikes a surface with the intensity I_0, parts of it will be reflected. The remaining light is being transmitted through the material where it experiences intensity losses through scattering events and absorption [27].

When light is being transmitted through a medium, it is 'slowed down' which is generally described by the refractive index n, equation (2).

$$n = \frac{c_0}{v} \tag{2}$$

where c_0 describes the speed of light in a vacuum and v is the speed inside the medium. If wavelength dependent attenuation also occurs inside a medium, the refractive index n is extended to the complex reflective index $\tilde{n}$, equation (3) [27].

$$\tilde{n} = n + ik \tag{3}$$

where k is the extinction coefficient which describes the intensity decay inside the medium. This extinction coefficient is incorporated in the Beer-Lambert law, which calculates the remaining intensity I depending on the initial intensity I_0 and the absorption over the thickness d of the optical medium, equation (4) [27].

$$I = I_0 e^{-\alpha d} \tag{4}$$

The intensity decreases exponentially with increasing depth at a rate set by α, the absorption coefficient, which is further expressed as follows, equation (5).

$$\alpha = \frac{2k\omega}{c} \tag{5}$$

In this equation, ω is the photon angular frequency and c is the speed of light.

The light which is absorbed by the material/medium is then converted into heat over time [27]. When the intensity of the absorbed light increases, multiple laser-matter interactions can take place which can then be used for laser machining, figure 3 [26].

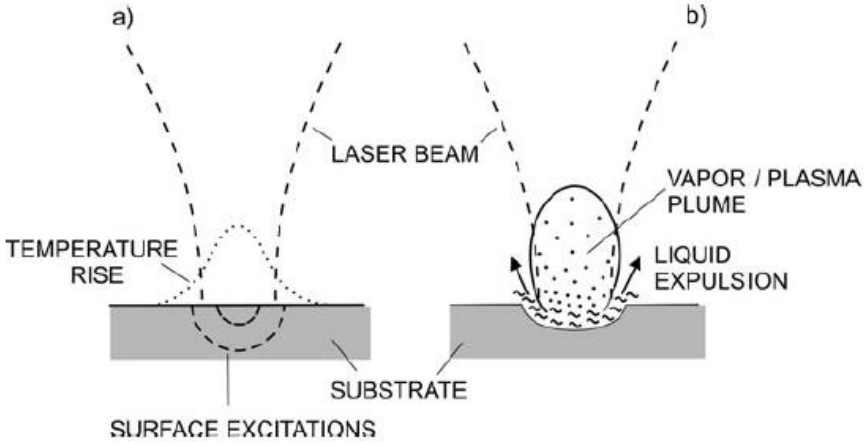

Figure 3: Two laser-matter interactions for conventional laser machining are shown. In (a) the material is heated due to the absorption of laser light, however, the intensity is not high enough to permanently change the surface structure. (b) shows a laser-matter interaction with a strong enough intensity where surface melting and vaporisation takes place [26].

Of course, the laser-matter interactions that take place during laser machining are far more complex than shown in figure 3 and the material response can be delayed up to hundreds of microseconds after the laser pulse has gone, figure 4 [28].

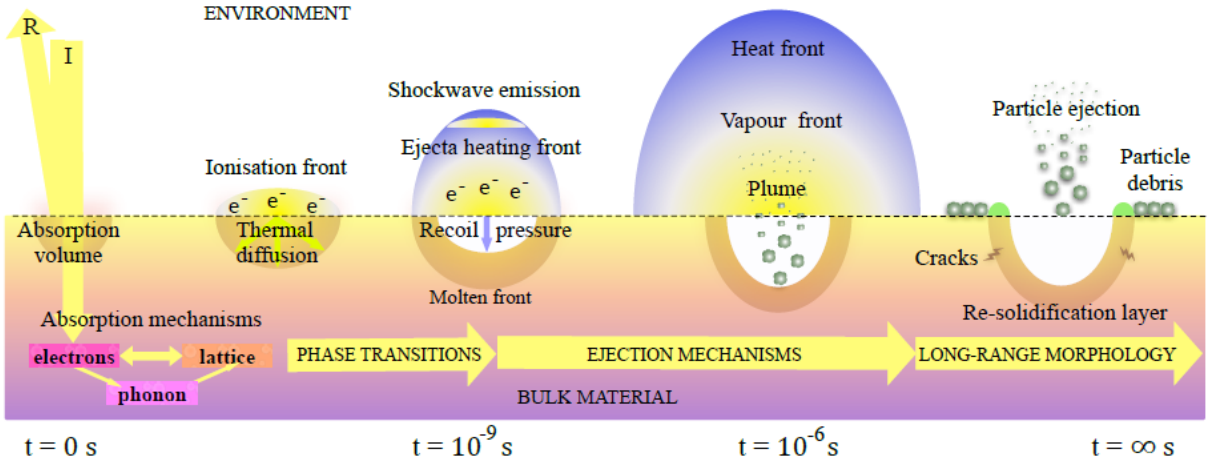

Figure 4: Laser-matter dynamics occur at different time scales. After the initial material response (absorption), the dynamics continue even long after the laser pulse. This delayed response can last hundreds of microseconds [28].

Due to the complexity of laser-matter interactions, which vary depending on the laser pulse duration, the next section will focus solely on the ultrafast/femtosecond laser machining regime.

2.2 Laser-matter interaction with an ultrafast laser

Ultrafast or femtosecond lasers offer high precision non-contact machining with flexible computer programming for virtually any material. Their ultrashort fs laser pulses possess very high peak power densities, which interact with matter on a timescale shorter than heat diffusion and lattice disorder. Ultrafast laser ablation occurs in localised areas with minimal to zero residual thermal stresses and melting due to direct solid-vapour transitions, figure 5 [29], [30], [31]. The mechanisms of ultrafast laser ablation depends on the laser properties and the specific material properties [31].

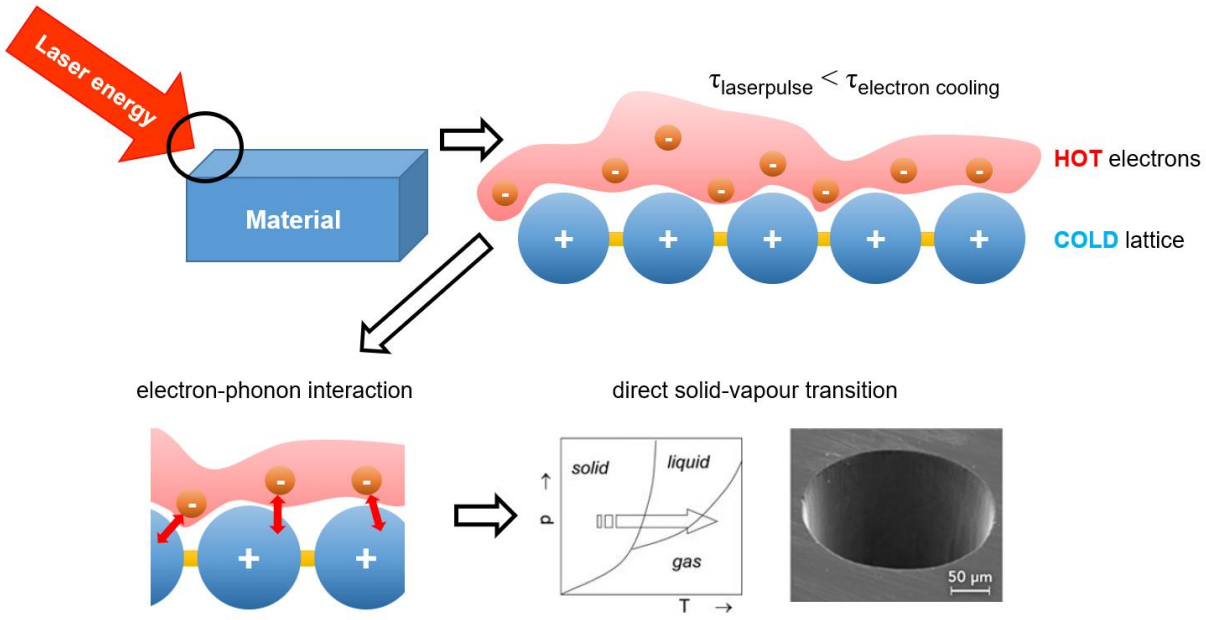

Figure 5: When the ultrafast laser strikes the material surface, the electrons are heated up while leaving the lattice 'cold'. After the laser pulse, electron-phonon interactions take place, leading to a direct solid-vapour transition [32] creating sharp machining edges [33].

The starting point for laser-matter interactions using an ultrafast laser is the photon absorption by electrons. Absorbed photons excite the electrons within ~ 100 fs [31]. Since the laser pulse duration in the femtosecond regime is shorter than the electron cooling time, the electron temperature can reach tens of thousands of Kelvin while the lattice remains 'cold'. After the laser pulse, electron-phonon coupling takes place where the electrons are cooled over a very short timescale (ps) due to energy transfer to the lattice. The absorbed energy from the electrons heats the lattice very quickly past its melting point leading to direct vaporisation of the material. The vapor moves rapidly away from the material surface without forming a recast layer, leading to fine features and a negligible heat affected zone (HAZ) [34], [29], [35], [36].

The ablated microstructure is also dependent on the material's electron band structure and electron-phonon interactions. This includes photon absorption which varies from a linear process in metals to a non-linear process in semiconductors and dielectrics. After the absorption, different stages of laser-matter interaction occur before the system returns to equilibrium [37], figure 6 [31].

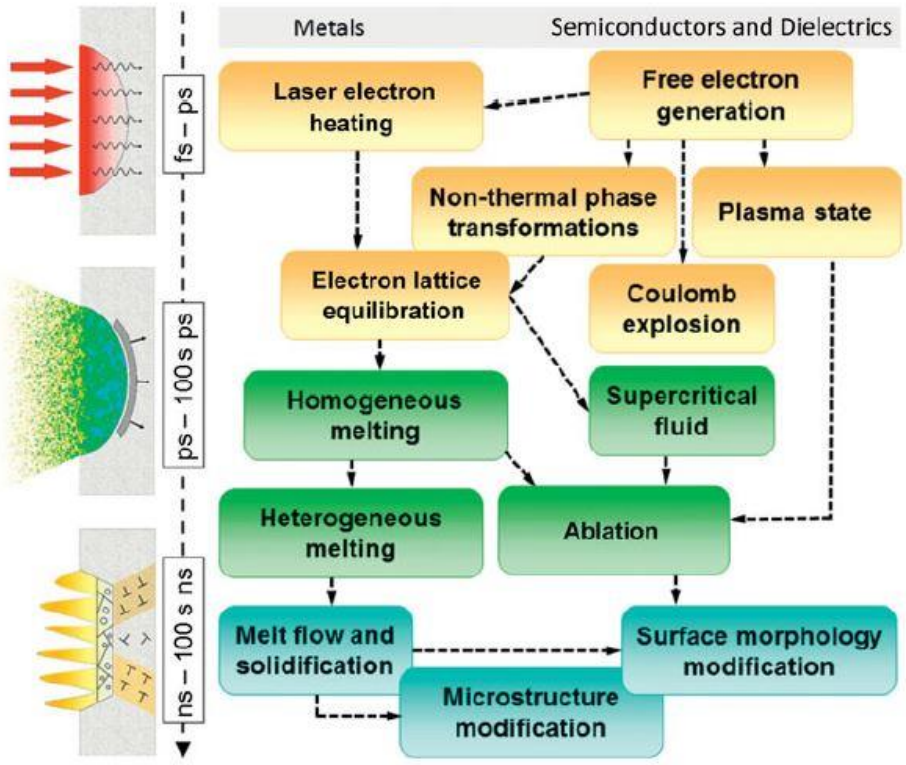

Figure 6: Phase transformations and energy dissipations after an ultrafast laser pulse [38].

The yellow coloured boxes in figure 6 describe the electronic excitation by the laser beam and subsequent ultrafast processes including the Coulomb explosion and the plasma state. At low laser intensities the Coulomb explosion is dominant. It is a gentle ablation process, which removes several nanometres of the lattice at a time due to charge separation. The charge separation is caused by the ejection of excited electrons, which builds up an electric field above the highly-ionised atoms in the material. This electric field then pulls ions out of the material [38], [39].

The subsequent energy exchange between electrons and phonons triggers rapid non-equilibrium phase transformations, which are marked in green. These non-equilibrium phase transformations are homogeneous and heterogenous melting, formation of a supercritical fluid and ablation. A supercritical fluid is a mixture of vapour and liquid droplets which expands at high velocities away from the sample surface (phase explosion) [31], [38].

The last stage, shown in blue, describes the subsequent cooling and local surface solidification that results in the final microstructure/surface morphology modification [38].

Metals can directly absorb the laser energy by inverse bremsstrahlung due to the electrons in the conduction band. The rate at which the absorbed energy transfers from the electrons to the lattice depends on the specific electron-phonon coupling constant of the metal. For metals with large electron-phonon coupling constants, the energy exchange between electrons and phonons is fast and no significant heat transfer into the material takes place. This means the absorbed energy accumulates close to the metal surface, leading to laser induced surface structures [31].

Semiconductors and dielectrics have a bandgap between their highest unoccupied and lowest occupied electron bands. If they absorb photons electrons are excited across this bandgap leading to ultrafast solid-solid phase transitions and ultrafast melting transformations. If a semiconductor/dielectric has a wide bandgap, the ablation process is dominated by multiphoton excitation and avalanche excitation. Multiphoton excitation occurs when several photons are absorbed simultaneously, although this requires the laser intensity to be adjusted accordingly. This allows the electron to gain enough energy to cross the bandgap to the conduction band. In the conduction band, the electrons can continue to absorb the laser energy due to inverse bremsstrahlung and through collisions with valence-band electrons. This produces an avalanche multiplication of the conduction band electron density [38].

In conclusion, the different phenomena that can occur are dependent on the material's optical properties and band structure. However, the intensity of the laser also determines the energy dissipation through the material. As such, the laser parameters need to be adjusted carefully. One important parameter for micro- and nanomachining is the material dependent ablation threshold. The ablation process and the quality of the result vary depending on the used laser fluence relative to the material's ablation threshold, which is further explained in the next section.

2.3 Determination of material dependent ablation thresholds

The ablation threshold is defined as the laser fluence necessary to enable material ablation and is expressed in peak fluences. To determine the ablation threshold, an idealised model of ultrafast laser ablation can be used. In this model, material is only ablated by a single pulse. When the laser beam is scanned over a surface and multiple pulses are involved further factors need to be considered [30].

2.3.1 Single pulse ablation

In the idealised model of ultrafast laser ablation, only the effects of a single pulse are considered. To determine the ablation threshold, the diameter of the ablated crater is related to the laser fluence.

The radial laser fluence distribution $F(r)$ of a Gaussian beam is presented in equation (6). F_{peak}, r and r_0 are further defined in equations (7) and (9).

$$F(r) = F_{peak}\, exp\left(-\frac{2r^2}{r_0^2}\right) \tag{6}$$

The peak fluence F_{peak} of a Gaussian laser beam is calculated with equation (7).

$$F_{peak} = \frac{2E_p}{\pi r_0^2} \tag{7}$$

where E_p is the energy of a single laser pulse and is further defined in equation (8).

$$E_p = \frac{P_{avg}}{f} \tag{8}$$

where P_{avg} is the average power of the beam measured with a power meter and f is the pulse repetition rate of the laser. r_0 is the theoretical beam radius, equation (9),

$$r_0 = \frac{l\lambda M^2}{\pi r} \tag{9}$$

and is dependent on the focal length l of the used objective, the laser wavelength λ, the beam quality factor M^2, and the raw beam radius r.

After rearranging equation (6), a linear relationship between the squared ablated crater diameter D and the logarithmic laser peak fluence $\ln(F_{peak})$ can be used to determine the ablation threshold F_{th}, equation (10) [30] ,[40].

$$D^2 = 2r_0^2\, ln\left(\frac{F_{peak}}{F_{th}}\right) \tag{10}$$

2.3.2 Scanned ablation

When multiple laser pulses hit the same location on a surface, ablation occurs at pulse energies less than the single pulse ablation threshold due to incubation effects [30].

Incubation effects are the result of the accumulation of process induced damage from individual pulses. Equation (11) summarises the incubation effect.

$$F_{th}(N) = F_{th}(1)N^{\xi inc-1} \tag{11}$$

The ablation threshold changes with the number of pulses N and the material specific incubation constant ξ_{inc}. N can be calculated using the focus spot diameter d, the processing speed s, and the repetition rate f, equation (12) [30].

$$N = \frac{d}{s/f} \tag{12}$$

A relationship between the ablated trench width D_N and the scanned ablation threshold $F_{th}(N)$ is given in equation (13) [30].

$$D_N = \sqrt{2r_0^2 \, ln\left(\frac{F}{F_{th}(1)N^{\xi inc-1}}\right)} \tag{13}$$

Depending on the machining strategy, the ablation threshold is determined in different ways. When a material is machined in a 'scanned' fashion, where multiple pulses are involved, incubation effects need to be considered.

2.4 Conclusion

Having compared the common machining techniques to create micro- and nanostructures on YBCO, ultrafast laser machining appears to be most promising. However, not much is known about the machining limits and possible processing damage of these lasers. To gain further understanding of how the ultrafast lasers differ from 'conventional' laser systems, different laser-matter interactions have been explained, starting with the general explanation of light propagation through an optical medium. The intensity of transmitted light decreases exponentially due to absorption, which then leads to the creation of heat. Depending on the intensity of the light, different ablation mechanisms are realised. These mechanisms are complex and depend on the material's band structure, which leads to interesting effects in YBCO as it can be in different electronic states (normal, semiconducting and superconducting), which is further discussed in the next chapter. To start machining trials, ablation thresholds need to be determined as they are characteristic for each material and affect

the machining approaches. For scanned ablations, such as machining trenches, incubation effects influence the results.

3 Meso- and nanoscale machining of high T_c superconducting thin films

This chapter highlights the unique properties of high temperature superconductors and the physics behind them. Starting with an introduction on basic superconductivity, this chapter then focusses on the structure of YBCO, the superconductor used for this work. The state of art of YBCO laser machining techniques are also investigated.

3.1 Background on superconductivity

Conventional conductors (metals) exhibit electrical resistance due to impurities and temperature dependent collisions between electrons and lattice ions [41]. A superconductor, however, shows zero resistance below a critical temperature T_c, figure 7 [42].

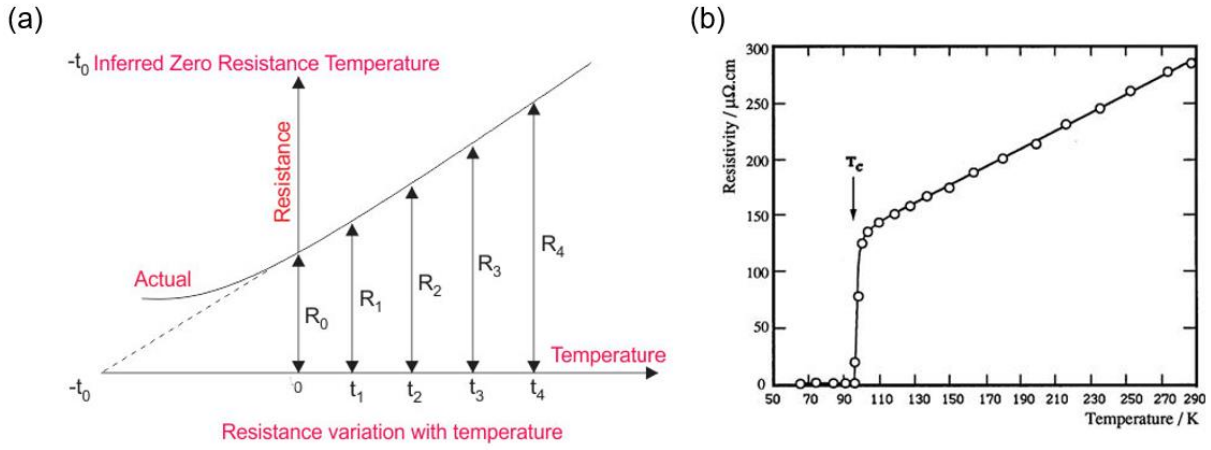

Figure 7: (a) Temperature dependence of the resistance in a metal [43]. (b) Once the critical temperature T_c of a superconductor is reached, the electrical resistance drops to zero [44].

A perfect conductor without any impurities would also demonstrate zero resistance as indicated in figure 7 (a). The main difference between a perfect conductor and a superconductor is a superconductor's unique ability to expel all magnetic fields, static and changing (at least for type I superconductors – see below). This ability makes superconductivity a distinct thermodynamic state [3]. A magnetic field is not only excluded from entering a superconductor, but it is also expelled from the superconductor once cooled below T_c. This perfect diamagnetism is called 'Meissner effect'. Weak magnetic fields can only penetrate the superconductor close to the surface depending on λ_L, the London penetration depth, with the magnetic field decreasing exponentially within λ_L, figure 8.

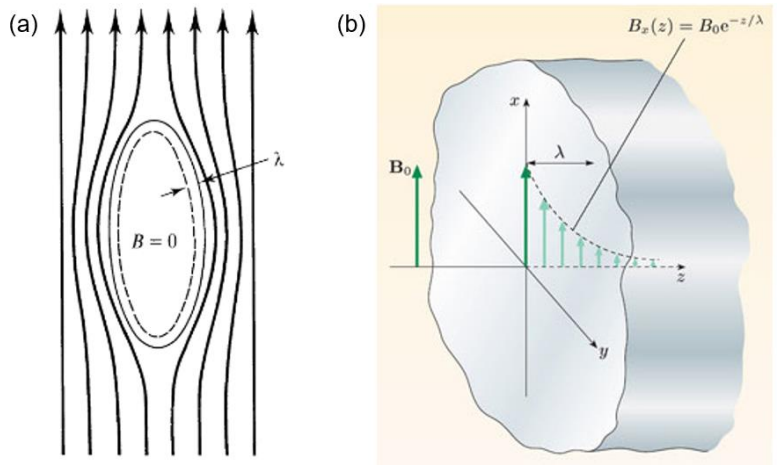

Figure 8: (a) Meissner effect - the magnetic field is excluded from the superconductor. λ_L is typically ~ 500 Å [42]. (b) An external magnetic field decays exponentially when entering a superconductor [45].

However, if a magnet field exceeds the critical magnetic field H_c, superconductivity breaks down [42]. The existence of the critical field limits the transport properties of superconductors as only a finite current can be carried. When a current exceeds the material dependent critical current I_c, the generated self-field surpasses the critical field H_c causing the collapse of the superconducting state [3]. The relationship between I_c and H_c is shown in equation (14) [46].

$$I_c = 2\pi r H_c \tag{14}$$

r is the radius of the superconducting wire.

Both I_c and H_c are also temperature dependent and decrease at higher operating temperatures. The operating temperature should be as stable as possible to not cause a sudden breakdown of the superconductivity due to changes in I_c and H_c, figure 9.

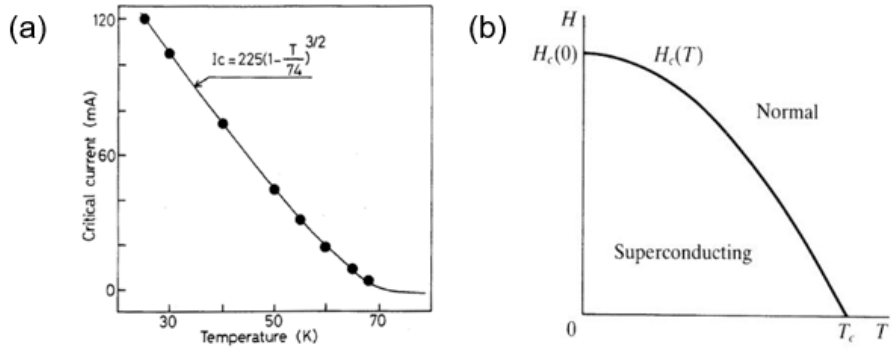

Figure 9: (a) The critical current decreases with rising temperatures [47]. (b) Critical field and temperature dependence [42].

For the purposes of this research, it is important to understand the connection between I_c and H_c. They are significant indicators of processing effects and application performances.

Since the discovery of superconductivity in 1911 many researchers have examined this new thermodynamic state and several theories and mathematical models emerged to describe the observed phenomenon of superconductivity [48]. These theories and models are described in Appendix 1.

3.2 Thin film high T_c superconductors

Due to the superior electrical properties of superconductors, the main goal of most studies has been to implement them into electrical applications. Although LTS are still used in some applications such as MRI and SQUID, the refrigeration system required to maintain the superconductivity is increasingly expensive and complex due the need for liquid helium [4]. In addition, their use in more prevalent applications such as motors and fault current limiters failed since the self-generated fields from the currents needed for industrial applications are above H_c. The introduction of high temperature superconductors or HTS in 1986 offered new possibilities for superconducting applications [49].

HTS are type II superconductors. This means they have two critical magnetic fields H_{c1} and H_{c2} which allow an intermediate state where superconducting and normal areas can coexist, figure 10 [4], [42].

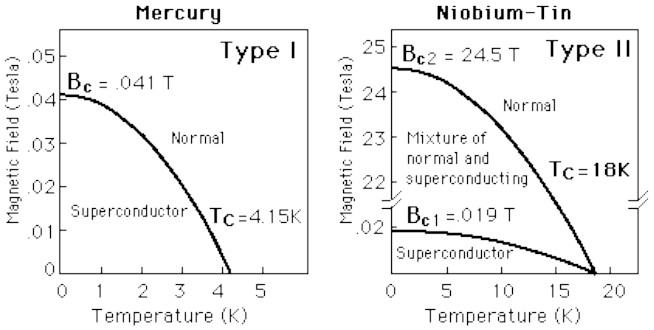

Figure 10: Critical magnetic field and critical temperature of both type I and type II superconductors [50].

Due to the second critical field, HTS can exhibit superconductivity at temperatures above 100 K [51]. The high H_{c2} and T_c make HTS favourable for industrial applications since higher currents can be carried and maintenance cost are significantly cheaper

due to the possibility of using liquid nitrogen instead of liquid helium [42]. Liquid helium is about 20 times the price of liquid nitrogen [52], [53].

HTS can be used as bulk material or in thin films depending on the specific application. This project focuses on processing techniques for HTS, specifically YBCO, thin films in the micro/nano regime, which are relevant for electrical applications. For electrical applications only HTS thin films are of interest as they show improved electrical performance and flux pinning capabilities. The electric properties of bulk HTS samples are dominated by low conducting grain boundaries which leads to poor performance, figure 11.

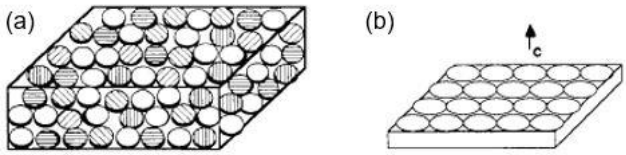

Figure 11: Microstructure of HTS in a bulk (a), and epitaxial thin film (b) [54].

This arises because HTS materials are highly anisotropic due to the layered elementary cell structure, with only some directions having strong current carrying ability. In a bulk the orientation of grains can only partially be controlled, leading to inhomogeneous conductivity, figure 11 (a). To avoid grain boundary effects, epitaxial HTS thin films are used. Those films are grown with the c-axis aligned normal to the substrate surface and the a/b axis pointing the same direction in each grain. This lowers the angular offset between adjacent grains, i.e. creates low-angle grain boundaries. Low-angle grain boundaries are able to conduct large amounts of current so epitaxial thin films can achieve strong consistent superconducting properties, figure 11 (b). The parallel ordered superconducting planes lead to a uniform high I_c along the sample surface and a large critical current density J_c [3], [55], [54].

3.2.1 Flux pinning

Another difference between type I and type II superconductors is the way they interact with magnetic flux. In contrast to type I superconductors which expel any magnetic flux, type II superconductors are penetrated by flux lines [49]. When flux lines are penetrating a type II superconductor, each flux line is screened by a circulating current. These circulating currents and localised flux lines are called flux vortices [3].

If an ideal HTS thin film is exposed to an external perpendicular magnetic field which is above H_{c1}, the film is penetrated by flux lines with a constant flux vortex density. By applying a transport current, the flux lines experience a driving force due to Lorentz's law which leads to vortex motion, equation (15) [56], where J and B describe the current density and magnetic field respectively:

$$\overrightarrow{F_L} = \vec{J} \times \vec{B} \tag{15}$$

The Lorentz force F_L causes the movement of the flux vortices which creates an energy dissipation for the superconductor [49]. In real materials, this behaviour is hindered by flux pinning. The pinning force F_P opposes F_L and prevents the movement of the flux vortices [49]. Flux vortices can be pinned by defects or pinning centres that show a local reduction of the Ginzburg-Landau order parameter Ψ [56]. Ψ characterises the superconducting state. There are two groups of pinning centres: ξ_{GL} dependent and λ_{GL} dependent. λ_{GL} is the Ginzburg-Landau penetration depth which describes the decay of magnetic fields in a superconductor. ξ_{GL} describes the Ginzburg-Landau coherence length which defines the distance a local disturbance in the superconducting electron density, caused by an electric or magnetic force, propagates in the material [3], [42], [57]. More information about the Ginzburg-Landau theory can be found in Appendix 1

Defects with a size similar to ξ_{GL}, such as cylindrical dislocation defects, are also referred to as 'core pinning'. Pinning effects caused by the interactions between defects of the order of λ_{GL} and screening currents are called 'magnetic pinning'. Both ξ_{GL} and λ_{GL} are in the nanometre regime [3], [58], [59]. Pinning centres can actively be created by planting nano-sized defects within the microstructure [58].

At the critical current density, J_c, the Lorentz Force F_L overcomes the pinning force F_P and the flux lines start moving, equation (16) [49].

$$F_p = J_c \times B \tag{16}$$

In HTS, there are three different resistive behaviours observable during transport measurements which are caused by vortex movements. They are Thermally Assisted Flux Flow (TAFF), flux creep and flux flow, figure 12 [49].

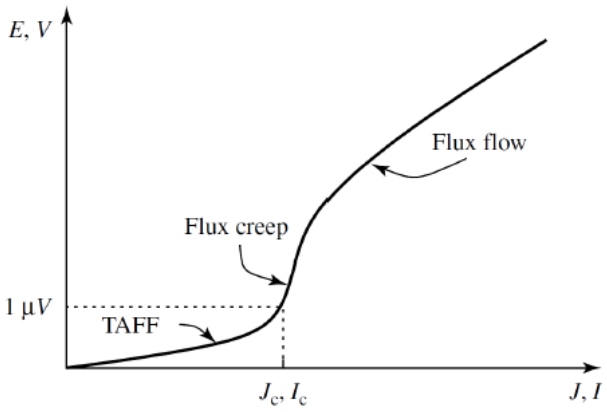

Figure 12: I-V measurement curve of a typical HTS [49].

At low currents ($I < I_c$), flux lines can 'jump' out of their pinning sites due to thermal excitation. This phenomenon is called TAFF. Above the critical current, the pinning force is overcome, and the vortices move away from their pinning sites. This is referred to 'flux creep'. Flux flow describes the regime where all vortices are depinned and move freely through the superconductor [49].

3.2.2 $YBa_2Cu_3O_{7-x}$ thin films

$YBa_2Cu_3O_{7-x}$ or YBCO was the first HTS to have a T_c at 92 K, above the boiling point of liquid nitrogen and it became one of the most studied HTS [60]. It can offer critical current densities of about 8 MA/cm² at 77 K [61] and critical fields of H_{c1} ~ 10 mT at 77 K and H_{c2} > 800 T at 0 K for fields parallel to the crystallographic *c* axis [62].

YBCO has a planar perovskite-like structure as shown in figure 13 [3].

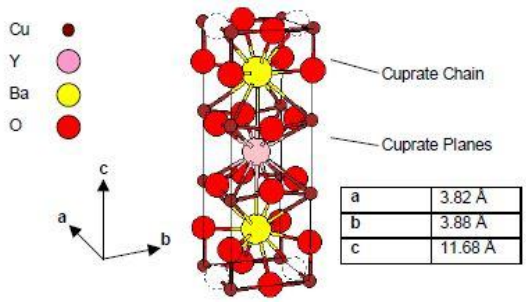

Figure 13: Elementary cell of $YBa_2Cu_3O_7$ with the three crystallographic directions a, b, c [3].

The elementary cell of YBCO is centred around Y^{3+} which lies between two CuO_2 planes. These CuO_2 planes are responsible for carrying the majority of the supercurrent. CuO chains connect the layers and act as charge-reservoirs [4] ,[63].

Depending on the oxygen content x of YBCO (where x is between 0 and 1) the lattice parameters and crystal structure of the elementary cell changes, this in turn influences its electrical properties, figure 14.

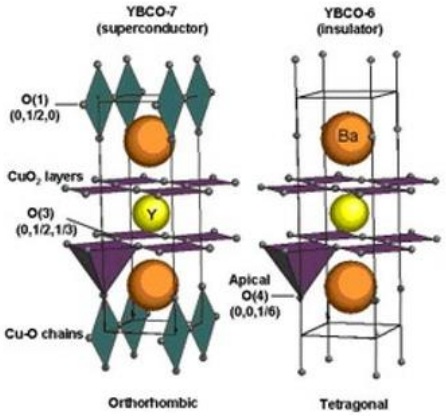

Figure 14: Structural changes depending on the oxygen content [64].

For 0 ≤ x ≤ 0.65, YBCO has an orthorhombic structure and transitions below T_c into a superconducting state. At x ≈ 0.07, YBCO features the highest T_c. As x increases beyond this, T_c falls and by x = 0.65, the normal state becomes semiconducting and superconductivity is completely lost. Above x = 0.65 the elementary cell structure of YBCO becomes tetragonal [15], [49].

This research uses YBCO since it is the most studied HTS and as such has highly developed fabrication techniques which produces high quality YBCO with strong superconducting properties [65].

However, the performance of YBCO can be further improved. This can be done not only from a material science point of view, but also through manufacturing engineering. Small changes to the structure of YBCO can significantly change the electrical properties of the material, but, machining YBCO while maintaining all the superconducting properties is very challenging. Different techniques have already been used for this brittle and delicate material, but improvements are still needed to make it more suitable for industrial applications.

3.3 State of the art – laser patterning of the high T_c superconductor YBCO

To use YBCO thin films in electrical applications, various laser machining approaches have been used to structure them into devices. Three main ways in particular, have been reported in papers since 1988:

- Structuring the substrate for selective YBCO growth.
- Local degradation/doping of YBCO using a laser in a controlled environment.
- Removal of YBCO via a laser ablation processes.

3.3.1 Selective growth of defected YBCO by locally induced surface damages on the substrate using laser irradiation

By structuring the substrate before the YBCO thin film deposition, defected thin films are grown on the roughened surfaces, leaving functional superconducting structures in the untreated areas. One paper [66] structured the surface of YSZ, $LaAlO_3$ and $SrTio_3$ substrates using an Excimer laser (KrF, ArF) to create YBCO bridges down to 10 µm wide. The substrates were machined with a range of different fluences (0.05 J/cm² to 20 J/cm²) to induce well-defined structural damages [66]. Figure 15 shows SEM images of a structured substrate before and after YBCO thin film deposition.

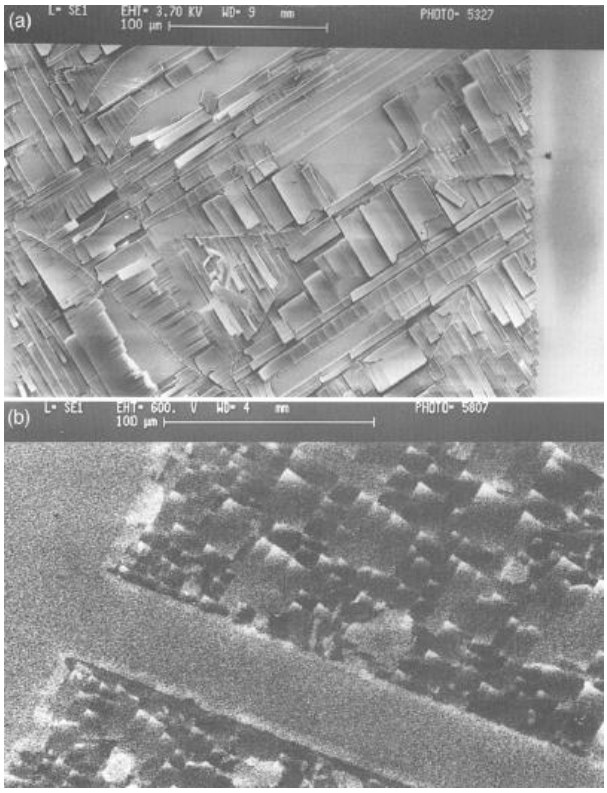

Figure 15: (a) Laser processed YSZ surface machined with 2 pulses at 1.8 J/cm² obtained by mask projection. (b) Clean microbridge pattern surrounded by surface structured SrTiO3 to selectively grow defective and high quality YBCO [66].

This approach has the advantage of avoiding the degradation that occurs during the patterning processes after the thin film's deposition.

3.3.2 Reversible laser induced degradation/doping of YBCO thin films

Another approach focussed on altering the oxygen level of YBCO using a laser. It is then possible to create patterns with either insulating, semiconducting or superconducting passages. Patterns are written and re-written in different controlled atmospheres such as O_2, N_2 or in a vacuum, where oxygen out-diffusion is deliberately accelerated in the writing process and oxygen doping is accelerated in the re-writing process. This approach has the advantage that any changes of the surface morphology are avoided while creating high resolution patterns down to micrometre scale [67]. It avoids the damaged boundary interface generated in conventional machining techniques which negatively influences the device performance [68]. Another advantage is the reversibility of this process as the superconductive properties can be restored [67].

For this technique, the laser is used to locally heat the YBCO thin film to change the oxygen content depending on the applied atmosphere [67]. When laser writing in a

vacuum or an N_2 atmosphere, the oxygen stoichiometry decreases independently of laser power and scanning speed leading, to a lower T_c or a phase transition to semiconducting/insulating states [69], [67], [70]. In an O_2 atmosphere the oxygen content can be both reduced and increased depending on the laser power density and scanning speed. Only when the laser power density is high (e.g. 2.3 mW/µm² using a 514 nm Ar^+ laser) and the scanning speed low (e.g. 1 µm/s), can the YBCO reach near full oxygenation. At lower power densities and/or scanning speeds, the amount of oxygen pickup is decreased, figure 16 [70].

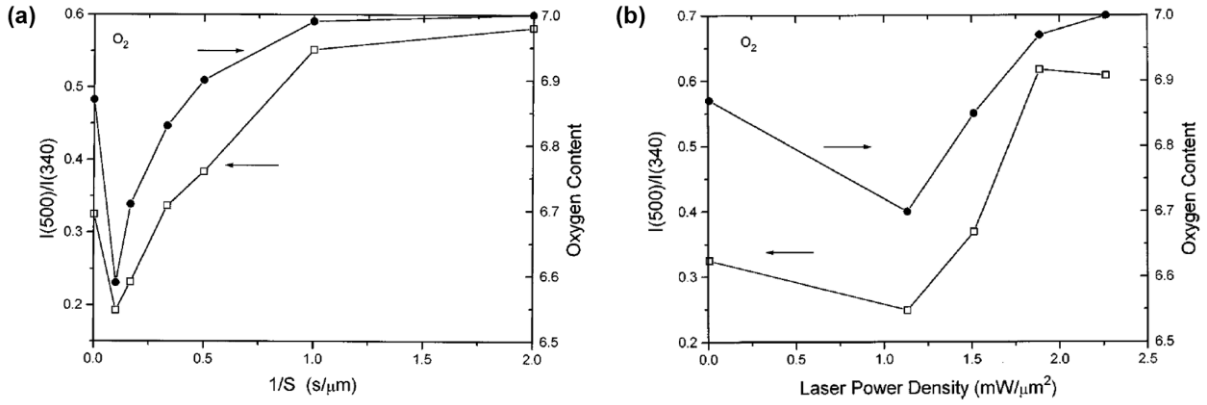

Figure 16: (a) The laser power density is held constant at 2.3 mW/µm² while the scanning speed is varied. The graph shows the development in oxygen content as an intensity ratio of two oxygen Raman peaks and a calculated oxygen content also based on Raman measurements over the inversed scanning speed (1/S). (b) The dependence of the oxygen content is ratioed against the laser power density while keeping a constant scanning speed of 1 µm/s [70].

The final amount of oxygen uptake is determined by the time needed for the YBCO to cool through the low-temperature annealing stage, located at 400 °C – 500 °C. The overall change in net oxygen content depends on three factors [70]:

1. Time interval during which oxygen is lost.
2. The time required to cool through the low-temperature annealing stage at 400 °C – 500 °C.
3. How close the sample temperature is to the thermal equilibrium during cooling and heating cycles.

Based on these factors and the chosen laser parameters, the net oxygen content can either be decreased or increased. For example, if the sample is heated just slightly above the low-temperature annealing stage, as the initial temperature drop is rapid, there is a net loss of oxygen, since the time interval for oxygen uptake is shorter than for oxygen loss. In contrast, if the initial sample temperature is significantly higher than

the low-temperature annealing stage, the time taken to cool through 500 – 400 °C increases. Since oxygen uptake occurs more rapidly than oxygen out-diffusion, an increase in net oxygen is expected [70].

Since the surface morphology remains unchanged, different measurement techniques are necessary to confirm the oxygen content of the samples. Throughout the studies, the doping levels after the laser annealing were analysed, in addition to transport measurements, using optical transmission/absorption, EDX and Raman spectroscopy, figure 17.

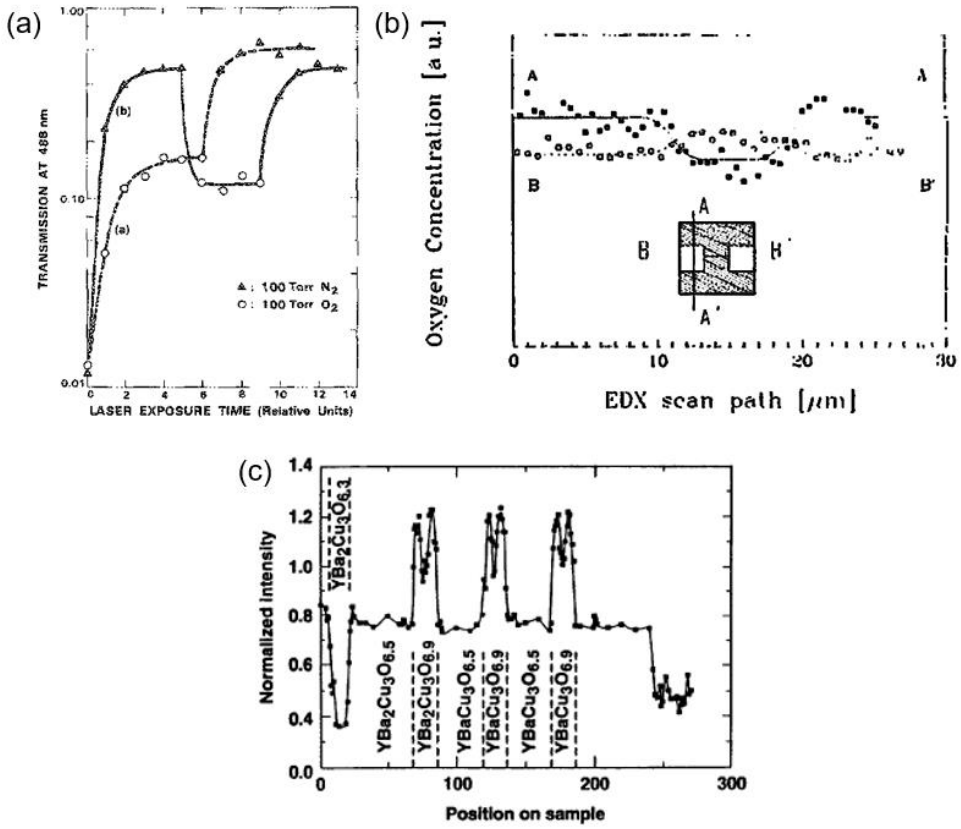

Figure 17: Different assessment techniques to determine the oxygen content of laser written YBCO thin films. (a) When a decrease in oxygen content, not only a loss of superconductivity is observed but also an increase in optical transmission. Here, the optical transmission was measured by using a digital electrometer and a silicon photodiode. The change in transmission is plotted against the laser exposure time for machining in O_2 and N_2 ambient [70]. (b) The oxygen distribution was determined by EDX. The black area is oxygen-rich while the white is oxygen depleted. The EDX count rate was normalised since it was not possible to display absolute values with the background oxygen signal from the MgO substrate [67]. (c) Raman spectroscopy was used to create an oxygen profile across a YBCO thin film [70].

This laser writing approach is useful as it enables flexibility in the design of electric circuits. By being able to locally 'replenish' lost oxygen using a laser process, electrical circuits can be corrected or changed at anytime.

However, there is one drawback to this approach. Annealing a sample in a furnace with oxygen is a common step used in multiple processing methods to reduce process-induced degradation and to ensure a constant doping level for the whole sample. This would not be possible with the laser writing technique as intentionally oxygen depleted areas which are supposed to act as insulators might regain their superconducting properties. In addition, the oxygen rich lines may develop different oxygen levels leading to conductivity variations. Therefore the final patterning method, the complete removal of YBCO, will also be investigated in detail.

3.3.3 Laser ablation of YBCO thin films

Unlike the previous methods, the goal of this method is to change the overall surface morphology of YBCO by either forming sub-microstructures or completely removing (ablating) parts of the thin film to create patterns.

Patterning via laser ablation is particularly interesting since it is a one-step procedure, unlike lithography which is currently the main technique used to pattern YBCO. The core issue of lithography is degradation due to the use of chemicals. It is also a multistep process which requires masks which limits the design flexibility.

When comparing the performances of laser ablation and lithography, a comparison between the damage to the boundary interfaces is important. Figure 18 shows YBCO bridges machined using four different methods [71]:

1. Photolithography
2. Nanosecond laser machining without protective layer
3. Nanosecond laser machining with protective layer
4. Femtosecond laser machining

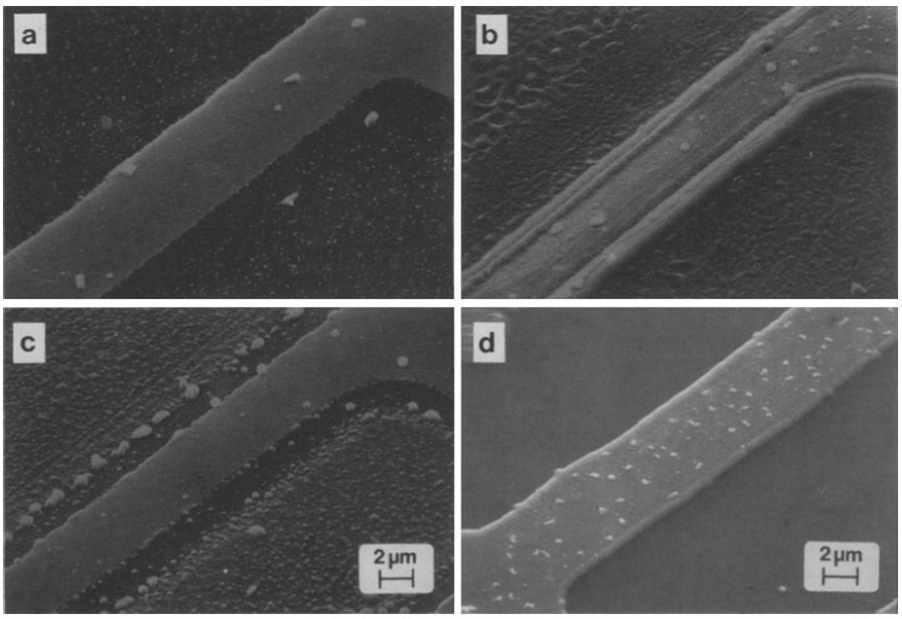

Figure 18: SEM images taken of YBCO bridges on MgO which were patterned using different techniques. (a) This bridge was patterned using standard photolithography followed by wet etching. (b) A nanosecond KrF-laser (λ = 258 nm with a pulse duration of 25 ns) was used to machine the YBCO without a protective layer. The laser fluence was 0.6 J/cm² and 100 pulses were necessary for full ablation. (c) This time the YBCO was machined through a protective photoresist layer with the same parameters as in (b). (d) The last bridge in this comparison was machined with a KrF femtosecond laser (500 fs) The laser fluence was 0.1 J/cm² using 50 pulses to machine the sample placed in a vacuum [71].

When the YBCO thin film was machined with a nanosecond laser without a protective layer, debris formations were observed in the surrounding area caused by material redepositions. The processed bridge also showed distinctive melted edges. When YBCO was machined through a protective layer, the width of the melt edges was reduced, and debris could be removed along with the protective layer post processing. However, in both cases fractions of the YBCO thin film remained on the substrate which could create shorts.

The main drawbacks of using nanosecond lasers are the damaged edges, the incomplete removal of the material from the substrate and finally the loss of oxygen caused by material being heated, leading to degradation of the bridge [71]. In contrast to nanosecond laser machining, thermal influences can be mitigated with a femtosecond laser due to its very short pulse duration [72]. The machined bridge from figure 18 (d) shows a comparable result to photolithography with almost no melting at the edges and complete removal of the film. It was possible to machine a bridge down to 4 µm with no degradation of T_c and J_c [71].

Based on these and similar results, femtosecond laser machining appeared to be promising, which is why it has been repeatedly used in recent studies. One example

is the use of femtosecond lasers to fabricate Josephson junctions [14]. A Josephson junction is a device consisting of two superconductors which are weakly coupled together across a thin barrier between them. They are mainly used in magnetometers and are being investigated for use in quantum computers. Depending on the type of barrier (insulator, normal metal, weaker superconductor, etc.), a Josephson junction shows different behaviours and properties, figure 19 [14], [73]. These differences can be used to identify the type of the junction which forms during machining providing information about the process induced degradation.

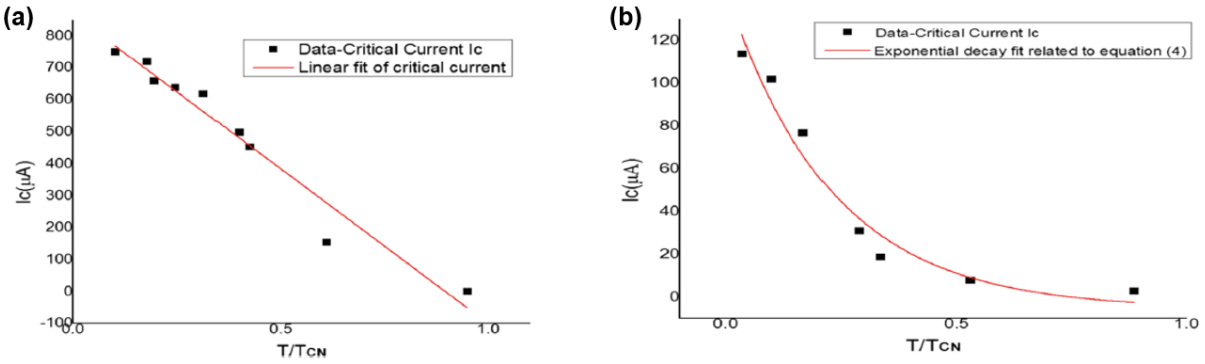

Figure 19: Depending on the type of the barrier, I_c shows a different relationship against the temperature. (a) When the superconductors are separated by a weaker superconductor, a linear trend of I_c over T_c is characteristic. However, if the barrier is a normal metal, this trend is becoming exponential (b). (T_{cN} = 87 K.) [14].

By using a femtosecond laser, micron (2.1 µm) and sub-micron (816 nm) sized Josephson junctions were successfully machined. Following transport measurements, the junctions were identified as a S-s'-S junctions (linear relationship between I_c and T_c) or S-N-S junctions (exponential relationship) respectively, where S stands for the unchanged superconductor, s' is the slightly degraded superconductor (with a lower T_c than S) and N means normal metal. Although both junctions were machined under the same conditions, their behaviour varies, which is assumed to be due to different amounts of process induced damage to the YBCO. While it has already been shown that the femtosecond laser process can significantly mitigate edge damage, thermal degradation still seems to occur to a certain extent [14]. Figure 20 shows AFM and SEM measurements of the sub-micron bridge as an example.

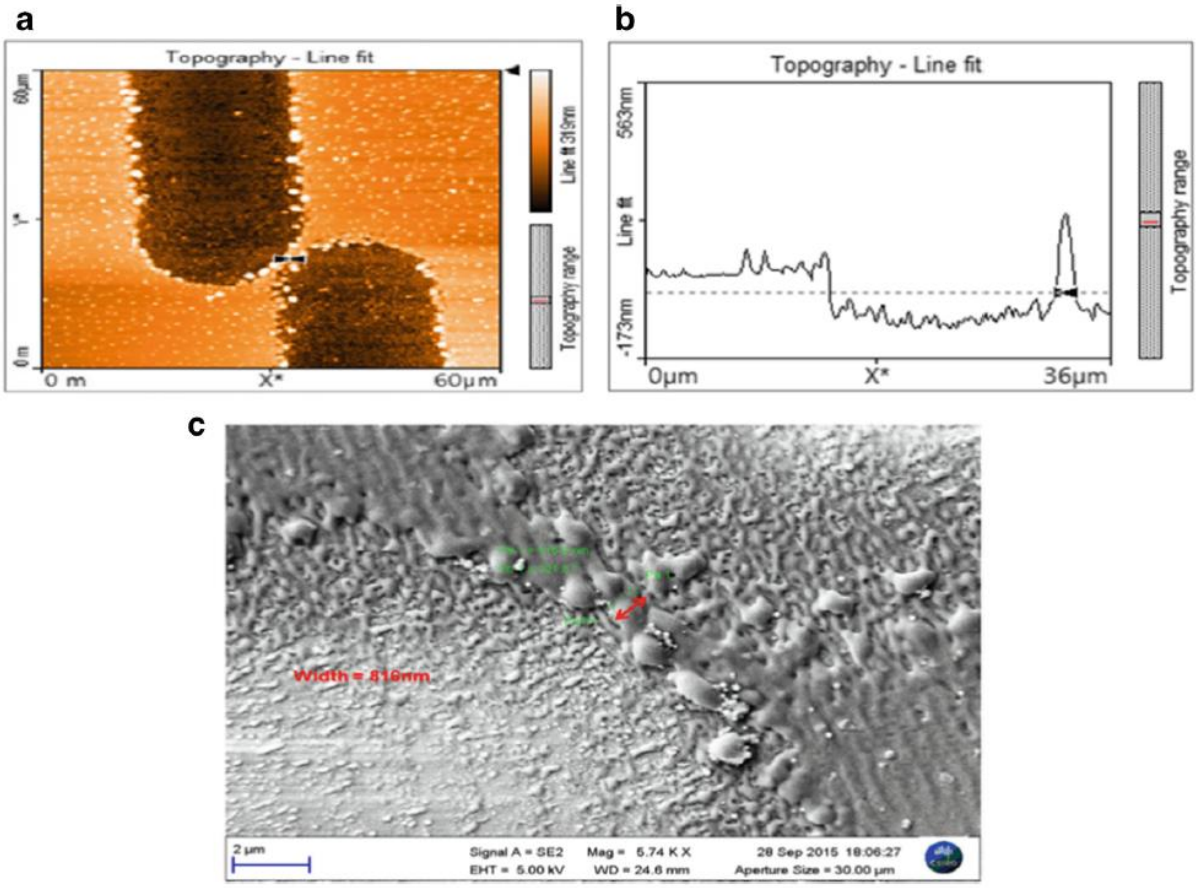

Figure 20: Measurements of a sub-micron Josephson junction made by a femtosecond laser with a pulse duration of 130 fs at 795 nm. (a) AFM profile of the junction. The black arrows in the middle mark the position of the junction. (b) The two-dimensional profile of the AFM measurement was used to measure the width of the junction (816 nm). (c) SEM image of the constriction. Lumps are spotted around the edges which is assumed to be due to spherical aberrations [14].

Femtosecond laser machining appears to be a promising technique to machine YBCO as it can completely remove YBCO from the substrate to create patterns even in the sub-micron regime. In addition to the complete local removal of YBCO, this technique can also be used to create ordered sub-micron array structures over a larger surface area. This approach could be used for the fabrication of microwave filter devices. Such organised structures were created for this study [74] by varying the laser fluence of an 800 nm femtosecond laser with a pulse duration of 35 fs to change the array type. Different fabricated array structures are shown in figure 21. The shape of the structures depended on the applied laser fluence [74].

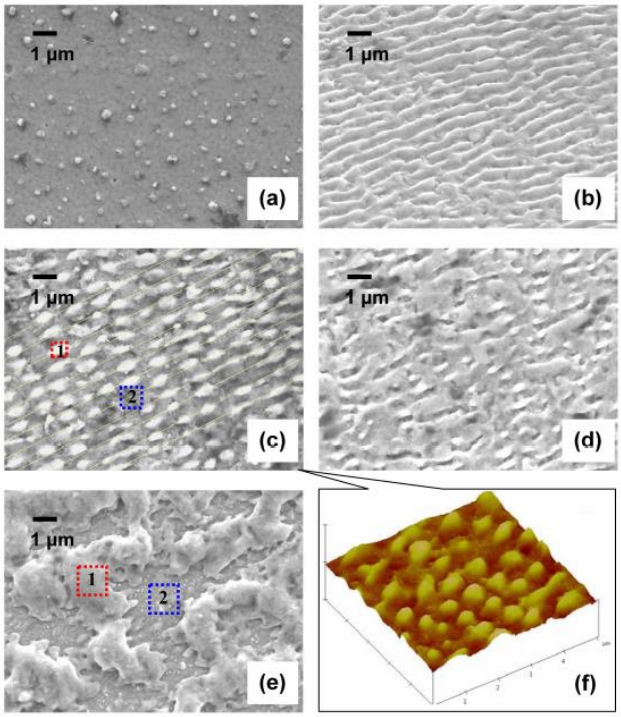

Figure 21: SEM images of multiple irradiated YBCO samples which were processed with a 800 nm laser and a pulse duration of 35 fs. (a) shows the surface morphology of an untreated sample for comparison. In (b), the film was machined with 0.21 J/cm². An organised ripple formation has been achieved. If the laser fluence is increased to 0.26 J/cm², the ripples change into an array of sub-micron dots (c). Above 0.32 J/cm², degradation and irregular patterns are observed (d). At 0.53 J/cm², the crystalline structure of the YBCO film has been destroyed which led to a loss of superconductivity (e). (f) shows an AFM image of the sub-micron dots in (c) [74].

When applying a fluence of 0.21 J/cm², a ripple formation with an orientation perpendicular to the laser polarization was achieved. This periodicity is likely caused by interference between incident and scattered laser light, resulting in an inhomogeneous energy input across the laser spot (110 µm). If the fluence is increased to 0.26 J/cm², the periodicity remains, but the ripples change to organised sub-micron dots approximately 150 nm high and with a diameter between 100 nm and 800 nm. The composition of the dots remained the same as the pre-treated YBCO and its intrinsic properties stayed intact. If the laser fluence is further increased to above 0.32 J/cm², the periodicity vanishes and the crystalline structure of YBCO is destroyed [74].

Overall, the femtosecond laser offers a flexible alternative to lithography, verifying the machining choice made for this thesis. It also shows mitigated heat effects with minimum degradation compared to the nanosecond laser. The femtosecond laser was not only successfully used to create Josephson junctions on the micron and sub-micron scale, but also used to create periodic structures with a high-quality crystalline structure.

3.4 Conclusion

This chapter provides a basic understanding of superconductivity with the main focus on the benefits of HTS, specifically thin films, for industrial applications. Superconducting thin films offer high critical current densities and as penetrating flux lines can be ‘pinned’ by structural changes and defects it is possible to further improve their performance. The material of choice for this thesis is YBCO which was also introduced. YBCO is the most researched HTS and while the fabrication methods have improved, machining YBCO remains challenging. There are many different approaches available, and even after narrowing it down to laser processing, different procedures could be used.

The current state of the art of laser machining YBCO has therefore been investigated in more detail. One approach described the patterning of the substrate before the film is deposited to grow defected YBCO on specified areas. While this procedure has the advantage that processing damage to the YBCO itself is avoided, it would require the non-bridge parts of patterned films to be tested to check if the defected YBCO is fully insulating. Another approach is to use the laser on YBCO directly to selectively dope and deplete the oxygen content. This technique is attractive as it can be easily reversed by changing the machining atmosphere and the laser parameters. The disadvantage of this approach is that most samples are annealed post processing in multi-step manufacturing lines. This could change the oxygen levels and lead to conductivity variations which would alter the circuit away from its design. The processing speed is also limited by the rate of oxygen uptake/depletion. To realize faster processing speeds (> 1 µm/s), another option is to ablate selective parts of the film to create superconducting tracks. This would ensure a high resistance between the superconducting tracks, so avoiding current jumps, and the processing speeds can be increased to mm/s and more depending on the equipment. The limits are not set by a chemical reaction but by the capabilities of the stage/scanning system, providing even more design/processing freedom. The limits of laser ablation in terms of processing damage has still not been formally evaluated and further investigation is needed.

4 Raman spectroscopy on YBCO

There are several measurement strategies next to transport measurements that are used to analyse the oxygen content of YBCO, such as optical transmission measurements [75], X-ray diffraction (XRD) [76], Energy-dispersive X-ray spectroscopy (EDX) [67] and Raman spectroscopy [77]. The oxygen doping of YBCO is directly connected to its electrical properties as discussed in section 3.1.2. While all of these measurement methods provide information about the oxygen content of YBCO, XRD and EDX require the sample to be moved to separate measurement devices, increasing the overall processing time and adding possible alignment errors which means a direct feedback loop cannot be provided. EDX is also not ideal for thin film samples as its interaction volume is larger than the film cross-section. In contrast, optical transmission measurements and Raman spectroscopy could be integrated into the machining process for in-line feedback.

For this work, Raman spectroscopy was chosen as an analysing tool due to its low cost and as it can be integrated either in-line or in parallel to the laser machining objective. It can also provide information about the chemical composition of YBCO by analysing the resulting complex spectra, as compared to optical transmission which only provides information about changes to the optical properties. The interaction volume on the sample is defined by the laser spot size and the wavelength-dependent optical penetration depth. Hence, the sampling area of interest can be adjusted accordingly by choosing suitable Raman settings.

Raman spectroscopy is able to characterise the physical properties and chemical compositions of different materials by investigating specific molecular electronic states and vibrational modes [78], [79]. This technique is a non-contact procedure and so avoids damage to the sample. To understand the basic principle of Raman spectroscopy, it is necessary to know the difference between Rayleigh and Raman scattering.

4.1 Rayleigh and Raman scattering

There are different scattering events which can occur when light strikes molecules. These scattering events can be mainly split into elastic and inelastic scattering.

Elastic scattering is also known as Rayleigh scattering. In this case a photon is scattered off molecules or particles with a size up to 1/10 of the light's wavelength. Since it is an elastic process, the photon's energy does not change during scattering, hence the wavelength of the photon remains the same [80].

Compared to Rayleigh scattering, Raman scattering is an inelastic scattering process. During this process, an energy exchange between photon and molecule occurs. The wavelength of the photon changes due to this interaction. However, the intensity of the Raman effect is much lower than the intensity of Rayleigh scattering as shown in figure 22 [81].

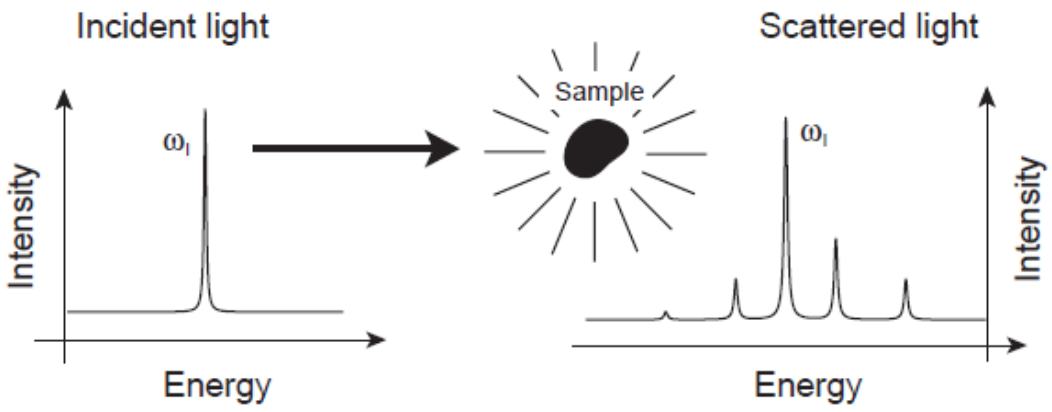

Figure 22: Monochromatic light strikes a sample. As a result, different energy peaks with different intensities are detected. The smaller signals are the result of Raman scattering processes. The energy of the incident wavelength has the highest intensity due to Rayleigh scattering [82].

In figure 22, the spectrum on the right shows the post-scattering spectrum, with a large Rayleigh peak at the incident light frequency and multiple smaller energy bands next to the Rayleigh scattering peak from Raman scattering. These Raman energy bands correspond directly to the vibrational modes of the sample. The number and Raman energy shift of the vibrational modes depend on the sample's chemical composition [83]. Each molecule or chemical compound has 3N degrees of freedom in which N resembles the number of atoms involved in the compound. These degrees of freedom describe translational and rotational motions [84].

The incident photons of a laser cause a disturbance in the compound, which excites the particles from their ground state to an unstable virtual energy level. Since each particle needs to return to a stable energy state, the photon loses energy corresponding to a certain phonon energy of the particle, changing the vibrational

mode of said particle. Therefore, the wavelength of the scattered photon is changed, and the particle moves to a stable excited vibrational state. This process is called Stokes scattering. In addition to Stokes scattering, the photon can also gain energy, which is called Anti-Stokes scattering. In this process, the photon hits an already excited particle. To reach again a stable energy state, the photon gains energy from a phonon before being re-emitted to return the particle to the ground state, figure 23 [85].

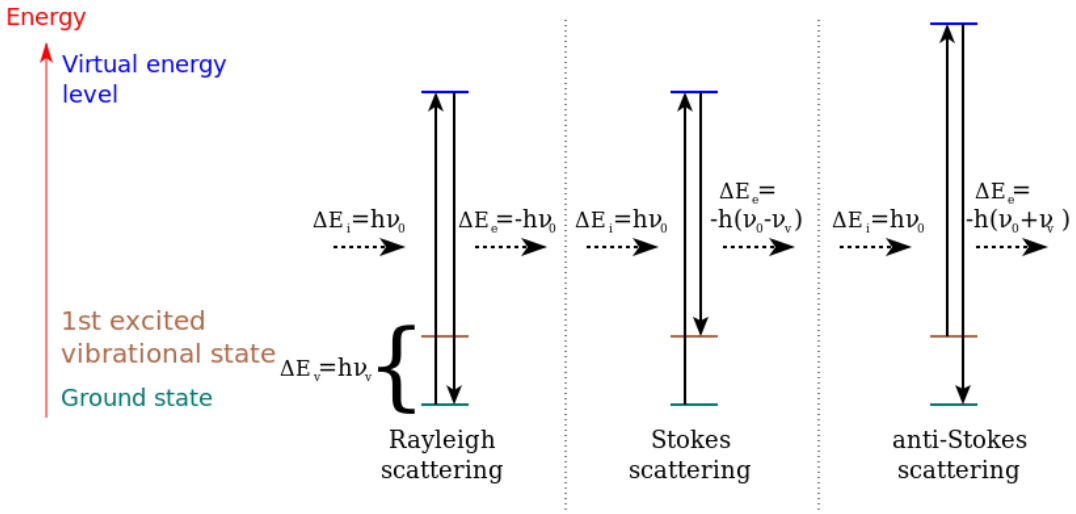

Figure 23: Light can be scattered in various ways. When light is exciting a particle to a virtual energy level and this particle emits the same amount of energy to return to its ground state, the scattering process is called Rayleigh scattering. For stokes scattering, a particle is excited to the virtual energy level. By emitting some energy, it then returns to the first excited vibrational state. Anti-stokes scattering occurs when a particle on the excited vibrational state is further excited to the virtual energy level. The particle then emits more energy to return to the ground state [86].

For further explanations regarding the photon-phonon interaction and the resulting Raman scattering see reference [87].

The most commonly used units for Raman spectra are intensity in arbitrary units (a.u.) [88] and wavenumbers in cm^{-1}. The wavenumbers are defined by the shift in wavelength between the incident monochromatic light and the wavelength of the scattered Raman light [89]. The wavenumber $\bar{\nu}$ can be calculated using the following equation (17) [83].

$$\bar{\nu} = \frac{1}{\lambda_{incident}} - \frac{1}{\lambda_{scattered}} \tag{17}$$

Since Raman spectroscopy measures the vibrational modes which are dependent on the chemical composition and structure, each material shows a unique spectrum. In the following section, the Raman spectrum of YBCO is introduced, and what information different Raman peaks is explained.

4.2 Raman signals measured on YBCO

In the case of YBCO, Raman spectroscopy can provide information about the crystallographic directions of the epitaxial growth and the oxygen ordering in the crystal structure [90]. This information can be used to qualify the quality of thin films as the Raman spectra stand in direct correlation to the film's superconducting properties [77].

4.2.1 Epitaxy

Most YBCO is grown epitaxially. The crystals are orientated with the *c*-axis perpendicular to the substrate, figure 24 (a) [91]. The superconducting properties of a thin film, such as the critical current density, have their optimal values when the crystalline axes within the plane (i.e. *a*/*b*) are also aligned [15]. Therefore, it is essential to know the epitaxial orientation, especially during the fabrication process, and Raman spectroscopy can provide a quantitative evaluation of this for YBCO thin films [91].

A schematic image of the crystalline axes in YBCO is shown in figure 24.

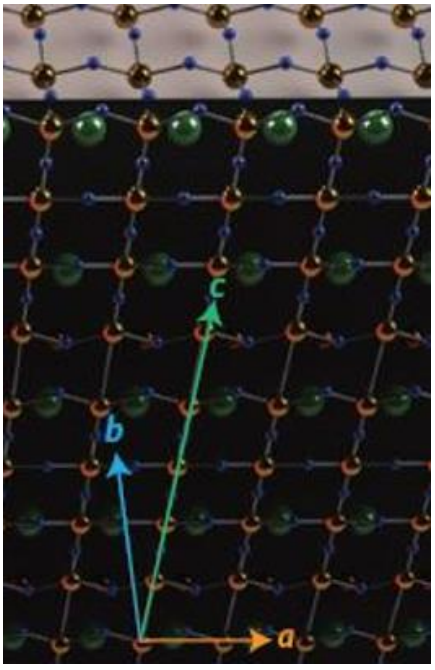

Figure 24: Crystalline axes (a, b, c) of YBCO [92]. The axes have different lengths. While a and b are similar with 3.82 Å and 3.88 Å respectively, the c axis measures 11.68 Å [3].

There are three different possible crystallographic orientations of the *a* and *b* axes which can be identified with Raman spectroscopy [91], [15]:

1. Untwinned: *a* and *b* axes possess a long-range order and match the substrate order. The film is truly epitaxial and has orthorhombic symmetry.

2. Twinned: *a* and *b* axes are ordered along the substrate axes but alternate randomly.
3. Textured: *a* and *b* axes are randomly orientated.

With Raman spectroscopy it is possible to determine the degree of epitaxy by using different polarisations of the excitation laser beam or different orientations of the sample if the orientation of the film's axes is known. The degree of epitaxy, η, of a film can be determined by the ratio, M, of parallel and perpendicular polarisation intensities of the oxygen vibration in the copper-oxygen planes which is located at 340 cm^{-1}, equation (18), (19) and figure 25 [15], [91].

$$\eta = \frac{1 - M}{1 + M} \tag{18}$$

$$M = \frac{I_{xx}}{I_{xy}} \tag{19}$$

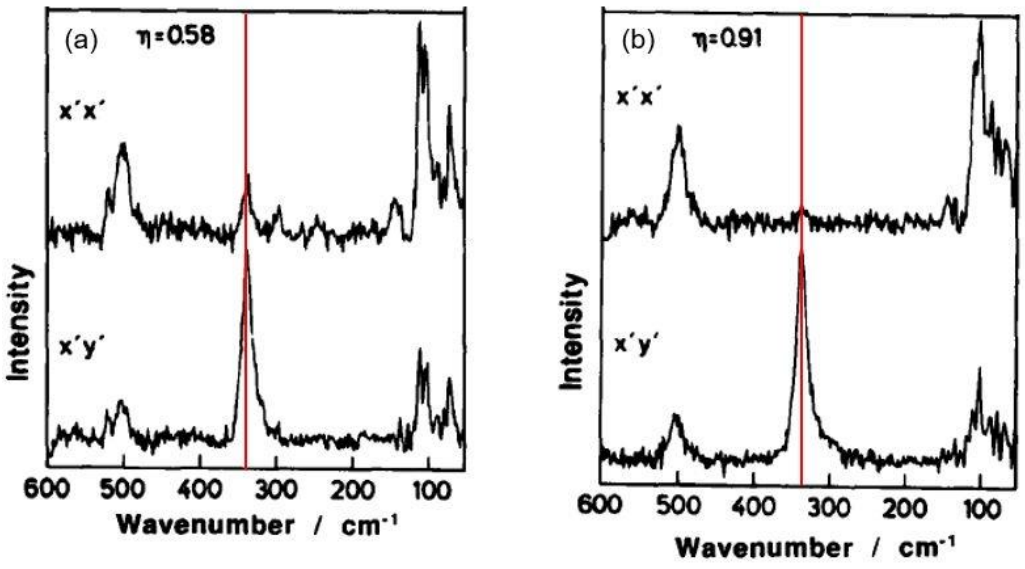

Figure 25: Two Raman spectra of different YBCO thin film samples. (a) The ratio of the peak intensities at 340 cm^{-1} indicate an epitaxy degree of 58%. (b) Nearly complete epitaxy. The epitaxy has a degree of 91%. The error in these measurements is ~ 2% [91].

4.2.2 Oxygen doping

YBCO or $YBa_2Cu_3O_{7-x}$ is very sensitive to its oxygen level which is indicated by x. For x = 0 YBCO has an orthorhombic elementary cell structure, also called Ortho I YBCO (superconductor) [90]. This structure consists of Y, Cu2-O2/O3, Ba-O4 and Cu1-O1. The oxygen content can be changed by, for example, thermal annealing. When O1 is fully removed and x = 1, the *a* and *b* axes become equivalent, and the

elementary cell structure is tetragonal (T YBCO, semiconductor) and remains like so for x > 0.65, figure 26 [90], [93].

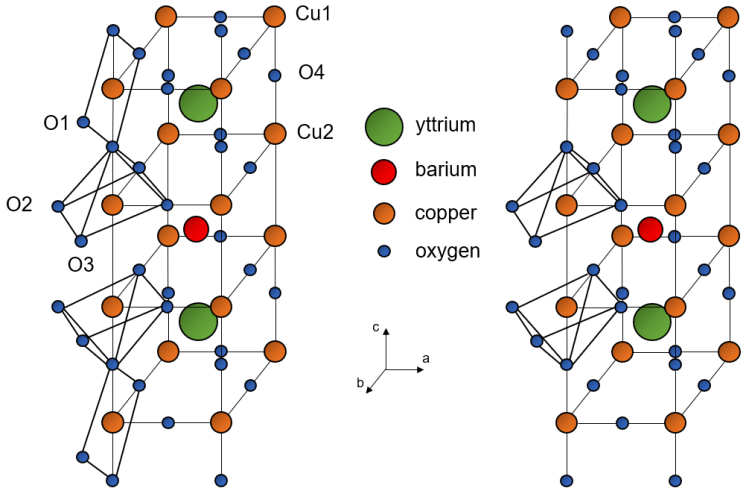

Figure 26: The orthorhombic elementary cell structure is shown on the left, and the tetragonal oxygen depleted cell structure on the right. The schematic was designed in reference to figure 1 of [94].

For intermediate oxygen values (0 < x < 1) an inhomogeneous distribution of the oxygen atoms occurs within the Cu1-O1 planes. This leads to a orthorhombic to tetragonal transition at x ~ 0.65, which also correlates with the loss of superconductivity [90], [93]. As x increases, due to the oxygen deficit the inter-grain regions within YBCO become larger and result in weaker grain coupling. This leads to low critical temperatures T_c and finally to the loss of superconductivity [95]. A Raman spectrum for YBCO at different oxygen levels is shown in figure 27.

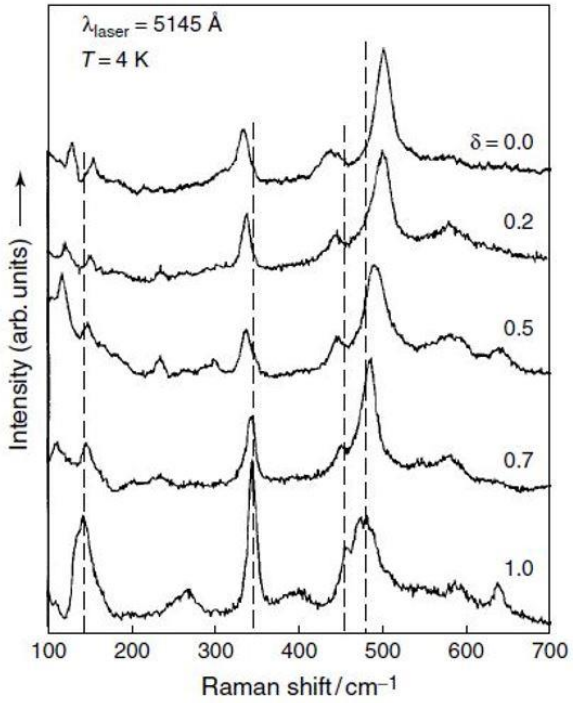

Figure 27: Transition from orthorhombic to tetragonal YBCO due to different oxygen levels [15]. δ equals x.

Both Ortho I and T YBCO structures have 15 Raman active vibrational modes. However, only the five phonons with their motional vector along the *c*-axis are detected with a noticeable intensity in epitaxial films, figure 28 [94].

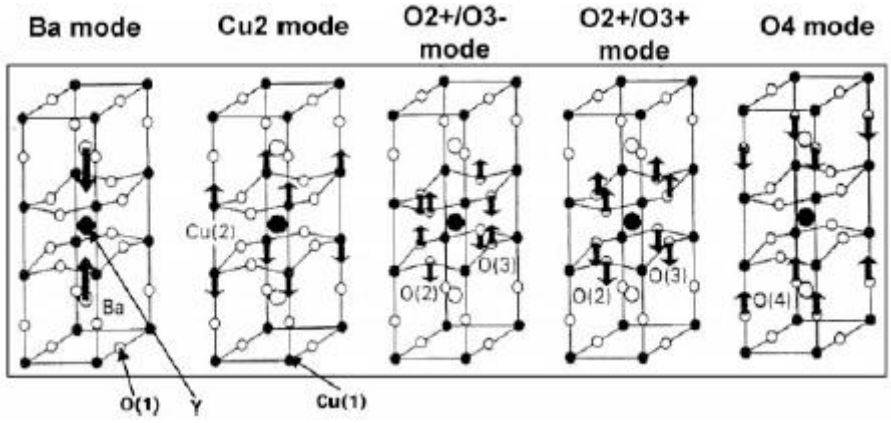

Figure 28: Raman active phonons with motional direction along c axis [94].

These five vibrational modes are the same for both Ortho I and T YBCO. They show five significant peaks at 115 cm^{-1} (Ba), 154 cm^{-1} (Cu2), 334 cm^{-1} (O2), 438 cm^{-1} (O3), and 502 cm^{-1} (O4) [15], [93]. However, during the transition from orthorhombic to the tetragonal structure, the vibrational modes at 115, 154, and 502 cm^{-1} soften, while the modes at 334 and 438 cm^{-1} harden [15].

In addition to Ortho I and T YBCO, there are other microdomains, which can coexists within one sample, figure 29 [93].

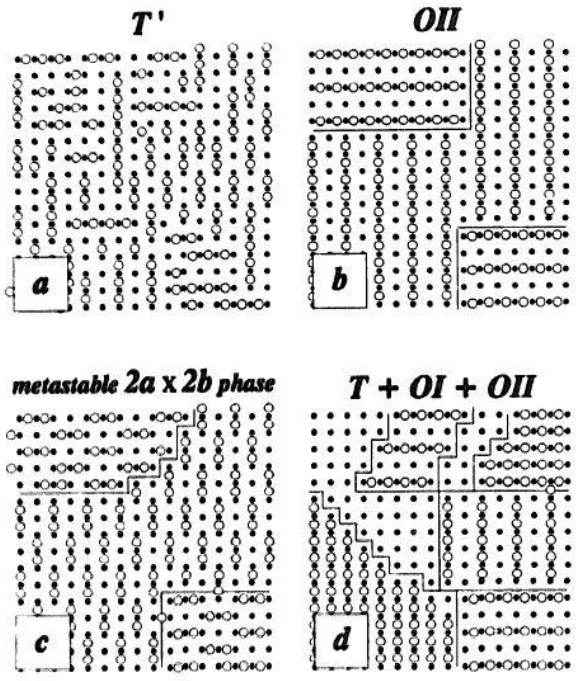

Figure 29: Possible oxygen arrangements for x = 0.5 in the Cu1-O1 layer. White: oxygen, black: copper [90].

Raman spectroscopy is sensitive to these microdomains as they have different Raman active vibrational modes [90], [93]. Ortho II, for example, originates from elementary cells which are doubled along the *a* axis with an oxygen level of x = 0.5. Hence, the number of Raman active modes becomes larger [15]. However, while the Ortho I and T domains are easy to detect within the Raman spectrum, Ortho II is significantly more difficult to detect. Overall, it is only clear that there are different microdomains within one spectrum, but they do not seem to be distinguishable so far.

Another way to gain information about the oxygen doping of YBCO is by using the O4 mode. The O4 mode shifts to lower wavenumbers when the sample is oxygen depleted. The change in oxygen content can therefore be calculated by analysing the shift of the O4 mode using equation (20) [96].

$$x = 0.025 v_{OIV} - 5.57 \tag{20}$$

where x describes the oxygen content and v_{OIV} is the wavenumber of the O4 vibrational mode. Using this information, the oxygen content of YBCO thin films can be calculated.

4.2.3 Comparison between normal and superconducting state

Raman peaks are characterised by their asymmetry and intensity. In the normal state of a superconductor, the lifetime of a phonon and its energy correspond to the linewidth and frequency of a peak in the Raman spectrum. By changing from the normal to the superconducting state, spectral changes are observed which are called superconductivity-induced anomalies. An example is shown in figure 30.

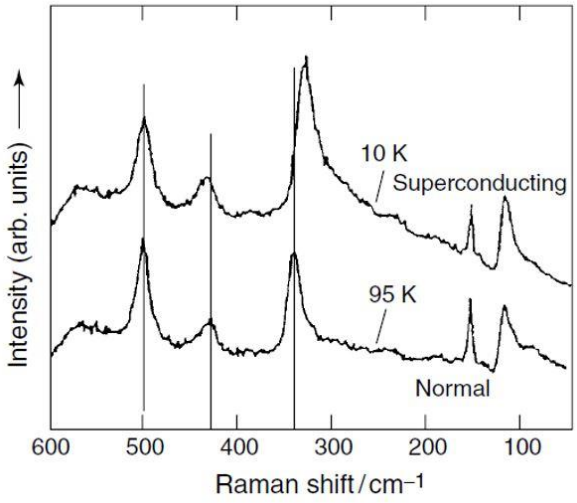

Figure 30: The superconductivity-induced anomalies are visible in linewidth, frequency, and amplitude of the Raman peaks [15].

Several anomalies occur caused by the transition from normal to superconducting state. The intensity of the 340 cm^{-1} mode increases and shifts towards lower wavenumbers. The shape is also changing for the 440 cm^{-1} mode with a slight shift to higher wavenumbers. The 440 cm^{-1} and 500 cm^{-1} modes also slightly broaden. The 500 cm^{-1} mode also appears to decrease in intensity. These changes are indicators of changing phonon properties [15].

4.2.4 Cation disorder

Despite the five mentioned Raman modes, another band often appears in the 570 cm^{-1} – 590 cm^{-1} range. This band is caused by cation disorder, figure 31 [94].

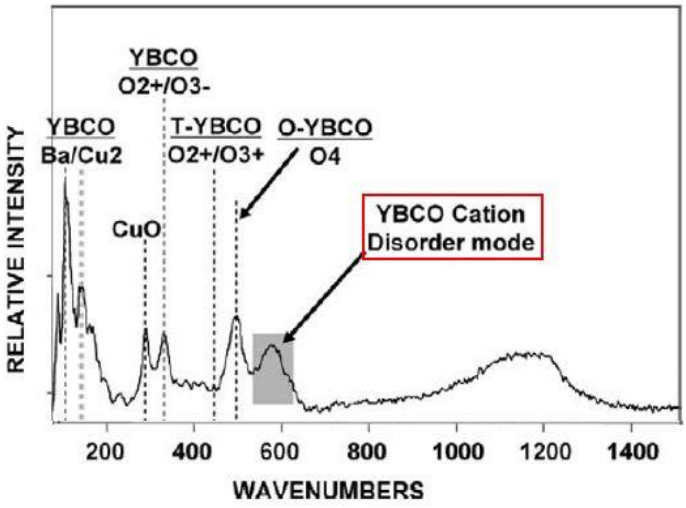

Figure 31: Cation disorder mode of T YBCO after oxygen anneal to produce Ortho I YBCO [96].

Cation disorder occurs due to an incomplete formation reaction, infiltration by foreign cations from the substrate or buffer layer, or anti-side misordered parent cations [94].

4.3 Limitations

There are some limitations to using Raman spectroscopy on YBCO. The spectra are complex, and the interpretation can be difficult, especially when intermediate oxygen levels need to be examined.

The measured spectra can also be influenced by the substrate, which can have Raman active modes depending on the excitation wavelength used. It might be necessary to subtract the Raman spectrum of the substrate as vibrational modes from the substrate could overlay modes from YBCO. An example is shown in figure 32. These spectra are from a YBCO sample grown on a $NdGaO_3$ substrate [95].

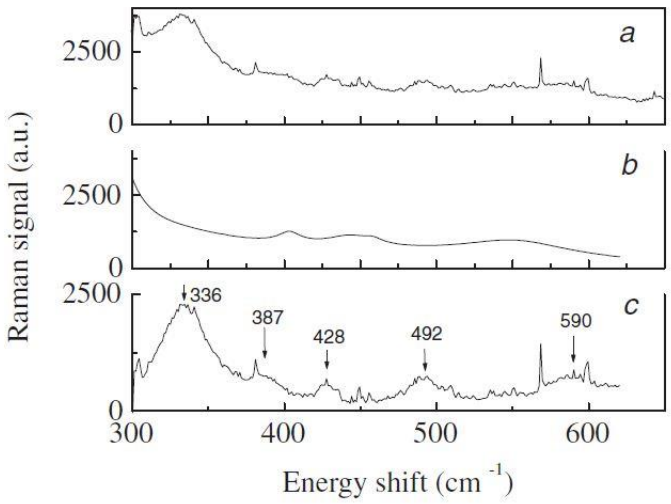

Figure 32: (a) Measured data. (b) Spectrum of $NdGaO_3$. (c) YBCO spectrum after subtracting the substrate spectrum [95].

Further limitations are system dependent. The vibrational modes can be shifted slightly when different laser wavelengths are used. Thus, the spectra might vary. Furthermore, the spot size is a limiting factor. If the feature of interest is significantly smaller than the spot size, the information from this feature might get lost in the Raman signal of the rest of the illuminated area.

4.6 Conclusion

Raman spectroscopy is a versatile tool providing a wide range of information about a sample's composition. For YBCO, the Raman spectrum is complex, and the number of modes can change depending on the laser polarisation, the material's quality and available microdomains. Due to the complexity of this measurement technique and since it is not a traceable technique, it is hard to compare individual results from different papers, however, most literature agree on the position of four modes [15], [90], [91], [93], [96], [97], [98]:

- Ba: the vibrational mode of barium is located at about 110 cm^{-1}.
- Cu2: the Cu2 atom is in the planes surrounding yttrium. Its vibrational mode is found between 140 cm^{-1} and 150 cm^{-1} depending on the oxygen doping.
- O2+/O3-: this mode is caused by the out-of-phase vibration of OII and OIII and is located at 336 cm^{-1}. This vibrational mode is stable in its location.
- O4: the vibrational mode of O4 changes in frequency depending on the oxygen doping and can be used as a direct indicator to determine whether the sample

is superconducting $YBCO_7$ or degraded $YBCO_6$. The signal moves from around 500 cm^{-1} to lower wavenumbers with decreasing oxygen doping.

While it was shown that the O4 mode has a direct correlation to the oxygen content of YBCO, it has not been connected to transport measurement results. In general, a direct comparison between spectral changes and transport measurements has not been determined.

4.7 Revised research questions

Based on the literature review, the original research question is extended by further, more detailed, questions based on identified research gaps and problems:

- Can process induced degradation due to heat be completely avoided? What are the best processing parameters to achieve this?
- What is the minimum achievable feature size? Is it possible to create sub-wavelength structures on YBCO to machine feature sizes in the nanometre regime?
- Since the ultrafast laser process depends on electron-phonon interactions, how does the machining behaviour change when superconducting Cooper pairs are involved?
- Could Raman spectroscopy be used as a tool to predict changes in the electrical properties, e.g. changes in J_c?

5 Sample preparation and experimental techniques

This chapter describes the sample layout and the different experimental setups that have been used in this work.

5.1 YBCO microbridges

Two types of YBCO thin film samples were available. For the initial machining trials and parameter optimisation, a 10 x 10 mm thin film sample supplied by Ceraco is used. R-cut sapphire substrates were deposited with a 40 nm CeO_2 buffer layer and a 200 nm thick M-Type YBCO. The YBCO film has a T_c of 86.6 K and a J_c of 3.4 MA/cm². The sample specifications can be found in Appendix 2.

In addition to the 10 x 10 mm YBCO thin film samples, bridge samples were specially designed to be measured using a local four-point probe setup. To ensure the compatibility of the new sample design and the measurement setup, the dimensions of an existing sample were measured and converted into a CAD model using SolidWorks, figure 33.

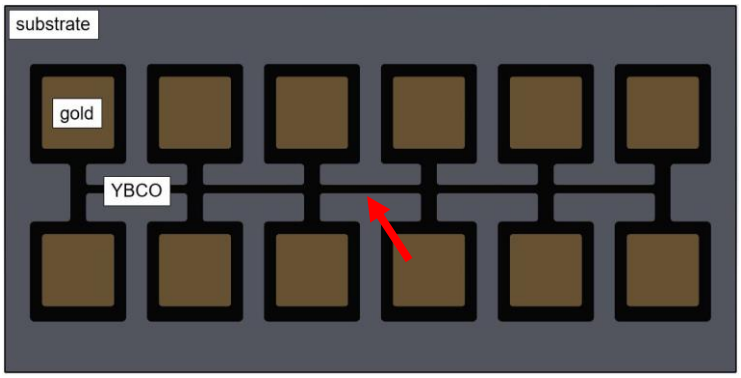

Figure 33: SolidWorks model of YBCO microbridges.

Each YBCO pattern contains five microbridges (red arrow) which can be measured individually. The gold pads on YBCO are necessary to create an electrical contact with minimum resistance to the four-point probe. This also requires the width of the contact lines between the gold pads to be significantly larger than the bridge width, as shown in figure 34.

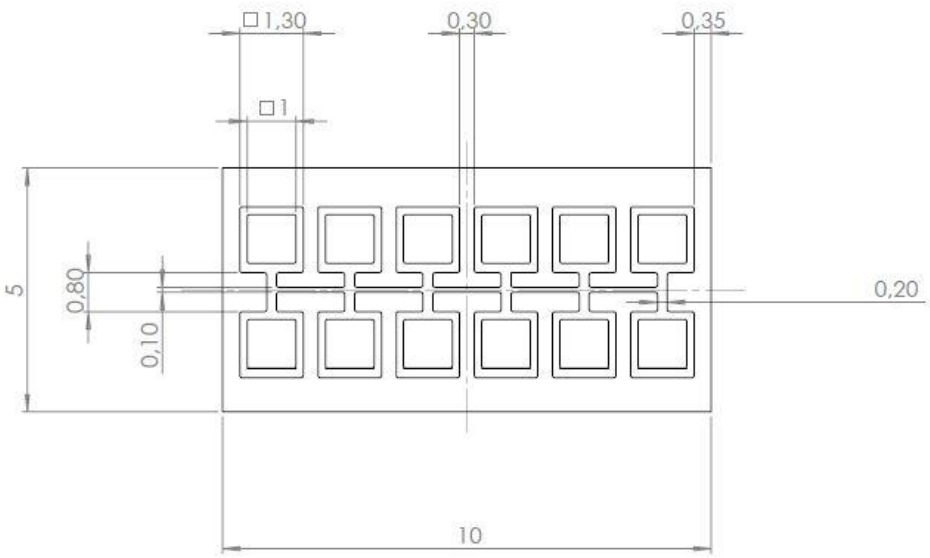

Figure 34: Drawing of the YBCO pattern on a substrate. The dimensions are in millimetres.

It shows that the contact lines between the pads are 200 µm wide while the bridges are between 10-100 µm. This ensures that the resistance of a bridge is measured and not the lines in-between the contacts. All corners were rounded with a 50 µm radius to avoid accidental flux pinning and local current crowding [8].

A photomask for a 2" MgO wafer with 28 patterns for 100 µm, 30 µm, and 10 µm bridges was designed and sent to StarCryo for manufacture, figure 35.

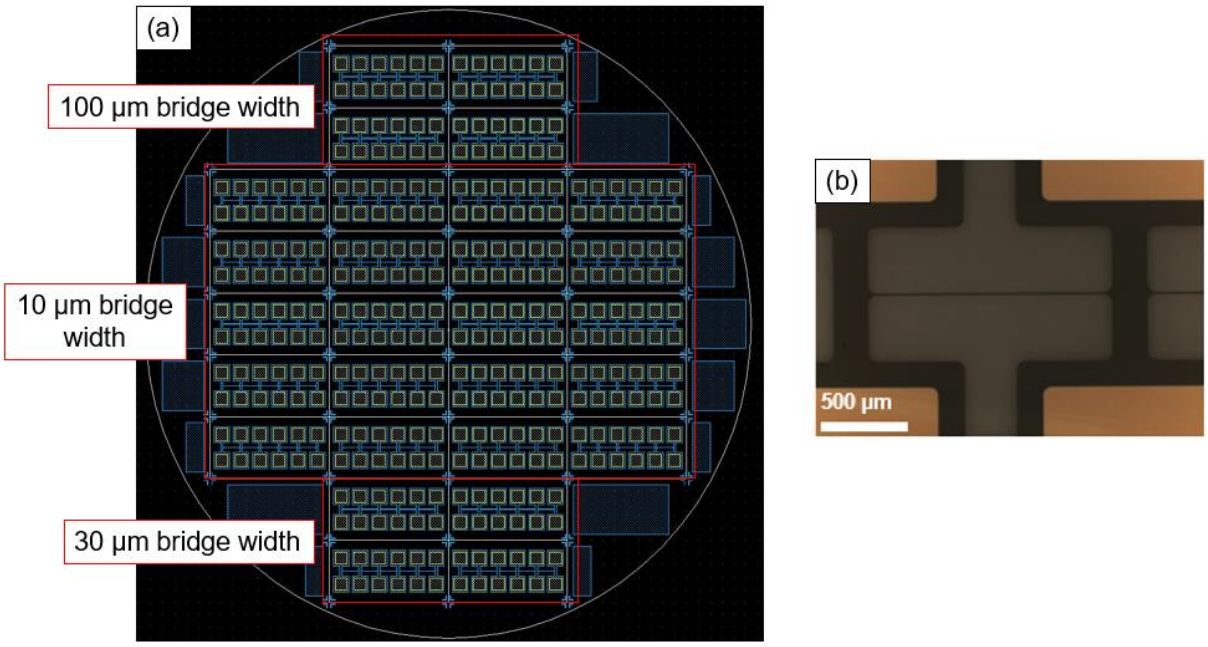

Figure 35: (a) Photolithography mask for YBCO samples made with Layout Editor. (b) Manufactured bridge by StarCryo using lithography. The bridges widths have an uncertainty of ± 0.5 µm.

The photomask was used on a 200 nm thick M-Type YBCO film deposited on a MgO substrate with 20 nm Au contact pads deposited in-situ in the positions outlined in the above design. Prior to lithography, a T_c of 86.2 K and J_c of 3.0 MA/cm² was measured for the YBCO film. The sample specifications can be found in Appendix 3. A SEM image of the film structure is shown in figure 36.

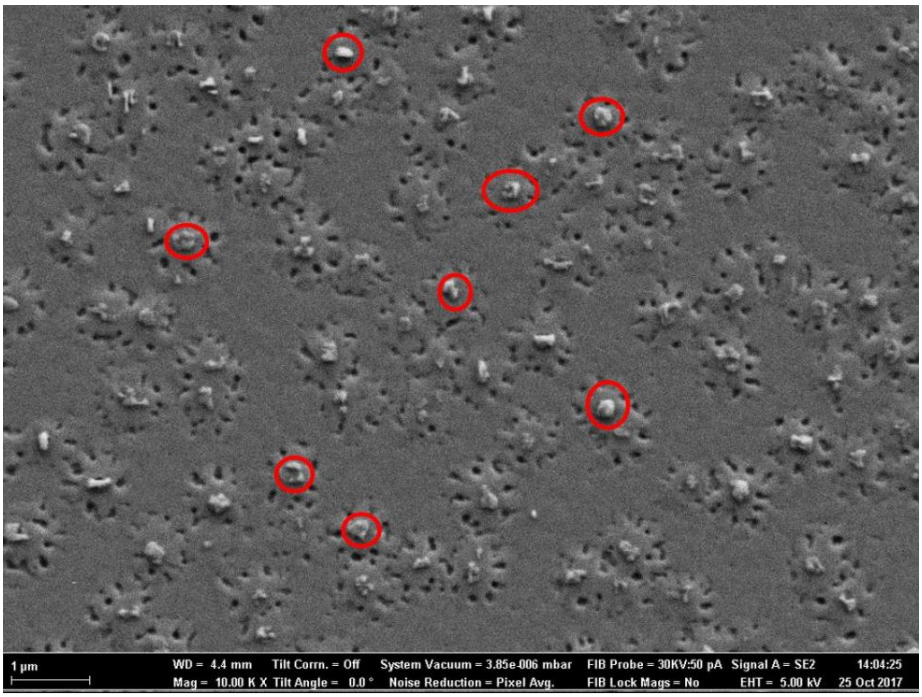

Figure 36: Surface structure of the YBCO thin film samples.

The film shows pores and crumb-like features. After a discussion with the film manufacturer, they clarified that the crumb-like features, marked with red circles, are copper oxide precipitations and the pores formed due to Yttrium excess. This structure is important for high T_c and high I_c.

The wafer is covered in a polymer film to protect the bridges from de-oxygenating. Before processing, the film is removed using acetone and flushed with isopropanol to avoid residues on the surface. Immediately afterwards, the sample is then dried with nitrogen gas to prevent any degradation due to the hydroscopic properties of the solvents used.

5.2 Transport measurements

To determine the I_c of YBCO bridge samples, a four-point-probe setup was used. A setup schematic is shown in figure 37.

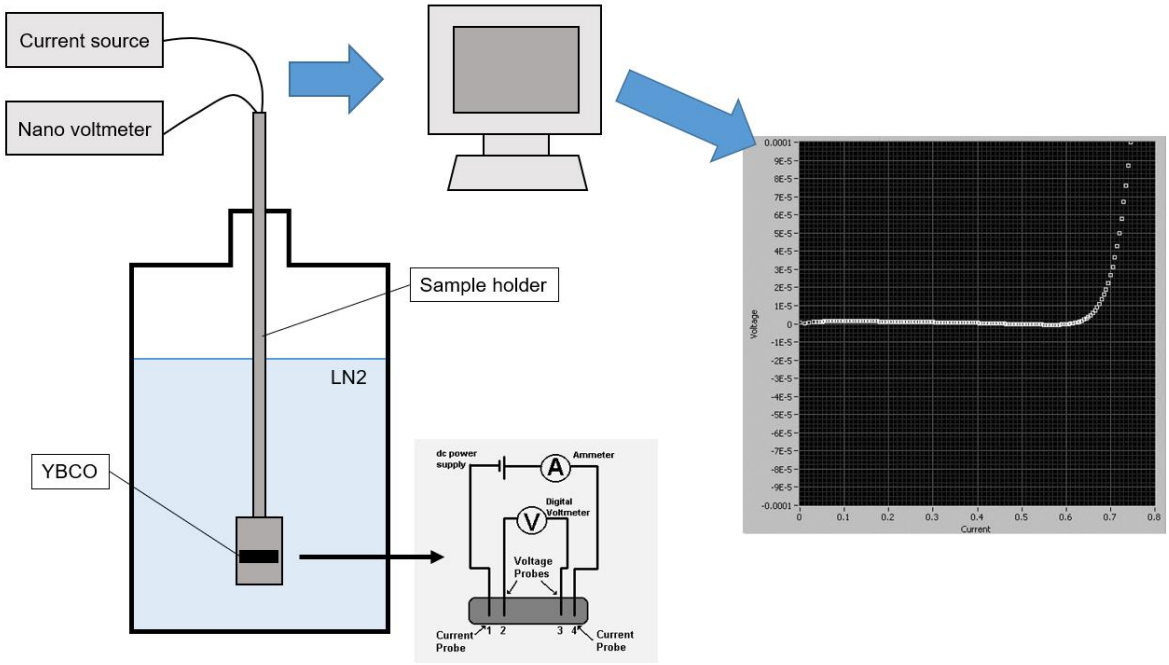

Figure 37: I_c measurement setup for YBCO bridges.

The I_c setup uses liquid nitrogen, which eliminates the necessity of a temperature sensor as the temperature will be constant for all measurements. Once cooled down to the boiling point of liquid nitrogen (~77 K), a Keithley 2440 5A current sourcemeter with a maximum current of 5.25 A sends pulsed currents through the sample. The generated voltage is picked up by a Keithley 2182 A nano voltmeter. A computer connected to both sourcemeter and nanovoltmeter then uses purpose built labview software to create a measurement curve and read out the I_c value once a set criterion voltage was surpassed.

Each sample contains five bridges which need to be measured individually. To flexibly change the measurement position, a sample holder for the YBCO bridges was designed and manufactured, figure 38.

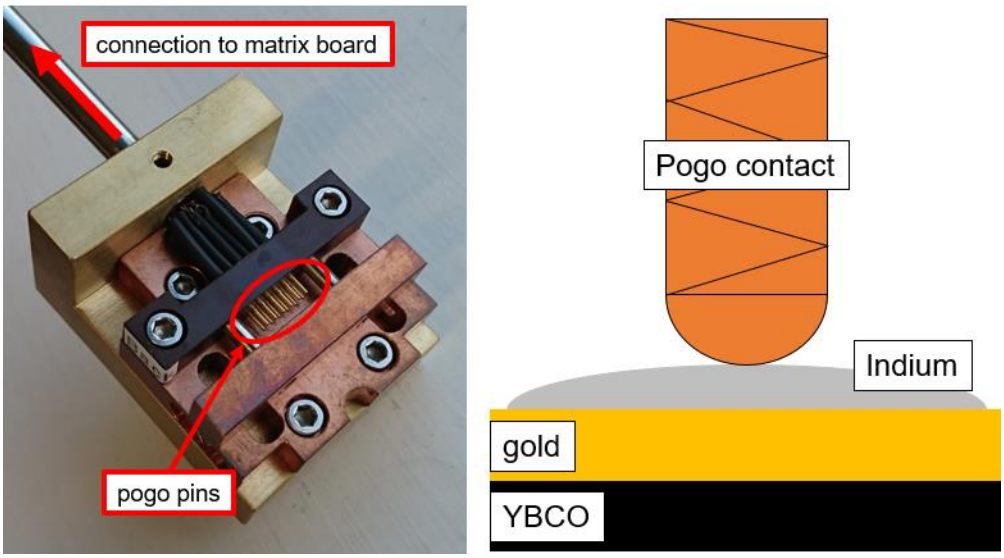

Figure 38: Designed sample holder for four-point I_c measurements. Indium is placed onto the gold pads to form a higher contact area with the pogo pin as shown in the right.

This sample holder contains 12 spring-loaded pogo pins which are connected to a matrix board leading to the current source and voltmeter. Before inserting a sample, indium was added on top of the gold pads to increase the contact area between the round tip of the pogo pin and the sample. Without the indium, contact could also be interrupted due to thermal contraction during measurement.

To decrease contact heating/TAFF and to improve the stability of the measurement setup, the time delays between the current pulses were varied, figure 39. One current pulse is 680 ms long.

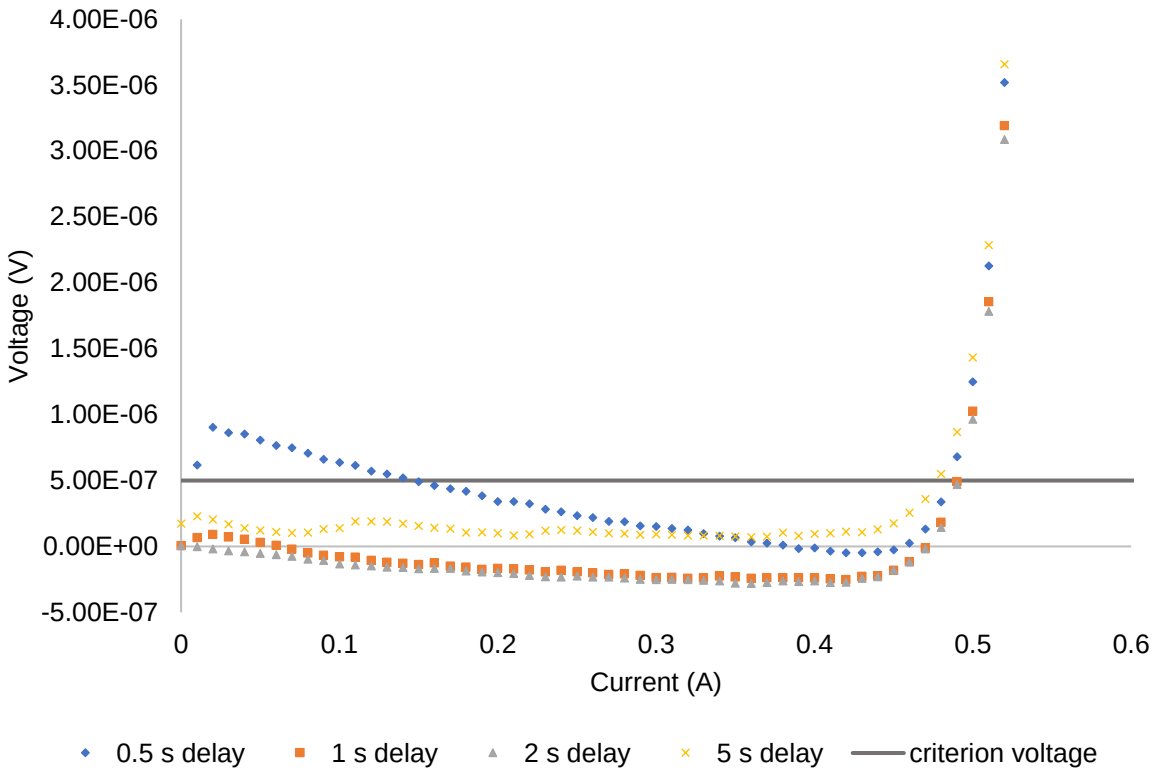

Figure 39: Voltage vs current plot with different time delays between the current pulses.

With a 0.5 s time delay, TAFF/contact heating seems to be more dominant as the curve rises in the beginning before it slowly stabilises around 0.35 A. For 1 s and 2 s time delays, both measurement curves show negative voltages until reaching the critical current. The measurement curve with the 5 s time delay appears stable, suggesting that with a 5 s delay the contacts have time to cool down after each current pulse. The time delay could be further increased, but a compromise between overall measurement time and result needed to be found. Following this result, all subsequent measurements were done with a 5 s delay and a criterion voltage of 0.5 µV. The criterion voltage is a defined voltage at which (once surpassed) the critical current is measured. This voltage was chosen due to the bridge widths being < 100 µm. Normally a 1 µV/cm criterion is used as a measurement standard [99]. For these YBCO samples that would mean that the criterion voltage is 0.15 µV. (The bridges are 1.5 mm long.) However, any criterion voltage below 0.5 µV would become erroneous due to inaccuracies at small voltages for this measurement setup.

5.3 Raman spectroscopy

As previously discussed, Raman spectroscopy is a non-contact procedure which can be used to characterise physical properties of materials based on their vibrational modes and molecular electronic states [100], [79]. This analytical tool can provide information about the oxygen ordering of YBCO thin films [90].

The available Bruker Senterra Raman microscope has three lasers (with wavelengths of 532 nm, 633 nm, and 785 nm) used to excite the sample for inelastic Raman scattering, figure 40.

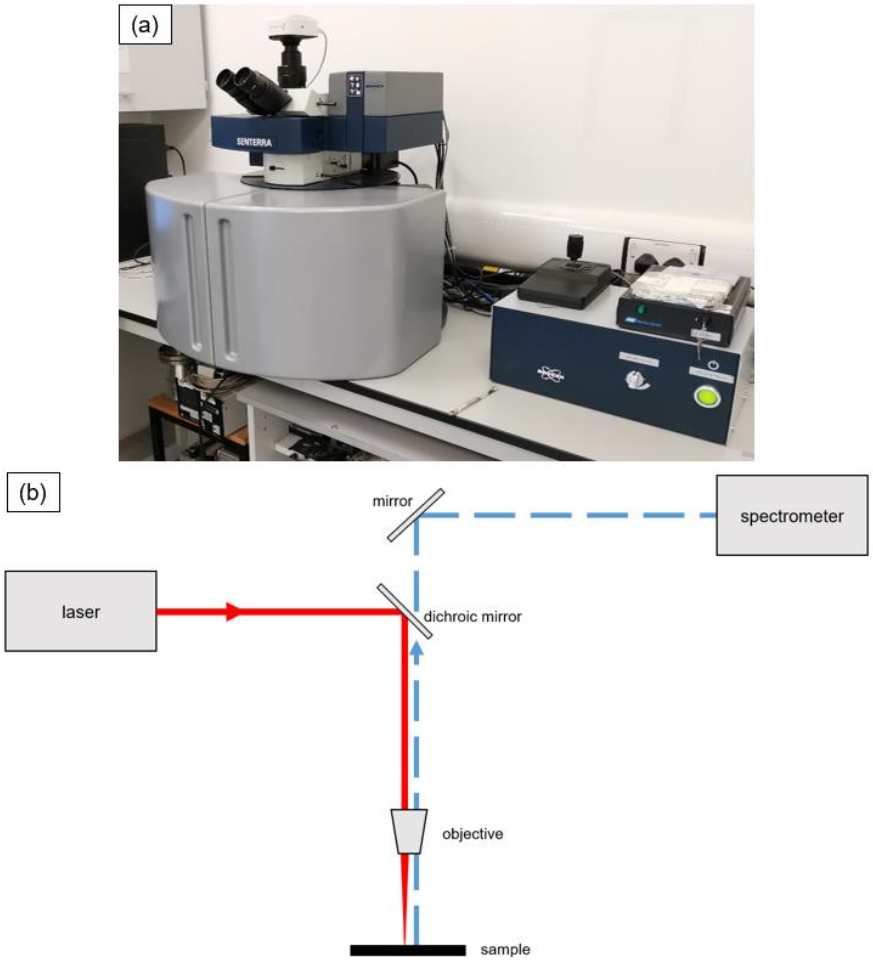

Figure 40: For the experiments the Bruker Senterra Raman microscope shown in (a) is used to analyse YBCO samples after various stages of machining. The schematic principle of a Raman microscope is shown in (b).

The lasers can be focused with three different objectives (4x, 20x, 50x). The respective spot sizes are listed in table 2.

Table 2: Raman spot sizes for each available objective.

Objective	Spot size
4x	~ 2 µm
20x	~ 0.5 µm
50x	~ 0.3 µm

The magnification, acquisition time, and laser power were varied to improve the signal-to-noise ratio of the spectra without damaging the samples. By increasing the acquisition time, the noise in the spectrum could be decreased, while the laser power increased the signal intensity. The Raman signals must be clearly visible to gain sufficient information about the state of the sample. Additionally, a YBCO thin film is measured before and after heat treatment to examine changes in the spectrum caused by this.

5.4 Laser processing

A femtosecond and picosecond laser with different wavelengths were used to machine YBCO to compare differences in the machining results. Both lasers were mounted on an optical bench with the optical setup shown in figure 41.

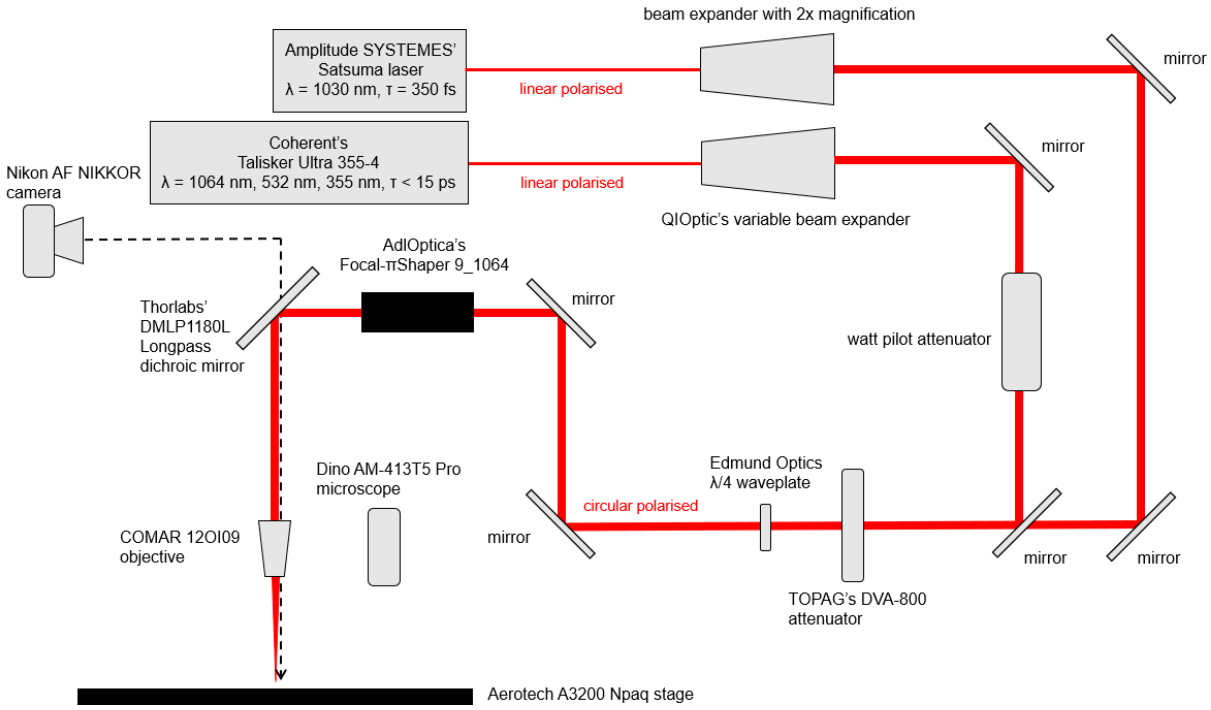

Figure 41: Experimental setup of the laser platform. The mirrors and objectives were exchanged depending on the used wavelength. At the beginning of the experiments, the both laser systems were mounted on the same optical table. The Talisker laser was later moved into another lab.

The Talisker and Satsuma laser parameters are listed in table 3 and 4.

Table 3: Talisker settings.

Wavelength	1064 nm / 532 nm / 355 nm
Pulse duration	< 15 ps
Pulse repetition rate	1-200 kHz
Raw beam diameter	2.0 ± 0.5 mm / 1.4 ± 0.3 mm / 1.3 ± 0.3 mm
M^2	< 1.3

Table 4: Satsuma settings.

Wavelength	1030 nm
Pulse duration	350 fs
Pulse repetition rate	1-2000 kHz
Raw beam diameter	2.0 ± 0.5 mm
M^2	1.1

For both lasers the beams are led through an array of optics and focused through an objective onto a stage. The stage has an accuracy of ± 3 µm in the X/Y directions and ± 0.5 µm in the Z direction. Further stage specifications are listed in Appendix 4.

A pi shaper was added for some machining trials to improve the quality of the cut by changing the beam profile from Gaussian to top hat.

To determine the ablation threshold of YBCO and substrates CeO_2 and MgO, arrays of single pulse ablations were performed while decreasing the laser power in a stepwise manner with an attenuator. A graph showing the transmission of the attenuator positions is attached in Appendix 5.

The laser is further used to machine single trenches and bridges in YBCO. For the trenches, the pulse repetition rate, processing speed, pulse overlap, and laser power were varied to find suitable parameters. Throughout different experiments, the laser power was measured with a Thorlabs PM100D power meter with the sensor head SN:11021020, S120C, 400-1100 nm, 50 mW.

6 Laser pattering of $YBa_2Cu_3O_{7-x}$ microbridges

Much is already known about laser machining YBCO. The first papers showed that it is generally possible to machine YBCO and create patterns while subsequent papers focussed on the creation or the measurement of Josephson junctions and their electrical transport characteristics, or SEM/AFM surface analysis. Throughout the years, this has been repeated for new laser systems and different pulse durations although no major discoveries in terms of the machining results were made, as discussed in section 3.2. Researchers continued investigating this processing technique since the design flexibility and absence of chemicals make laser machining very attractive.

One thing that is still not adequately understood is the laser induced damage to YBCO and to what proportion it effects the superconducting properties of YBCO and how this degradation depends on the created feature's size. So far, the damage, especially at the edges of features, has only been assessed in a few papers using SEM imaging. In addition, while SEM images provide a physical investigation of the edge damage, it does not provide any information on the electrical damage, which might not necessarily be to the same extent. Also while Raman spectroscopy has been used to analyse the oxygen doping of YBCO films to assess their quality, these results have neither been linked to electrical transport measurements nor used to examine laser induced heat damages during machining.

It is important to be able to determine the physical and electrical damages induced by different types of laser, as this damage provides a limit to the minimum achievable feature size and thus determines which laser should be chosen for the desired application/pattern. The laser wavelength and pulse duration may also have different effects on YBCO which need to be quantified.

The following chapter has the following objectives with the aim of closing the gap identified in literature:

- choose suitable substrate for YBCO microbridges
- determine suitable processing parameters for YBCO thin films
- investigate different machining strategies for YBCO microbridges
- compare machining results from different laser wavelengths and pulse durations

- determine the physical and electrical machining limit for YBCO
- investigate edge-barrier pinning effects on laser machined bridges

6.1 Single pulse ablation threshold of YBCO and substrates

Prior to ordering the manufacture of a YBCO wafer with microbridges it was necessary to choose a suitable substrate. To do so, the ablation threshold of YBCO and the two most common substrates MgO and sapphire (i.e. Al_2O_3) plus CeO_2 buffer layer were determined. A substrate with a higher ablation threshold than YBCO was required to avoid damaging the substrate while selectively removing YBCO. The ablation thresholds were calculated by relating the diameters of ablated craters to the peak fluence for single pulses.

To create single pulse arrays on YBCO the Satsuma laser (λ = 1030 nm) with an initial a power of 0.358 µW, a frequency of 1 Hz and a processing speed of 0.006 mm/s was used. The attenuation was then increased until no ablation was visible. After this the diameters of the single pulse arrays were measured using an Olympus BX51 optical microscope. An example of a single pulse array and its measurements are shown in Appendix 6. The relationship between the squared ablated diameter and the logarithmic peak fluence is shown in figure 42.

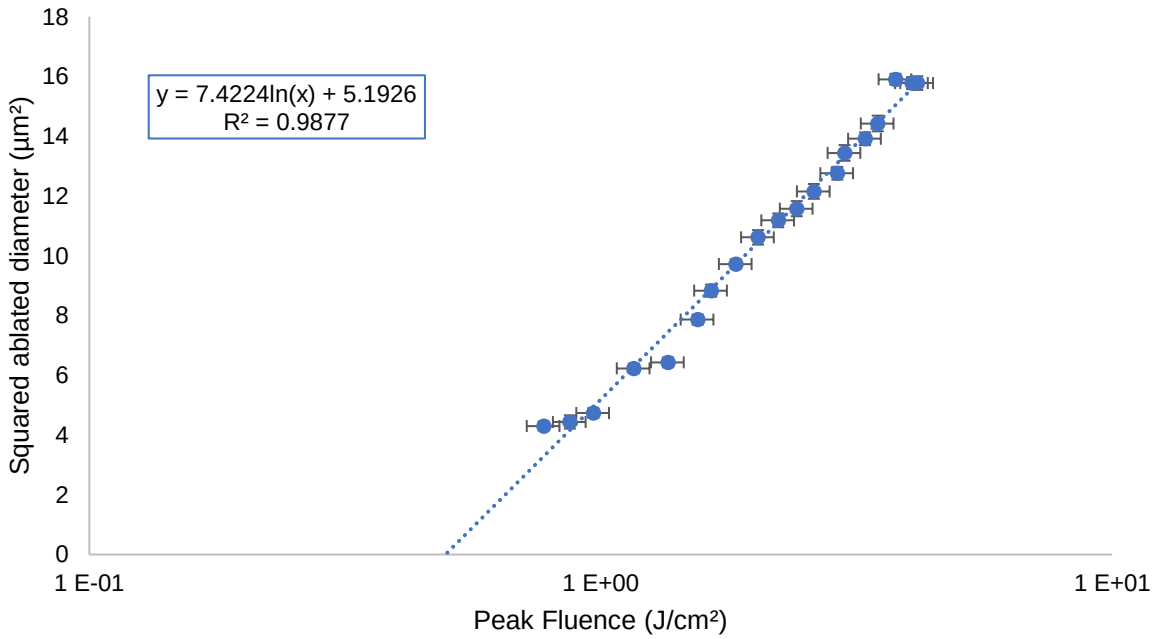

Figure 42: The squared ablated diameter was related to the logarithmic peak fluence. A linear trendline was used to calculate the ablation threshold of YBCO.

As mentioned in references [30] and [40], a linear trendline was added between the squared ablated diameter and the logarithmic of the peak fluence. The trendline equation shown in figure 42 was then used to calculate an ablation threshold for YBCO of $F_{th,pulse}(YBCO)$ = 0.5 J/cm².

For the MgO and sapphire test samples, the frequency of 1 Hz and the processing speed of 0.006 mm/s remained unchanged. Only the initial laser power was adjusted. For the sapphire substrate, where the ablation threshold of the deposited CeO_2 buffer layer was to be determined, the initial laser power was 0.406 µW (with 1 nW resolution and a measurement uncertainty of max. ± 7 %). For MgO the initial laser power was 0.639 µW. The results for both substrates are shown in figure 43 and 44.

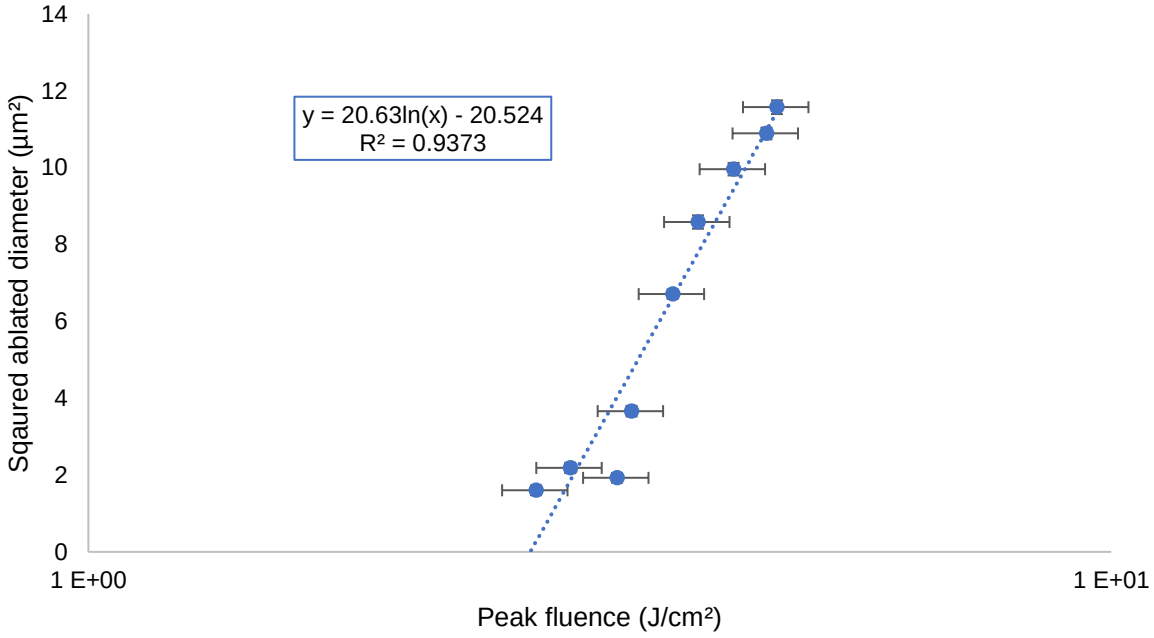

Figure 43: Ablation threshold for the CeO_2.buffer layer which is required if sapphire is used as a substrate. The ablation threshold was calculated using the equation of the linear trendline.

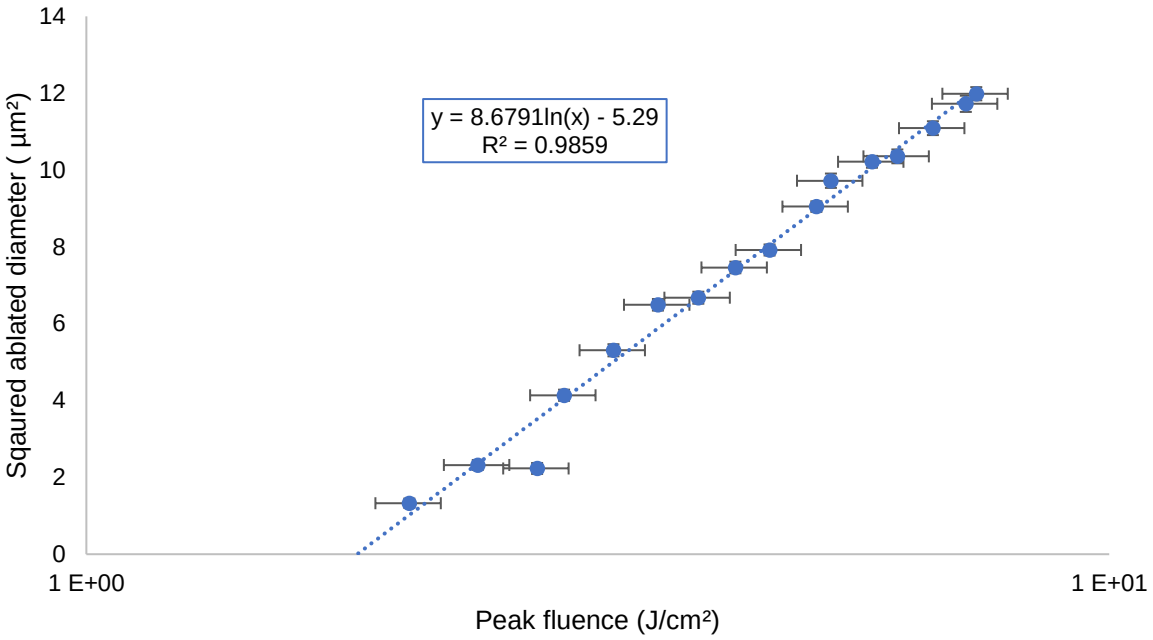

Figure 44: Determination of the ablation threshold of MgO.

For the sapphire buffer layer, an ablation threshold of $F_{th,pulse}(CeO_2)$ = 2.704 J/cm² was calculated while $F_{th,pulse}(MgO)$ = 1.84 J/cm² was determined for MgO.

Both substrates have significantly higher ablation thresholds than YBCO which is favourable for the laser machining process, as the substrate will remain undamaged once the laser successfully cuts through the film.

Consequently both substrates are suitable for the laser machining process. Sapphire is comparably cheap compared to other substrates but requires a CeO_2 buffer layer to avoid degrading the YBCO. MgO does not require a buffer layer and the YBCO can be grown directly onto it. Taking this into consideration, MgO was chosen for the YBCO bridge samples to avoid any possible interferences that can be caused by back reflections through a transparent buffer layer. For first machining trials cheaper thin film samples with sapphire substrate (and CeO_2 buffer layer) were used.

6.2 Scanned ablation threshold

Previously, the single pulse ablation threshold for YBCO was calculated to help choose a substrate. However, in order to machine YBCO bridges effectively it is also necessary to determine the scanned ablation threshold of YBCO. Compared to single pulse ablation, incubation effects occur in scanned ablation which leads to lower threshold values [30].

The scanned ablation threshold of YBCO was determined by machining multiple trenches, with each subsequent trench created using a decreased peak fluence and observing the material removal rate (MRR). To do so, a processing sequence was used to machine multiple trenches at a processing speed of 1 mm/s, a repetition rate of 100 kHz, and a MOD efficiency of 40 %. The power was decreased between each programme run using optical attenuators. The trenches were then measured using a Veeco interferometer with Vision32 software and its 2D analysis tool, which evaluated the cross-section area of the trenches. This area is then multiplied with the processing speed to calculate the MRR. The scanned ablation threshold of YBCO using the Satsuma laser determined using this technique is shown in figure 45.

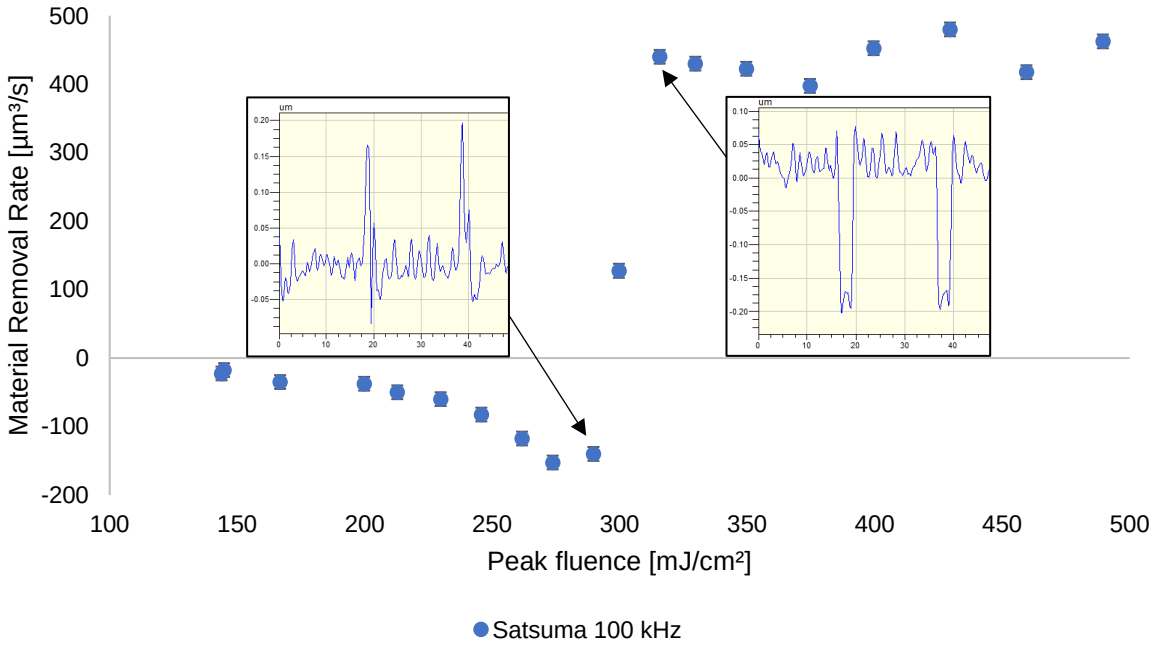

Figure 45: Scanned ablation threshold of YBCO using the Satsuma laser (λ = 1030 nm). The MRR is plotted over a range of peak fluences with the aim to determine the ablation threshold at MRR = 0. The 2D profiles of the trenches where measured by an interferometer. Starting with a positive MRR when machining trenches at peak fluences above 300 mJ/cm², the MRR turns 'negative' indicating surface swelling at reduced peak fluences.

Figure 45 shows the transition from machining trenches to apparent swelling of the film resulting in a 'negative' MRR. The cross-section area of a trench or groove is considered positive while swelling is considered negative (negative removal). Laser induced surface swelling has been observed in a range of different materials for femtosecond laser machining previously [101]. This phenomenon has been interpreted as chemical outgassing below the surface [102], interactions with impurities [103], effects of shockwaves unloading tensile stress [104] and slower energy transfers causing the molten phase formed immediately after the laser absorption to exist longer, leading to a radial convective liquid flow called the Marangoni effect [105]. For YBCO, it is assumed that the swelling is caused by either chemical outgassing or void formation below the surface. The surface structure of YBCO is porous and could have led to an uneven distribution and penetration of the laser energy throughout the film. Once the laser energy increases, ablation mechanisms start to dominate the machining process.

As surface swelling at lower pulse energies appears to be a normal occurrence for femtosecond laser machining, this has not been further investigated. Instead, this change in MRR from positive to negative was used to calculate the exact point where MRR = 0 by applying a second degree polynomial trendline between the three points in the transition area, figure 46.

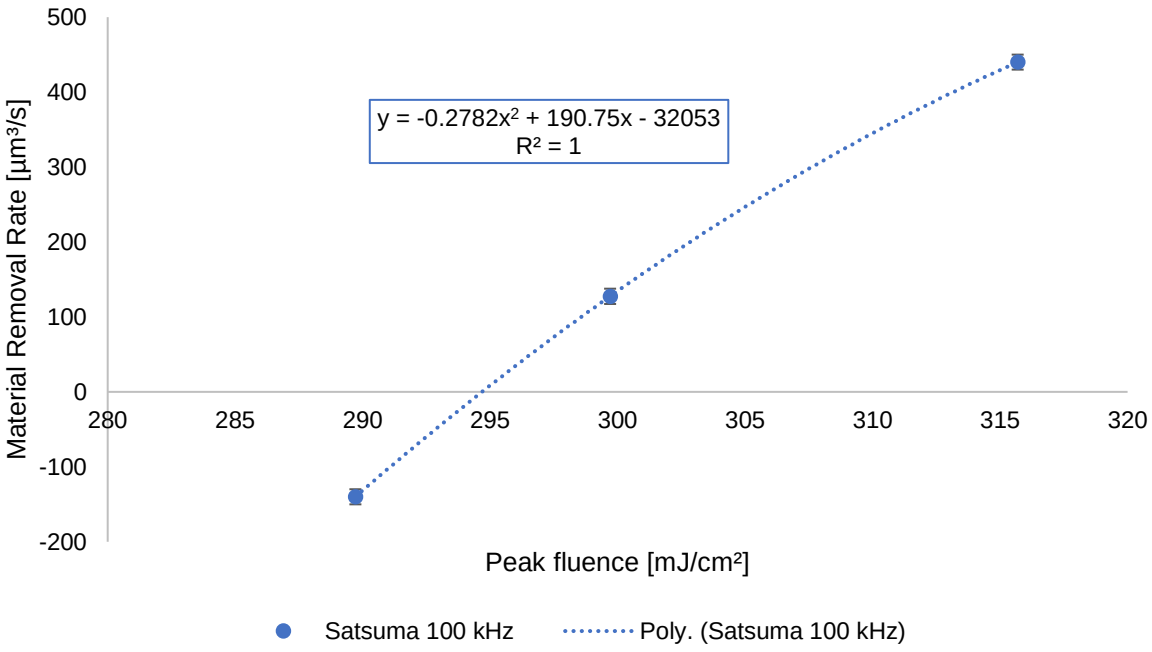

Figure 46: Transition area between machining and swelling of YBCO with the Satsuma laser.

The polynomial equation which describes this trendline is shown in figure 46, and can then be used to calculate the transition point or scanned ablation threshold of YBCO. The scanned ablation threshold for YBCO using the Satsuma laser at a repetition rate of 100 kHz is $F_{th,scanned}(YBCO)_{S100}$ = 295 mJ/cm². As expected this ablation threshold is smaller than the single pulse ablation threshold ($F_{th,pulse}(YBCO)$ = 0.5 J/cm²) due to incubation effects.

Using the experimentally determined scanned and single pulse ablation thresholds of YBCO, the incubation constant ξ_{inc} can be calculated using equation (16) and (17). With $F_{th,scanned}(YBCO)_{S100}$ = 295 mJ/cm² and $F_{th,pulse}(YBCO)$ = 0.5 J/cm² an incubation constant of ξ_{inc} = 0.91 is calculated.

After determining the scanned ablation threshold of YBCO at 100 kHz, the MRR was related to the repetition rate in another experiment. The processing speed was kept constant at 1 mm/s, while the repetition rate was varied between 0.5 kHz and 500 kHz. The trenches were machined with three different peak fluences (304 mJ/cm², 325 mJ/cm², 330 mJ/cm²) which are close to the ablation threshold of 295 mJ/cm². Again, the cross-section areas of the trenches were then evaluated using the Veeco interferometer, figure 47.

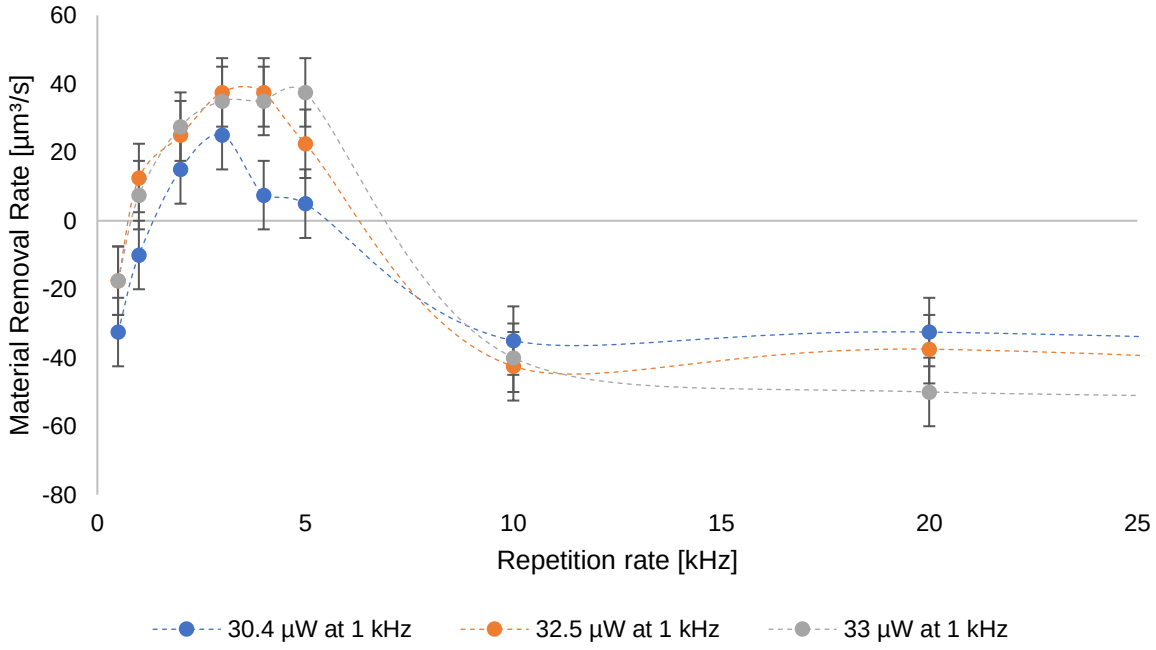

Figure 47: MRR vs repetition rate for three different peak fluences close to the scanned ablation threshold of YBCO. To compare the laser power, the power was measured at 1 kHz as a starting point before stepwise increasing the repetition rate.

Below 3 kHz a steady increase in MRR is observable which can be interpreted as pure ultrafast ablation [106], [107]. Between 3 kHz and 10 kHz, the MRR decreases. The main cause for this reduction in MRR is assumed to arise due to plasma shielding effects. When laser pulses interact with matter they can form a plasma [108]. Such plasmas exist for a certain finite lifetime, differing depending on the material. If the plasmas from previous pulses are still present during a later laser pulse, the plasma will shield the material [106]. This energy absorption process is described by the inverse bremsstrahlung mechanism [28]. Above 10 kHz, the MRR remains relatively constant until 500 kHz. In this regime, it can be assumed that evaporation takes place. Plasma shielding is still present but the increasing laser irradiance and repetition rate compensate for it, keeping the MRR constant yet negative [106], [28] ,[109]. Due to the plasma shielding, less energy appears to reach the material surface, causing swelling effects rather than actual ablation.

Based on these results, a repetition rate of 1 kHz and scanning speeds of 1 mm/s is suggested as the optimal processing parameters. This is because at the same processing speed the pulse overlap varied significantly between 100 kHz and 1 kHz, meaning changes to the ablation threshold are expected. A comparison between 1 kHz and 100 kHz is shown in figure 48 and 49.

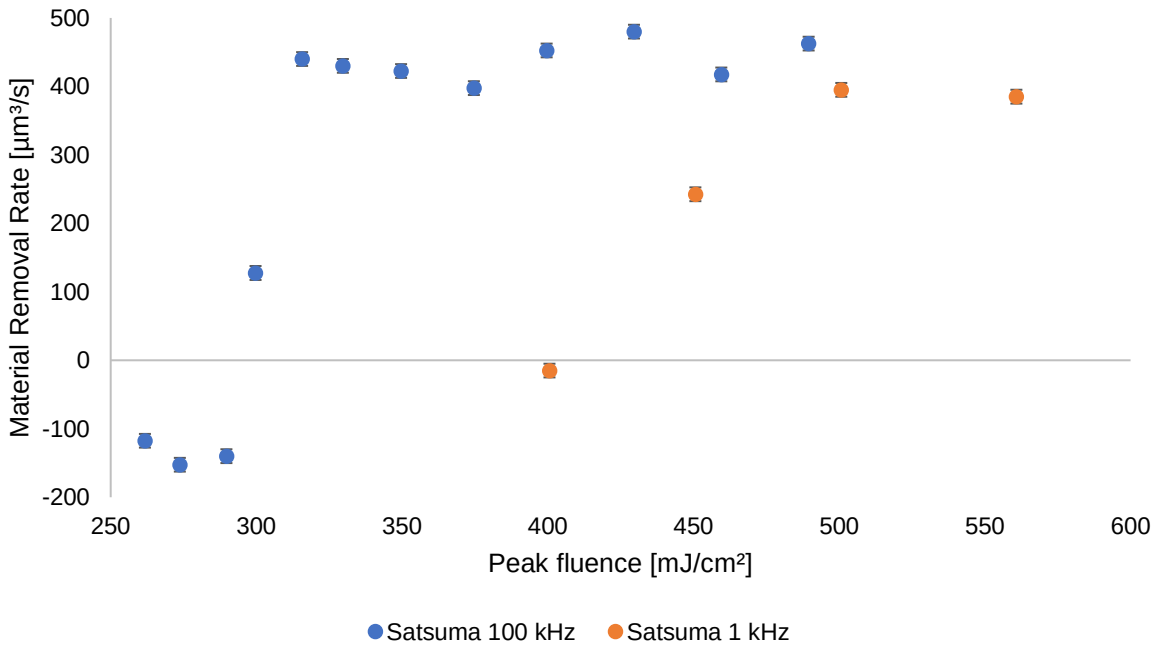

Figure 48: Machining trials to determine the scanned ablation threshold of YBCO at 100 kHz and 1 kHz for the Satsuma laser. The material removal rate is related to the peak fluence.

The exact ablation thresholds are calculated in figure 49 by using second degree polynomials.

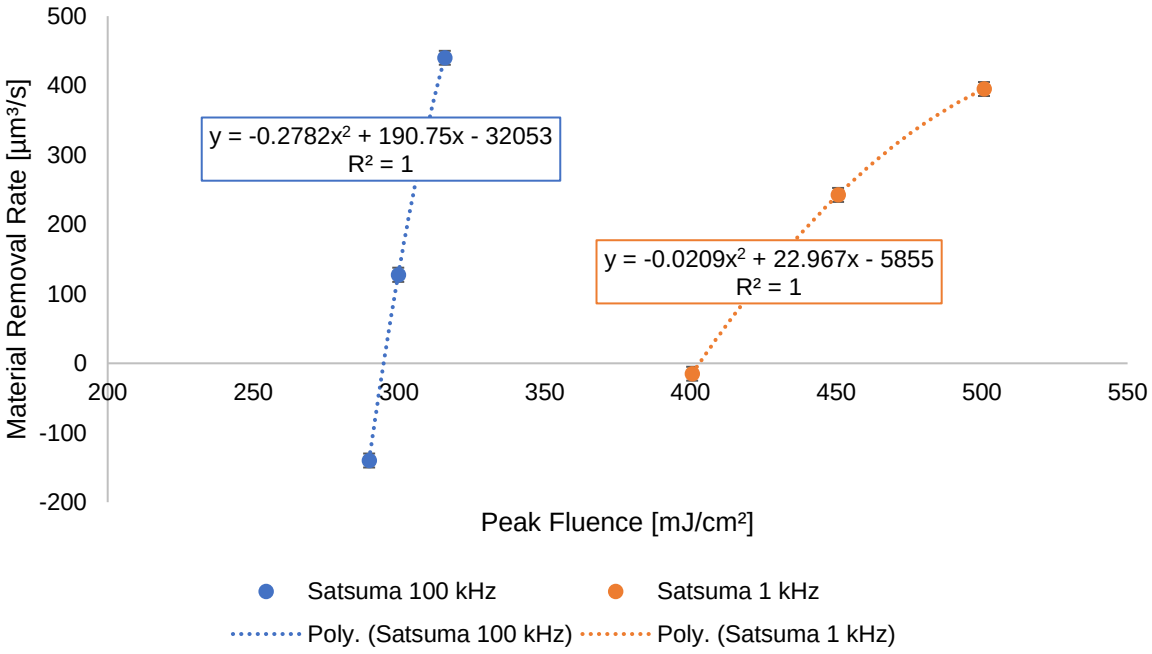

Figure 49: Approximation of the ablation thresholds for the Satsuma and Talisker laser by using second degree polynomial trendlines.

The experimentally calculated ablation threshold for the Satsuma at 1 kHz is $F_{th,scanned}(YBCO)_{S1}$ = 402 mJ/cm². This value is larger than the ablation threshold at 100 kHz (295 mJ/cm²) which can be explained by the reduced incubation effects at 1 kHz compared to 100 kHz. By using the previously calculated ξ_{inc}, an ablation threshold of 436 mJ/cm² would be expected for 1 kHz. This variation between the calculated and the experimental values is most likely caused by uncertainties in the experimental approach both for single pulse and scanned ablation, such as the transmission of the objective, the beam diameter, and the uncertainties of the measurement equipment. However, using the incubation constant is a good approximation for ablation threshold values at different repetition rates.

Moving forward, a repetition rate of 1 kHz and a processing speeds of around 1 mm/s are used as starting parameters to machine trenches in YBCO thin films.

6.3 Machining trenches in YBCO thin films

After calculating the ablation threshold of YBCO using interferometer measurements, trenches in YBCO thin films were machined for visual inspection using an SEM. While

keeping the power as low as possible, it is important that the whole depth of the film is machined, with minimum debris, and with defined edges. To optimise the processing results, changes in the pulse overlap, number of multiple passes, the machining environment and the power settings were considered.

To stay in the ultrafast regime, only energies/peak fluences up to three times the ablation threshold should be used [110], [111]. At the ablation threshold, trenches with different overlaps were machined by changing the repetition rate, figure 50.

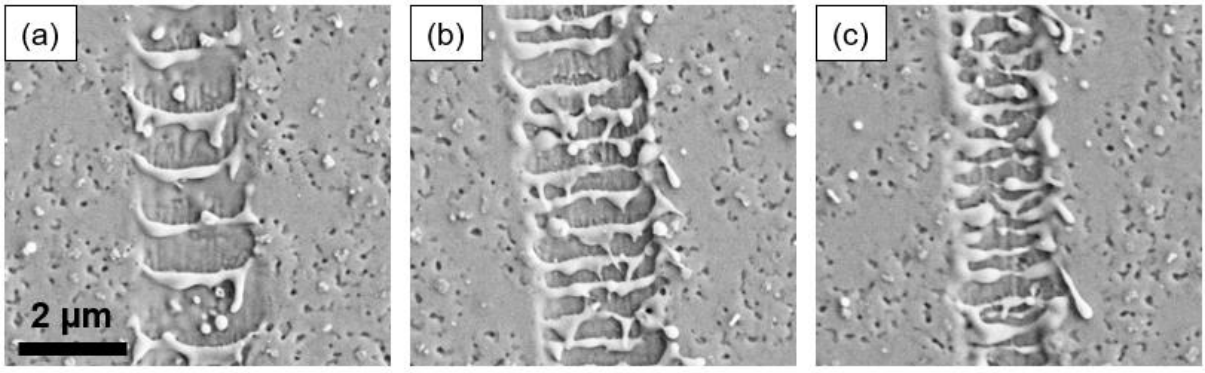

Figure 50: Three trenches were machined at a constant processing speed of 1 mm/s. The repetition rate was changed from 1 kHz to 3 kHz resulting in an overlap of (a) 76 %, (b) 88 %, (c) 92 %.

Comparing the results in figure 50, less overlap appears to produce a better result. The number of melt-like structures seem to increase the higher the overlap gets. However, in all three cases, the whole depth of the YBCO film was not machined. In another attempt to machine through the entire film, the processing sequence was adjusted to machine the sample in multiple passes while keeping an overlap of 76 % and with the same peak fluence. The results are shown in figure 51.

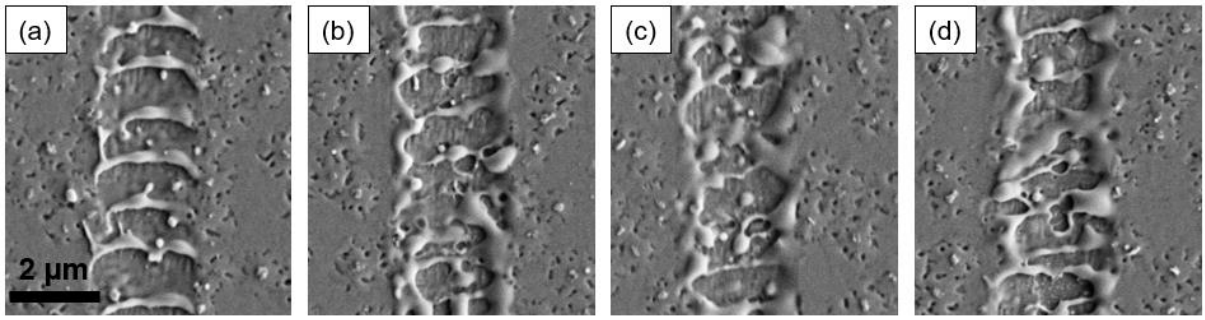

Figure 51: Trenches were machined with a pulse energy of 28 nJ and a constant processing speed of 1 mm/s and repetition rate of 1 kHz. The number of passes were changed from (a) 1 pass, (b) 5 passes, (c) 7 passes, and (d) 10 passes.

Again, it was not possible to machine through the whole YBCO film despite machining it in multiple passes. Even when increasing the number of passes even further, the

machining result could not be improved. Although the trenches in figure 50 and 51 were all machined with pulse energies in the ultrafast regime, melt-like structures could not be avoided. It was also not possible to remove the full width of the YBCO film; neither with higher overlaps nor with multiple passes.

Apart from changing the overlap and or number of passes, another option was to increase the power, figure 52.

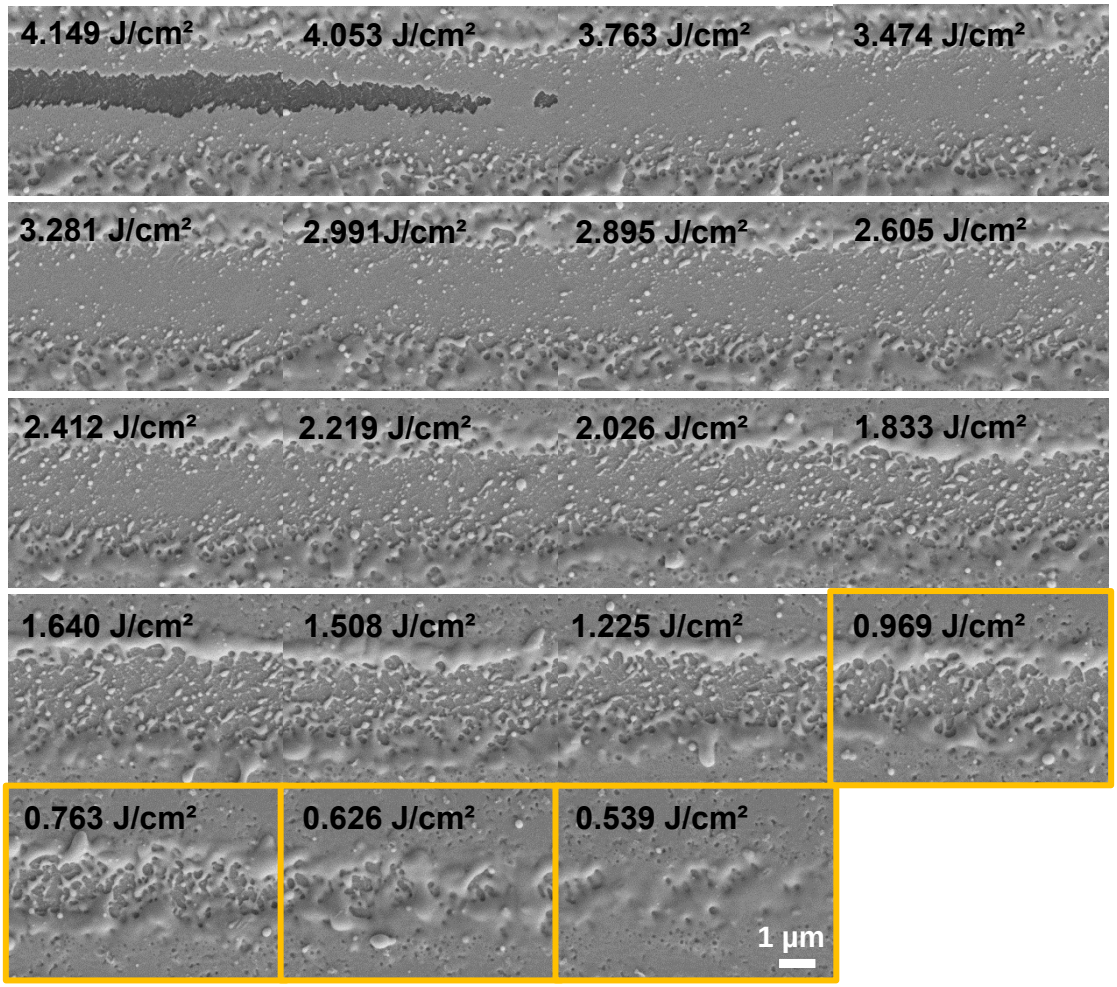

Figure 52: The trenches were machined with the Satsuma laser with increasing peak fluences at 1 kHz. The sections marked with an orange frame are within the ultrafast regime. The power was stepwise decreased using the attenuators and shielding gas and an ultrasonic bath were used before inspection.

Melt and material re-depositions were observable throughout the experiment, and at peak fluences above 3.474 J/cm², the 40 nm CeO_2 buffer layer of the thin film sample was damaged. The amount of debris within the ultrafast regime would be disadvantageous for machining bridges and electrical connections. Previous trials showed that working within the ultrafast regime was not sufficient even when changing overlaps or the number of passes, and in order to machine through the film peak

fluences above the ultrafast regime were required. Based on figure 52 and the debris within the trench, peak fluences above ~2 J/cm² at 1 kHz and 1 mm/s would be needed.

To investigate if the debris can be decreased, a thin film was machined under different atmospheric conditions. A sample was sequentially machined in a vacuum chamber which was first filled with air, then pumped down to a vacuum ($10^{-1.5}$ mbar) for another machining trial and finally filled with nitrogen. The sample was machined through a fused silica window, figure 53.

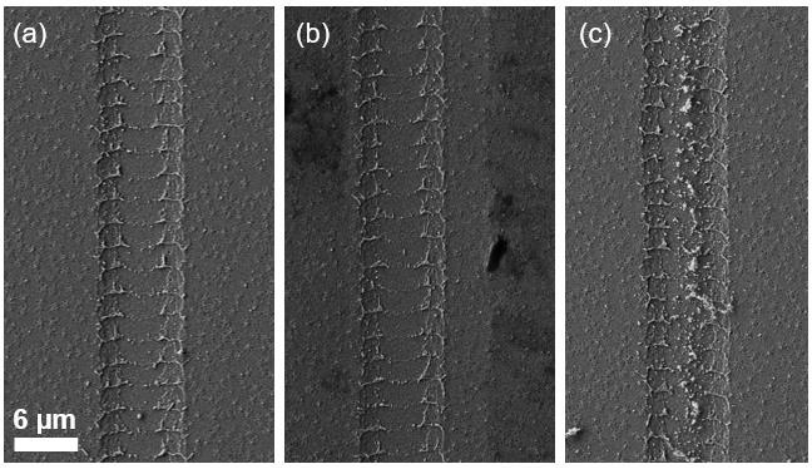

Figure 53: Ablated trenches on YBCO in (a) air, (b) $10^{-1.5}$ mbar vacuum, (c) Nitrogen.

The trenches machined in air and in vacuum do not show a significant difference. Melt-like formations are present in both. This might change if a higher vacuum is used leaving less oxygen or other reactants. When YBCO was machined in a nitrogen atmosphere, an amorphous compound in form of flakes were found within the machined trench. Similar results were reported in [112] where an amorphous-phase nitrogen compound formed on a YBCO surface. Given the sensitive nature of YBCO, any chemical reactions should be avoided.

Due to this, all the following YBCO microbridges were processed in air, in one pass and with peak fluences above the calculated ultrafast regime. The following laser parameter were chosen as the most suitable after the initial trials described so far:

- Repetition rate: 1 kHz
- Processing speed: 1 mm/s
- Peak fluence: ~ 2 J/cm² which translates to an average power of ~ 200 µW or a pulse energy of ~ 165 nJ (~ 6 x ablation threshold).

6.4 Investigation of beam shaping technologies and machining strategies for YBCO bridges

With the determined processing parameters, further experiments were conducted with the aim of further improving the edge quality and finding the physical machining limit for the Satsuma laser. Additionally, different machining strategies were investigated.

Based on the trench machining results, melts could not be avoided, even when working at the ablation threshold. In another attempt to improve the edge quality when machining bridges, a pi shaper was used to change the beam profile of the satsuma laser, figure 54.

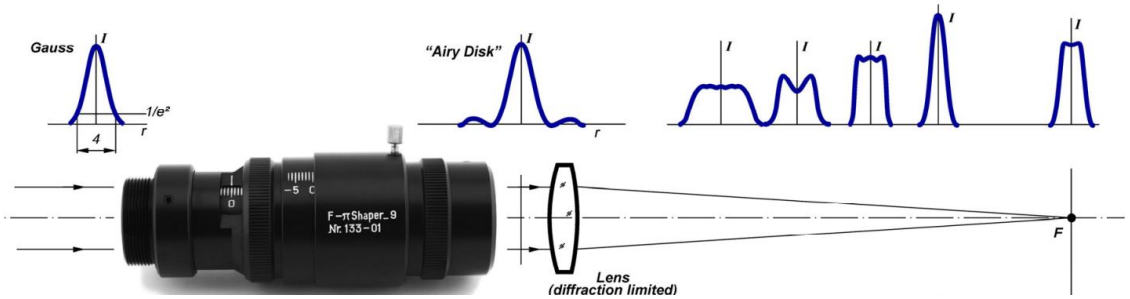

Figure 54: The pi shaper can change the incoming Gaussian beam profile to a variety of beam profiles depending on the focal plane [113].

The aim of this was to achieve a flat top profile which should produce a more even cut. The position of the different profiles in the beam path produced by the pi shaper varied depending on the focussing objective used. The beam profiles will also be affected if the pi shaper is not aligned properly. For the Satsuma laser, the pi shaper mount was roughly aligned in four axes (x, y, tip, tilt). A detailed description of the mount alignment can be found in Appendix 7. After aligning the mount, the pi shaper was added, after which the alignment of the mount was refined. To do so, a 1 m focusing lens was added to the pi shaper and a beam passed through it was focussed on a Spiricon beam profiler (IEEE-1394 Digital Camera, LBA-FW-SCOR20), figure 55.

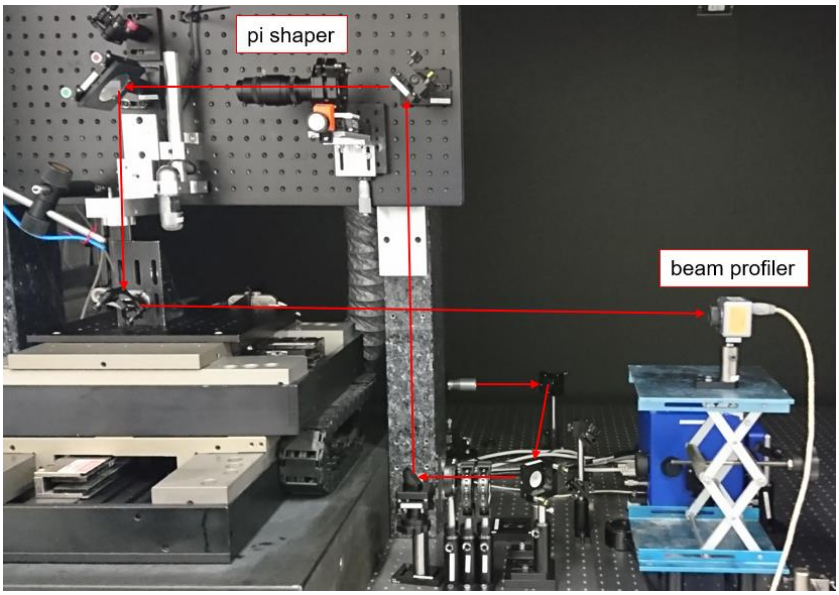

Figure 55: Alignment setup for the pi shaper. The beam path was increased by adding another mirror on the Aerotech stage.

By rotating the focussing ring on the pi shaper, the beam was first focussed onto the Spiricon camera. The ring was then further rotated until a donut-beam profile was detected. Any misalignment would then be visible as asymmetries in the donut shape. The angular alignment of the mount was then adjusted until the donut shape was symmetric, figure 56.

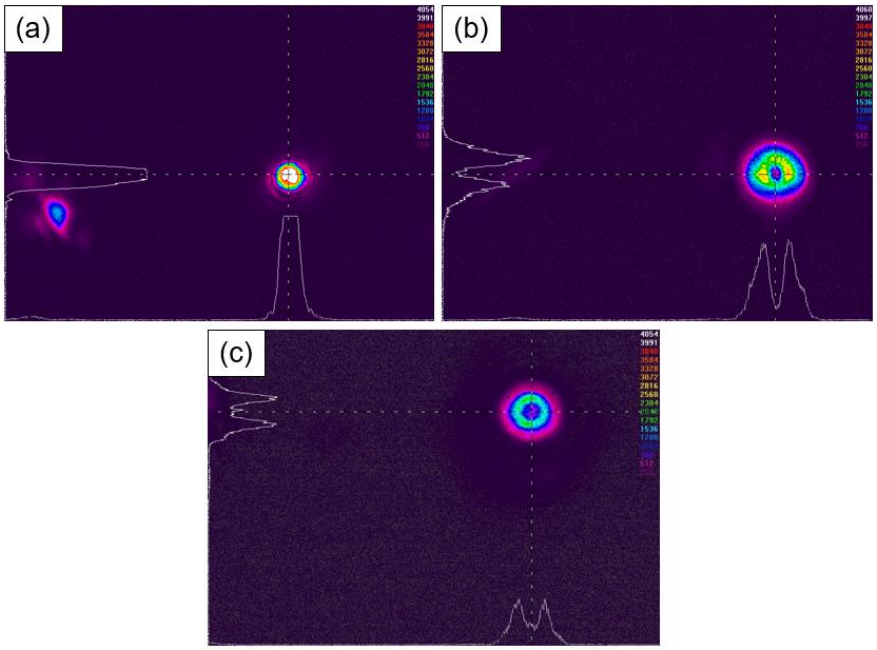

Figure 56: Images were taken with a Spiricon beam profiler (IEEE-1394 Digital Camera, LBA-FW-SCOR20). (a) Focal position using the focusing ring on the pi shaper. The parasite spot on the left side can be ignored and is caused by the 1 m focusing lens which does not have AR coating. (b) Donut beam profile with angular misalignment. (c) Donut beam profile after final alignment steps.

Once the pi shaper was aligned, the 1 m focusing ring was replaced by the COMAR 12OI09 objective. To find the different beam profiles for the COMAR objective, the Z-axis of the Aerotech stage was moved in small increments (ΔZ) while firing single pulses. The focal point of the objective served as a starting point (Z = 0). After discussing this procedure with the supplier, a ΔZ increment of 2 µm was found to be suitable for the COMAR 12OI09 objective with its focal length of 12.9 mm. The supplier also advised to only work in planes closer to the lens (ΔZ > 0), figure 57.

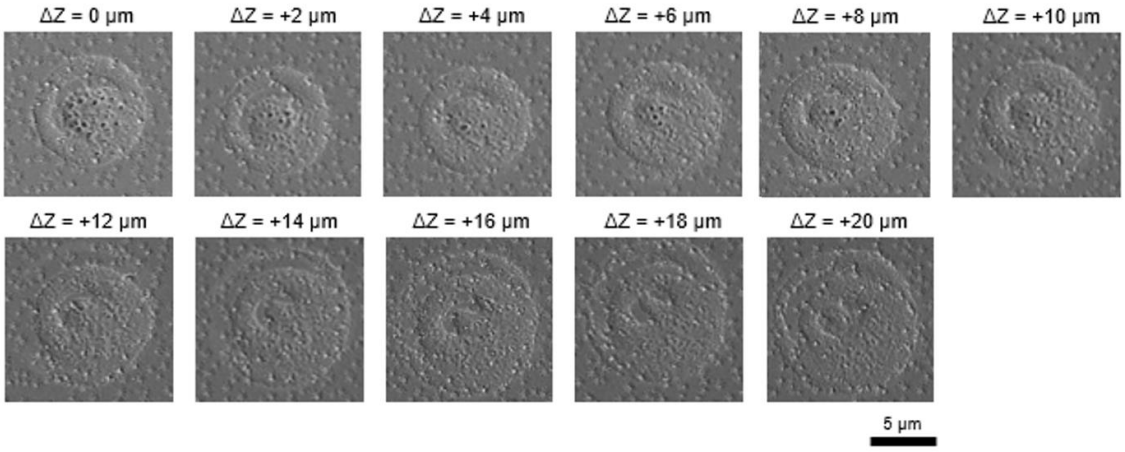

Figure 57: Single pulses at different positions from the focal point (ΔZ = 0). The beam shape is changing depending on the position. The pulse energy was 215 nJ at 1 Hz.

When this was used a change in beam shape was observed. An offset of ΔZ = +4 µm was initially used for the first bridge machining trials due to its round shape. For initial bridge machining trials with the pi shaper, the repetition rate was set to 100 Hz, as a higher repetition rate with an adjusted processing speed would cause variations in the length of the cut. The processing speed was adjusted in respect to the changing spot size.

The YBCO bridge samples were aligned using the Dino AM-413T5 Pro microscope and additional tip/tilt (GNL10/M and GNL18/M) and rotary (PR01/M) stages from Thorlabs. Once aligned, the first machining trial of a YBCO bridge was conducted. Both sides of a 100 µm bridge were processed, figure 58.

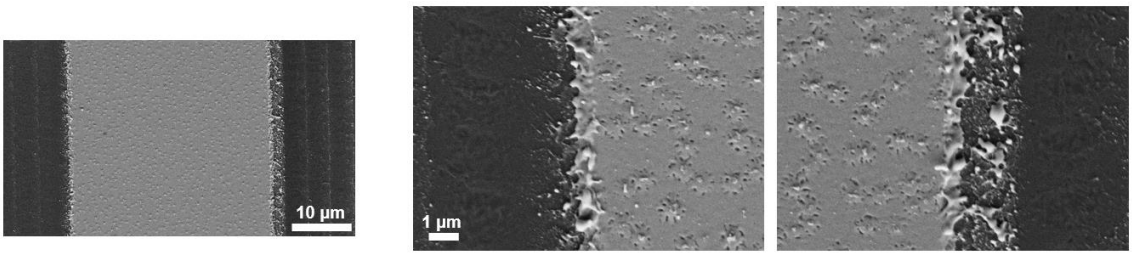

Figure 58: Both sides of a 100 µm bridge were machined with 189 nJ per pulse.

The machining result on the left side shows less melt and material debris than the right side. A more detailed view of the left edge is shown in figure 59.

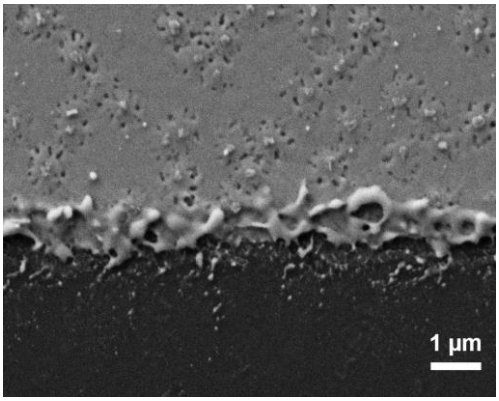

Figure 59: The melt film at the edge is about 1 µm wide.

No real improvement to the trenches machined without a pi shaper were visible. As the offset of ΔZ = +4 µm did not seem to be sufficient, beam profiles in focal planes away from the sample (ΔZ < 0) were investigated against the supplier's recommendation, figure 60.

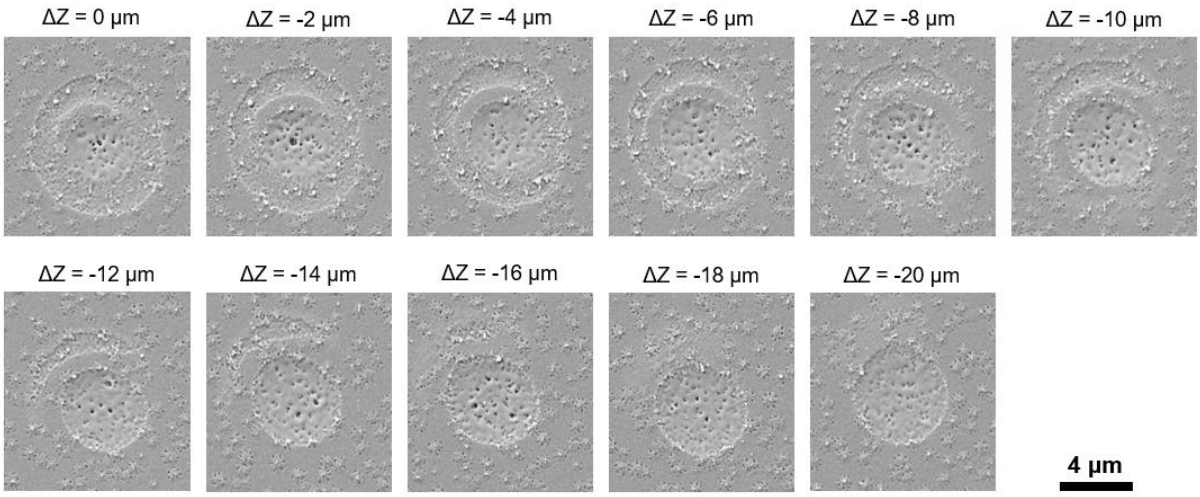

Figure 60: Single pulses at different positions away from the focal point (ΔZ = 0). The beam shape is changing depending on the position. The pulse energy was 215 nJ at 1 Hz.

Figure 60 shows that the beam profiles in planes away from the sample appear more suitable. At ΔZ = -20 µm the energy distribution looks uniform. This offset was used in another bridge machining trial while keeping the remaining settings constant, figure 61.

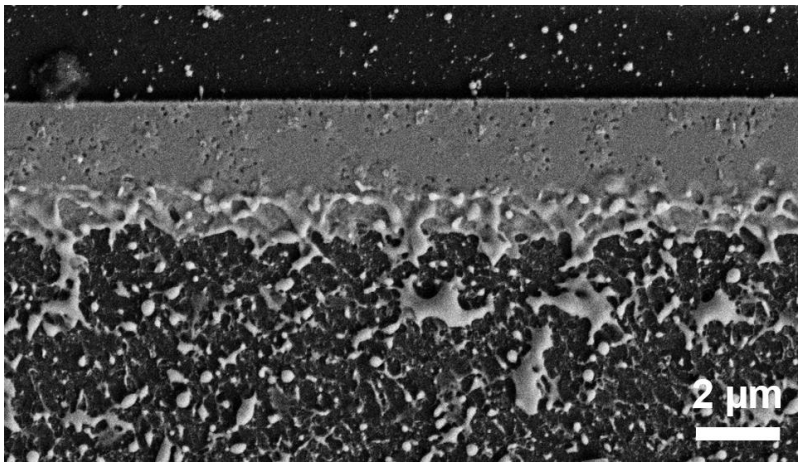

Figure 61: The bridge was processed with 189 nJ per pulse at a repetition rate of 100 Hz and a processing speed of 0.2 mm/s while having an offset in Z of -20 µm.

The material debris had increased significantly, and the result looked worse than before. To try and improve it while keeping an offset of ΔZ = -20 µm, the processing speed was decreased to 0.1 mm/s for a higher overlap. By changing the processing speed, the machining result improved, figure 62.

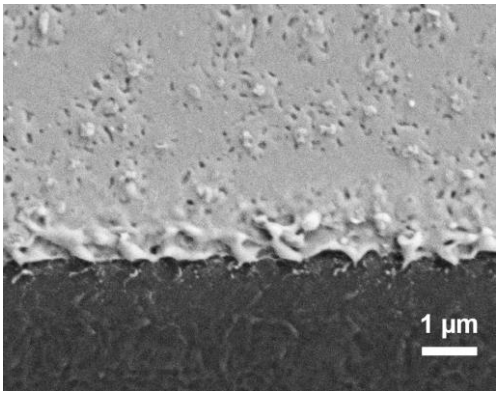

Figure 62: The edge quality was improved. The bridge was machined with with 189 nJ per pulse at a processing speed of 0.1 mm/s while having an offset in Z of -20 µm.

The edge quality improved with the decreased processing speed and pi shaper with an offset of ΔZ = -20 µm. A new bridge was then machined from 30 µm to 7 µm and the edges before and after the laser process were compared, figure 63.

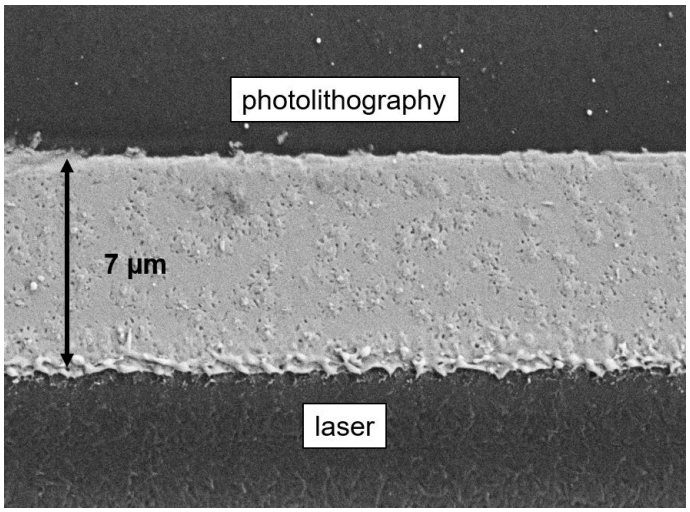

Figure 63: Comparison between the photolithography and the laser processed edge.

The machining result improved. The melt and debris decreased significantly. ImageJ, an open source image processing software, was used to analyse the edges of bridges produced by photolithography and via a laser. The RMS roughness for the lithography edge is 0.955 µm with a peak-to-peak roughness of 3.43 µm. For the laser the RMS edge roughness is comparable to the lithography value at 0.957 µm. The peak-to-peak value is slightly higher at 4.19 µm. Overall, the performance of laser made bridges appear comparable to photolithographically made bridges. However, in the laser bridges melt could still not be avoided but the width of the melt film was decreased from 1.5 µm to about 700 nm. This suggests that the machining limit for YBCO bridges using the Satsuma laser would be > 700 nm. After tuning the Aerotech stage, the repetition rate could also be changed back to 1 kHz with a processing speed of 1 mm/s without a change in machining result.

Although the pi shaper did show some improvement in the machining result, its performance is not very repeatable and the alignment procedure is very time consuming. The pi shaper needs to be re-adjusted for every experiment and a difference of only 4 µm can deliver a completely different result. The tip/tilt correction is manually adjusted using the DINO microscope which also limits the accuracy of the beam shape. By machining YBCO bridges with and without the pi shaper, no differences were found in the electrical properties.

In addition to investigating beam shaping technologies, different bridge machining strategies were also considered, figure 64.

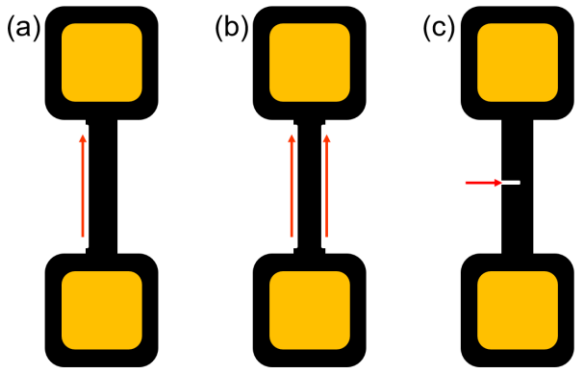

Figure 64: Used machining strategies. (a) one-sided laser machining, (b) both-sided laser machining, (c) line cut. Laser cuts across the bridge to create a small 4 µm long bridge. The length of the bridge is determined by the diameter of the laser spot.

Different approaches have different advantages and disadvantages. For the 'one-sided' machining approach, only one side of the bridge was 'damaged', but due to alignment limitations the bridge width could accidentally decrease along its length. A constant bridge width could be achieved with the 'both-sided' approach since both sides of the bridge would have the same tilt. The drawback would be that the machining result might vary on both sides due to beam distortions, objective defects etc as shown in figure 58. The line cut would induce the least damage as the area machined by the laser is decreased, and can create a bridge with a length equal to the laser spot size. All three approaches were used to investigate possible differences in the critical current density.

Following the machining trials on YBCO thin films, further machining trials were conducted on YBCO bridges. Again, it was only possible to successfully machine YBCO at pulse energies about 6-8 times the ablation threshold. Instead of trying to improve the pulse energy, other processing aspects such as beam shaping technologies were investigated in this chapter. By shaping the beam of the Satsuma laser with a pi shaper, it was possible to reduce the physical machining limit from about 1.5 µm to > 700 nm. However, due to the lack of repeatability, and the time-consuming alignment, a decision was made to not use the pi shaper in further trials as it did not lead to any significant improvement in the critical current density. To conclude this chapter, possible machining strategies and their benefits were discussed.

6.5 Laser machining with different wavelengths and pulse durations

The machining results are dependent on a range of parameters, one of them being the laser wavelength. It is known that the optical penetration depth of YBCO decreases with decreasing laser wavelength. For example, the optical penetration depth at 1064 nm is about 120 nm [114], while it is around 73 nm at 514 nm [70] and 50 nm at 248 nm [115]. Not only does the wavelength influence the penetration depth of a material, it can also change the absorption. For YBCO, the absorption was measured from 355 nm to 1100 nm with a UV-Vis spectrometer, figure 65.

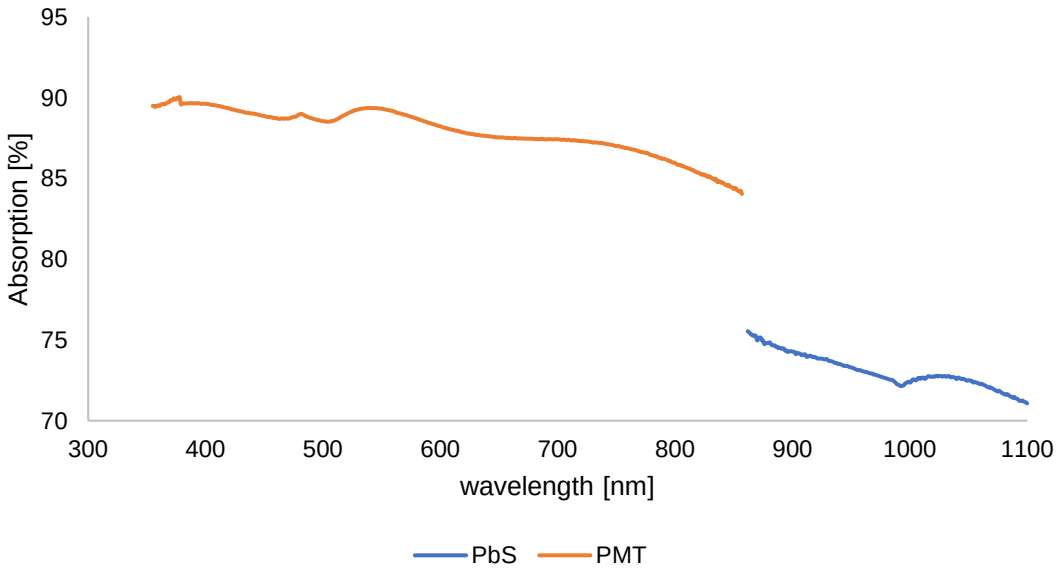

Figure 65: Absorption spectrum of YBCO measured with a UV/VIS/NIR spectrometer Lambda 750 over a range of 355 nm to 1100 nm. A detector change at 860 nm was required to measure the whole spectrum.

The YBCO sample was mounted at a 4° angle to measure the total reflection (specular and diffuse [116]). The gap in the spectrum is the result of a detector change from PbS to PMT (photomultiplier tube). The PbS sensor is used for the infrared region, while the PMT detector covers the UV to the visible spectrum [117]. Hence, the absorption spectrum was measured in two parts: from 1100 nm – 862 nm and 857 nm – 355 nm. This detector change is likely to have caused the 'jump' at ~850 nm and can be explained as a technical artefact rather than a material one. The sample size and its alignment, variations in the reference measurements for each detector and the possibility of a general system fault could have been the cause for the difference in absorption. An edited continuous graph is shown in figure 66.

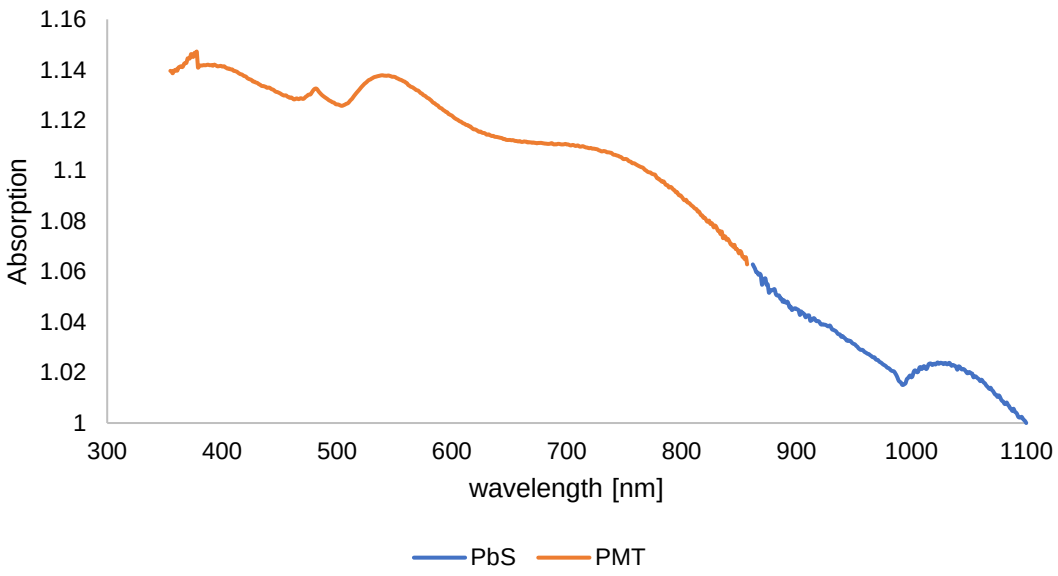

Figure 66: The absorption spectrum from figure 65 was normalized and the difference between the two detectors subtracted.

A similar 'jump' has also been reported when changing between lamps for example, supporting the assumption of a technical issue. While not being able to work with the measured absorption values directly, the spectrum does show that the absorption is increasing for shorter wavelengths which could lead to different machining results for these wavelengths. A comparison of ablation thresholds from different lasers is shown in figure 67.

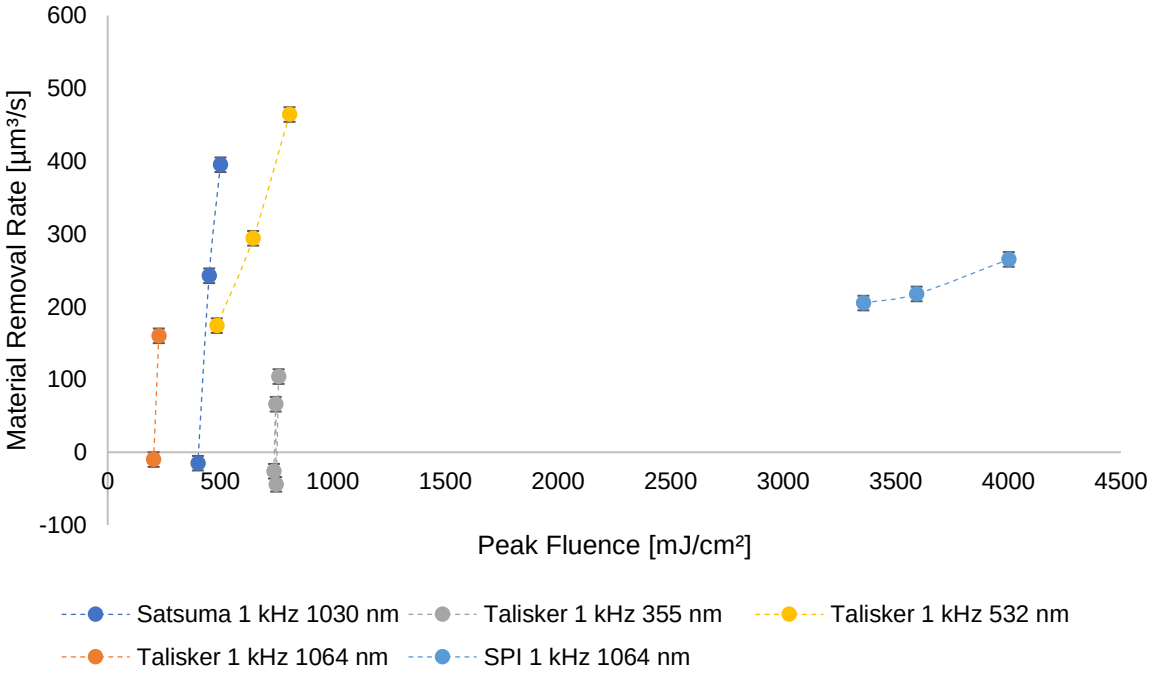

Figure 67: Ablation thresholds over a range of different wavelengths and pulse durations.

The ablation thresholds for the pico- and femtosecond systems are all below 1 J/cm² and the machining results look similar under the SEM. No visual differences were detected between the different wavelengths. When using the SPI nanosecond laser, melt formations, rather than ablation, were observed, as shown in the SEM images of figure 68 (a).

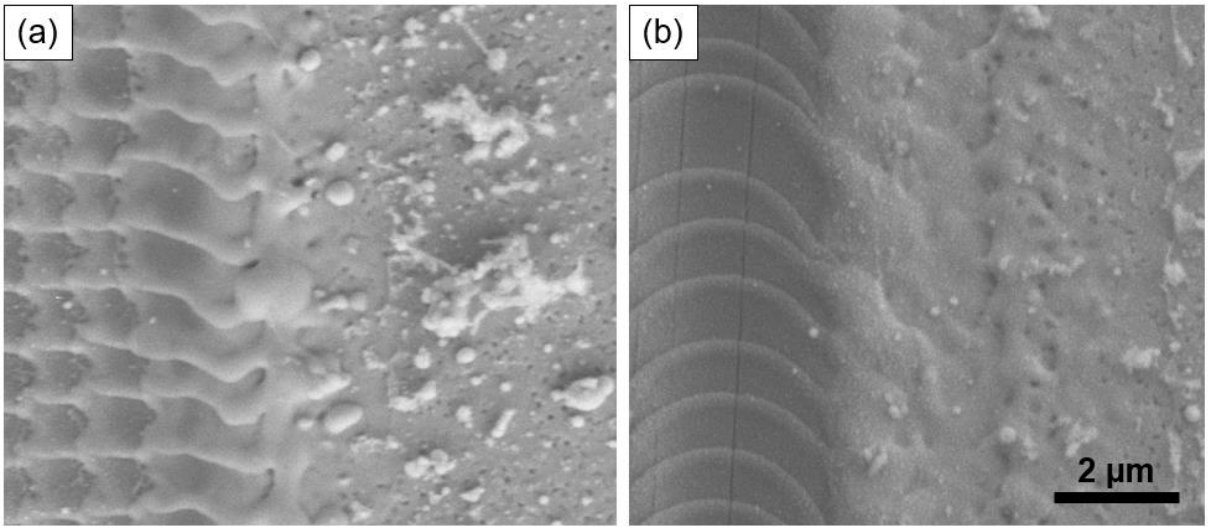

Figure 68: SEM images of the machining result when using a SPI nanosecond laser with a wavelength of 1064 nm with a pulse duration of 20 ns. In (a) a pulse energy of 318 nJ was used while in (b) the pulse energy was increased to 2.23 µJ. In both experiments a repetition rate of 1 kHz and at a processing speed of 1 mm/s was used.

As the melt residues could be conducting and act as unwanted current carriers, the machining result in figure 68 (a) was insufficient. When increasing the power of the nanosecond laser, the melt formation decreased, however, the substrate was machined as well and the damage at the edge of the bridge had a width of over 2 µm, figure 68 (a). As such to machine YBCO bridges, the pico- and femtosecond lasers were preferred, figure 69.

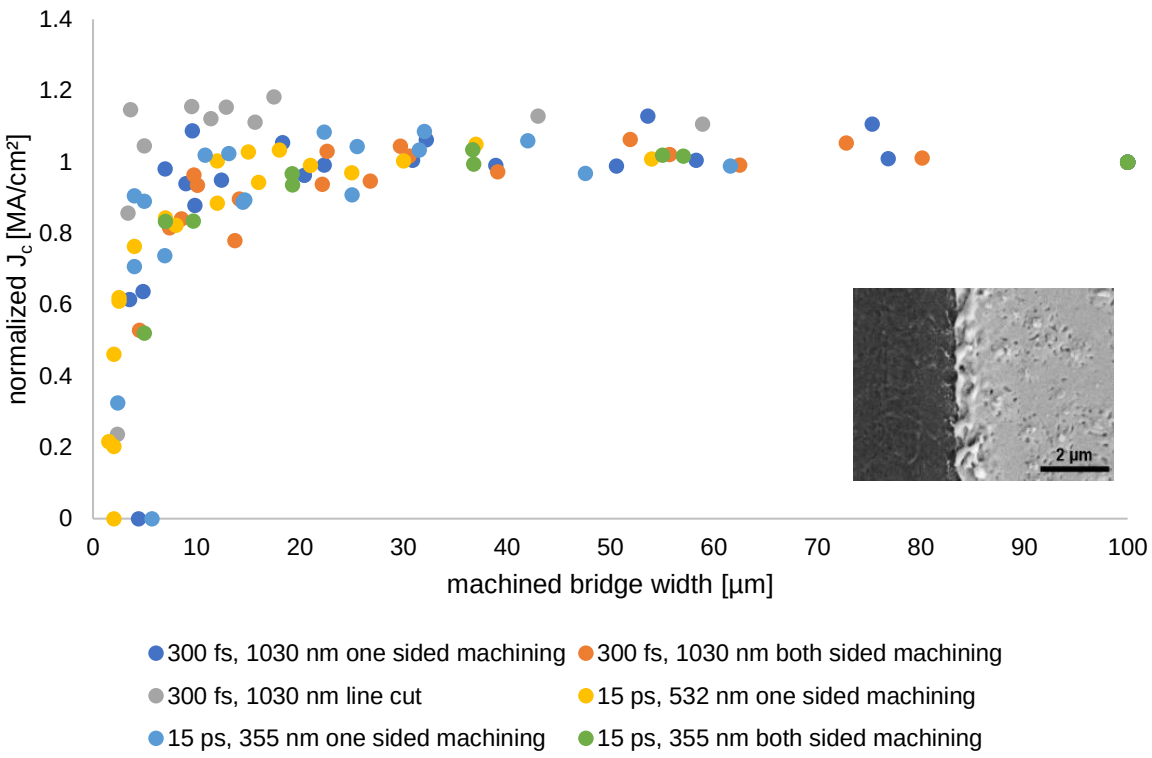

Figure 69: Development of J_c over different bridge widths. The J_c values were normalized over the initial J_c before the laser processing. A SEM image of a machining example is shown in the lower right corner.

Independent from the wavelength and the pulse duration, J_c starts to decline below a ~10 µm bridge width. All bridges were machined with a repetition rate of 1 kHz and a processing speed of 1 mm/s. The peak fluences were adjusted depending on the laser. The bridges were machined with a peak fluence of 1.8 J/cm² (6 x ablation threshold) at 532 nm and 1.35 J/cm² (1.9 x ablation threshold) at 355 nm.

As there was no visible difference between the results of the different lasers, the Satsuma laser was primarily used for the following experiments and analysis.

6.6 Edge-barrier pinning effect in laser machined YBCO samples

Flux pinning is an important factor when wanting to achieve better performances in superconducting applications, such as superconducting magnets, cables etc [49]. So far it has been shown that flux can be pinned by nano-sized defects. Another form of pinning is edge-barrier pinning which uses the geometrical barriers of HTS thin films [2], [119].

The edge of an HTS sample can act effectively as a barrier, delaying magnetic flux from entering the sample. This can affect the overall pinning of a YBCO thin film. Edge-barrier pinning can improve the J_c of YBCO microbridges with width of a few

microns as compared to much wider films. According to a recent paper [118], under certain conditions it could be possible to achieve up to a 200 % increase in the critical current density, figure 70.

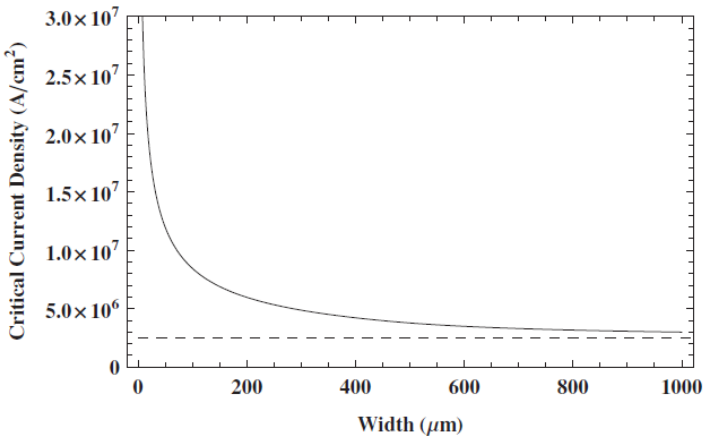

Figure 70: The curve represents the maximum J_c enhancement due to edge-barrier pinning on a HTS strip. The dotted line shows the critical current density only from bulk pinning [118].

Their corresponding results are shown in figure 71.

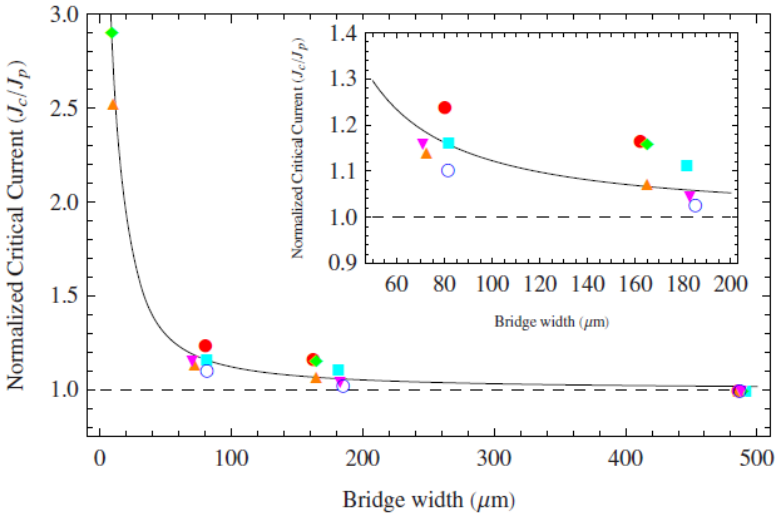

Figure 71: The black line is the scaled normalized J_c curve. The coloured markers are measured data points. Each marker colour represents a single sample at different bridge widths. Data points are normalized to the J_c of the 500 μm bridge. All measurements were done at 77.2 K [118].

To replicate this result, YBCO bridges were stepwise machined to smaller widths, with the J_c measured at each step. A plot J_c versus the bridge width is shown in figure 72.

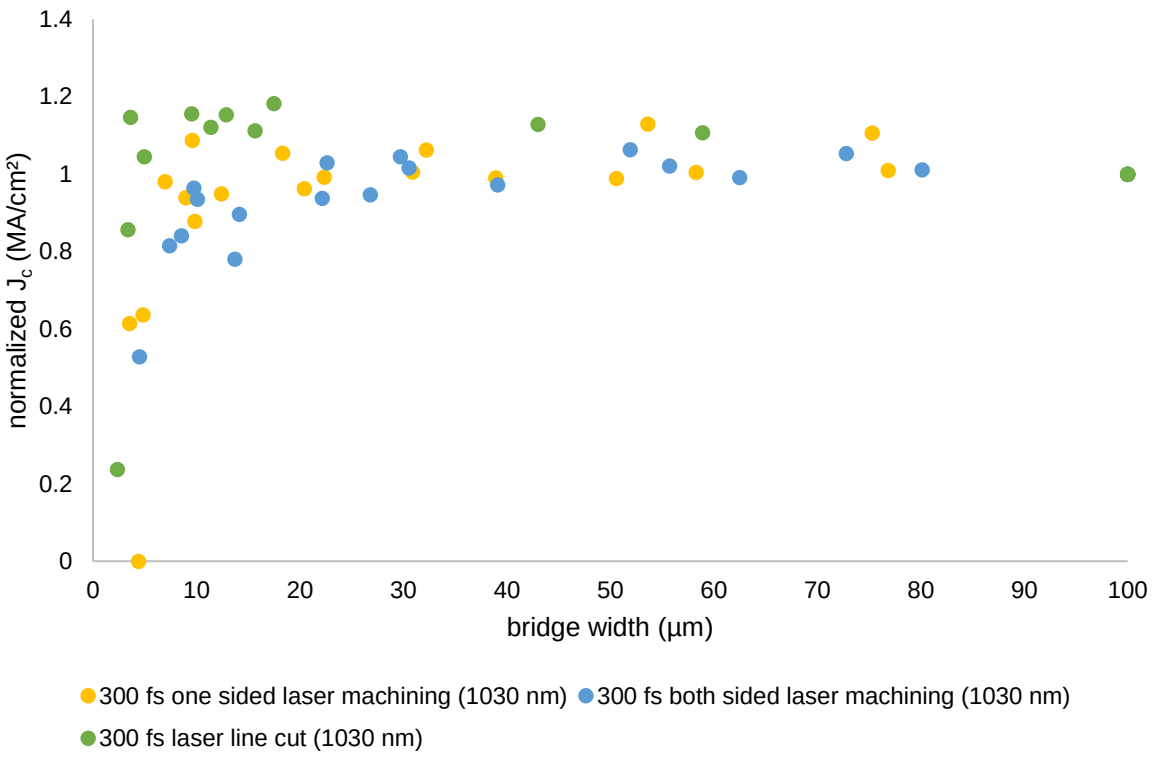

Figure 72: J_c vs bridge width for laser machined YBCO using a femtosecond laser (1030 nm, 300 fs). J_c is normalized by the measured J_c prior to any laser machining.

The results from the laser machining appear to show an opposite trend to the prediction made in reference [118]. Rather than seeing a significant increase in J_c towards smaller bridges, a decline is observed below 10 µm. For a direct comparison between figure 71 and 72, the measured J_c values of the laser machined samples need to be normalized by J_p (critical current density from bulk pinning without considering edge-barrier pinning) as well [118]. In [118], J_p is calculated using the following empirically derived equation (21):

$$J_p = c(1 - t^a)^b \tag{21}$$

with c = 7*10^7, a = 9/10, b = 7/4, and $t = {}^{T}/_{T_c}$ = 77/92 [118] leading to J_p = 2.47 MA/cm².

For the laser machined samples, the T_c is stated as 86.2 K, however, when adjusting J_p by changing t only could lead to a false value since a-c might need to be adjusted accordingly. Since there is no information given in the paper on how these values were

derived and what they stand for, the same J_p from the paper has been used in figure 73.

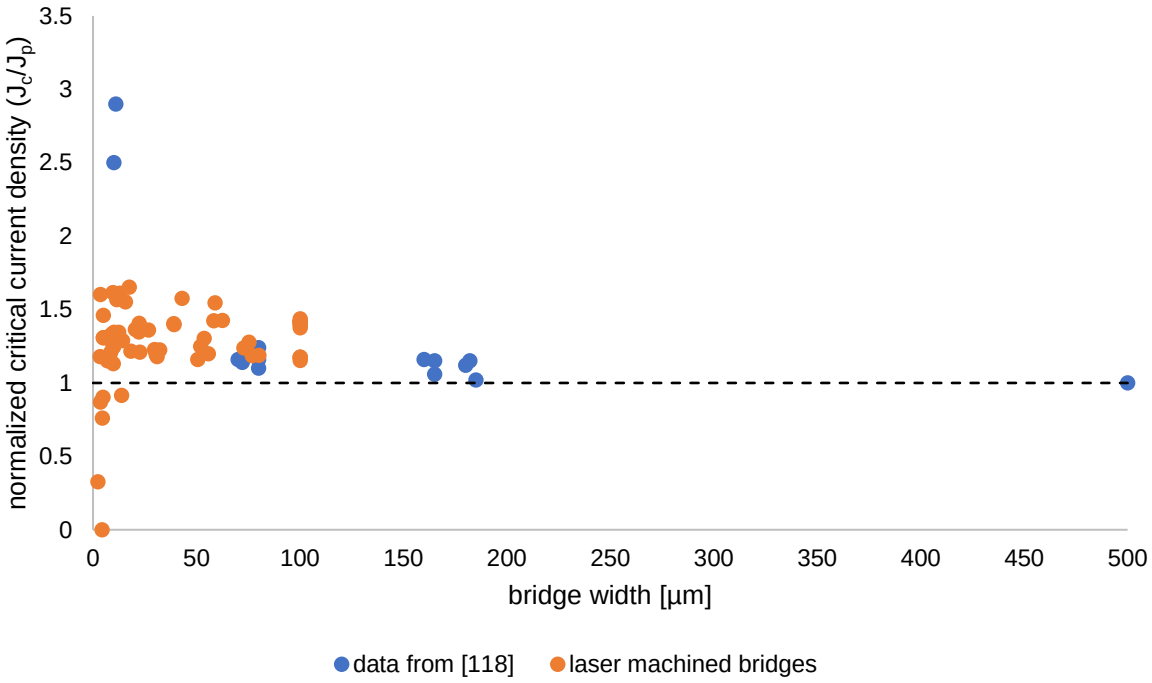

Figure 73: Comparison between laser machined samples and the data presented in [118]. Both sets of data were normalized by J_p = 2.47 MA/cm².

The laser machined bridges with widths down to ~15 µm seem to agree with the prediction shown in figure 73, but for bridges with widths below 10 µm a decline in J_c appears to be inevitable. This declining trend towards smaller bridge widths could be an artefact of the laser machining process. In the paper, they only used bridges made by lithography and FIB. To investigate whether this decline is related to the processing technique, the laser machined bridges are compared to further bridges made by lithography and FIB.

6.6.1 Comparison of the laser process with lithography and FIB

The results from the laser machined bridges were compared with lithography and FIB results provided by Dr Timothy Haugan, figure 74. In contrast to what was proposed in [118] about edge-barrier pinning, the lithography values also show a decreasing trend at smaller bridge widths. An increase is only shown for FIB but even there only one out of five data points shows an increase.

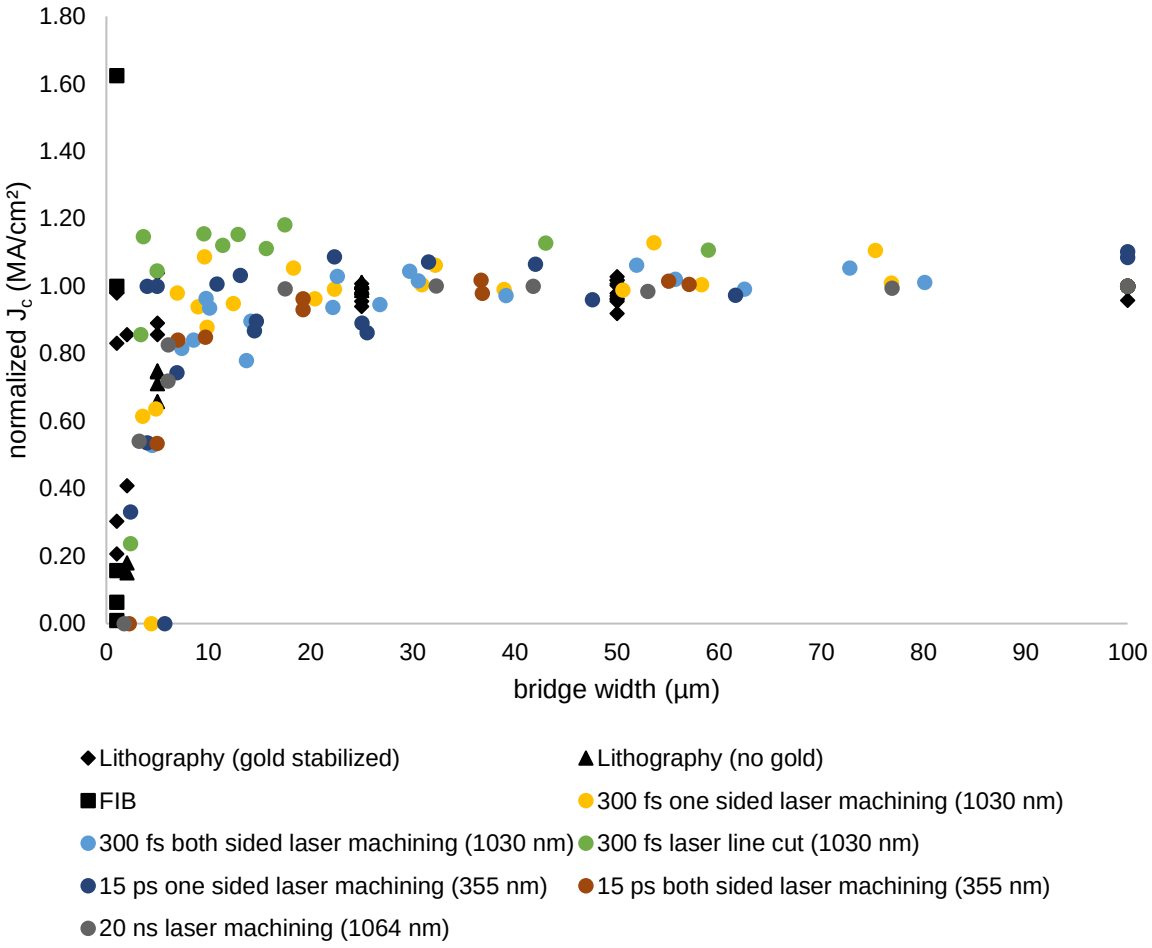

Figure 74: Comparison of J_c values from bridges made by different techniques (lithography, FIB, femtosecond laser machining).

Overall, laser machining produces comparable results to lithography, with slightly better results between 30 µm and 10 µm. Below 10 µm both techniques, lithography and laser machining, show a decline in J_c. Apart from the one FIB data point, the predicted exponential increase especially towards smaller bridge widths could not be verified. To explain the observed decline in J_c below 10 µm, the laser machined bridges were further analysed. Possible process induced damages could prevent the bridges from showing the predicted edge-barrier pinning effects.

6.6.2 Process limitations and edge damage

Aiming to find an explanation as to why bridges seem to degrade at a higher rate below 10 µm, the current machining process was investigated for possible degradation sources. While the laser process in itself is a 'clean' technique, which does not induce any of the known degradation sources such as chemicals and only very limited heat effects, thermal cycling due to repeated transport measurements could be an issue.

With each transport measurement, the sample undergoes drastic temperature changes which could potentially also degrade it. While warming the sample up after each measurement, icing and condensation cannot be avoided completely. To investigate thermal cycles as a potential degradation source, two more bridges were directly machined from 100 µm down to ~10 µm. These bridges only experienced two thermal cycles, once when measuring the J_c of the 100 µm bridge and once when measuring the 10 µm bridge. Their measurement results were then compared to other bridges with more thermal cycles, figure 75.

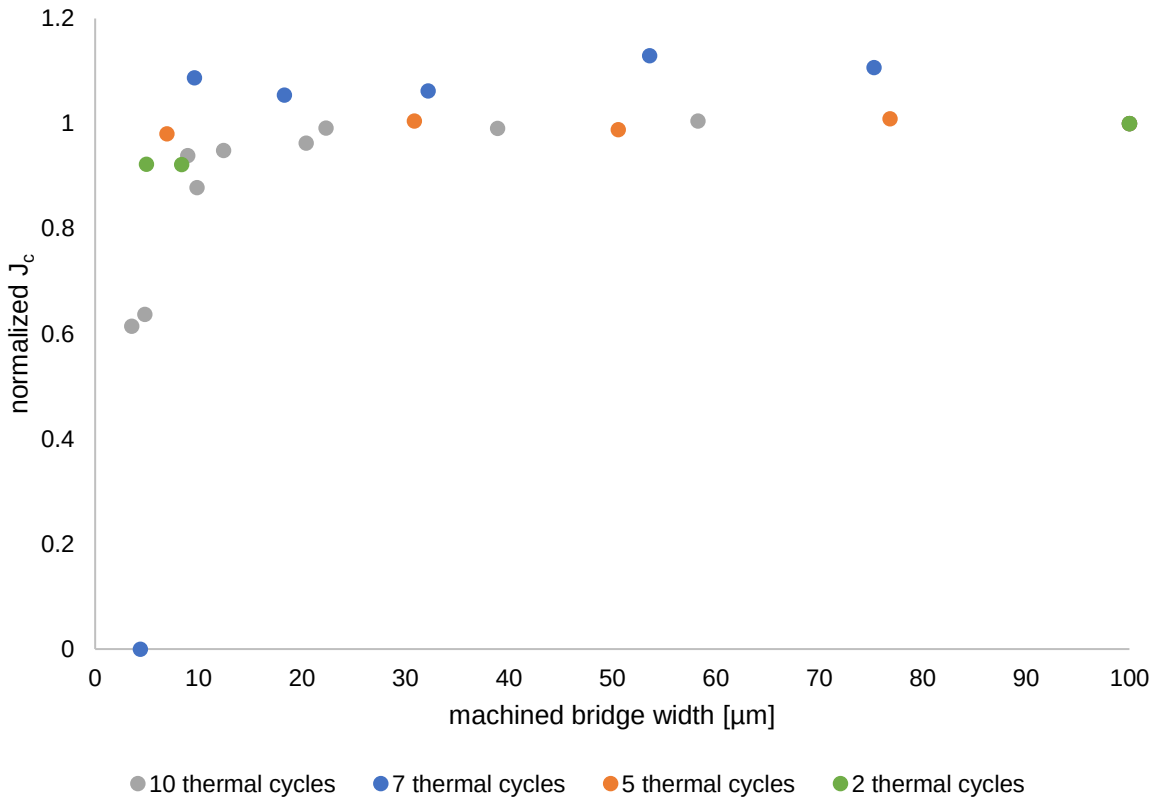

Figure 75: Transport measurements of laser machined YBCO bridges summarized in number of total thermal cycles.

Based on the results in figure 75, it seems unlikely that thermal cycling has been affecting the previous machining results. While the J_c of the '10 thermal cycles' appears lower than the remaining ones, there does not seem to be a clear trend connecting a decline in J_c to the number of thermal cycles.

After ruling thermal cycling out as one of the possible causes for the decline in J_c, another possibility was investigated. As the bridges are decreasing in width, a local variation of T_c close to the laser processed edges could influence their performance.

In paper [14], two Josephson junctions in the micro- and nanometer range were machined using a femtosecond laser. Similar to the results in this study, they have found a decline in the critical current density with smaller bridges. They explain this with a spatial distribution of T_c in an area close to the laser machined edge as shown in figure 76. The T_c variation is split into three different sections.

- N (T_c < 4.2 K): the material is not superconducting anymore and in its 'normal' state.
- S' (4.2 K < T_c < $T_{c,bulk}$): the material is slightly degraded.
- S (T_c = 87 K): the material has its original properties.

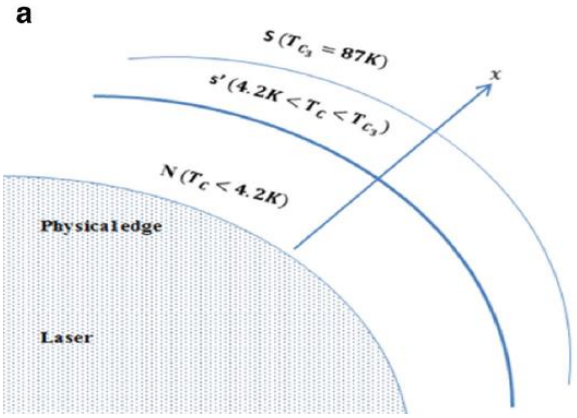

Figure 76: Spatial distribution of T_c around the laser machined area [14].

Assuming a spatial distribution of T_c around the edges, these variations can be expressed as shown in equation (22) [14]:

$$T_c(x) = T_{cBulk}\left(1 - e^{\frac{-x}{x_0}}\right) \tag{22}$$

with x being the distance from the processed edge and x_0 the characteristic length of the T_c variation.

Unfortunately, paper [14] does not mention the value they used as a characteristic length. The original paper that derived this equation used it on YBCO thin films structured by electron beam lithography and a focused ion beam [120]. The author used 50 nm as x_0. This decision seems to be based on experimental values. It is stated that between 50 nm and 350 nm the critical current of the nanobridges is a linear function.

To use this T_c variation approach, it would have been necessary to measure YBCO bridges over a temperature range. In this study, as the samples were measured at a constant temperature of 77 K, the spatial T_c distribution could not be measured. Therefore, it was attempted to find a way of using the measured I_c values to determine the edge damage of the laser processed bridges.

The effective cross section of a YBCO bridge is $t_{film}(w-d)$ or $t_{film}(w-2d)$ depending on the machining approach ('one-sided' or 'both-sided') with t_{film} being the film thickness, w the bridge width and d the damaged edge, figure 77.

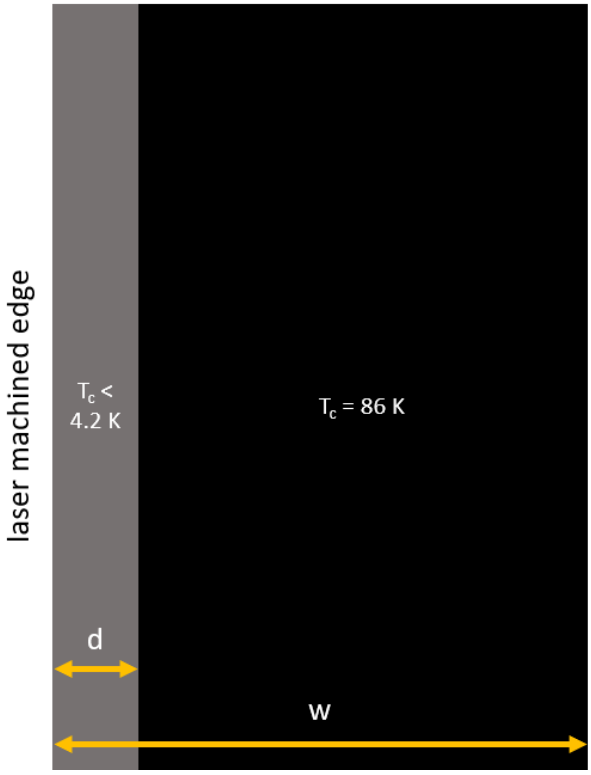

Figure 77: Schematic for calculating the electrical edge damage of laser machined bridges.

Assuming the laser causes damage a certain distance into the material at the processed edges, the true J_c can be expressed with the following equation (23) for 'both-sided' machined bridges:

$$J_c = \frac{I_c}{(w-2d)t_{film}} \tag{23}$$

which can then be rearranged to I_c as shown below, equation (24).

$$I_c = J_c t\,(w - 2d) \tag{24}$$

For this calculation, a few assumptions were made:

- d is treated as damaged area which is not superconducting anymore.
- J_c is uniform throughout the material and the laser machining does not affect it.
- d is constant for an ultrafast laser and only depends on T which is kept constant at 77 K.
- t_{film} is constant.

To determine d, w and normalized J_c values of machined YBCO samples were used and a linear trendline was added, figure 78.

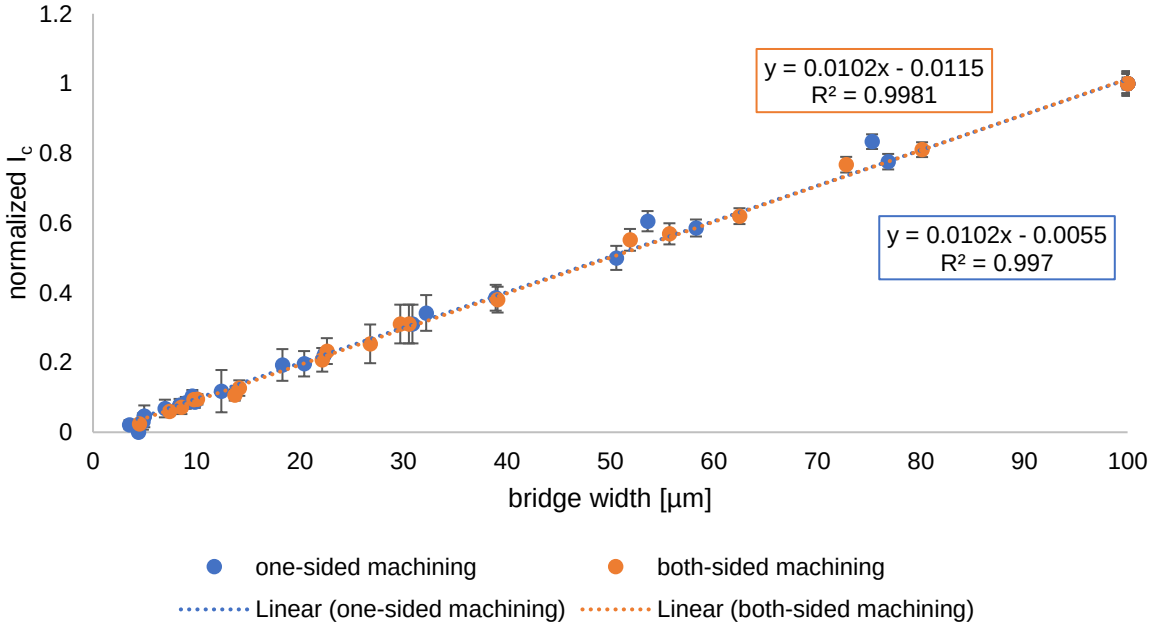

Figure 78: A linear trendline was added to measured and normalized I_c values over different bridge widths of multiple machined bridge samples.

With the given trendline equations, d can be calculated. Using the trendline of the 'both-sided' machined bridges, the gradient of the trendline (0.0102) equals $J_c t_{film}$, while the y-intercept (-0.0115) is $-J_c t_{film} * 2d$ at w = 0. In this case, d would be 0.56 µm. A similar result is calculated for the 'one-sided' machining process as well (0.54 µm).

These values can then be used to 'correct' the previous calculated J_c values by adjusting the bridge w to the superconducting part only, figure 79.

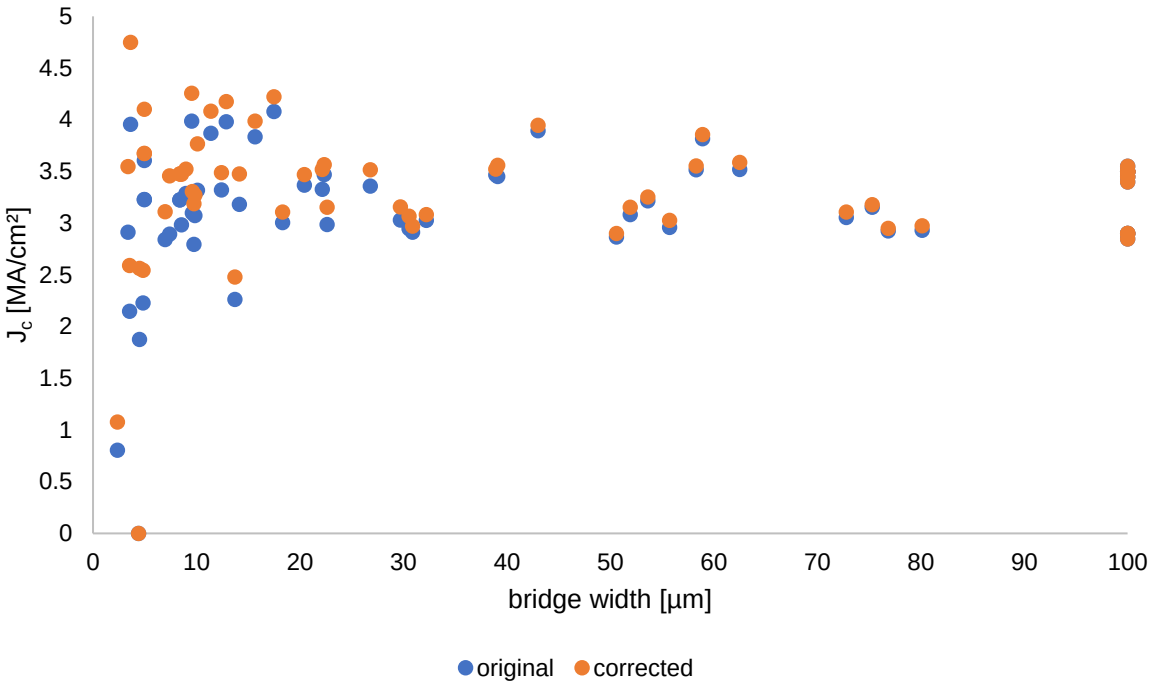

Figure 79: Corrected J_c values considering only the superconducting part of YBCO bridges.

The smaller the bridges, the more significant the damaged edge becomes and larger the difference between the original and the correct values. The uncertainty/error in d also becomes more significant for narrower bridges, causing increased scattering in the J_c values. Figure 78 shows the corrected values normalized by J_p.

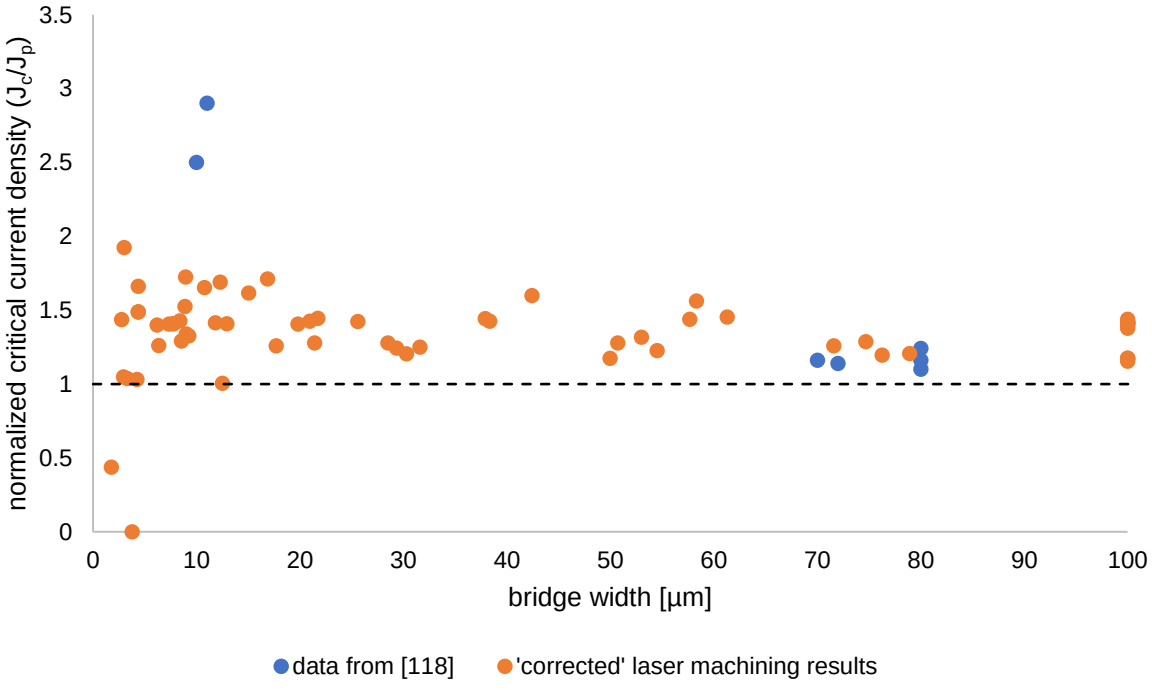

Figure 80: Comparison between the 'corrected' laser machining results and the data from [118].

Although accounting for the edge damage provides an improvement to the J_c behaviour, it does not confirm the theory stated in [118]. Even after empirically removing the process induced damages, the J_c decreases for smaller bridge widths, which leads to the assumption that this trend is not dependent on the machining technique (lithography or laser). Based on the discussed data, only FIB seems to show an exponential increase, however, there are only 3-4 data points supporting this claim due to high failure rates.

In summary based on the presented data and discussion, the presented theory in [118] appears questionable, especially considering that it is based on a 'perfect' edge. While it does accommodate for some imperfections, it might not have considered that smaller bridges are more prone to fail as they become more delicate, and possible inhomogeneities have a larger influence on the performance. The amount of data produced here also significantly exceeds the amount of data presented in [118], reducing measurement variations over a larger range of bridge widths.

6.7 Device manufacture

One emerging area of research for YBCO structures is the detection, generation, guidance, and manipulation of electromagnetic radiation across the microwave to infrared electromagnetic spectrum. In terms of YBCO antennas, decreasing and sharpening the feature sizes and shapes is expected to improve radiation efficiency and broaden the bandwidth. This could also potentially lead to an improved understanding of the fundamental physical phenomena in superconductors and potentially new engineering applications.

This chapter focusses on the fabrication of mainly ring-shaped emitters on a centimetre scale. It has been shown that terahertz electromagnetic radiation is emitted by YBCO rings when Cooper pairs are temporarily excited, causing them to break and recombine within picoseconds. Cooper pairs can be locally excited by a near-infrared ultrafast laser pulse. When exciting the current carriers, additional processes can be observed depending on the laser pulse energy and the total current in the ring [121]. This includes:

- Flux motion
- Photonic flux nucleation
- Fast voltage transients
- Superconducting gap suppression caused by non-equilibrium heating of electrons
- Bolometric response

Under the assumption that all of the listed processes are present, the total photoresponse would be a superposition of these extending the emission range to a broadband spectrum below the terahertz regime (e.g. microwave emissions) [121]. As there are still lots of questions regarding superconductors acting as antennas and emitters, ongoing research was conducted on the physical phenomena enabling emissions and how they can be shaped. These devices are attractive as they combine components such as antennas, waveguides, power supplies, and oscillators in one compact shape [12].

In a recent study [121], microwave emissions of an optically triggered YBCO ring were investigated over a range of different diameters. Here, YBCO rings prepared by

photolithography were cooled in a Styrofoam cup with liquid nitrogen. An ultrafast laser (pulse duration 45 fs at 790 nm) centred on the track illuminated the rings with a spot size of 5 mm. The rings were inductively charged with a solenoid prior to the trigger event. In addition to other findings, it was shown that the energy emitted is proportional to the energy stored in the ring, and that the dominant frequency of the emissions inversely depends on the ring diameter [121]. These results show the importance of the emitter shape as it directly influences the emitter's properties.

When making these devices with lithography, their designs need to be planned in advance to cover multiple shapes, however; this process would benefit from a more incremental approach where the shape of the emitter is improved based on the results of the previous one. Laser machining could be used to tune the emitted response. Another possibility would be reducing the track width of the same sample rather than using 'sister' samples from the same wafers. Investigating variations in track width could provide an insight into the non-linear behaviour of the current changes in the rings with each trigger laser pulse as observed in [121]. By using laser machining it might even eventually be possible to combine the machining setup with the measurement setup, avoiding additional alignment steps and greatly reducing the time required to optimise the various designs.

In this work, the Satsuma ultrafast laser has been used to machine multiple YBCO emitters with different shapes. Two sets of samples were provided. One with a MgO substrate and the other with a LaO substrate. The machined samples are shown in figure 81. After machining the samples were sent to the Wright Patterson Air Force Base in Ohio, US. There, their J_c was measured, table 5.

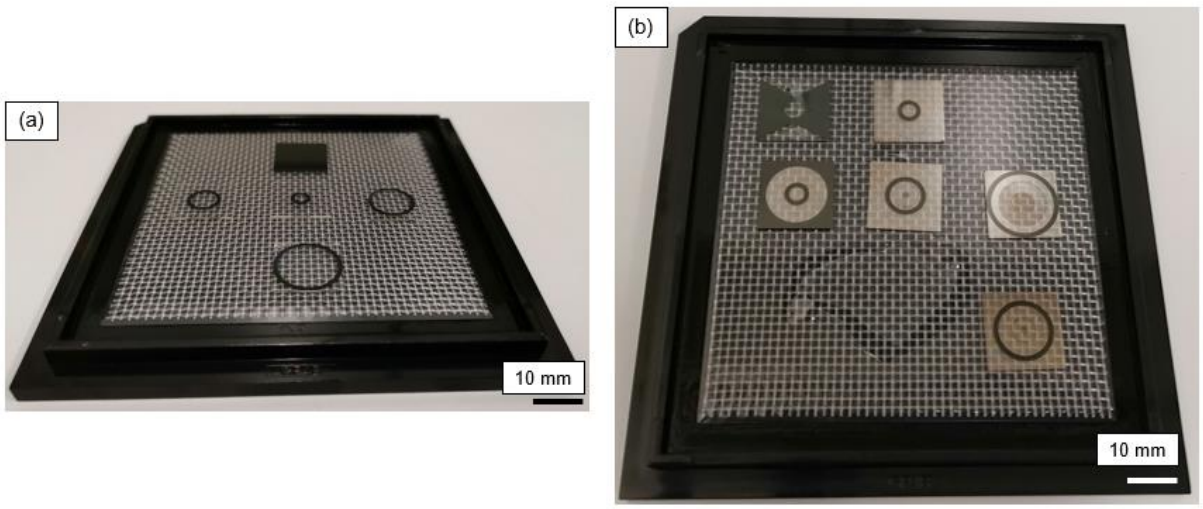

Figure 81: The rings in (a) were machined with a constant pulse energy of 220 nJ. The inner and outer edge were 1 kHz at 1 mm/s processing speed to ensure a similar processing result compared to previous reported bridges. After that, the frequency and the processing speed were increased by the factor 10 to reduce the overall processing time. The power was measured for each setting to ensure constant pulse energies. The rings and bowtie in (b) were machined in a similar fashion with an average power of 1.9 mW at 10 kHz and 10 mm/s.

Table 5: Summary of the machined devices. J_c was measured in the laboratory of the Air Force Base in Ohio.

Sample N°	Shape	Substrate	Outer diameter (OD) (mm)	Trackwidth (mm)	J_c post machining (MA/cm²)
1	Ring	MgO	11.867	1	2.5-3.19
2	Ring	MgO	8.34	1	2.45-3.1
3	Ring	MgO	5	1	0.3-0.4
4	Ring	LaO	14.84	1	2.6-2.9
5	Ring	LaO	12	1	0.3-0.4
6	Ring	LaO	8.5	1	1.9-2.3
7	Ring	LaO	5	1	0.6-0.8
8	Bowtie	MgO	-	-	1.9-2.6

Before processing, the manufacturer reported a nominal J_c of about 2.5 MA/cm² for the thin films. Compared to rings made by lithography, the laser machined samples delivered comparable results while also offering the opportunity to flexibly tune the emitters. Independent from the substrate and technique, 5 mm rings show a decline in J_c compared to larger rings. A 5 mm ring made by lithography measured 1.2-1.6 MA/cm². The cause for this decline is not yet known and will require further tests and investigations. The 12 mm ring on the LaO substrate also shows a decreased J_c, although the processing parameters were held constant and the remaining rings do

not show significant changes. This could be due imperfections in this specific sample, which is more likely to occur with a LaO substrate as it has a more complex crystalline structure than MgO and this can cause problems due to twinning, i.e. the decline could have occurred for other reasons than the laser machining. The difference in substrate structure is shown in figure 82.

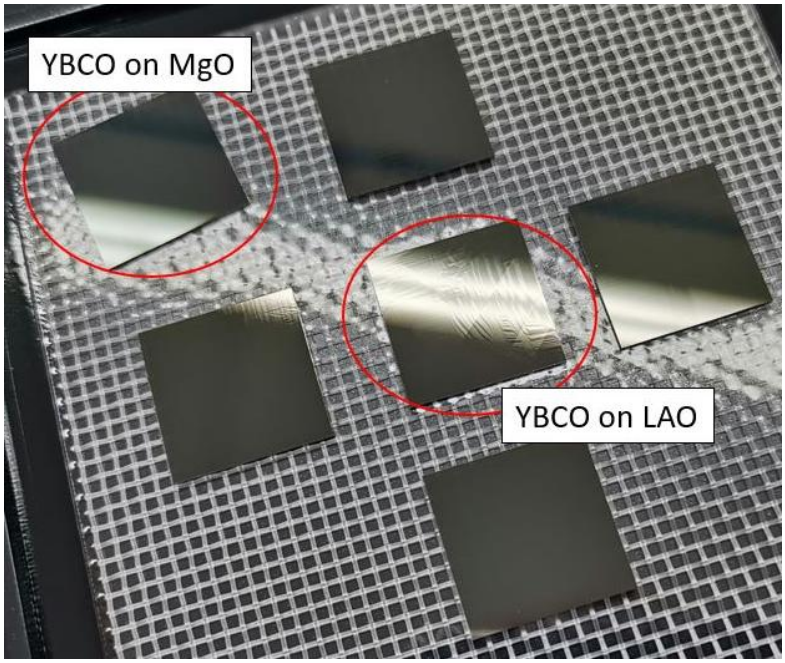

Figure 82: Structural difference of the substrates MgO and LaO.

Such sample to sample variations make it difficult to make meaningful comparisons and it highlights the need for a flexible patterning approach.

Finally, we tested, and successfully created, making a different shape with laser machining. This took the form of a bowtie with a hole in the centre. This shape is designed for broad band emissions which has been investigated in [122].

6.8 Conclusion

The pulsed ablation thresholds of YBCO, Al_2O_3 and MgO were compared to choose a suitable substrate for the YBCO bridge wafer. The ablation thresholds of both substrate options were about 3 times higher than YBCO making them suitable for the laser machining process. MgO was chosen to avoid any interferences caused by the buffer layer also present on the Al_2O_3 substrate. Until the arrival of the YBCO bridge wafer, YBCO thin film samples were used to find suitable processing parameters after determining the scanned ablation threshold. Based on multiple trials with changing

variables, a repetition rate of 1 kHz at 1 mm/s processing speed and a peak fluence of ~ 2 J/cm² were chosen as the processing parameters for the Satsuma laser. To improve the edge quality of the machined trenches, a pi shaper was added to the setup to change the intensity profile of the Satsuma laser. The width of the melt film at the machined edge could be reduced from about 1.5 µm to 700 nm setting a physical machining limit of > 700 nm for the Satsuma laser. Apart from the visual improvement, the pi shaper did not seem to influence the critical current density. Since the alignment procedure was very time consuming and was not repeatable on a day-to-day basis, it was decided to not include the pi shaper in further trials.

When machining YBCO bridges, different machining strategies were discussed. The majority of bridges were machined using a 'one-sided' process to avoid damages on both sides and variations in the machining result based on the beam path. The aforementioned trials were then repeated for different laser wavelengths (UV-IR) and pulse durations (ns-fs). Only the nanosecond laser showed insufficient machining results due to an increased melt residue. When comparing the remaining results in the pico- and femtosecond regime with different wavelengths, no significant difference in the electrical properties was detected. For the following experiments and analysis, the Satsuma laser was primarily used.

When machining YBCO bridges over a range of widths, the aim was to see an exponential increase of J_c as predicted in [118]. The measurement results showed the opposite trend, which could be caused by laser induced damages. After calculating the edge damage (~ 0.55 µm for the Satsuma laser), the width of the machined bridges was adjusted to represent only the part which is superconducting. However, even with this correction, the theory could not be confirmed. In general, it appears, that only FIB processing might be able to achieve significant edge-barrier pinning effects. While not being able to confirm the theory, the electrical machining limit of YBCO for the Satsuma laser was determined.

To complete the investigation of laser patterning YBCO, centimetre-scale rings/bowties were made which act as emitters. The results again showed a similar performance of laser machining as compared to lithography, but with the advantage of design flexibility with which the electromagnetic emission can be tuned and circuit shaped in a step-by-step approach.

7 Raman spectroscopy: analysing de-oxygenated YBCO

While Raman spectroscopy has been used in studies before, it has not been used in conjunction with transport measurement results. By combining the advantages of Raman and transport measurements, the drawbacks of each individual technique could be offset, table 6.

Table 6: Advantages and disadvantages of Raman spectroscopy and transport measurements to evaluate YBCO.

Raman spectroscopy	**Transport measurements**
+ fast non-contact procedure	+ simple and direct information about electrical properties
+ possible inline measurement setup	+ reliable
- complex spectra	- sample needs to be moved to another setup
- no direct information about electrical properties	- time intense

To correlate Raman spectroscopy and transport measurements, general Raman studies on YBCO need to be conducted. The following objectives were set for this chapter:

- determine suitable Raman measurement parameters
- investigate changes in I_c and the Raman spectrum caused by thermal energy
- link transport and Raman measurement results to predict the quality of the YBCO
- analyse laser machined YBCO samples

7.1 Characterising Raman measurement parameters

For Raman measurements, parameters such as wavelength, focusing objective, power and acquisition time need to be adjusted depending on the material. Suitable Raman parameters were investigated for both sets of YBCO samples grown on Al_2O_3 (sapphire) and MgO substrates. First, different excitation wavelengths (532 nm,

633 nm, 785 nm) were tested on both samples. Due to the film thickness of 200 nm, background interference from the substrates could occur. This needs to be avoided as important information from the YBCO Raman spectrum could be lost. Using a Bruker Senterra Raman microscope, the spectra of the substrates was acquired as shown in figure 83.

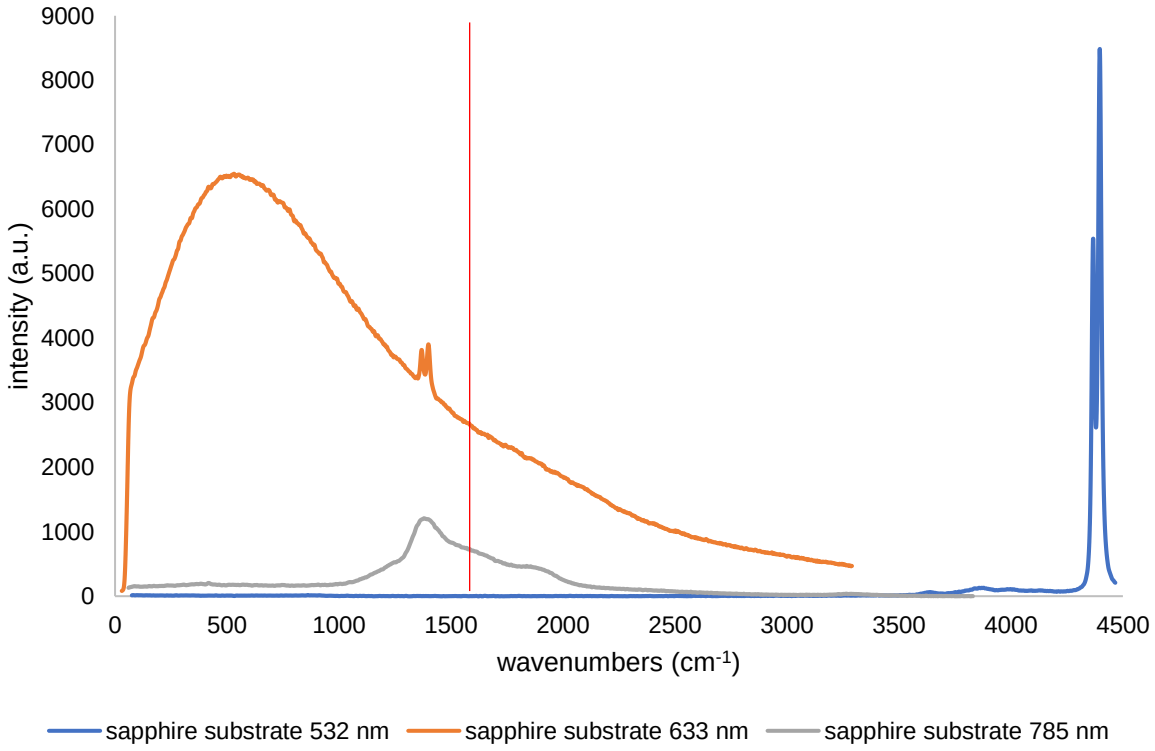

Figure 83: Raman spectra of the sapphire substrate taken with three excitation wavelengths to avoid interference with the vibrational modes of YBCO.

Starting with the sapphire substrate, the Raman response of a YBCO film was investigated. The main vibrational modes of YBCO are located between 100 cm^{-1} and 1600 cm^{-1} [96] and a spectral overlap between the YBCO and the substrate should be avoided in this wavenumber range. This renders a Raman excitation wavelength of 633 nm as not suitable. In addition, measuring with the 633 nm excitation required a warm-up time of about an hour, increasing the overall duration of the Raman experiments. A 785 nm wavelength showed a sapphire background spectrum at > 1000 cm^{-1} and so could be used for the investigation as the main vibrational modes of YBCO, listed in Chapter 4.6, are below 1000 cm^{-1}. Similarly the 532 nm wavelength spectrum of sapphire shows a negligible background signal until ~ 4500 cm^{-1} far outside the range of interest for this work. The Raman spectra for YBCO on a sapphire substrate using 532 nm and 785 nm wavelengths are compared in figure 84.

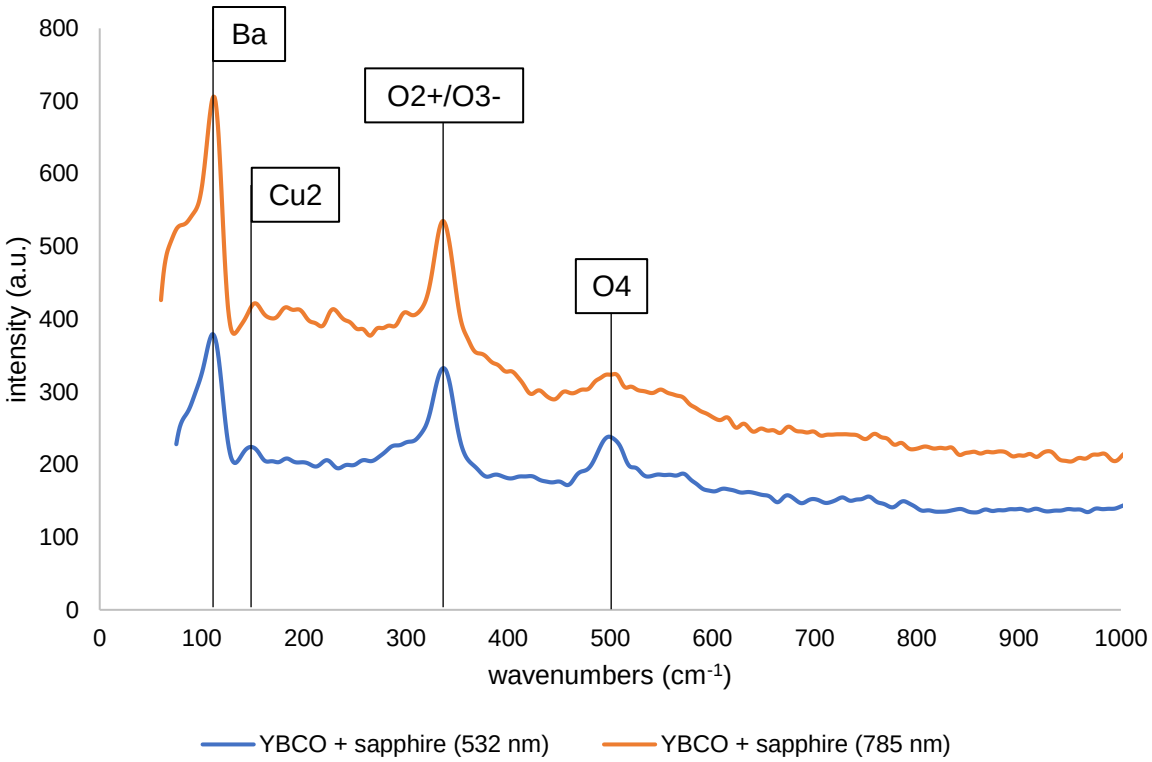

Figure 84: Comparison of the four main YBCO vibrational modes at 532 nm and 785 nm. These spectra were taken from a YBCO sample with sapphire substrate.

The values of each YBCO related vibrational mode is listed and compared in Table 7.

Table 7: Location of the vibrational modes at 532 nm and 785 nm on sapphire substrate.

Vibrational mode	**532 nm (cm^{-1})**	**785 nm (cm^{-1})**
Ba	110.5	112
Cu2	148	152
O2+/O3-	336.5	336
O4	498.5	504

A wavelength of 532 nm tends to shift the vibrational modes to lower wavenumbers, especially visible with the O4 mode. The lower wavenumbers at 532 nm could falsely indicate decreased oxygen levels as a wavenumber below 500 cm^{-1} for the O4 mode is characteristic of decreased oxygen doping [96]. For the sample under test, 785 nm appears to deliver more accurate results as they match the transport measurements and had results expected of a sample with optimal oxygen levels ($YBCO_7$).

Both excitation wavelengths were also tested on the YBCO samples grown on MgO substrates, figure 85.

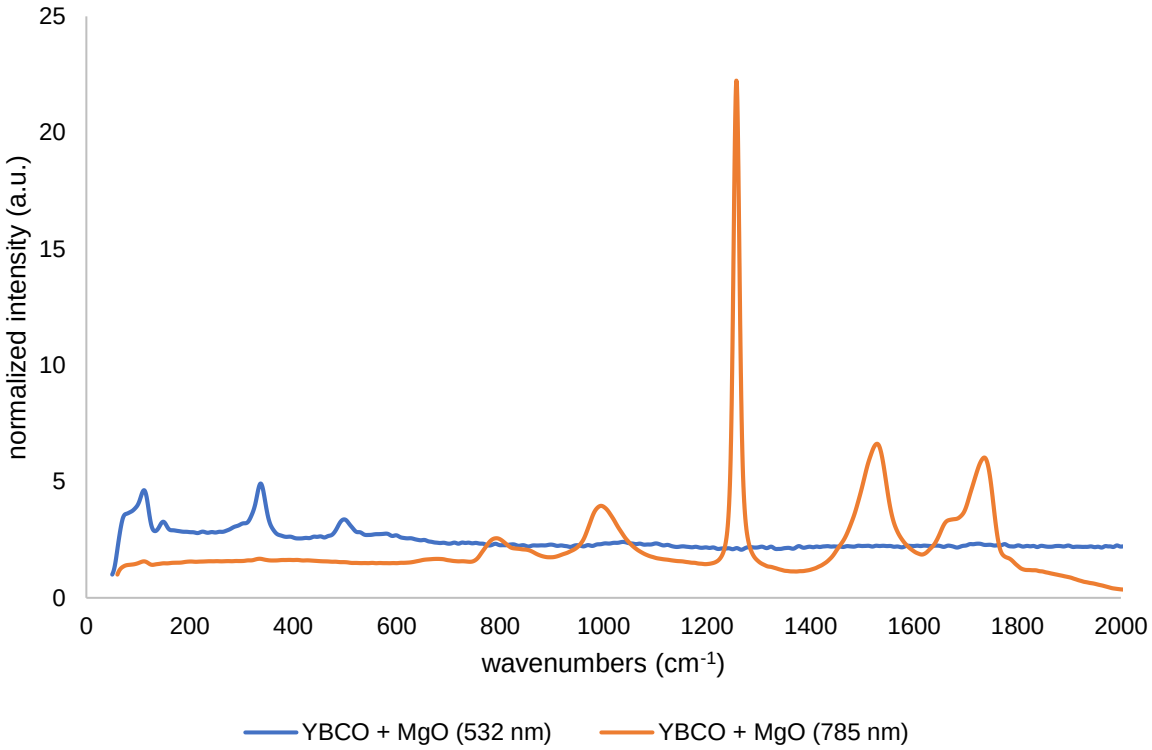

Figure 85: Raman spectrum of YBCO samples on MgO substrate at 532 nm and 785 nm. The spectra differ depending on the excitation wavelengths due to the Raman activity of the substrate.

MgO shows a Raman peak at 785 nm which interferes with the YBCO spectrum, rendering the 785 nm wavelength unsuitable for these measurements. Therefore, for samples on the MgO substrate the excitation wavelength 532 nm is chosen.

Following the wavelength selection, the available objectives (4X, 20X, 50X) were investigated, figure 86.

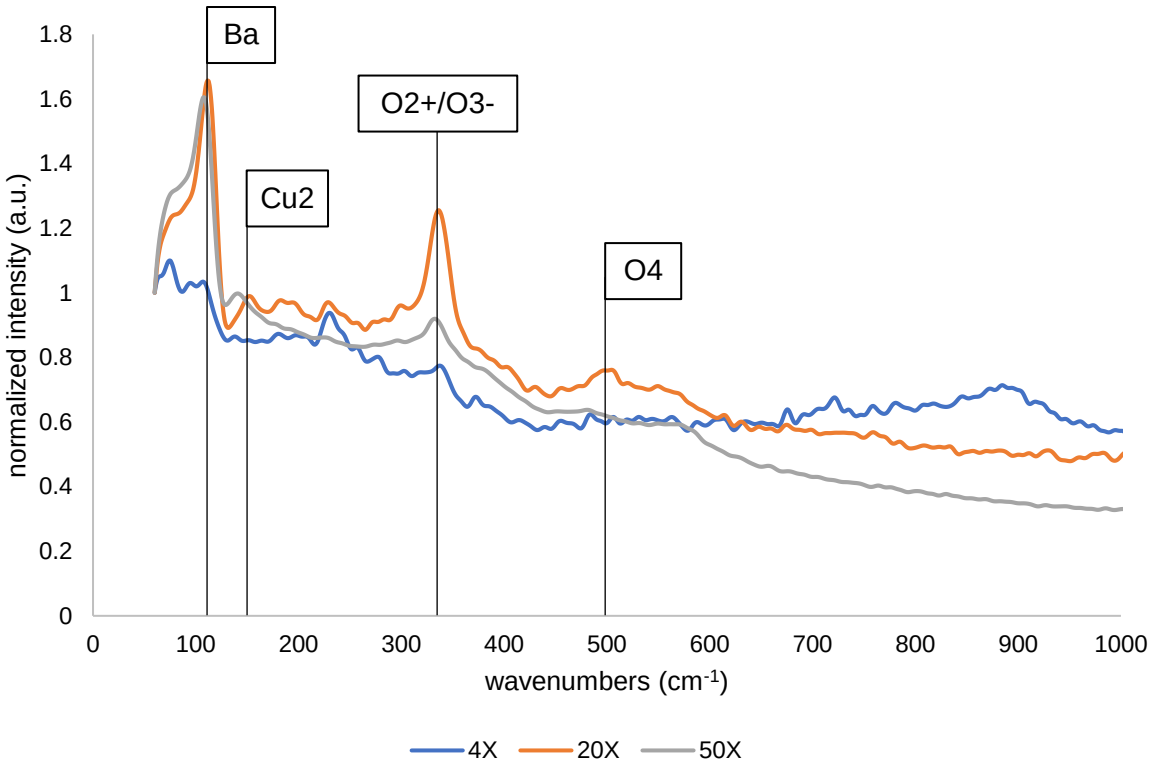

Figure 86: Raman Spectra of YBCO on sapphire taken with 4X, 20X, and 50X objectives at 785 nm. The positions and intensities of the main vibrational modes are compared.

By varying the magnification/spot size, the area of inspection changes, which sets a limit on the detectable features and also influences the spectra as the signal intensity changes. The Raman signals achieved with the 4X objective are difficult to distinguish from noise and the O4 mode is not visible. The 20X objective shows all four main Raman modes. Similarly, the 50X objective also offers a Raman spectrum with most of the main modes, however, the modes are shifted to lower wavenumbers and the O4 mode is not visible. These shifts could be caused by measurement inaccuracies of the system such as the focal position for example. Based on these results, the 20X objective is used for all subsequent Raman measurements.

After evaluating the wavelengths and objectives, the following Raman settings were chosen for the measurements:

- The samples on sapphire substrates used parameters set to 785 nm wavelength, 20X magnification, 25 mW power, and 5 s acquisition time. The optical penetration depth is thought to be around 80 nm [70], [114].

- For MgO, 532 nm, 5 mW, and a 10 s acquisition time with the 20X objective were chosen. At 532 nm the optical penetration depth of YBCO is 73 nm [70], approaching half the film thickness.

7.2 Analysis of de-oxygenated YBCO samples due to heat treatments

One of the degradation mechanisms that could occur during laser machining is de-oxygenation of YBCO due to increased thermal energy [90], [93]. As discussed in section 4.2.2, the oxygen content is directly connected to the superconducting properties and crucial for assessing the materials functionality.

Using equation (23) from section 4.2.2, the oxygen content of YBCO thin film samples was calculated. Using the Raman spectrum of the YBCO sample with the sapphire substrate taken at 785 nm, an oxygen value of x = 7 is calculated for v_{OIV} = 504 cm^{-1}. The sample was measured within a week of arrival; hence, it can be assumed that the samples did not show any aging processes. However, this may not be true of later measurements as, although the samples are stored in a desiccator, slight degradation might occur over time.

While this approach delivers direct information about the oxygen content of the sample, it also has drawbacks that have not been addressed including:

- The position and intensity of the O4 mode varies depending on the settings of the Raman spectrometer as previously shown in figure 84 and 86. These variations introduce uncertainties into the results and a lack of comparability between different setups.
- It appears that the equation needs to be adjusted to the specific measurement setup as several researchers have used this approach but with slight variations of equation (23), e.g. in [70]. However, no information has been given on how to adjust the equation. Presumably it is via an empirical approach based on given measurement results.

Given these drawbacks, the aim in this work is to investigate further spectral changes caused by increasing the amount of thermal energy to find more dominant changes and, for the first time, connect them to transport measurements.

As a first step, a YBCO thin film sample was exposed to multiple heating cycles on a hot plate (30 min at 300 °C) in air, figure 87.

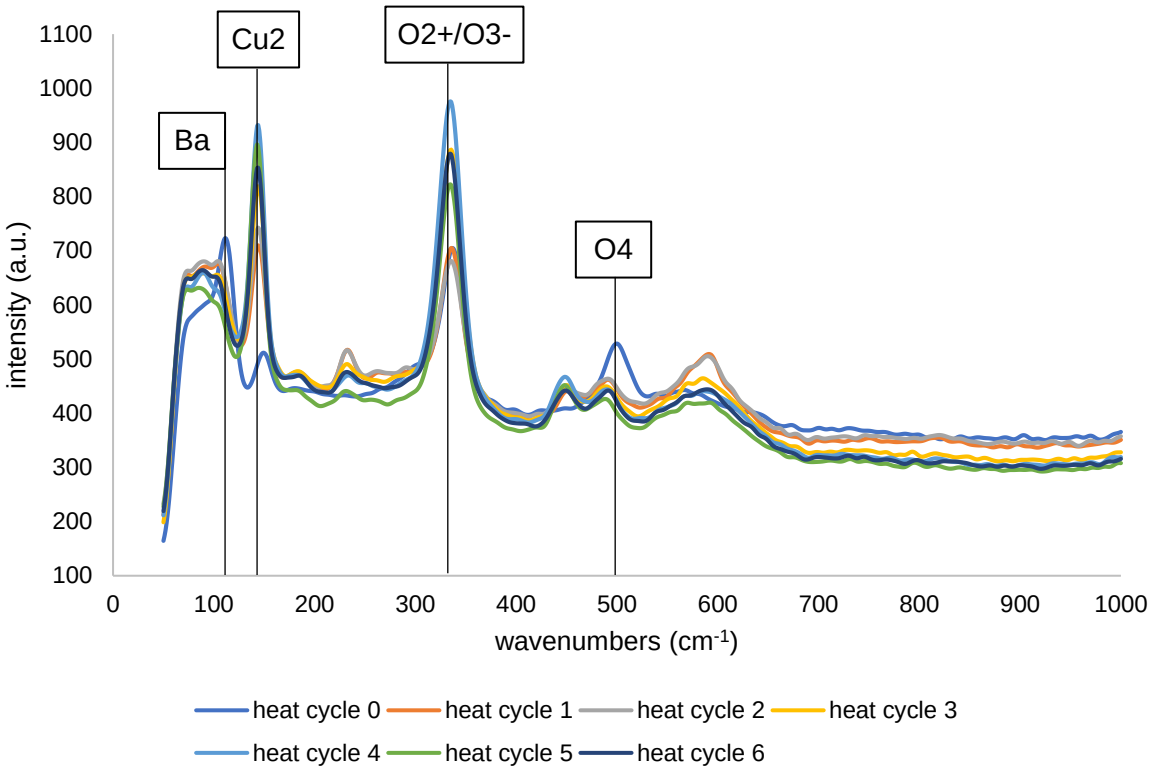

Figure 87: A YBCO thin film on MgO exposed to 6 heat cycles at 300 °C for 30 min each, Raman spectra taken before and after. The 20X objective was used at 532 nm with a laser power of 5 mW and an acquisition time of 10 s.

The following spectral changes were observed to the peaks after the heat treatments, figure 88:

- Ba peak: change of peak shape and intensity.
- Cu2 peak: strong increase in the intensity of around 1.6 times and shift of about 5.6 cm^{-1} to lower wavenumbers.
- Additional peak at ~ 230 cm^{-1}.
- O2+/O3- peak: increase of intensity.
- O4 peak: shift to 11 cm^{-1} to lower wave numbers and the appearance of a second peak.
- Cation disorder mode at ~590 cm^{-1}.

These changes can be interpreted as signs of degradation and show the potential of using Raman to assess laser damage.

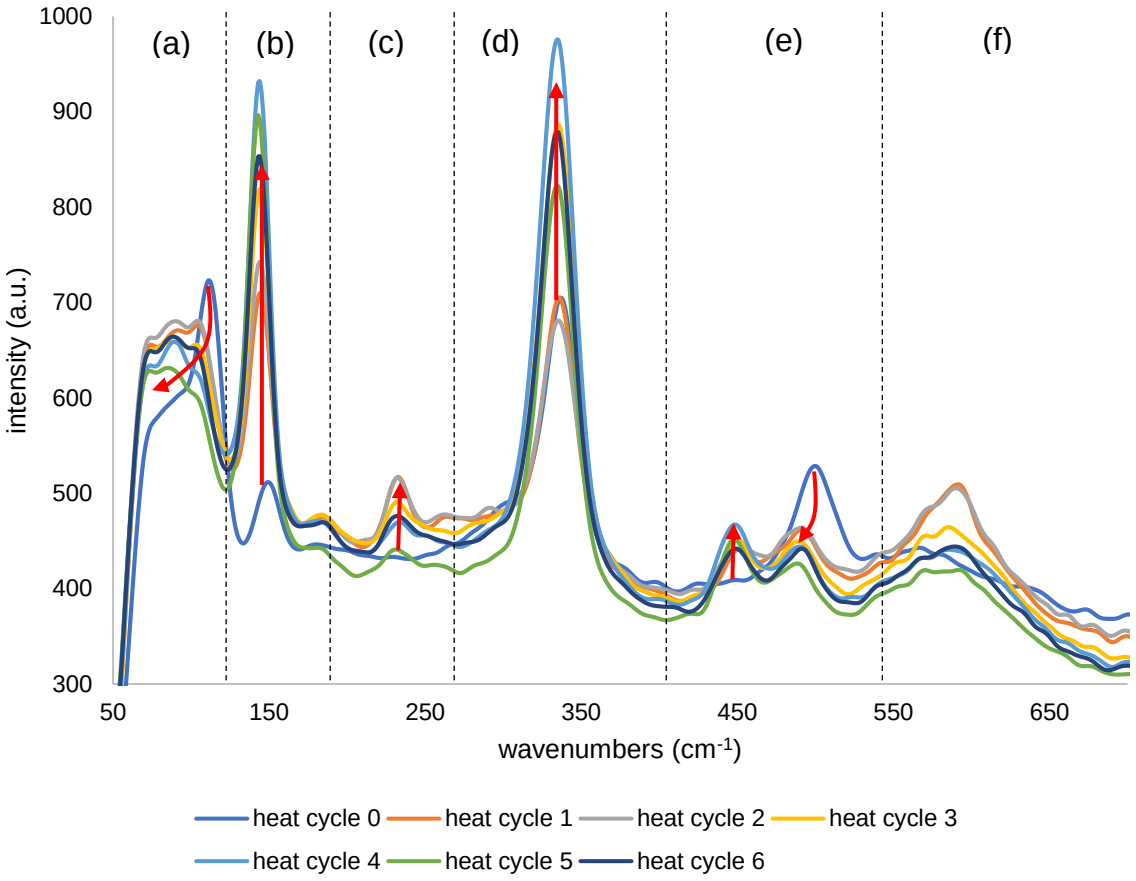

Figure 88: Spectral changes due to heat treatments on YBCO. The blue colour is getting brighter for each heat treatment. (a) The Ba peak is getting flatter. (b) The intensity of Cu2 increases. (c) An additional peak appears at ~230cm^{-1}. (d) Increase of the O2+/O3- peak. (e) The O4 peak shifts to lower wavenumbers indicating loss of oxygen and a second peak appears. (f) Cation disorder mode.

The shift from the O4 peak to lower wavenumbers indicating the loss of oxygen and the appearance of the cation disorder mode were expected. Another characteristic of degraded YBCO is that the Ba peak is lower in intensity than the Cu2 peak, figure 88 (a), (b) [96]. When oxygen loss occurs, the vibrational mode of Cu2 changes due to the lack of surrounding oxygen in the tetragonal (insulating) form of YBCO, figure 89.

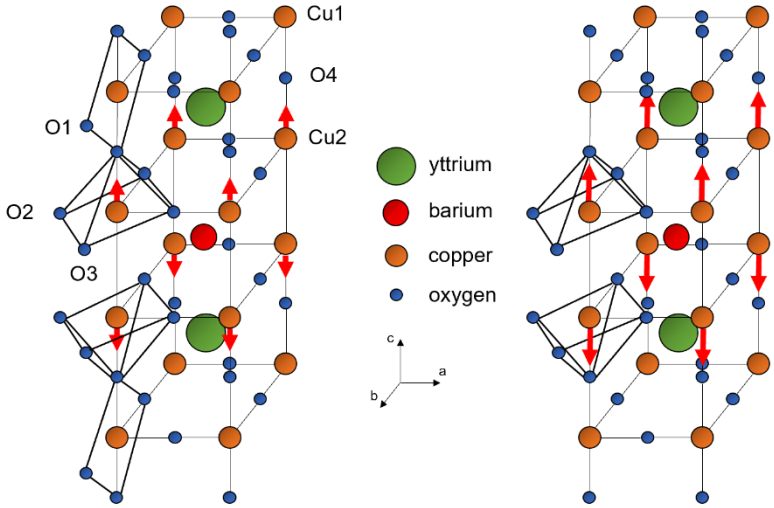

Figure 89: Crystalline structure of YBCO. The schematic on the right shows the orthorhombic structure of YBCO (superconducting) while on the left the tetragonal structure (insulating) is shown. The red arrows are indicating the Cu2 vibrational mode which is detected by Raman spectroscopy. The direction of the vibrational modes is further explained in reference [94].

As stated in [96], once YBCO is degraded, the Cu2 peak intensity surpasses the Ba peak. Instead of focussing only on one peak (as it can change shape and position) we investigated the ratio between two peaks, namely between Ba and Cu2.

This involved analysing the change to this ratio during thermal treatments and then relating these changes to transport measurement results. To do so, a YBCO bridge sample was repeatedly heated in short cycles (10 s at 300 °C) and the I_c measured, figure 90.

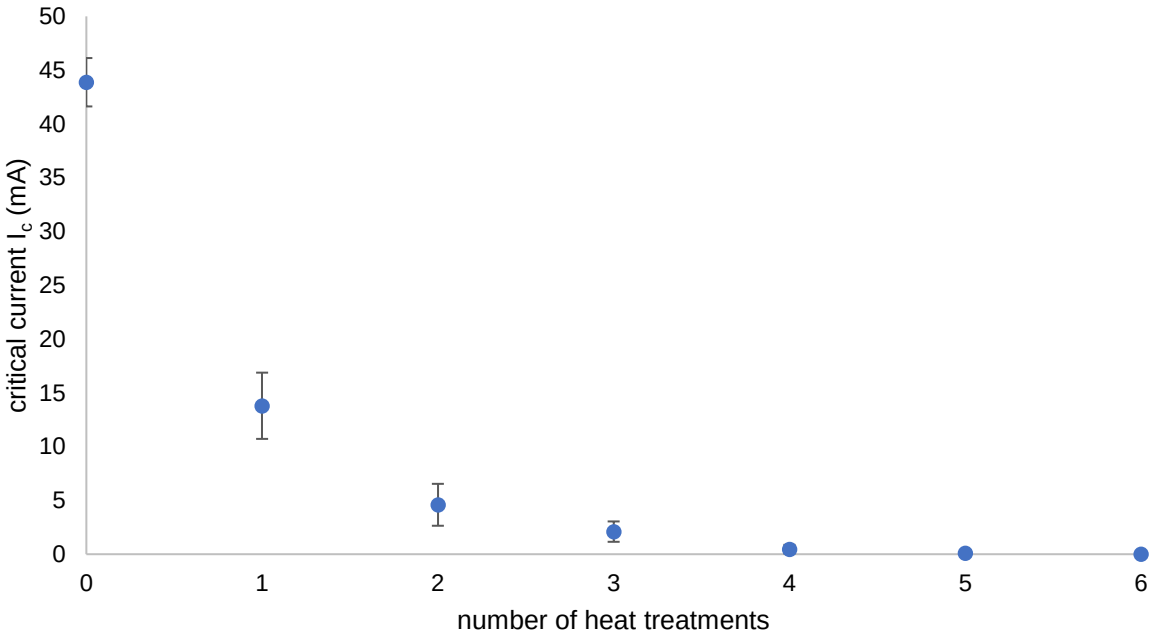

Figure 90: Critical current decrease over multiple heat treatments of a 10 µm YBCO bridge sample. The error for the critical current is 140 µA at a criterion voltage of 0.5 µV.

In addition to the transport measurements, the Raman spectra were also measured after each heat treatment, figure 91.

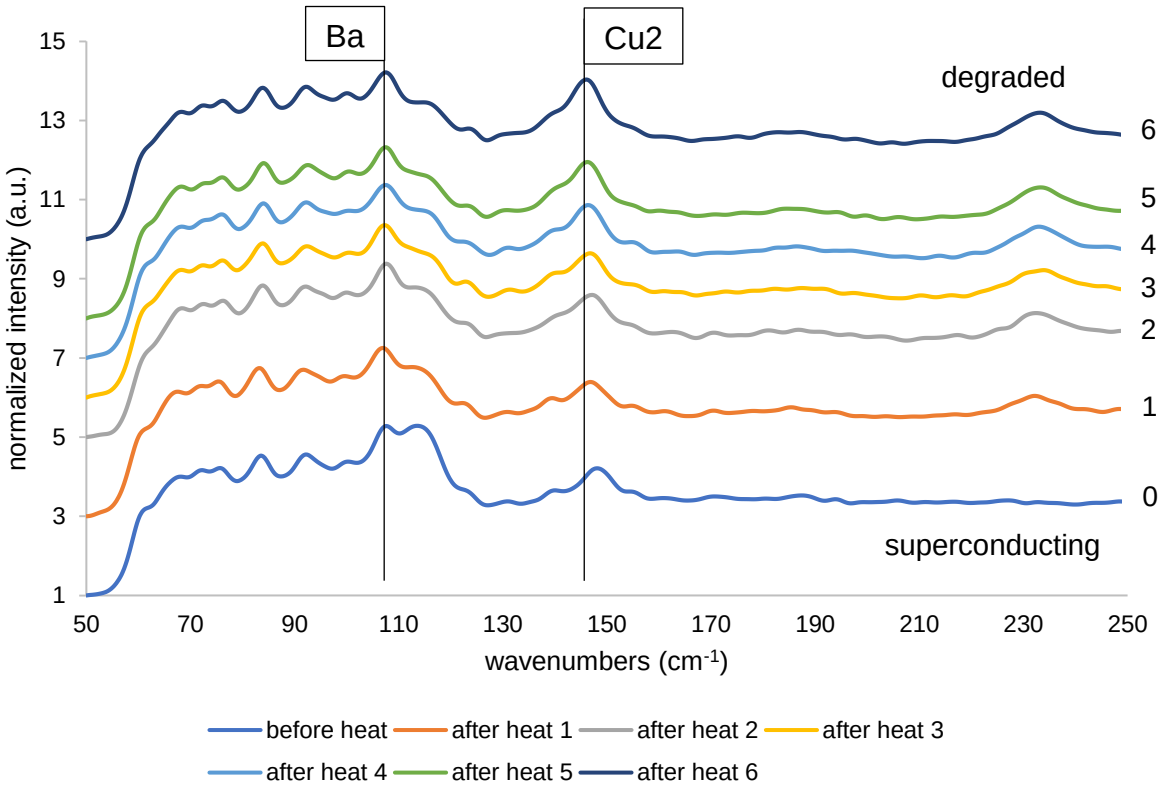

Figure 91: Changes in the Raman spectra are observed while the sample changes from superconducting to complete degradation. The different spectra are displayed with an offset to determine the changes.

With a 10 s heating time, multiple intermediate data points could be measured during the material's phase transition from superconducting to degraded. With longer heating times, the number of intermediate data points would be insufficient.

To combine the measurement results of Figure 90 and 91, the Ba/Cu2 ratio has been calculated and plotted in respect to I_c, figure 92.

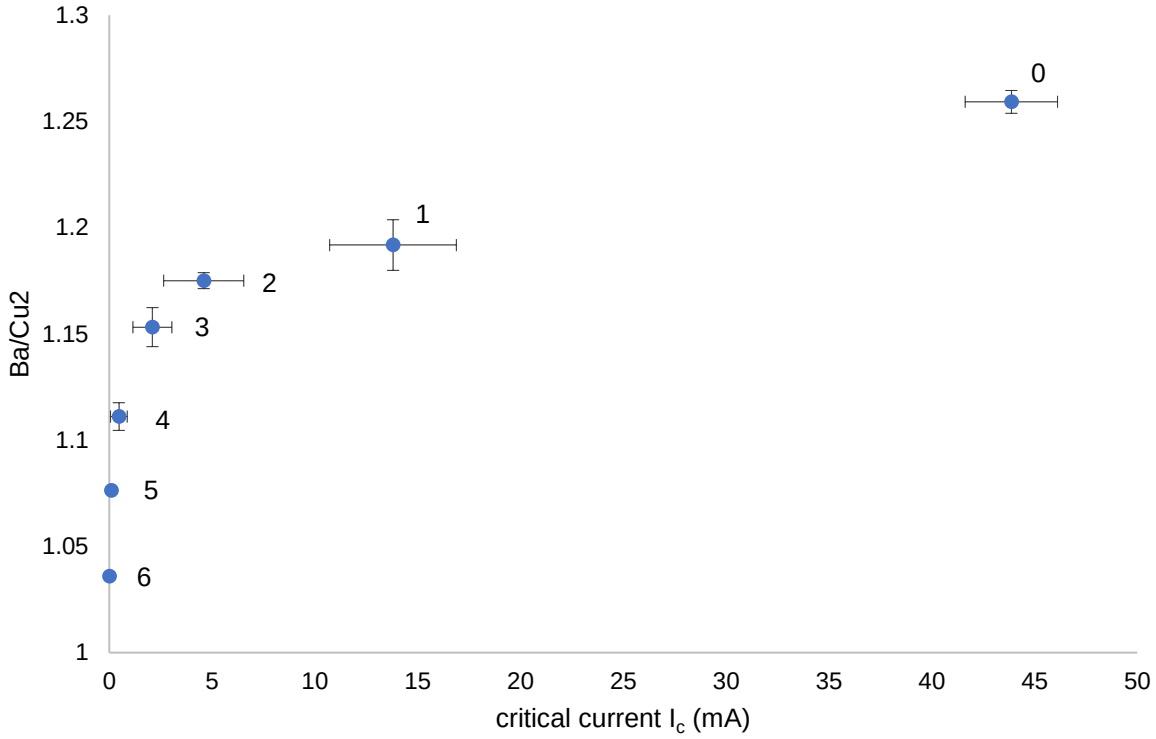

Figure 92: The calculated Ba/Cu2 ratio are plotted against the critical current measured before and after each heat treatment.

As expected, as the Ba/Cu2 ratio declined, the critical current also decreased. More specifically, it appears that below a Ba/Cu2 ratio of 1.15, the YBCO sample is completely degraded (3 out of 6 samples). This could be used as a threshold for a quick and easy inline assessment of the superconducting properties. An in-line or parallel assessment procedure would eliminate unnecessary movement of the sample for transport measurements. When machining microbridges it is difficult to judge whether the sample is still superconducting or already degraded especially for machining widths below 10 µm. Inline assessments would support the decision-making process in deciding to continue with a sample if further processing steps were needed.

In a further step to investigate whether Raman spectroscopy is a suitable tool for analysing a machined sample's performance in-line or parallel to the laser process, laser machined samples need to be investigated as well since the results obtained so far are valid only for degradation caused by direct thermal heating on lithographically etched samples.

7.3 Analysis of laser machined YBCO samples

Laser machined bridges were examined to identify laser induced damage and possible heat influences. Raman spectra from laser machined bridges pre- and post-processing are shown in figure 93.

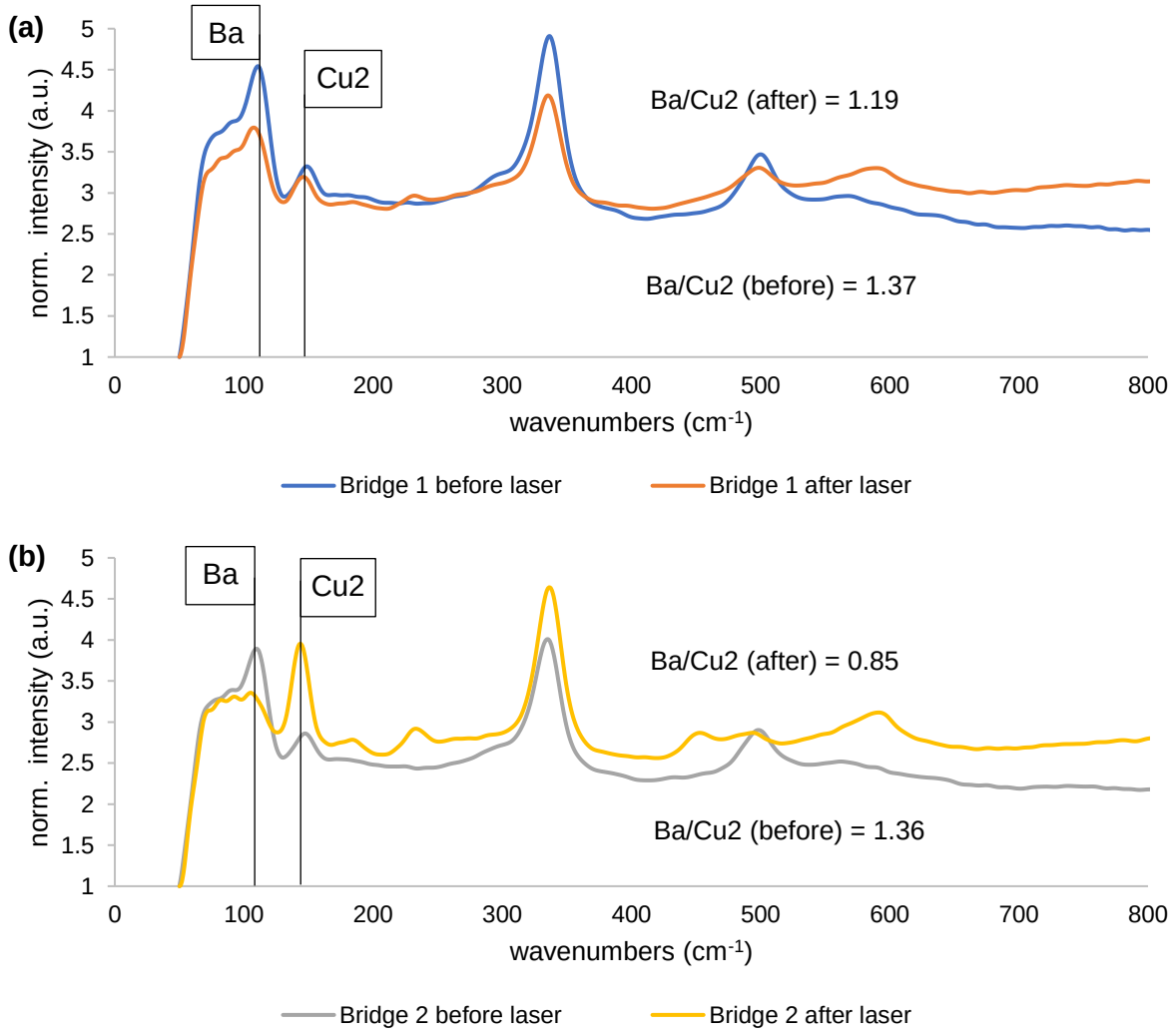

Figure 93: Raman spectra before and after the laser machining of two bridges (a), (b). A pulse energy of 215 nJ was used at a processing speed of 1 mm/s and a repetition rate of 1 kHz.

Bridge 1 was machined from 100 µm to ~ 30 µm and the Raman spectra showed slight changes to peak intensities, especially a decrease in Ba. The width of Bridge 2 was reduced from 100 µm to ~ 10 µm and the Raman spectra showed a significant change in the Ba/Cu2 ratio, similar to the changes observed during the heat treatments. This suggests that the sample has degraded, which was later confirmed by transport measurements. More laser machined bridges were inspected with Raman spectroscopy to investigate whether these spectral changes are repeatable, figure 94.

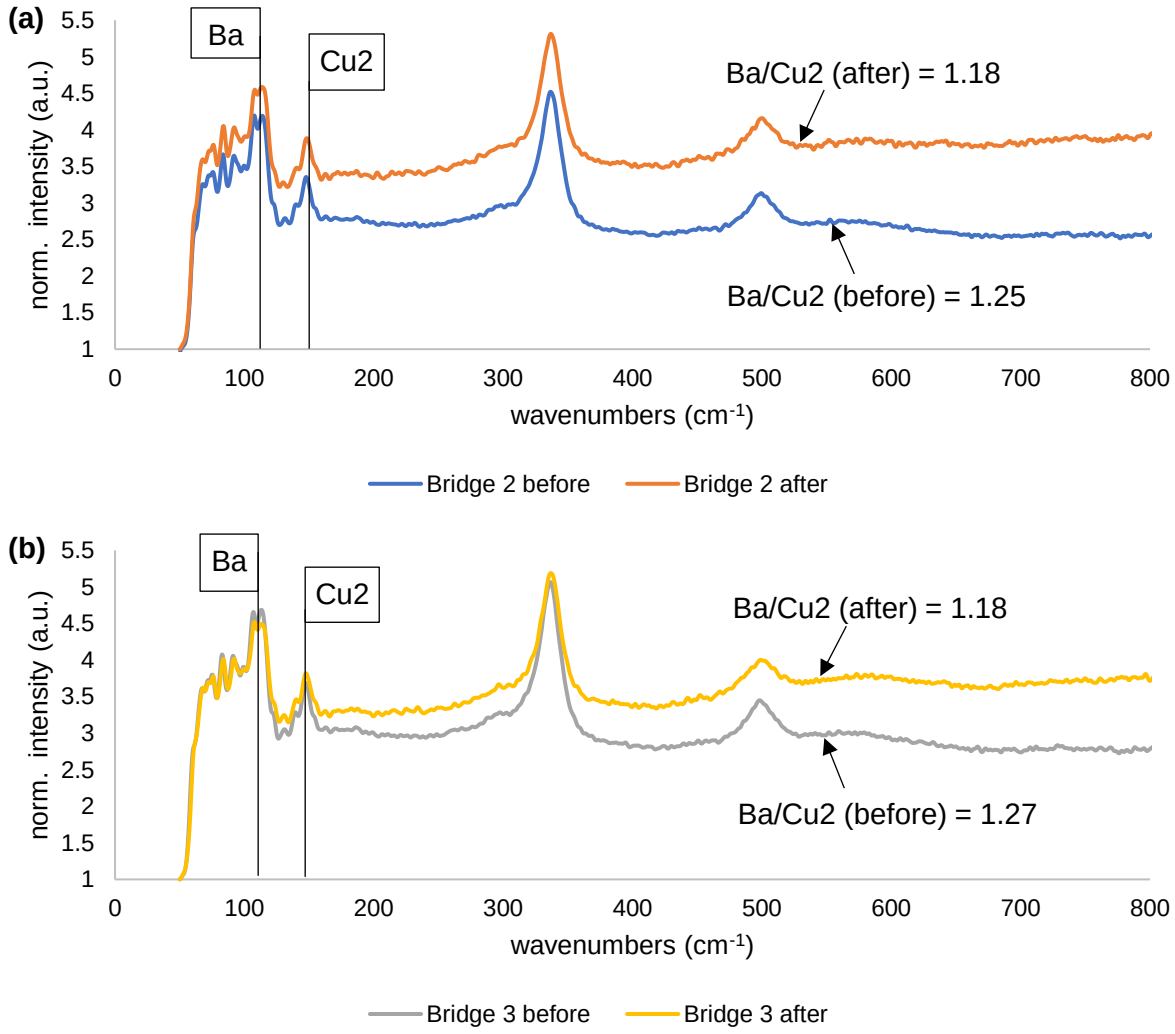

Figure 94: Two bridges were machined from 30 µm to 15 µm (a) and 6.8 µm (b). They were machined at 1 kHz with a processing speed of 1 mm/s. (Pulse energy: 215 nJ)

The Raman intensity for both bridges changed after the laser process. The Ba/Cu2 ratio decreased from 1.25 to 1.18 for Bridge 2 (and a 4 % J_c decrease) and from 1.27 to 1.18 for Bridge 3 (and a 12 % J_c decrease). Similar to the thermal treatment results, as the Ba/Cu2 ratio decreased so did the current density. Yet, during the heat treatments, a Ba/Cu2 ratio of 1.18 already showed an 83 % decrease in J_c, compared

to a J_c decrease of only 4 % and 12 % when using the laser. Laser machining is a far more complex process than the heat treatments. These results let us assume that the Ba/Cu2 ratio can offer information about the state of a bridge after the laser process and that the bridges seem to have suffered from limited thermal effects. Defects (e.g. structural) might also play another role in terms of possible degradation sources.

It has been shown that laser machined YBCO samples display similar changes in the Raman spectrum as observed during the heat cycles which supports the proposal of using Raman spectroscopy as a possible in-line/parallel measurement tool. In further tests, YBCO bridges were stepwise machined and characterised using transport and Raman measurements. Both 'one-sided' and 'both-sided' machined bridges were investigated, figure 95 and 96.

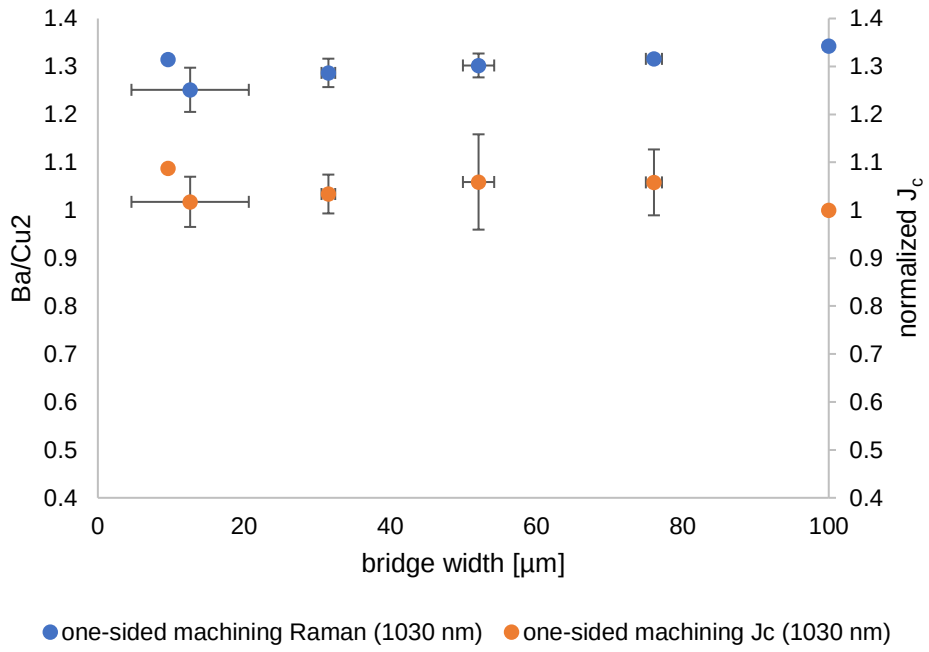

Figure 95: The Ba/Cu2 ratio was related to the normalized J_c for one sided machined bridges over a decreasing width from 100 µm down to ~ 10 µm. The pulse energy was set to 229 nJ at 1 kHz and 1 mm/s.

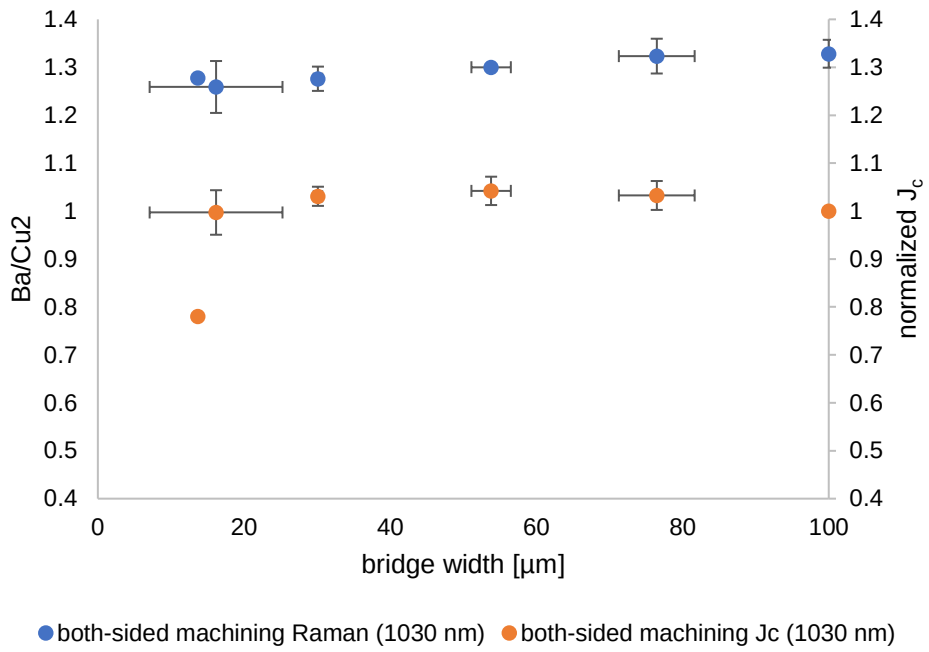

Figure 96: The Ba/Cu2 ratio was related to the normalized J_c of both-sided machined bridges over a decreasing width from 100 µm down to ~ 10 µm. The pulse energy was set to 229 nJ at 1 kHz and 1 mm/s.

The normalisation of the J_c values was necessary to make the results comparable and to create equal axes for J_c and Ba/Cu2. J_c was normalised by dividing the transport measurement results with the initial pre-processing J_c. The graphs also became more comparable between different samples.

There is no significant difference visible between one- and both-sided machined samples, which is likely due to the resolution limits (spot size) of the Raman system and the previous (section 6.6.2) calculated edge damage well below 1 µm. The average difference between normalized J_c value and Ba/Cu2 ratio is about 0.25. This offset was used to predict J_c changes from measured Raman spectra post laser machining. It was possible to get a J_c approximation using the 0.25 offset with an error of 4 %. For a more accurate prediction, more trials and the inclusion of more Raman peaks should be used, however, this new approach is useful for a first prediction which could be used in-situ during laser processing.

This procedure was repeated to determine how the offsets changed for different machining wavelengths. For the second data set, the Talisker laser with a 355 nm wavelength was used to machine another set of bridges, while again measuring the changes that occurred to the Raman spectrum and J_c, figure 97.

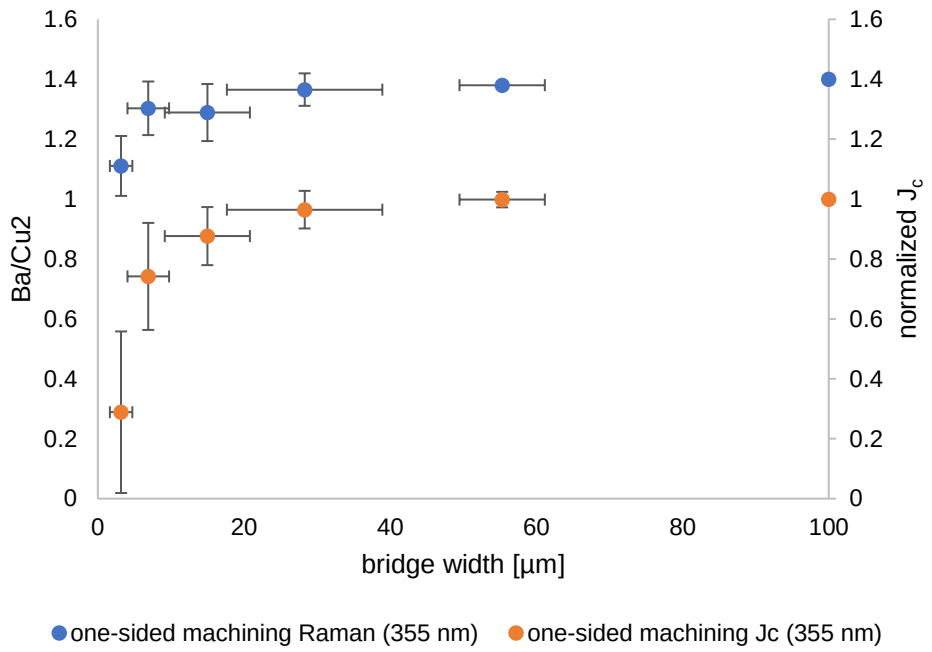

Figure 97: Bridges have been machined with 355 nm to determine the offset needed to predict J_c based on the Ba/Cu2 ratio. The samples were machined over a wider range of widths explaining the larger error bars.

For 355 nm, an offset of 0.44 was calculated which led to a J_c prediction with a error of 12 %. Compared to the previous results, the spread in width was larger leading to increased uncertainty. The spread increased for bridges < 10 µm, as the spectra became more inconclusive due to the limitations in the Raman spot size and due to some cases of complete degradation.

Overall we have developed a procedure which can be used to predict J_c changes by analysing the Ba/Cu2 peak ratio in a Raman spectrum. It can be used for different laser wavelengths by calibrating the correct offset.

7.4 Conclusion

In this chapter, the possibility of using Raman spectroscopy as an in-line/parallel assessment tool for YBCO was investigated. To do so, Raman and transport measurement results were linked through the phase transition of YBCO from superconducting to degraded. In order to degrade YBCO thin films, the samples were exposed to thermal treatments at 300 °C for 10 seconds. After investigating how the Raman spectrum changed throughout the process, focus was put on the change of the intensity ratio between the Ba and Cu2 peaks. A decreasing Ba/Cu2 ratio indicated a decreasing current density. A threshold value of 1.15 was chosen, above which the sample was still superconducting and below which it was not. With this ratio, Raman

spectroscopy appears to be promising as a new in-line/parallel measurement method to assess YBCO bridges for degradation.

In a second step, laser machined YBCO bridges were analysed. The laser process introduces more variables that could act as degradation sources compared to 'simple' thermal treatments. Specifically, the femtosecond laser process is a non-linear process with electron-phonon interactions which have been shown to be able to split the superconducting Cooper pairs [121]. Not much is known about the exact laser-matter interactions. Comparing the results from thermal treatments and initial laser machining, correlations between Ba/Cu2 ratios and the bridges' critical current density were observed. Through repeated measurements of machined bridges, it was possible to find a stable 'offset' between the normalised J_c values and Ba/Cu2 ratio. This offset was then used to predict the J_c values of machined bridges. Depending on the number of data points and the machining wavelength, the post machining J_c was predicted with an error between 4 % and 12 %. These errors are due to the spread in machined bridge widths and the limitations of the Raman microscope, mostly its positional inaccuracy and the size of the Raman spot. To improve the estimate, more samples could be tested with fixed machining step sizes to create a smaller spread in the bridge widths. Additionally, a Raman sample stage with a higher positional accuracy could be used or the stage used for machining itself could be used when implementing the Raman spectroscopy onto the laser platform. This would mean the positional accuracy for the Raman measurements would equal the accuracy of the laser machining.

This offset is beneficial for laser machining YBCO as it is possible to integrate a Raman spectroscope parallel, if not in-line, to the machining path. With it, J_c changes can be easily estimated and unnecessary movements of the sample between machining stage and transport measurement rig can be avoided which is time consuming. This becomes especially important for bridges below 10 µm due to their delicacy and another laser pass could be one too many leading to the sample's degradation.

8 Laser Machining in a cryogenic environment

After assessing the performance of laser patterning YBCO by SEM, transport measurements and using Raman spectroscopy, we also investigated laser machining YBCO in its superconducting state. This study is the first time such machining has been investigated. This new machining method would be very attractive as YBCO tracks could be machined down to a set I_c, rather than a set width, which would eliminate the problem of similar sized YBCO bridges behaving different due to inhomogeneities. This could be especially interesting for fault current limiters.

Fault current limiters (FCLs) play an important role in the protection of any electric circuit or power transmission system. To protect electric circuits from large short circuits (i.e. fault currents) an FCL needs to have a variable impendence, a fast response time and the ability to recover back into a low impendence state after being triggered [123], [124]. Superconducting FCLs fulfil these requirements and do so with no power loss when in normal operation (i.e. when there is no fault current) [125]. Due to their unique material properties, superconducting FCLs detect excessive currents within microseconds, and automatically limit the current passed when $I > I_c$ as the material becomes non-superconducting [124], [126]. As soon as the transient current has passed, these FCL recover and return to their original superconducting state [124]. It is important for these components that I_c is constant over the entire structure (e.g. meander-like patterns) since any variations will lead to false triggers and to a degraded performance over time [126]. For example, if one strand has a smaller I_c, the developed resistive heat could permanently destroy this section, which will influence the current distribution during the next fault current possibly away from that expected during its design and so leading to more damaged sections or damage to the connected electrical circuit. Therefore, a machining procedure where it is possible to precisely determine I_c would become attractive.

Apart from developing a new machining approach for superconducting FCLs, laser machining under superconducting conditions could also offer some insight into light-matter interactions with Cooper pairs as it has been previously predicted that, a measurable transient voltage will be induced due to Cooper pairs breaking and recoupling under the energy input of an ultrafast laser [127].

In order to machine YBCO (while superconducting) to a specific I_c value, a current needs to be constantly passed through the bridge and the voltage monitored. This means similar to the transport measurement setup, a nanovoltmeter would need to be connected and used as a feedback system for the machining. The process would then involve injecting a current with the same magnitude as the pre-determined I_c, and continually machining the bridge with the laser until the nanovoltmeter recorded the threshold voltage had been reached. To demonstrate a proof of concept a container design was required which would enable the simultaneous laser patterning and cooling of the sample. The setup design using this container would need to fulfil the following requirements:

- The container needs to be a good insulator while also being able to withstand extreme temperature changes.
- The air bearings of the CNC stage should only be exposed to minimal temperature changes.
- The laser objective needs to be protected from the cold fumes to avoid icing over.
- The sample temperature needs to be monitored continuously to ensure $T < T_c$ during the machining.
- As it is a first proof-of-concept design the costs should be kept to a minimum.

In the following chapter, the development of a possible design is described and discussed after which the first machining trials were conducted.

8.1 Design development for cryogenic laser machining

For the design of the insulating LN container, different shapes were considered to begin with. The focus was on circular and rectangular shapes. Circular shapes have the advantage that their expansion/contraction with temperature is more uniform whereas tensions are expected for rectangular designs. It would also be beneficial if a closed system could be used to prevent fumes from icing the laser objective.

In a first test, a cup made out of tufnol with an aluminium lid was used. Tufnol is a common material used in cryogenic applications because of its dimensional stability and insulating properties even at cryogenic temperatures [128] while aluminium was used due to its high thermal conductivity. The setup worked by pouring LN into the cup,

which cooled the aluminium lid and subsequently the sample, which was held onto the lid via a specially placed groove, figure 98.

Figure 98: Tufnol test cup for a first test. After the cup is filled with LN, the aluminium lid with a sample is added. The whole in a lid is supposed to redirect the evaporated fumes to the back of the sample to cool it. The copper wire is an aid to lower the cup into a LN dewar avoiding unnecessary spillage.

The lid also contained a temperature sensor which measured the temperature on the back of the sample and determined whether the LN vapour was sufficient to cool the sample down below its critical temperature (T_c = 86 K). The measurements showed that after the cup was filled with LN for the first time, the sample was cooled down to about -20 °C. After refilling the cup, the sample was further cooled to about -50 °C and then finally -68 °C. This procedure could have been repeated until the sample would reach the required temperature of < -187.15 °C but it would have been very time consuming and the lid was already covered in ice at -68 °C, figure 99.

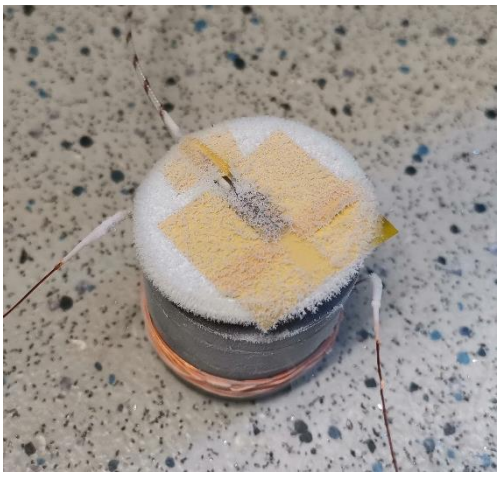

Figure 99: The lid with the YBCO sample was covered in ice after refilling the cup with LN multiple times.

With this approach, laser machining would not have been possible as it will not only disrupt the laser process but also degrade the sample.

In a second approach, the cup together with the lid and the sample were submerged into a LN dewar. The setup was submerged until the temperatures equalized at -196.15 °C. Once the LN stopped boiling, the setup was removed from the dewar. The setup warmed up and surpassed the sample's T_c in 10-12 s. 12 s would not be enough time, to laser machine a bridge. As such this test setup did not provide a suitable solution and other options had to be explored.

Based on these first results, the overall setup for the superconducting laser machining was changed and an open box system was investigated. In another experiment, the thermocouple was attached to the surface of a heatsink using Kapton tape and cryogenic grease. The heatsink was then placed in a conventional food storage box which was then filled with LN, figure 100.

Figure 100: A heatsink was placed in a LN bath in an open box system while the thermocouple measured the surface temperature. The temperature during the cool down and warm up was observed.

In this setup, the surface of the heatsink had a temperature below -187 °C for about 6 minutes which would be enough to machine a YBCO bridge. Another advantage of this setup is that the box could easily be refilled with LN if needed to extend the machining time. This could be realized without a cryogenic pump reducing costs. The fumes also only developed around the edges of the box which would make it possible to use optical components without damaging/icing them. A schematic of an open box design is shown in figure 101.

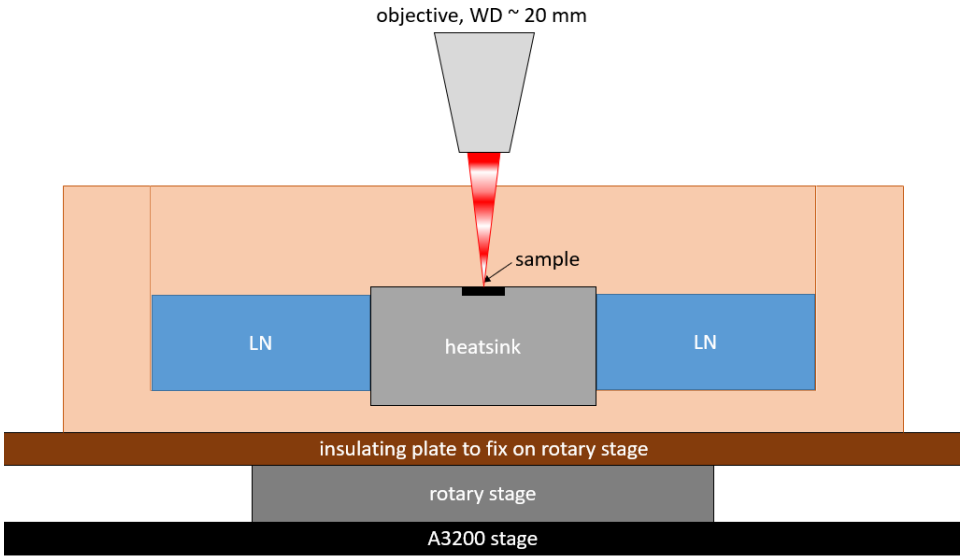

Figure 101: Cross-section through a design concept using an open box layout with a heatsink as sample mount. Underneath the LN container is another insulating plate to protect the rotary stage which is required to align the bridges. An objective with a longer focal range is also chosen.

This setup gives a ~ 6 min machining time with one LN filling. If more is required, the box could be refilled. Due to the size of this setup (250 mm x 150 mm x 50 mm) it is not possible to carry out tip/tilt correction but given the size of the bridges, it should be possible to still machine the samples if they are mounted sufficiently flatly on the heat sink. On the other hand the rotary stage is vital for bridge alignment and is mandatory.

Regarding the material for the box, there are different options [129]:

- PEEK: typical material for cryogenic applications. Strong and stable against heat related shape changes but very expensive. For the needed box dimensions, PEEK would cost about 450 GBP.
- Carp Tufnol: Tufnol is a cryogenic material made of laminated cotton fabric. Due to inhomogeneities in the cotton it tends to have defects that carry throughout the different layers. If it has a defect it might leak, but is half the price of PEEK.
- Natural Polypropylene (PP): PP is not officially labelled as a cryogenic material but seemed fine during the LN tests. It does become brittle so sudden impacts need to be avoided. PP is the typical material for food containers like the one used in the previous test. It is significantly cheaper than PEEK and Tufnol.

- Natural high molecular weight (HMW) 500 Polyethylene (PE): Between PP and HMWPE there is no significant difference for the LN setup. HMWPE is even cheaper than PP.

Considering the different material properties and their prices, HMWPE was chosen for the box setup.

8.2 Temperature measurements and design optimisation

Upon completion of the open box design using HMWPE, the setup was filled with LN and the temperature of the heatsink surface was measured. The heatsink surface reached temperatures below T_c (-186 °C) for several minutes. To avoid LN droplets going into the Aerotech stage, the setup was modified with a plastic cover acting as a shield, figure 102.

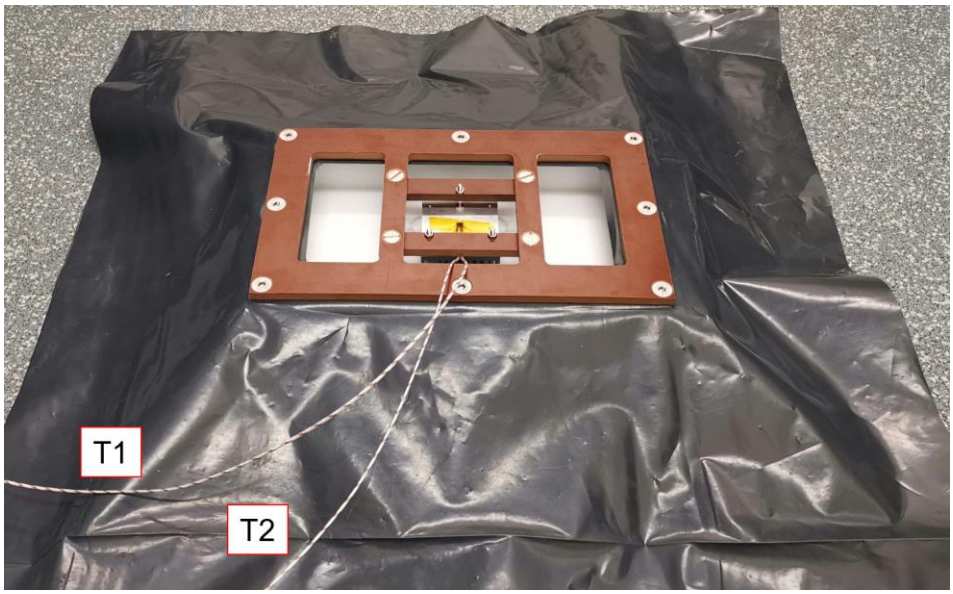

Figure 102: Cryogenic setup. An HMW-PE box is sandwich between two tufnol plates and surrounded by plastic foil. A second thermocouple (T2) has been added to measure the thermal load of a YBCO sample.

The design was further modified by adding tufnol sheets to the setup and connecting them to the heatsink with screws. This can then be used as a tip tilt correction mechanism for the heatsink surface. In addition, the thermal load of a YBCO sample was measured using a second thermocouple. This was used to ensure that the temperature of the YBCO on the substrate surface was also below T_c and to determine if there was an offset between the temperatures below and above the sample. During the laser process, only the temperature below the sample can be measured. Both thermocouples were connected to the sample with kapton tape and cryogenic grease. The temperature values are shown in figure 103.

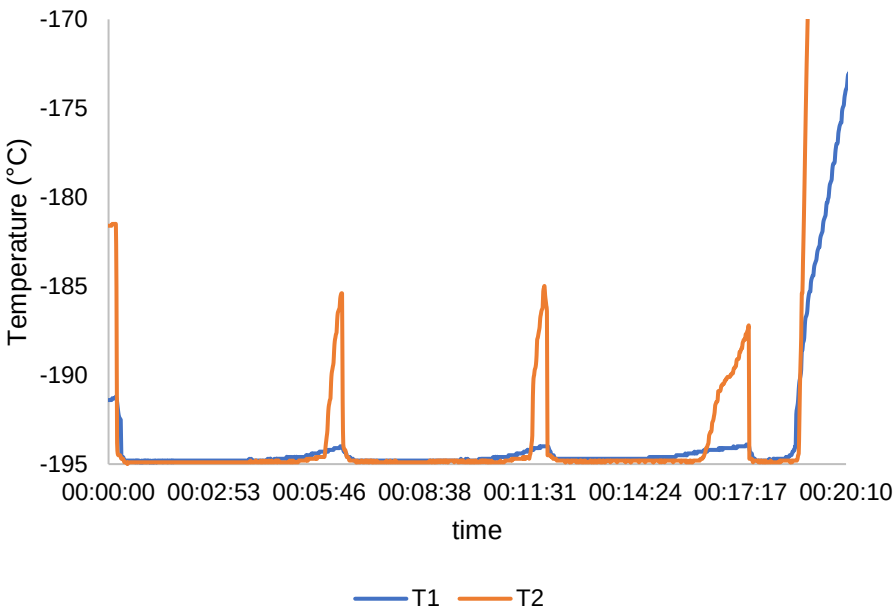

Figure 103: Temperature measurements below (T1) and above (T2) a YBCO sample. The recorded temperature spikes result from the rise in sample temperature before the box was refilled with LN. The spike just before 20 min shows the end of the experiment.

Once T1 reaches a temperature of -194 °C, the YBCO will not be superconducting anymore. Overall, one 10 L LN dewar will last for over 20 min of machining time which should be more than enough to machine a few bridges on a sample. One issue was the icing of the setup, as once the setup warmed up it started to freeze over with ice. To avoid damages the sample had to be quickly removed from the setup after the machining process.

After multiple stress tests with LN, the material gave in and started to crack. The damage is shown in figure 104 (a). Following this design failure, tension simulations were run using the original design via finite element methods (FEM), figure 104 (b).

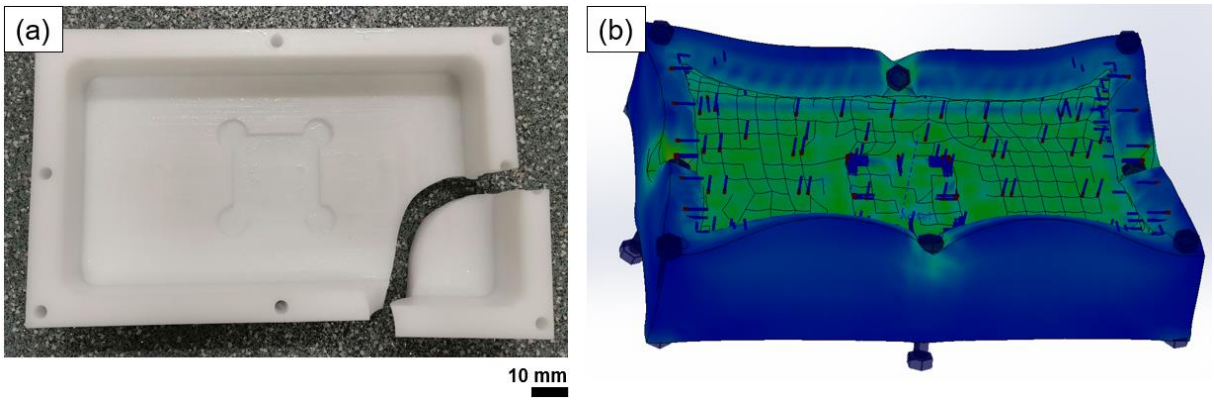

Figure 104: (a) Resulting damage from multiple temperature shocks. (b) Tension simulation based on cooling the internal walls to -194.8 °C (77 K).

To avoid future damages, the box design was optimised based on the tension simulation results from the FEM simulation, figure 105.

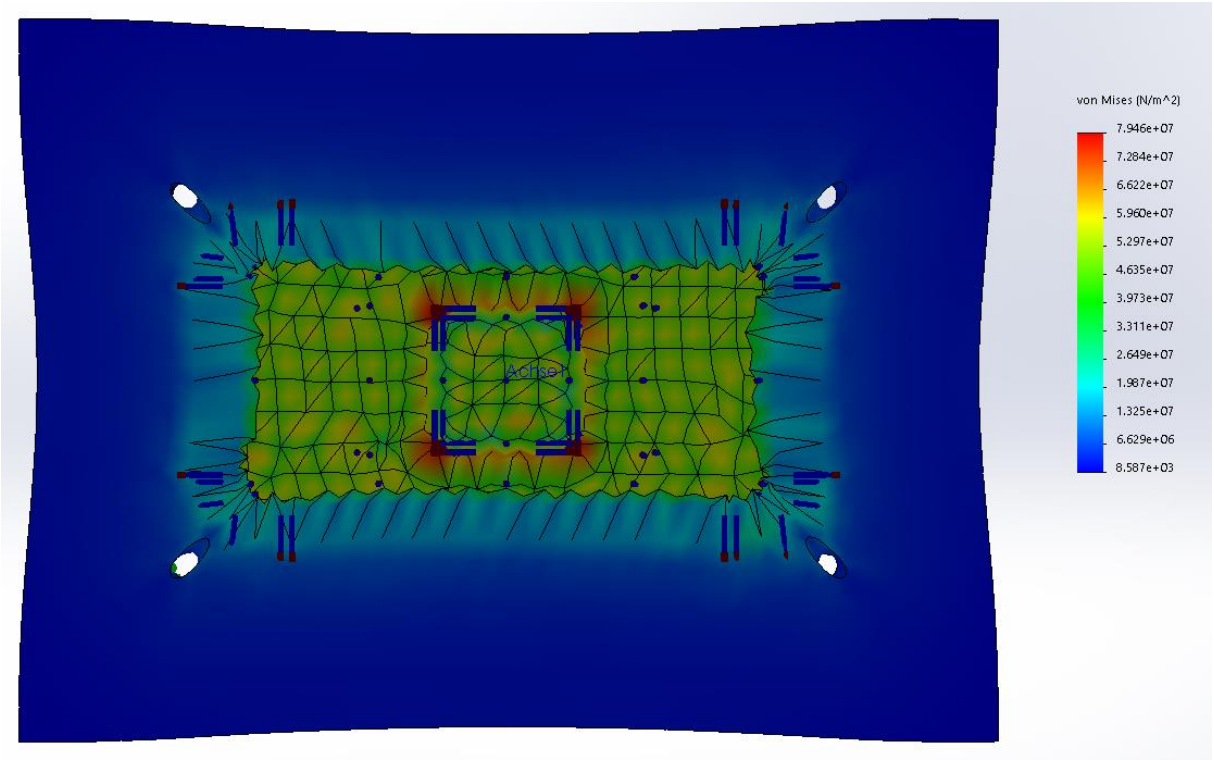

Figure 105: Tension simulation of an optimised box design. The wall thickness has been increased and the number of clearance holes reduced. The diameter of the holes has also been increased to leave the screws more spiel to avoid unnecessary tension points.

In addition to optimising the design, the material was also upgraded to a higher grade of PE. UHMW-PE1000 (ultra high molecular weight PE) provides an operating temperature down to -260 °C with good stress resistance and it is only a tenth of the price of PEEK.

This improved setup passed multiple stress test and was mounted onto the aerotech stage (along with the plastic cover) for first laser machining trials.

8.3 Laser machining of YBCO thin film at different temperatures

The optimised setup ensured that the sample was cooled safely below T_c while protecting the laser equipment. As a next step, a machining strategy needed to be created due to the time sensitive nature of the experiment.

To be able to machine anything on YBCO the focus point of the laser optics needs to be found. Under normal conditions, the laser focus is found by using the in-line camera and a DINO microscope for orientation. When using the cryogenic setup, the DINO

microscope could not be used due to the LN fumes and the cold temperatures, as such it was not initially possible to accurately focus the microscope onto the sample surface. As an alternative, a confocal probe was added as another tool to find the focus more reliably, figure 106.

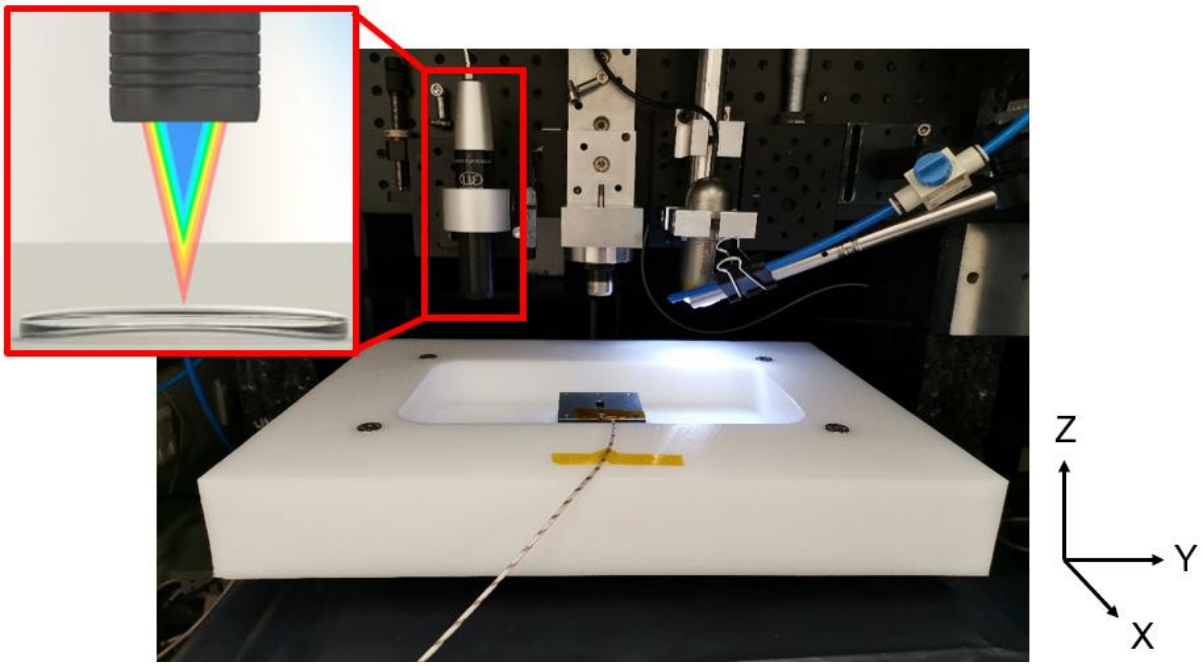

Figure 106: In addition to the DINO microscope (right from the objective) a confocal probe was added to the setup. A closer look on the left shows the measurement principle using polychromatic light [130], [131].

The confocal probe (micro-epsilon, IFS2405-0,3) is used to measure the displacements and thicknesses of multi-layered transparent materials. It does this by dispersing the white light and shining the dispersed set of monochromatic beams onto the sample. Of the many wavelengths only the one focused on the sample surface by the probe's optics returns to be recorded. Using this, samples can be measured with a 10 nm resolution. In this specific application, this measurement technique has also the advantage of being a 'passive' sensor, meaning that electronics and controller can be mounted separately from the probe in a different location [131]. Therefore, measurement uncertainties due to a change in temperature of the electronics and controller are mitigated. In this setup, a micro-epsilon probe (IFS2405-0,3) with a measuring range of 0.3 mm was used. It is less effected by fumes and icing than optical microscopes.

After changing the setup, the offsets between objective, DINO microscope and the confocal probe were found. At room temperature, the Z offset between the focal point

of the objective and confocal probe were chosen so that the sample was in the middle of the measurement range (0 mm – 0.3 mm) of the confocal probe at 0.15 mm. This was to ensure that the expected deformations are within the measurement range as deformations occurred in both directions (towards and away from the confocal probe). After filling the box with LN, the Z stage was moved until the surface under the probe remained relatively still (Z height variations < 50 µm). Afterwards, the sample was moved to the objective and a programme was run which would machine through different Z increments (20 µm) around the laser focus. This way ensured that part of the trenches were machined in focus and thus can be compared to the machining results at room temperature and above T_c. The machining results are shown in figure 107.

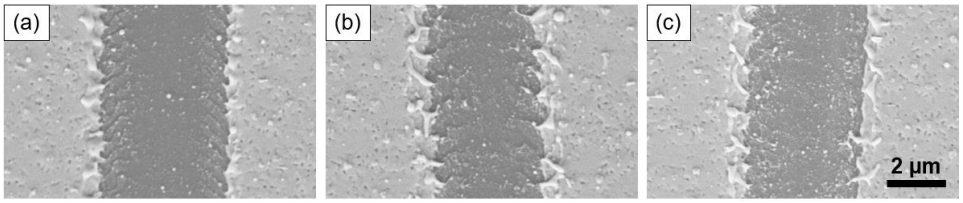

Figure 107: Trenches were machined at (a) room temperature, (b) T > T_c, and (c) T < T_c with a pulse energy of 199 nJ at 1 kHz and 1 mm/s.

Under the SEM there was no noticeable difference between the machining results for films machined below and above T_c. The temperature of the sample does not appear to influence the machining visually and the confocal probe seems to be a suitable tool to find the laser focus. Ideally, it would not be necessary to machine in multiple passes or to have to use an offset around the focus.

To investigate whether this is possible, first the mechanical contractions/distortions due to the thermal shock needed to be investigated. Distortions such as twisting and changes in the heatsink surface were observed. Starting with the deformation in the Z axis of the Aerotech stage, which influences the laser focus and machining quality directly, the confocal probe was used to map the surface profile of a YBCO thin film in the X direction of the stage at different time increments, figure 108.

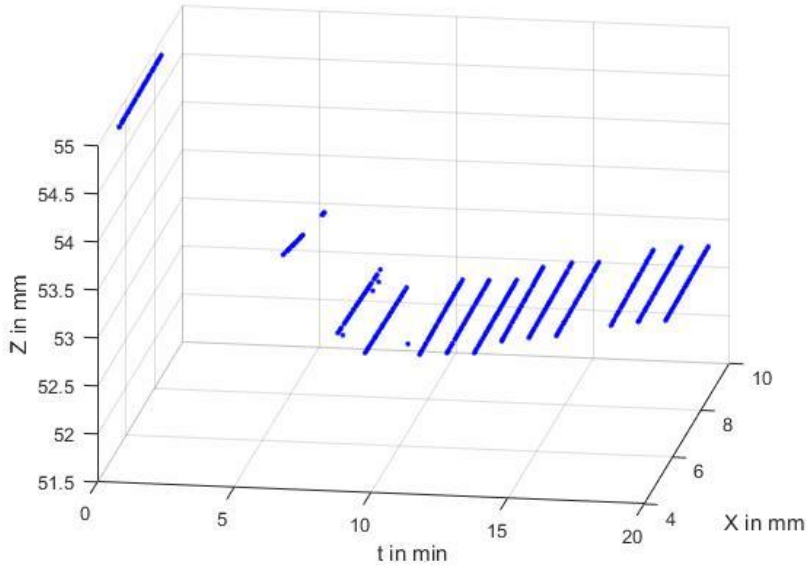

Figure 108: 3D plot of the distortion in Z measured with the confocal probe. At t = 0 min the surface of the sample was scanned at room temperature over 3 mm in X at 0.1 mm/s. LN was added for the following data points.

This plot shows a distortion of the setup's position over 2 mm due to the first thermal shock. After about 10 minutes of cooling time, the setup appears to be stabilizing. In addition to the overall distortion of Z over time, the Z distortion over X has been investigated to see how the profile changes. For comparison, figure 109 shows a two-dimensional plot of the distortion in Z along the sample's surface. In this graph, the Z profile measured at room temperature has been removed assuming, the sample is in focus at X_0. Ideally, ΔZ is only a few microns to ensure that even laser machining was achieved throughout the sample.

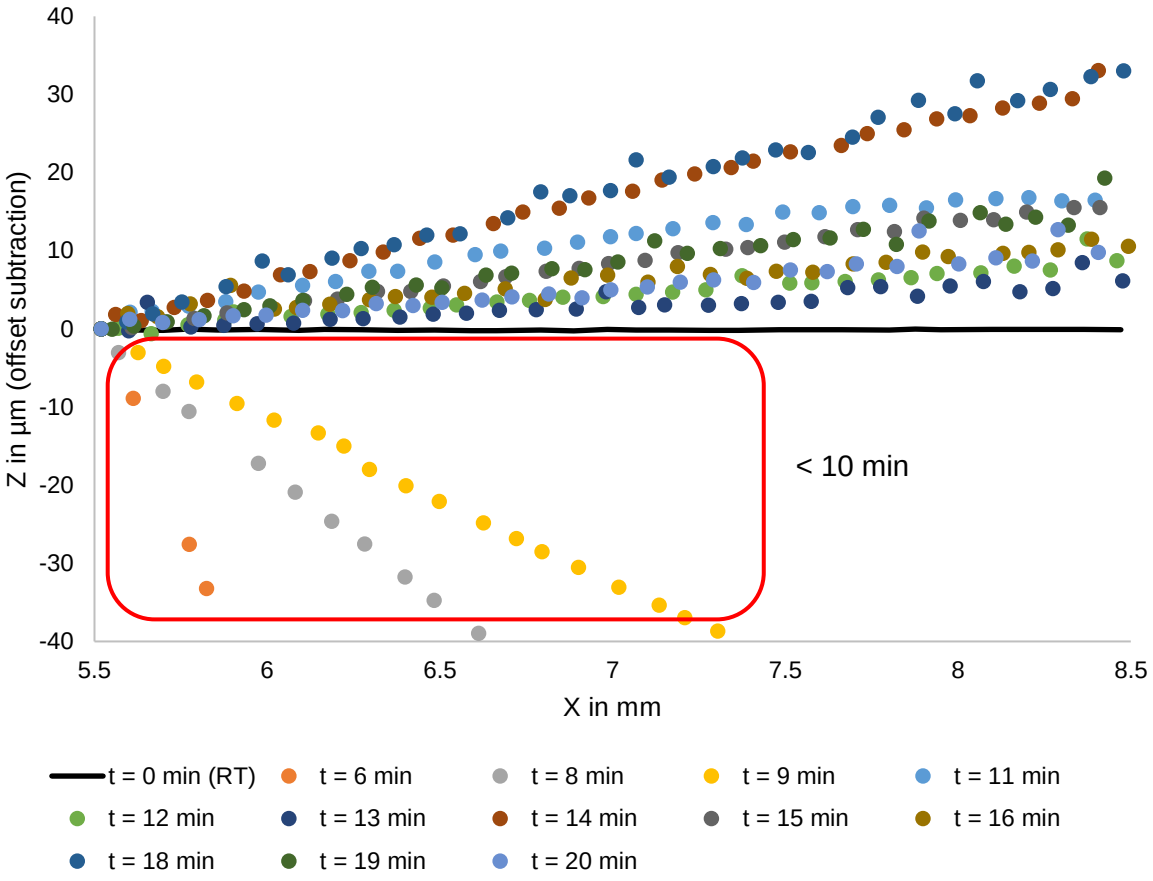

Figure 109: Z deformation in microns after the sample profile at room temperature (RT) has been subtracted and for comparison reasons it has been assumed that each measurement started in focus at Z = 0 µm.

After the stabilization period (10 min), a further increase in Z of up to 30 µm in 30 s can be observed. While the calculated depth of focus (DOF) of the used objective COMAR 20DQ10 is 53 µm for a focal length of 20 mm, this distortion is crucial, as moving from the confocal probe to the objective takes about 20 s before the machining begins. If the increase in Z is repeatable, this could be accounted for within the machining programme; however, further tests showed that any temperature fluctuations distort the offset in Z randomly, figure 110.

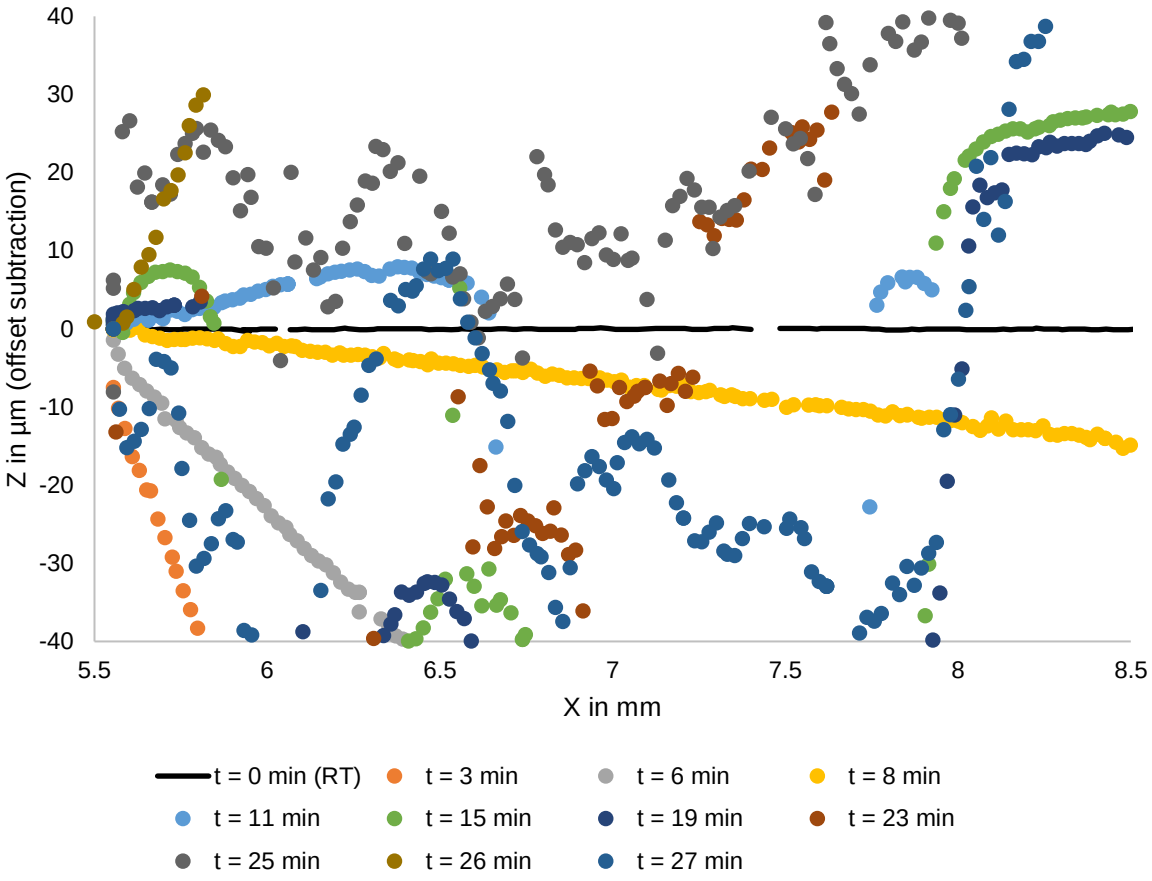

Figure 110: Z deformation in microns affected by temperature fluctuations and increased time steps between the measurements. The sample profile at room temperature (RT) has been subtracted and for comparison reasons it has been assumed that each measurement started in focus at Z = 0 µm.

The temperature fluctuations were less than 1 °C and the time interval between measurements only increased by 1.4 min on average, displaying the sensitivity of this experimental setup.

Based on these results, the machining programme for YBCO bridges needs to be as short as possible to ensure repeatable machining results. It will also be necessary to machine in multiple passes around the focus to ensure, that the YBCO has been fully removed. A suitable machining strategy is investigated in the next section.

8.4 Laser machining of YBCO microbridges in superconducting state

From the results of the previous mapping of the distortion in Z, it is required to machine YBCO bridges with Z offsets around the focus. So far only the distortion around one axis has been investigated. In a next step, to machine bridges, a reliable method for finding the location of each bridge on the sample without visual feedback needs to be developed. This alignment step and machining approach should be as quick as possible due to the changing distortion in Z over time shown before. One way to align the sample, could be to use the corner of the sample as a reference for X and Y. In order to also decrease the overall machining time, instead of machining the whole length of the bridge, the bridges can be machined using only a single perpendicular line cut, figure 111.

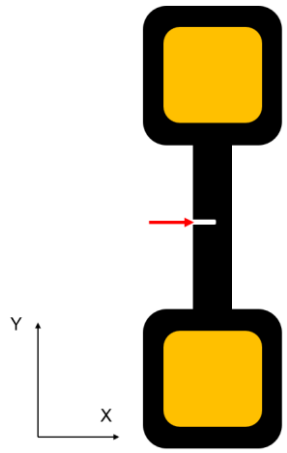

Figure 111: Machining strategy for bridges while superconducting. Instead of machining along the whole length of the bridge, there will be a cut perpendicular to the bridge width.

However, this machining strategy will suffer from inaccuracies in X and Y due to distortions. This strategy was then tested on a thin film sample to assess possible machining offsets and repeatability. To compensate for the deformation in Z, the programme machined trenches in 20 µm increments around the initial focus position. Using the corner of the thin film sample, the theoretical bridge locations were calculated as offsets in X and Y an origin placed at the sample corner. To investigate how accurate and repeatable this approach would be, trenches were machined at pre-determined positions as follows:

- Find the corner of the sample with the confocal probe to within an accuracy of 10 µm and set it as 0.

- Machine a vertical reference line to check the offset in X at room temperature.
- Use a trench machining programme which machines the same trench at different Z offsets from the focus to compensate for the deformation in Z at room temperature at a defined offset in Y.
- Fill the setup with LN, let it cool for 10 min and adjust Z to focus the confocal probe on the sample surface.
- Find the edges of the sample first in Y then in X.
- From the edge, move to a desired location using X and Y offsets and adjust Z again.
- Start the trench machining programme to move over to the machining point and machine the film.

This approach has been repeated until the deformation in X and Y could be predicted with sufficient accuracy (< 50 µm). While Y was sufficiently accurate (< 10 µm) after the first cool down, an offset of 0.45 mm needed to be added to the X position to reach an accuracy of < 50 µm, figure 112.

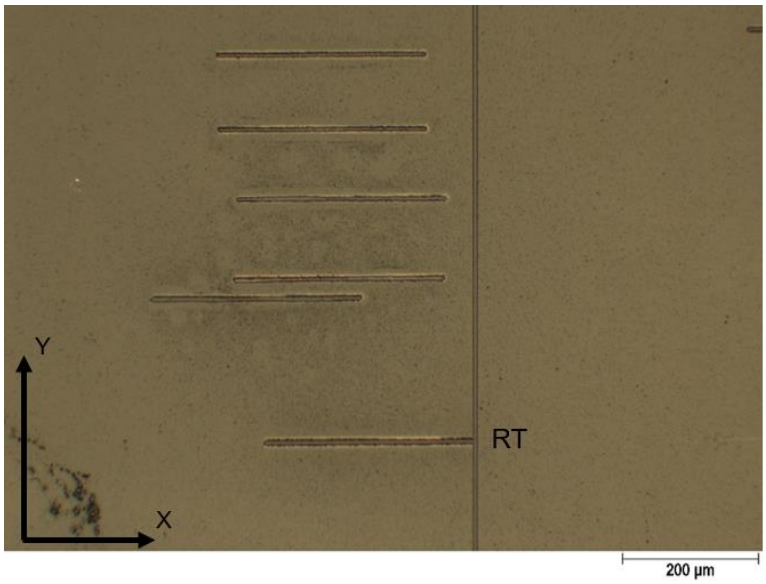

Figure 112: Machining trials on YBCO thin film to navigate on the sample in LN using the confocal probe only. The long vertical line was machined at room temperature as reference point. The first horizontal trench marked with RT was made with the bridge machining programme as a reference. The subsequent trenches were made after the setup has been cooled with LN.

After successfully testing this machining strategy on a thin film, it was possible to machine three bridges whilst they were in their superconducting states. To compare

the transport measurement results, the machining process was replicated on identical bridges at room temperature as well, table 8.

Table 8: Transport measurement results for bridges machined in LN and at room temperature. Bridges that were machined while superconducting are marked in blue.

Bridge number	I_c before machining (A)	J_c (MA/cm²)	Machined width (µm)	Calculated I_c (A)	Measured I_c (A)	$\lvert\Delta I_c\rvert$
B1	0.6744	3.372	42	0.2832	0.3957	0.1125
B2	0.679	3.395	51	0.3463	0.3205	0.0258
B3	0.66	3.3	81	0.5346	0.5773	0.0427
B4	0.6735	3.3675	44	0.2963	0.3556	0.0593
B5	0.6674	3.337	45	0.3003	0.3384	0.0381
B6	0.6659	3.3295	78	0.5194	0.5698	0.0504
B7	0.6597	3.2985	77	0.5080	0.5593	0.0513

An expected I_c was predicted using the J_c measured prior to the machining and by assuming that the J_c remains constant after machining. The measured values after machining were within a sensible range of these predictions (by < 0.05 A). This shows that if one were to inject a current, bridges with a pre-defined I_c, rather than a width, can be machined. The proof-of-concept design shows great promise and with a few minor improvements, could be used as a novel technique for machining electrical superconducting applications.

8.5 Conclusion

A new machining approach to enable I_c-determined YBCO bridge machining has been developed. As nothing similar has been done before, a proof-of-concept needed to be evaluated and tested. In order to allow for such machining, a low-cost test setup, which could be filled with LN to cool samples below T_c was created. After the first tests, the design was further optimised, and the thermal deformations were measured using a confocal probe. The results showed distortions at a rate of over 1 µm/s, however, any temperature fluctuation would increase this deformation rate making this experiment very time and temperature sensitive.

To compensate for these changes, the machining strategy for bridges was adjusted by making a line cut rather than machining the whole length of a bridge. Additionally, the programme is run with 20 µm increments around the focus position to include possible changes in the sample position due to the deformations. Finally, after evaluating the offsets in all three axes, YBCO bridges were machined while they were in their superconducting states.

Replicates of these bridges were also machined at room temperature to compare the I_c values. The measured and calculated I_c were within the same range (< 0.05 A) independent of the machining environment (i.e. superconducting or normal). This is a very promising first result as this concept has shown, first, that it is possible to laser machine YBCO in its superconducting state and, second, that it would be generally possible to inject a pre-determined I_c and machine a bridge until a threshold voltage is reached.

For this step to work, however, it is necessary to optimise the setup and include in-line position sensors with feedback to compensate for any deformations to the Aerotech stage. The current injection and voltage measurements could then be realised similar to a transport measurement rig by mounting pogo pins on the sample, which also gives enough space for the laser to machine the bridge in-between. Unfortunately, this was not possible within the scope and time frame of this work but offers a promising project for the future. Potential applications for such machining technique include circuit breakers with a specified I_c and finely tuned THz emitters.

9 Research outcomes and future work

Superconductivity will continue to fascinate researchers all over the world as it has the potential to revolutionize the use electricity as we know of it today. The year 2020 saw the publication of another milestone in superconductivity [132]. A new compound was able to conduct electricity at 15 °C under the immense pressure of 267 gigapascal. Even now, much is still not fully understood despite years of research, however, the number of potential applications is increasing due to developments in quantum computing and more. Superconductivity remains to be a highly researched phenomenon.

In this work, new aspects of laser machining YBCO have been investigated which add to the knowledge currently available in literature and pave the way to new machining possibilities for superconducting applications. The main achievements are summarized below:

- Development of a method to calculate the edge damage caused by laser processing.
- Investigation of the possibility of having an in-line/parallel assessment tool integrated on the laser machining platform to assess the quality and changes in the superconducting properties of the samples.
- Design of a first of its kind test setup for laser machining under superconducting conditions and showing a successful proof of concept.

For a more detailed summary of the achievements of this study: YBCO bridges have been machined with different lasers and under different conditions. Throughout the machining experiments with femto- and picosecond lasers, it was not possible to completely avoid melt artefacts, even after optimising the processing parameters by machining trenches on thin films under various conditions. However, these laser machined bridges had a superior aspect ratio compared to most bridges found in literature. Bridges reported in literature often showed a machined length in the micrometre regime while the bridges processed here were 1.4 mm long with the possibility to machine even greater lengths. As for the machining limit, below a bridge width of 10 µm, a decline in J_c was observed. This decline was observed at different laser wavelengths and pulse durations. To explain this phenomenon, the edge damage was further investigated.

Bridges were stepwise machined to different widths while monitoring the change in I_c. With these measurement results, the width of the damaged edge was calculated by using linear trendlines and referring them to J_c and I_c. The width of the damaged edge also provides a theoretical machining limit for the respective laser. For the Satsuma laser, an edge damage of around 550 nm was calculated. This evaluation of the edge damage is a new approach and, for the first time, provides a numerical machining limit based on experimental data. Such an approach has not been reported before as previous workers have used an optical evaluation of the edge damage using SEM or AFM measurements. With this approach, it is possible to evaluate how suitable a machining technique is for a given application and its geometrical requirements. In this study, this approach was developed with the results from laser machined samples, however, it could be used for other machining techniques as well.

Due to the possibility of a superior aspect ratio and the general laser setup, the Satsuma laser was further used to manufacture superconducting centimetre scale emitter devices. The results are comparable with those created via lithography while offering additional fine-tuning capabilities due to the design flexibility given by laser systems.

In addition to the machining trials, the possibility of using Raman spectroscopy as a possible in-line/parallel measurement tool was investigated. Due to the delicacy of YBCO, it is crucial to closely observe its electrical properties while machining in the micrometre regime. An integrated measurement device would greatly improve the overall machining efficiency and decrease the failure rate. While Raman spectroscopy has been used by research groups before, in this work it was for the first time linked to transport measurements. Since Raman spectra are often complex, the aim was to find a correlation between Raman and transport measurements with which it would be possible to predict changes in J_c. To do so, samples were heated with a conventional hot plate to measure the phase transition from superconducting to insulating material. Several changes in the Raman spectrum were observed, however, the ratio between Ba and Cu2 stood out. It was known from the literature that the Cu2 peak grows larger in intensity than the Ba peak when YBCO gets degraded. In this work, we first investigated at which Ba/Cu2 ratio the phase transition occurs and a threshold value of 1.15 was found when connecting Raman and transport measurement results. Moving from thin films to laser machined bridges, a study looked at the changing

Ba/Cu2 ratios after each machining step and related them to the normalized J_c. The normalization took place with respect to the measured critical current density prior to any machining. With this approach, it was possible to predict J_c changes with an uncertainty between 4 % and 12 %. By using Raman spectroscopy to estimate the change J_c, the way for an integrated measurement system for machining YBCO was created. Additionally, here a ratio between two Raman peaks was used rather than a single peak, eliminating measurement variations between different Raman setups.

To conduct further investigations on the processing behaviour of YBCO, a cryogenic setup was designed to machine YBCO in its superconducting state. This is a completely new approach which has not been attempted before. This procedure would enable the tailoring of bridges to a specified I_c. Live processing of superconducting FCL would become one of the many possibilities. An experimental setup was created as a proof of concept. The setup consisted of an open box-like structure which could be refilled with LN throughout the experiments. The sample was placed on top of a heatsink in the middle and monitored via a nearby temperature sensor. The focus position was determined by using a confocal probe instead of an optical microscope due to the effect of ice build-up blocking the lens of the microscope. While it was possible to machine bridges at 77 K, further improvement would be required to machine more complex structures over longer time periods due to thermal deformations in the cooling period. Overall, the proof of concept can be considered successful and this novel technique opens new machining possibilities to a large area of applications.

With regards to future work, improving the cryogenic setup would be one option. The setup used here was simple but could be extended to enable current injection to machine YBCO bridges to tailored I_c. The current injection could be realised by adding a pogo pin holder connected to a current source and a voltmeter. The design could be similar to the sample holder used for the transport measurements. More difficult would be to track the setup's deformation over time and feed this information back to the machining programme in order to compensate for any changes, thus ensuring repeatable results. To track the deformation multiple sensors would be needed which would trace the deformations in at least three axes (X, Y, Z). Tracking rotations could follow in a second step. In addition to improving the cryogenic setup, it would also be interesting to do Raman spectroscopy while the samples are in their superconducting

state and carrying current. The spectrums and interactions with the phonons might show different results when Cooper pairs are present and carrying current, such as those reported in previous studies which predicted the occurrence of metastable states in single crystal YBCO samples [133], [134].

More research could also be done for the changes in the Raman spectrum for different oxygen levels. In this work, additional Raman peaks were registered during the heat treatments. Their meaning is currently unknown.

10 References

[1] S. Aghabagheri *et al.*, “High temperature superconducting YBCO microwave filters,” *Phys. C Supercond. Its Appl.*, vol. 549, pp. 22–26, Jun. 2018, doi: 10/gdn4xk.

[2] N. Curtz *et al.*, “Patterning of ultrathin YBCO nanowires using a new focused-ion-beam process,” *Supercond. Sci. Technol.*, vol. 23, no. 4, p. 045015, 2010, doi: 10/fp48bd.

[3] J. H. Durrell, “Critical Current Anisotropy in High Temperature Superconductors,” Thesis, University of Cambridge, 2001.

[4] T. M. Silver, S. X. Dou, and J. X. Jin, “Applications of high temperature superconductors,” *Europhys. News*, vol. 32, no. 3, pp. 82–86, 2001, doi: 10/bz2pjb.

[5] S. Administrator, “Superconducting Maglev,” *The Engineer*. https://www.theengineer.co.uk/issues/may-2004-online/superconducting-maglev/ (accessed Mar. 23, 2017).

[6] E. Wiener-Avnear *et al.*, “Laser patterning of YBaCuO weak link bridges,” *IEEE Trans. Magn.*, vol. 25, no. 2, pp. 935–938, Mar. 1989, doi: 10/dt98rf.

[7] K. E. Hix, M. C. Rendina, J. L. Blackshire, and G. A. Levin, “Laser Micromachining of Coated YBa2Cu3O6+x Superconducting Thin Films,” *ArXivcond-Mat0406311*, Jun. 2004, Accessed: Oct. 18, 2016. [Online]. Available: http://arxiv.org/abs/cond-mat/0406311.

[8] S. Nawaz, “Microwave Response of Superconducting YBCO Nanowire Bridges Sustaining the Critical Depairing Current: Evidence of Josephson-like Behavior,” *Phys. Rev. Lett.*, vol. 110, no. 16, 2013, doi: 10/f23skk.

[9] J. G. Thompson *et al.*, “Atmospheric degradation of the high-temperature superconductor, YBa2Cu3O7−x,” *Mater. Res. Bull.*, vol. 22, no. 12, pp. 1715–1724, Dec. 1987, doi: 10/b3xsp6.

[10] S. Yazaki, A. Karasawa, T. Kotoyori, A. Ishiyama, and N. Miyahara, “Critical Current Degradation in High-Temperature Superconducting Tapes Caused by Temperature Rise,” *IEEE Trans. Appl. Supercond.*, vol. 23, no. 3, pp. 4602304–4602304, Jun. 2013, doi: 10/gbc8fw.

[11] Y. Quere, “Irradiation damage in superconductors,” Ecole Polytechnique, CEA-CONF--9881, 1989. Accessed: Jan. 12, 2017. [Online]. Available: http://inis.iaea.org/Search/search.aspx?orig_q=RN:21039530.

[12] J. Bulmer *et al.*, “Tunable Broadband Radiation Generated Via Ultrafast Laser Illumination of an Inductively Charged Superconducting Ring,” *Sci. Rep.*, vol. 5, no. 1, Art. no. 1, Dec. 2015, doi: 10/gf4k98.

[13] M. A. Nielsen and I. L. Chuang, “Quantum computation and quantum information,” *Phys Today*, vol. 54, pp. 60–2, 2001.

[14] P. Umenne, S. Lam, J. Du, and V. V. Srinivasu, “Josephson Effect in the Micron and Submicron YBCO Constrictions Fabricated Using the Femtosecond Laser Technique,” *J. Supercond. Nov. Magn.*, vol. 31, no. 5, pp. 1341–1350, May 2018, doi: 10/gdc37j.

[15] C. Thomsen and G. Kaczmarczyk, “Vibrational Raman Spectroscopy of High-temperature Superconductors,” in *Handbook of Vibrational Spectroscopy*, John Wiley & Sons, Ltd, 2006.

[16] G. J. Clark, F. K. Legoues, A. D. Marwick, R. B. Laibowitz, and R. H. Koch, “Radiation Damage in Thin Films of High Tc Superconductors,” *MRS Online Proc. Libr. Arch.*, vol. 99, Jan. 1987, doi: 10/bt7njq.

[17] L. D. Fitch and V. L. Burdick, “Water Corrosion of YBa2Cu3O7−δ Superconductors,” *J. Am. Ceram. Soc.*, vol. 72, no. 10, pp. 2020–2023, Oct. 1989, doi: 10.1111/j.1151-2916.1989.tb06025.x.
[18] K. Osamura and I. Hirabayashi, *Advances in Superconductivity X: Proceedings of the 10th International Symposium on Superconductivity (ISS ’97), October 27–30, 1997, Gifu Volume 1–3*. Springer Science & Business Media, 2013.
[19] J. Dumas, H. W. Neumüller, H. F. Braun, V. P. Seminozhenko, and Y. D. Tretyakov, *High Tc Superconductors*. Elsevier, 1993.
[20] S. A. Cybart *et al.*, “Nano Josephson superconducting tunnel junctions in YBa2Cu3O7–δ directly patterned with a focused helium ion beam,” *Nat. Nanotechnol.*, vol. 10, no. 7, pp. 598–602, Jul. 2015, doi: 10/gf4k87.
[21] P. H. Ballentine, A. M. Kadin, M. A. Fisher, D. S. Mallory, and W. R. Donaldson, “Microlithography of high-temperature superconducting films: laser ablation vs. wet etching,” *IEEE Trans. Magn.*, vol. 25, no. 2, pp. 950–953, Mar. 1989, doi: 10/cbw6rz.
[22] U. of Sheffield, “Overview - EBL Patterning - Electron Beam Lithography - The University of Sheffield.” https://www.sheffield.ac.uk/ebl/patterning (accessed May 15, 2017).
[23] R. Arpaia, S. Nawaz, F. Lombardi, and T. Bauch, “Improved Nanopatterning for YBCO Nanowires Approaching the Depairing Current,” *IEEE Trans. Appl. Supercond.*, vol. 23, no. 3, pp. 1101505–1101505, Jun. 2013, doi: 10/f24hq9.
[24] S.-G. Lee, S.-H. Oh, C. S. Kang, and S.-J. Kim, “Superconducting nanobridge made from YBa2Cu3O7 film by using focused ion beam,” *Phys. C Supercond.*, vol. 460–462, Part 2, pp. 1468–1469, Sep. 2007, doi: 10/c4v46g.
[25] C. H. Wu, F. J. Jhan, J. H. Chen, and J. T. Jeng, “High- T c Josephson junctions fabricated by focused ion beam direct milling,” *Supercond. Sci. Technol.*, vol. 26, no. 2, p. 025010, 2013, doi: 10/gf4k9g.
[26] D. W. Bäuerle, *Laser Processing and Chemistry*, 4th ed. Berlin Heidelberg: Springer-Verlag, 2011.
[27] C. Gerhard, “Grundbegriffe der Optik,” in *Tutorium Optik: Ein verständlicher Überblick für Physiker, Ingenieure und Techniker*, C. Gerhard, Ed. Berlin, Heidelberg: Springer, 2016, pp. 27–62.
[28] Krste Pangovski, “Temporal pulse design and analysis of silicon ablation using advanced pulse shaping and digital holography in the nanosecond domain,” University of Cambridge, 2014.
[29] K. C. Phillips, H. H. Gandhi, E. Mazur, and S. K. Sundaram, “Ultrafast laser processing of materials: a review,” *Adv. Opt. Photonics*, vol. 7, no. 4, pp. 684–712, Dec. 2015, doi: 10/gf4k8v.
[30] C. Park, R. Xue, J. J. Lannutti, and D. F. Farson, “Ablation characteristics of electrospun core-shell nanofiber by femtosecond laser,” *Mater. Sci. Eng. C*, vol. 65, pp. 232–239, Aug. 2016, doi: 10.1016/j.msec.2016.04.046.
[31] K. M. Ahmmed, C. Grambow, and A.-M. Kietzig, “Fabrication of micro/nano structures on metals by femtosecond laser micromachining,” *Micromachines*, vol. 5, no. 4, pp. 1219–1253, 2014, doi: 10/gcfp34.
[32] J. Reif, “Basic Physics of Femtosecond Laser Ablation.” http://www.springer.com/cda/content/document/cda_downloaddocument/9783642033063-c1.pdf?SGWID=0-0-45-856056-p173916408.
[33] A. H. Hamad, “Effects of Different Laser Pulse Regimes (Nanosecond, Picosecond and Femtosecond) on the Ablation of Materials for Production of

Nanoparticles in Liquid Solution," *High Energy Short Pulse Lasers*, Sep. 2016, doi: 10/gg7r7r.
[34] J. Cheng *et al.*, "A review of ultrafast laser materials micromachining," *Opt. Laser Technol.*, vol. 46, pp. 88–102, Mar. 2013, doi: 10/gf4k8w.
[35] B. N. Chichkov, C. Momma, S. Nolte, F. von Alvensleben, and A. Tünnermann, "Femtosecond, picosecond and nanosecond laser ablation of solids," *Appl. Phys. A*, vol. 63, no. 2, pp. 109–115, Aug. 1996, doi: 10.1007/BF01567637.
[36] "Femtosecond laser micromachining: A back-to-basics primer." http://www.industrial-lasers.com/articles/2012/06/femtosecond-laser-micromachining-a-back-to-basics-primer.html (accessed May 30, 2017).
[37] S. K. Sundaram and E. Mazur, "Inducing and probing non-thermal transitions in semiconductors using femtosecond laser pulses," *Nat. Mater.*, vol. 1, no. 4, pp. 217–224, Dec. 2002, doi: 10/bwbgvw.
[38] M. V. Shugaev *et al.*, "Fundamentals of ultrafast laser–material interaction," *MRS Bull.*, vol. 41, no. 12, pp. 960–968, Dec. 2016, doi: 10.1557/mrs.2016.274.
[39] S. S. Harilal, J. R. Freeman, P. K. Diwakar, and A. Hassanein, "Femtosecond Laser Ablation: Fundamentals and Applications," in *Laser-Induced Breakdown Spectroscopy*, S. Musazzi and U. Perini, Eds. Springer Berlin Heidelberg, 2014, pp. 143–166.
[40] "Femtosecond laser ablation properties of borosilicate glass," *J. Appl. Phys.*, vol. 96, no. 9, pp. 5316–5323, Oct. 2004, doi: 10.1063/1.1787145.
[41] G. T. Meaden, *Electrical Resistance of Metals*. Springer, 2013.
[42] M. Tinkham, *Introduction to Superconductivity*. Courier Corporation, 1996.
[43] "Resistivity and Laws of Resistance | Electrical4u." https://www.electrical4u.com/electrical-resistance-and-laws-of-resistance/ (accessed Apr. 29, 2017).
[44] G.-J. Lee, "Superconductivity Application in Power System," 2011, doi: 10/gf4k8r.
[45] "Superconductivity," *OpenLearn*. http://www.open.edu/openlearn/science-maths-technology/engineering-and-technology/engineering/superconductivity/content-section-0 (accessed May 02, 2017).
[46] "The critical current of superconductors: an historical review," *Low Temp. Phys.*, vol. 27, no. 9, pp. 713–722, Sep. 2001, doi: 10/bh8pv6.
[47] M. Ohmukai, T. Fujita, and T. Ohno, "The temperature dependence of critical current in YBa2Cu3O7-d thin films deposited on MgO by an eclipse PLD," *Braz. J. Phys.*, vol. 31, no. 3, pp. 511–513, Sep. 2001, doi: 10/dqdxbw.
[48] "Superconductor History." http://superconductors.org/history.htm (accessed May 10, 2017).
[49] Marcello Spera, "Pinning Mechanisms in YBCO tapes," May 01, 2015. https://cds.cern.ch/record/2104459/files/CERN-ACC-2015-0141.pdf.
[50] "Critical magnetic fields for superconductors." http://hyperphysics.phy-astr.gsu.edu/hbase/Solids/scbc.html (accessed May 09, 2017).
[51] A. V. Narlikar, *High Temperature Superconductivity 2*. Springer Science & Business Media, 2013.
[52] K. D. Timmerhaus, R. W. Fast, and R. Reed, *Advances in Cryogenic Engineering*. Springer Science & Business Media, 2013.
[53] P. Kittel, *Advances in Cryogenic Engineering: Parts A & B*. Springer Science & Business Media, 1996.
[54] M. R. Beasley, "High-temperature superconductive thin films," *Proc. IEEE*, vol. 77, no. 8, pp. 1155–1163, Aug. 1989, doi: 10/cq7jcg.

[55] R. Hott, “Materials Aspects of High-Temperature Superconductors for Applications,” *ArXivcond-Mat0306442*, Jun. 2003, Accessed: May 15, 2017. [Online]. Available: http://arxiv.org/abs/cond-mat/0306442.
[56] Víctor Rouco Gómez, “Controlling Vortex Pinning and Dynamics of Nanostructured YBCO Thin Films Grown by Chemical Solution Deposition,” 2014. https://www.tdx.cat/bitstream/handle/10803/133329/vrg1de1.pdf?sequence=1.
[57] “superconductivity - Higher-temperature superconductivity | physics,” *Encyclopedia Britannica*. https://www.britannica.com/science/superconductivity/Higher-temperature-superconductivity (accessed May 09, 2017).
[58] Roger Wordenweber, “Chapter 2 High-Tc Films: From Natural Defects to Nanostructure Engineering of Vortex Matter.” http://www.springer.com/cda/content/document/cda_downloaddocument/9783642151361-c1.pdf?SGWID=0-0-45-1016255-p174029773.
[59] B. Aktaş and H. Z. Durusoy, “Penetration Depth Measurements in Epitaxiel YBCO Thin Films by the ESR Technique,” in *Physics and Materials Science of High Temperature Superconductors, IV*, Springer, Dordrecht, 1997, pp. 249–256.
[60] “Superconducting Cuprates.” http://hoffman.physics.harvard.edu/materials/CuprateIntro.php (accessed May 11, 2017).
[61] Y. Chen *et al.*, “High Critical Current Density of YBa2Cu3O7−x Superconducting Films Prepared through a DUV-assisted Solution Deposition Process,” *Sci. Rep.*, vol. 6, p. 38257, Dec. 2016, doi: 10/f9g58j.
[62] “Chapter 1 Superconductivity.” https://www.repository.cam.ac.uk/bitstream/handle/1810/34597/Chapter%201.pdf?sequence=5.
[63] D. Larbalestier, A. Gurevich, D. M. Feldmann, and A. Polyanskii, “High-Tc superconducting materials for electric power applications,” *Nature*, vol. 414, no. 6861, pp. 368–377, Nov. 2001, doi: 10/dhnnmf.
[64] kc429@cam.ac.uk, “Functionalization of high critical temperature cuprate superconductors for nanoelectronic devices — Thin Film Magnetism Group (TFM).” http://www.tfm.phy.cam.ac.uk/directory/research-themes/magnetic-mesostructures/functionalization-of-high-critical-temperature-cuprate-superconductors-for-nanoelectronic-devices (accessed May 11, 2017).
[65] W. A. Jones *et al.*, “Impact of edge-barrier pinning in superconducting thin films,” *Appl. Phys. Lett.*, vol. 97, no. 26, p. 262503, Dec. 2010, doi: 10/b5c6br.
[66] R. Aguiar, F. Sánchez, and M. Varela, “Single crystal laser patterning for selective YBa2Cu3O7−x growth,” *Appl. Surf. Sci.*, vol. 96–98, pp. 405–409, Apr. 1996, doi: 10/btx5vw.
[67] Y. Q. Shen, T. Freltoft, and P. Vase, “Laser writing and rewriting on YBa2Cu3O7 films,” *Appl. Phys. Lett.*, vol. 59, no. 11, pp. 1365–1367, Sep. 1991, doi: 10/czvc2f.
[68] R. C. Dye, R. E. Muenchausen, N. S. Nogar, A. Mukherjee, and S. R. J. Brueck, “Laser writing of superconducting patterns on YBa2Cu3Ox films,” *Appl. Phys. Lett.*, vol. 57, no. 11, pp. 1149–1151, Sep. 1990, doi: 10/bwgn7v.
[69] R. R. Krchnavek *et al.*, “Transport in reversibly laser-modified YBa2Cu3O7−x superconducting thin films,” *J. Appl. Phys.*, vol. 65, no. 4, pp. 1802–1805, Feb. 1989, doi: 10.1063/1.342911.

[70] Y. B. Li *et al.*, “Raman studies of laser-written patterns in YBa2Cu3Ox films,” *J. Appl. Phys.*, vol. 80, no. 5, pp. 2929–2934, Sep. 1996, doi: 10/bnk6z3.
[71] S. Proyer, E. Stangl, P. Schwab, D. Bäuerle, P. Simon, and C. Jordan, “Patterning of YBCO films by excimer-laser ablation,” *Appl. Phys. A*, vol. 58, no. 5, pp. 471–474, May 1994, doi: 10/fgjxk9.
[72] P. Umenne and V. V. Srinivasu, “Femtosecond-laser fabrication of micron and sub-micron sized S-shaped constrictions on high Tc superconducting YBa2Cu3O7−x thin films: ablation and lithography issues,” *J. Mater. Sci. Mater. Electron.*, pp. 1–10, Dec. 2016, doi: 10/gf4k8x.
[73] “Josephson Junctions - an overview | ScienceDirect Topics.” https://www.sciencedirect.com/topics/physics-and-astronomy/josephson-junctions (accessed Mar. 21, 2020).
[74] C. W. Luo *et al.*, “Ordered YBCO sub-micron array structures induced by pulsed femtosecond laser irradiation,” *Opt. Express*, vol. 16, no. 25, pp. 20610–20616, Dec. 2008, doi: 10/cwq292.
[75] M. Rothschild, J. H. C. Sedlacek, J. G. Black, and D. J. Ehrlich, “Reversible laser chemically induced phase transformations in thin-film Ba2YCu3Ox superconductors,” *Appl. Phys. Lett.*, vol. 52, no. 5, pp. 404–406, Feb. 1988, doi: 10.1063/1.99452.
[76] S. Degoy *et al.*, “Oxygen content of YBaCuO thin films,” *Phys. C Supercond.*, vol. 256, no. 3, pp. 291–297, Jan. 1996, doi: 10/d8zp9f.
[77] Y. B. Li *et al.*, “Raman studies of laser-written patterns in YBa2Cu3Ox films,” *J. Appl. Phys.*, vol. 80, no. 5, pp. 2929–2934, Sep. 1996, doi: 10/bnk6z3.
[78] M. s. Dresselhaus, A. Jorio, and R. Saito, “Characterizing Graphene, Graphite, and Carbon Nanotubes by Raman Spectroscopy,” *Annu. Rev. Condens. Matter Phys.*, vol. 1, no. 1, pp. 89–108, Jul. 2010, doi: 10/bngjs6.
[79] “Raman spectroscopy.” https://www.st-andrews.ac.uk/seeinglife/science/research/Raman/Raman.html (accessed May 24, 2017).
[80] “Rayleigh Scattering.” http://hyperphysics.phy-astr.gsu.edu/hbase/atmos/blusky.html.
[81] “Raman effect | physics,” *Encyclopedia Britannica*. http://www.britannica.com/science/Raman-effect (accessed Mar. 09, 2016).
[82] T. S. Jespersen, “Raman Scattering in Carbon Nanotubes,” 2003. http://www.nbi.dk/~nygard/SandRamanThesis.pdf.
[83] J. Hodkiewicz, “Characterizing carbon materials with Raman spectroscopy,” *Thermo Sci. Appl. Note*, vol. 51901, 2010.
[84] “Number of vibrational modes for a molecule,” *chemwiki.ucdavis.edu*, Oct. 02, 2013. http://chemwiki.ucdavis.edu/Core/Physical_Chemistry/Spectroscopy/Vibrational_Spectroscopy/Vibrational_Modes/Number_of_vibrational_modes_for_a_molecule (accessed Mar. 09, 2016).
[85] A. C. Ferrari and D. M. Basko, “Raman spectroscopy as a versatile tool for studying the properties of graphene,” *Nat. Nanotechnol.*, vol. 8, no. 4, pp. 235–246, Apr. 2013, doi: 10.1038/nnano.2013.46.
[86] “Raman scattering,” *Wikipedia, the free encyclopedia*. Mar. 04, 2016, Accessed: Mar. 09, 2016. [Online]. Available: https://en.wikipedia.org/w/index.php?title=Raman_scattering&oldid=708169101.

[87] M. S. Dresselhaus, G. Dresselhaus, R. Saito, and A. Jorio, “Raman spectroscopy of carbon nanotubes,” *Phys. Rep.*, vol. 409, no. 2, pp. 47–99, Mar. 2005, doi: 10.1016/j.physrep.2004.10.006.
[88] “Laser Raman Spectroscopy.” http://www.chm.bris.ac.uk/pt/diamond/stuthesis/chapter2.htm (accessed Jun. 18, 2020).
[89] “Raman Spectroscopy,” *Omega Optical*, Oct. 28, 2014. http://www.omegafilters.com/applications/raman-spectroscopy/ (accessed Mar. 14, 2016).
[90] M. N. Iliev, P. X. Zhang, H.-U. Habermeier, and M. Cardona, “Raman spectroscopy as analytical tool for the local structure of YBa2Cu3Ox thin films,” *J. Alloys Compd.*, vol. 251, no. 1, pp. 99–102, Apr. 1997, doi: 10.1016/S0925-8388(96)02777-6.
[91] C. Thomsen, “Raman Scattering Analysis of High-Tc Superconductors,” *J. Raman Spectrosc.*, vol. 27, no. 3–4, pp. 329–332, Mar. 1996, doi: 10.1002/(SICI)1097-4555(199603)27:3/4<329::AID-JRS959>3.0.CO;2-3.
[92] S. A. Cybart *et al.*, “Nano Josephson superconducting tunnel junctions in YBa2Cu3O7–δ directly patterned with a focused helium ion beam,” *Nat. Nanotechnol.*, vol. 10, no. 7, pp. 598–602, Jul. 2015, doi: 10.1038/nnano.2015.76.
[93] M. N. Iliev, V. G. Hadjiev, and V. G. Ivanov, “Raman Spectroscopy of Local Structure and Reordering Processes in YBa2Cu3O7-δ-Type Compounds,” *J. Raman Spectrosc.*, vol. 27, no. 3–4, pp. 333–342, Mar. 1996, doi: 10.1002/(SICI)1097-4555(199603)27:3/4<333::AID-JRS955>3.0.CO;2-W.
[94] K. Venkataraman, R. Baurceanu, and V. A. Maroni, “Characterization of MBa2Cu3O7-x Thin Films by Raman Microspectroscopy,” *Appl. Spectrosc.*, vol. 59, no. 5, pp. 639–649, May 2005, doi: 10/csk9h6.
[95] C. Camerlingo, I. Delfino, and M. Lepore, “Micro-Raman spectroscopy on YBCO films during heat treatment,” *Supercond. Sci. Technol.*, vol. 15, no. 11, p. 1606, 2002, doi: 10.1088/0953-2048/15/11/321.
[96] V. A. Maroni, J. L. Reeves, and G. Schwab, “On-line Characterization of YBCO Coated Conductors Using Raman Spectroscopy Methods,” *Appl. Spectrosc.*, vol. 61, no. 4, pp. 359–366, Apr. 2007.
[97] P. V. Huong, “Microstructure of high temperature superconductor thin films as studied by micro-Raman spectroscopy,” *Phys. C Supercond.*, vol. 180, no. 1, pp. 128–131, Sep. 1991, doi: 10/bzkt2w.
[98] C. Camerlingo, I. Delfino, and M. Lepore, “Micro-Raman spectroscopy on YBCO films during heat treatment,” *Supercond. Sci. Technol.*, vol. 15, no. 11, p. 1606, 2002, doi: 10/dgtnjn.
[99] H. Yamasaki and Y. Mawatari, “Electric-Field Criterion for the Magnetic Measurement of Critical Current Densities of Oxide Superconductors,” in *Advances in Superconductivity XII*, Springer, Tokyo, 2000, pp. 473–475.
[100] M. S. Dresselhaus, A. Jorio, and R.Saito, “Characterizing Graphene, Graphite, and Carbon Nanotubes by Raman Spectroscopy,” *Annu. Rev. Condens. Matter Phys.*, vol. 1, no. 1, pp. 89–108, 2010, doi: 10/bngjs6.
[101] P. R. Herman, R. Marjoribanks, and A. Oettl, “Burst-ultrafast laser machining method,” US6552301B2, Apr. 22, 2003.
[102] J. Krüger *et al.*, “Femto- and nanosecond laser treatment of doped polymethylmethacrylate,” *Appl. Surf. Sci.*, vol. 247, no. 1, pp. 406–411, Jul. 2005, doi: 10/df4hng.

[103] K. T. Voisey, S. Fouquet, D. Roy, and T. W. Clyne, “Fibre swelling during laser drilling of carbon fibre composites,” *Opt. Lasers Eng.*, vol. 44, no. 11, pp. 1185–1197, Nov. 2006, doi: 10/crwp8p.
[104] H. Tamura, T. Kohama, K. Kondo, and M. Yoshida, “Femtosecond-laser-induced spallation in aluminum,” *J. Appl. Phys.*, vol. 89, no. 6, pp. 3520–3522, Mar. 2001, doi: 10/bppqj5.
[105] F. Korte, J. Koch, and B. N. Chichkov, “Formation of microbumps and nanojets on gold targets by femtosecond laser pulses,” *Appl. Phys. A*, vol. 79, no. 4, pp. 879–881, Sep. 2004, doi: 10/c9k8hv.
[106] P.A. Atkin, “FEMTOSECOND LASER MACHINING FOR 3D BIOLOGICAL IMAGING SYSTEM,” 2017.
[107] P. Mulser and D. Bauer, *High Power Laser-Matter Interaction*. Berlin Heidelberg: Springer-Verlag, 2010.
[108] N. Bulgakova *et al.*, “Impacts of Ambient and Ablation Plasmas on Short-and Ultrashort-Pulse Laser Processing of Surfaces,” *Micromachines*, vol. 5, pp. 1344–1372, Dec. 2014, doi: 10/gcfp39.
[109] P. Gibbon, “Short Pulse Laser Interactions with Matter: An Introduction.” http://www.fz-juelich.de/cae/servlet/contentblob/1076020/publicationFile/26069/SPLIM_Lecture01.pdf.
[110] W. Steen and J. Mazumder, *Laser Material Processing*, 4th ed. London: Springer-Verlag, 2010.
[111] R. E. Samad and N. D. Vieira, “Geometrical method for determining the surface damage threshold for femtosecond laser pulses,” *Laser Phys.*, vol. 16, no. 2, pp. 336–339, Feb. 2006, doi: 10/fcbp9b.
[112] K. Hara, *High Temperature Superconducting Electronics: Basis for Materials and Device Structures*. IOS Press, 1993.
[113] “BEAM SHAPING OF FOCUSED BEAMS FOR MICROPROCESSING APPLICATIONS.” Accessed: Jan. 09, 2018. [Online]. Available: http://www.pishaper.com/pdfs/icaleo2014_bs_for_microprocessing_applications.pdf.
[114] D. Gupta, W. R. Donaldson, and A. M. Kadin, “Transient flux dynamics in optically irradiated YBCO thin-film switches,” *IEEE Trans. Appl. Supercond.*, vol. 5, no. 2, pp. 1371–1374, Jun. 1995, doi: 10/ftxn5b.
[115] J. Cheung and J. Horwitz, “Pulsed Laser Deposition History and Laser-Target Interactions,” *MRS Bull.*, vol. 17, no. 2, pp. 30–36, Feb. 1992, doi: 10/gf4k83.
[116] M. Peters, C. Ulbrich, J. C. Goldschmidt, J. Fernandez, G. Siefer, and B. Bläsi, “Directionally selective light trapping in a germanium solar cell,” *Opt. Express*, vol. 19, no. 102, pp. A136–A145, Mar. 2011, doi: 10/cjts7d.
[117] “C101-E128A.pdf.” Accessed: Apr. 08, 2020. [Online]. Available: https://www.ssi.shimadzu.com/sites/ssi.shimadzu.com/files/Products/literature/Spectroscopy/C101-E128A.pdf.
[118] W. A. Jones *et al.*, “Impact of edge-barrier pinning in superconducting thin films,” *Appl. Phys. Lett.*, vol. 97, no. 26, p. 262503, Dec. 2010, doi: 10/b5c6br.
[119] E. Zeldov *et al.*, “Geometrical Barriers in High-Temperature Superconductors,” *Phys. Rev. Lett.*, vol. 73, no. 10, pp. 1428–1431, Sep. 1994, doi: 10/bg7jwd.
[120] M. V. Pedyash, D. H. A. Blank, and H. Rogalla, “Superconducting quantum interference devices based on YBaCuO nanobridges,” *Appl. Phys. Lett.*, vol. 68, no. 8, pp. 1156–1158, Feb. 1996, doi: 10/fwz77r.

[121] T. J. Bullard *et al.*, “Microwave antenna properties of an optically triggered superconducting ring,” *Supercond. Sci. Technol.*, vol. 32, no. 12, p. 125012, Nov. 2019, doi: 10/gg7r89.
[122] M. Tonouchi, M. Tani, Z. Wang, K. Sakai, N. Wada, and M. Hangyo, “Novel Terahertz Radiation from Flux-Trapped YBa 2Cu 3O 7-δ Thin Films Excited by Femtosecond Laser Pulses,” *Jpn. J. Appl. Phys.*, vol. 36, no. 2A, p. L93, Feb. 1997, doi: 10/dtzc4f.
[123] R. F. Giese, M. Runde, and T. P. Sheahen, “Fault Current Limiters,” in *Introduction to High-Temperature Superconductivity*, T. P. Sheahen, Ed. Boston, MA: Springer US, 2002, pp. 465–481.
[124] D. N. Shawel and G. Bekele, “Design Procedure of a Hybrid YBCO-Superconductor Fault Current Limiter (SFCL) for a High Voltage Substation,” in *2019 IEEE PES/IAS PowerAfrica*, Aug. 2019, pp. 313–318, doi: 10/gg7r86.
[125] B. Xiang *et al.*, “Influencing Factors on Quench and Recovery of YBCO Tapes for DC Superconducting Fault Current Limiter,” *IEEE Trans. Appl. Supercond.*, vol. 29, no. 2, pp. 1–6, Mar. 2019, doi: 10/gg7r85.
[126] B. Gromoll *et al.*, “Resistive current limiters with YBCO films,” *IEEE Trans. Appl. Supercond.*, vol. 7, no. 2, pp. 828–831, Jun. 1997, doi: 10/dxdp3v.
[127] B. Dolasinski, J. Bulmer, T. Bullard, P. E. Powers, J. W. Haus, and T. Haugan, “Ultrafast photo response in superconductive isotropic radiators for microwave generation,” 2015, vol. 9347, pp. 93470H-93470H–11, doi: 10/gf4k86.
[128] “Tufnol - Carp brand.” https://www.edplastics.co.uk/Tufnol%20Carp.htm (accessed Jul. 11, 2020).
[129] “Engineering & Design Plastics Ltd - Distributors of plastics to industry.” https://www.edplastics.co.uk/ (accessed Jul. 12, 2020).
[130] “Confocal sensor systems for displacement, distance, position and thickness.” https://www.micro-epsilon.com/displacement-position-sensors/confocal-sensor/?sLang=en (accessed Apr. 28, 2020).
[131] “Factors to consider when selecting confocal displacement sensors.” https://www.eurekamagazine.co.uk/design-engineering-features/technology/factors-to-consider-when-selecting-confocal-displacement-sensors/174617/ (accessed May 01, 2020).
[132] D. Castelvecchi, “First room-temperature superconductor excites — and baffles — scientists,” *Nature*, vol. 586, no. 7829, Art. no. 7829, Oct. 2020, doi: 10.1038/d41586-020-02895-0.
[133] M. Bakr *et al.*, “Lattice dynamical signature of charge density wave formation in underdoped YBCO,” *Phys. Rev. B*, vol. 88, no. 21, p. 214517, Dec. 2013, doi: 10/gg7r9z.
[134] H. Gretarsson *et al.*, “Light-induced metastable state in charge-ordered YBCO,” *Phys. Rev. B*, vol. 98, no. 7, p. 075134, Aug. 2018, doi: 10/gd3t9g.
[135] F. London and H. London, “The electromagnetic equations of the supraconductor,” in *Proceedings of the Royal Society of London A: Mathematical, Physical and Engineering Sciences*, 1935, vol. 149, pp. 71–88, Accessed: May 01, 2017. [Online]. Available: http://rspa.royalsocietypublishing.org/content/royprsa/149/866/71.full.pdf.
[136] J. Bardeen, L. N. Cooper, and J. R. Schrieffer, “Theory of Superconductivity,” *Phys. Rev.*, vol. 108, no. 5, pp. 1175–1204, Dec. 1957, doi: 10/fw8k5d.
[137] “Superconductivity - BCS Theory.” http://www.chm.bris.ac.uk/webprojects2000/igrant/bcstheory.html (accessed May 07, 2017).

[138] K.-H. Bennemann and J. B. Ketterson, *Superconductivity: Volume 1: Conventional and Unconventional Superconductors Volume 2: Novel Superconductors*. Springer Science & Business Media, 2008.
[139] J. F. Annett, *Superconductivity, Superfluids and Condensates*. OUP Oxford, 2004.

11 Appendices

Appendix 1: Basic theory of superconductivity

The London Equations

The two London equations describe the electrodynamics in superconductors, equations (25), (26). These equations are based on a phenomenological theory which is reasoned from observations of superconducting behaviour. The supercurrent is hereafter carried by superconducting electrons [3].

$$E = \frac{\partial}{\partial t}(\Lambda J_s) \tag{25}$$

$$h = -curl\,(\Lambda J_s) \tag{26}$$

where E is the electric field, h the microscopic flux density and J_c describes the superconducting current density. Λ can be further expressed as:

$$\Lambda = \frac{m}{n_s e^2} \tag{27}$$

with m defining the mass of the superconducting electrons, e their charge, and n_s is their number density [42], [135].

Equation (25) describes the perfect conductivity of a superconductor. When a constant electric field is applied, the superconducting electrons are accelerated due to zero resistance leading to a continuous increase of J_c [42], [3].

The London equations helped to understand the electrodynamics of superconductors and the decay of any applied magnetic field below H_c close to the surface of a superconductor. However, the origin of the superconducting electrons remained unclear at that time. Twenty-two years later, in 1957, the Bardeen, Cooper, Schrieffer (BCS) theory offered an explanation.

The BCS Theory

The BCS theory is a microscopic description of superconductivity [136]. According to this theory, the supercurrent in superconductors is carried by Cooper pairs.

Cooper pairs are electron pairs which are formed by electron-phonon interactions. In the ground state of a material an electron locally distorts the cation lattice, resulting in an area of increased positive charge density. Due to this charge distortion (phonon), a second electron is attracted, and a Cooper pair is formed. Those Cooper pairs are more resistant to lattice vibrations compared to single electrons and therefore enable zero-resistance and the supercurrent.

The BCS theory is only valid for conventional, low T_c, superconductors (LTS) as it predicts a maximum T_c of 30-40 K. This limit was broken with the discovery of high T_c superconductors (HTS). Neither the London equations nor the BCS theory were sufficient to describe the difference between LTS and HTS. Only with the Ginzburg-Landau parameters a description was possible, however, the exact origin of the electron pairing in HTS has not yet been discovered [3], [137].

The Ginzburg-Landau Theory

The Ginzburg-Landau theory is a macroscopic theory which describes superconductivity near the transition point from a thermodynamic point of view and each phase transition can be defined by order parameters [137], [138], [139]. For the superconducting-normal phase transition an order parameter Ψ was proposed to characterise the superconducting electrons. Using Ψ, the local density of superconducting charge carriers n_s is defined, equation (28).

$$n_s = |\psi(x)|^2 \tag{28}$$

Only two characteristic lengths of the Ginzburg-Landau theory are further discussed since they are the main parameters of interest for mathematically distinguishing type I and type II superconductors. The theory can be used to extract the Ginzburg-Landau penetration depth λ_{GL} and the Ginzburg-Landau coherence length ξ_{GL}, equation (29), (30).

$$\lambda_{GL} = \sqrt{\frac{m\beta}{4\mu_0 e^2|\alpha|}} \tag{29}$$

$$\xi_{GL} = \sqrt{\frac{\hbar^2}{2m|\alpha|}} \tag{30}$$

α, β are expansion coefficients.

The Ginzburg-Landau penetration depth λ_{GL} describes the decay of magnetic fields in a superconductor and is equivalent to the London penetration depth. The coherence length ξ_{GL} defines the distance a local disturbance in the density of superconducting electrons, caused by an electric or magnetic force, propagates in the material [42], [3], [57].

The Ginzburg-Landau parameter κ is the ratio between the penetration depth λ_{GL} and the coherence length ξ_{GL}, equation (31).

$$\kappa = \frac{\lambda}{\xi} \tag{31}$$

If κ is less than 1/√2 the Meissner effect occurs. Such materials are type I superconductors or LTS.

For κ > 1/√2 the magnetic flux is partially penetrating the material in its superconducting state. These materials are type II superconductors and most HTS belong to this group [3].

These theories provide the basics to understand superconductivity. In every machining process, the material is an important factor which has a great influence on the processing result. It is necessary to know about the properties of a material and the physics of its behaviour.

Appendix 2: Supplier's specifications of YBCO thin films

ceraco

YBCO film on 10×10 mm sapphire substrates

Customer:	**Institute of Manufacturing**	**M-type**	
Deposition:	**X040717B**	**T_c:**	**86,6 K**
Thickness:	**200 nm YBCO**	**J_c:**	**3,4 MA/cm²**

SEM:

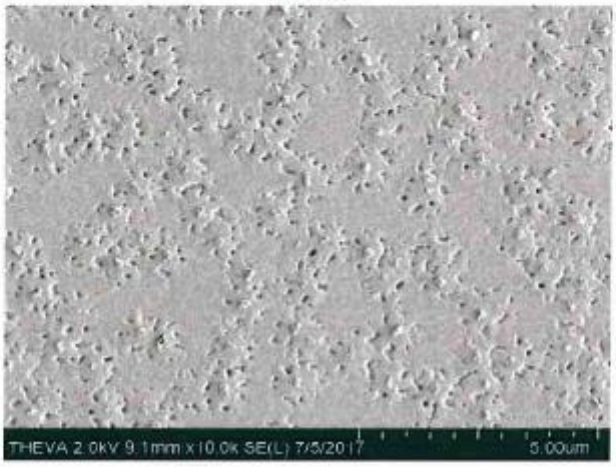

Appendix 3: Supplier's specifications of YBCO bridge samples

THEVA

YBCO film on 2" MgO wafer

Customer:	AFRL	M-type	
Deposition:	X050717A	T_c:	86,2 K
Thickness:	200 nm YBCO	J_c:	3,0 MA/cm²
	20 nm Au in situ		

SEM

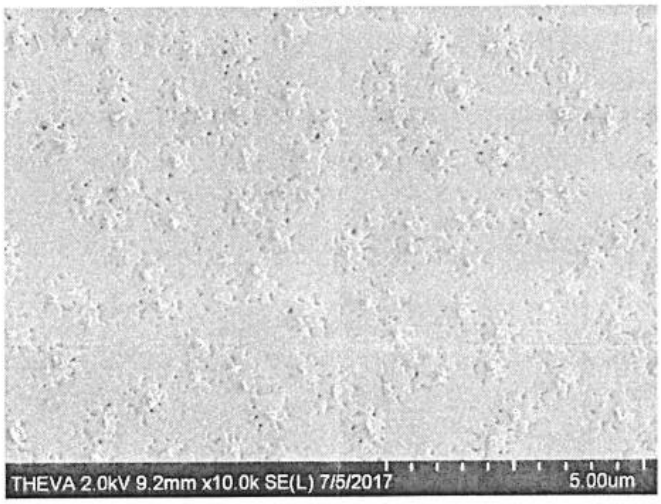

Appendix 4: Specifications of the Aerotech stage in ARG.004

Specs for Aerotech stage mounted on a granite base G04 room

	Axis		
	X	Y	Z
Stage model	ATS 80020	ATS80020	ATS100-100
Motor	BLM-264-A	BLM-203-A	BM75_UF
Encoder steps/rev (PRMx44)	250 Lines/mm x50 x 4	250 Lines/mm x50 x 4	-
Lead/Gear Ratio	Direct	Direct	2 mm/rev
Machine resolution [µm]	0.02	0.02	0.5
Programing resolution [µm]	0.1	0.1	-
Maximum Speed [mm/s]	300	300	100
Accuracy [µm]	±3	±3	±0.5

These specifications are taken from the lab equipment folder in ARG.004

Appendix 5: Attenuation of wheel 2 of the Satsuma platform

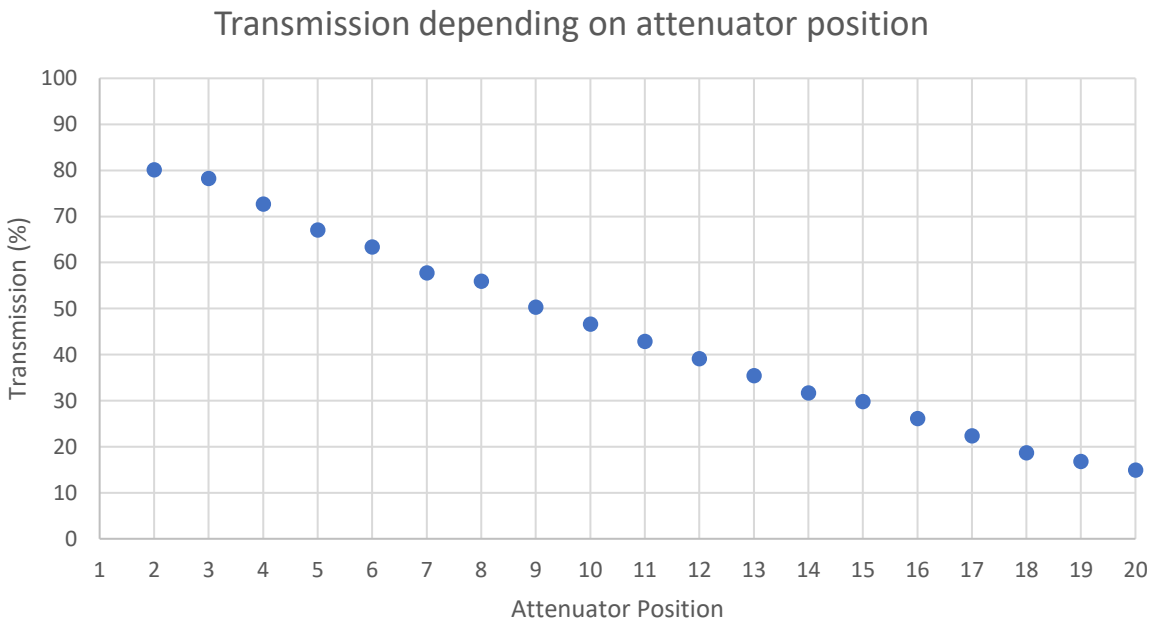

Appendix 6: Measurement of single pulse ablation array

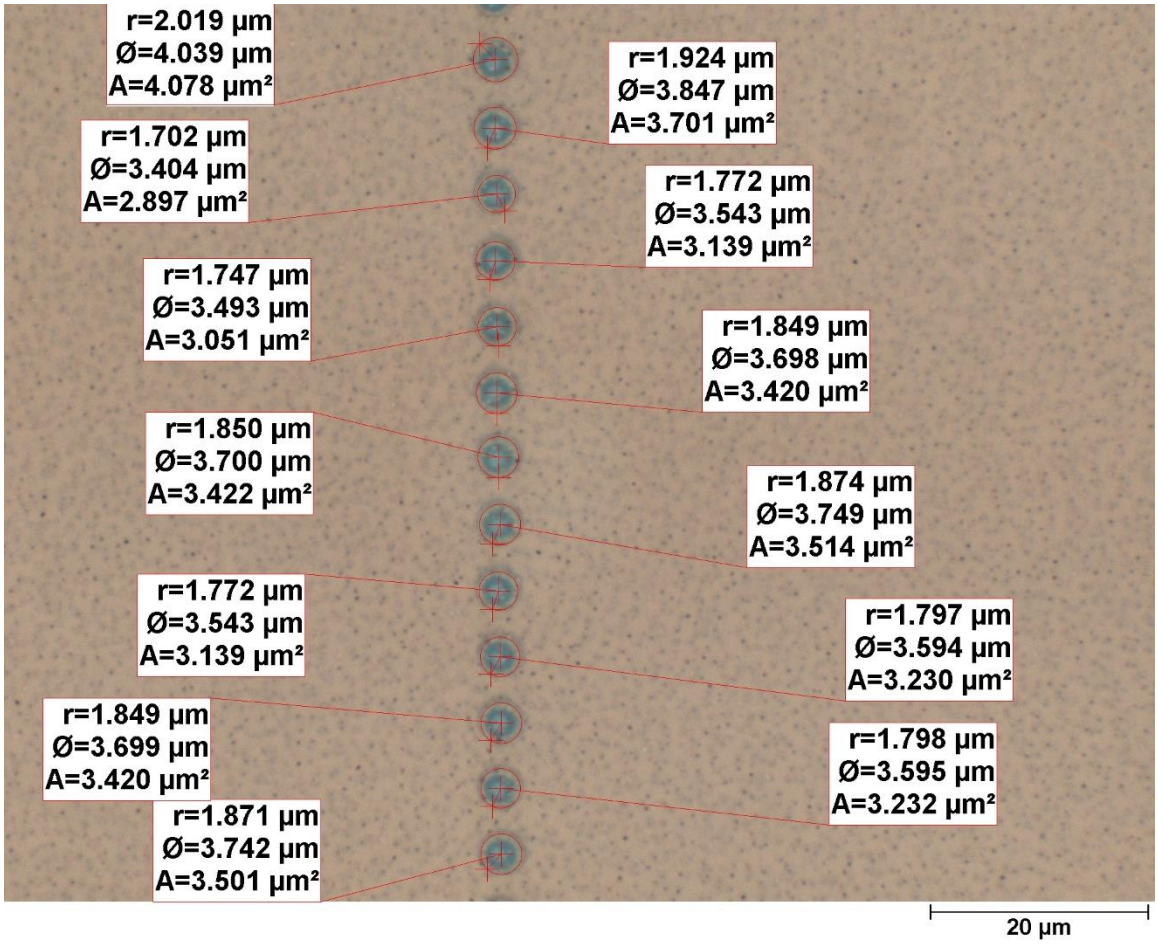

The ablated holes were measured using an Olympus BX51 optical microscope at the highest magnification. In addition to the variation in diameter between the different holes, the uncertainty of the measurement procedure itself was determined by measuring the same hole 20 times.

Appendix 7: Alignment procedure of pi shaper mount and Spiricon positioning

1. Spiricon beam profiler

To align the pi shaper on the Satsuma platform, the pi shaper alignment tool and Spiricon beam profiler (IEEE-1394 Digital Camera, LBA-FW-SCOR20) are needed. First, the Spiricon is set up after the dichroic mirror, figure 113.

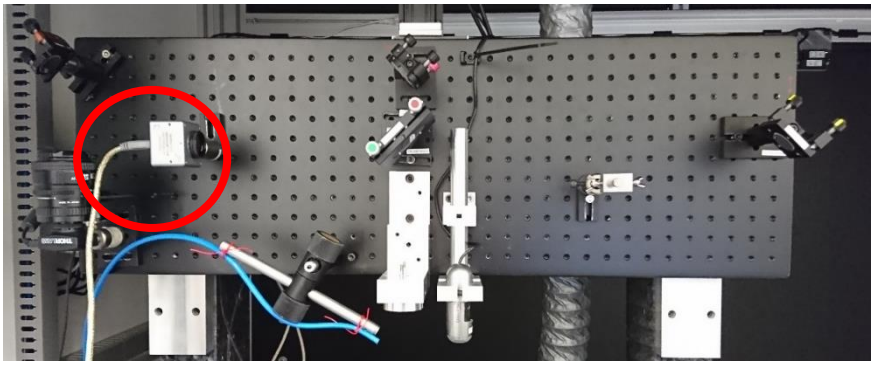

Figure 113: The Spiricon beam profiler is mounted behind the dichroic mirror. The dichroic mirror will decrease the laser power hitting the Spiricon.

The Spiricon is then connected to the 'ACER marker laptop'. (The cable connections are quite fragile and should not be moved during use as the Spiricon could lose connection.) After starting the laptop, open LBA-FW-SCOR and use 'ultracal' in the tool bar next to 'Start!'. After the 'ultracal' action is finished, press start and fire the laser (e.g. with 150 kHz and 80% MOD efficiency) to check the Spiricon alignment.

Once the Spiricon is aligned, the crosshair in LBA-FW-SCOR needs to be positioned in the middle of the beam, figure 114.

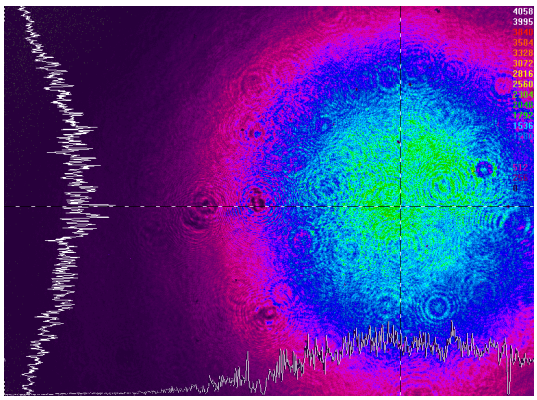

Figure 114: Raw beam after the dichroic.

The crosshair position of the raw beam will be used as reference during the pi shaper alignment.

(Note: There are dust and glue residues on the neutral density filters which are causing little circular distortions. To avoid some of them, the beam is located slightly right from the centre.)

2. Alignment tool

After aligning the Spiricon, the pi shaper stage can be set up on the platform, figure 115.

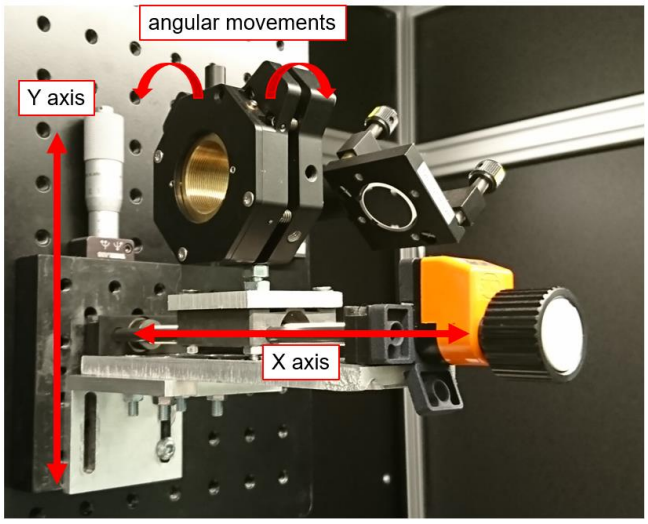

Figure 115: Pi shaper mount for X, Y, tip and tilt alignment.

The alignment tool shown in figure 116 (a) is then screwed into the pi shaper mount for further alignment steps, figure 116 (b).

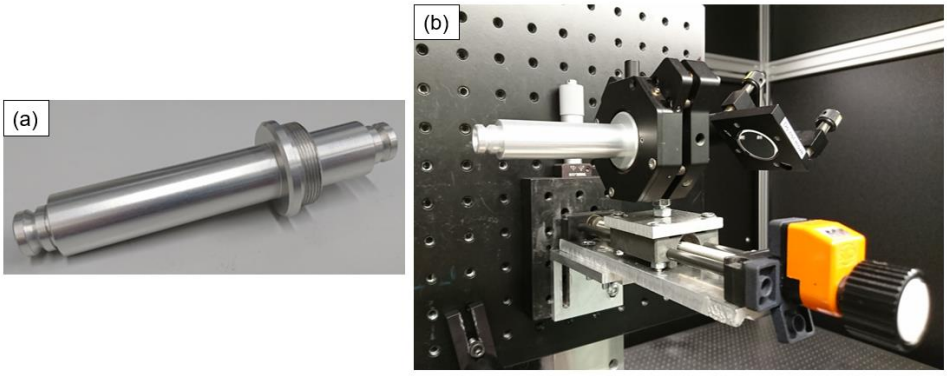

Figure 116: (a) Pi shaper alignment tool. (b) The alignment tool is screwed into the pi shaper mount.

First, the stage is aligned **only in X/Y direction**. The laser is switched on with the alignment tool in the beam path and the stage is adjusted in X/Y until the beam is in the middle of the previously defined crosshair, figure 117.

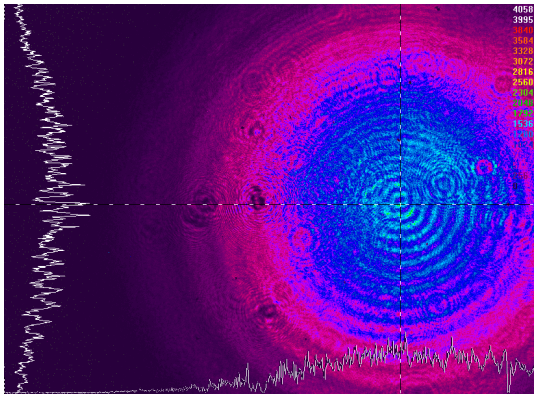

Figure 117: Beam through the alignment tool after X/Y adjustments. Laser parameters: 150 kHz, 80 %.

X and Y can be further adjusted by using additional apertures with different diameters, figure 118.

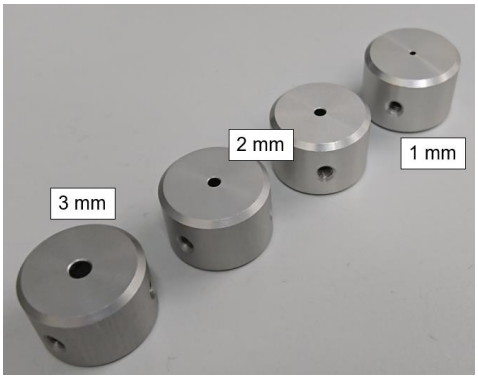

Figure 118: Apertures for the alignment tools with different hole diameters.

By adding apertures, the laser beam forms ring-shaped interference patterns. The centre of the rings is then aligned to the centre of the crosshair. The apertures are placed on the short end of the alignment tool, figure 119.

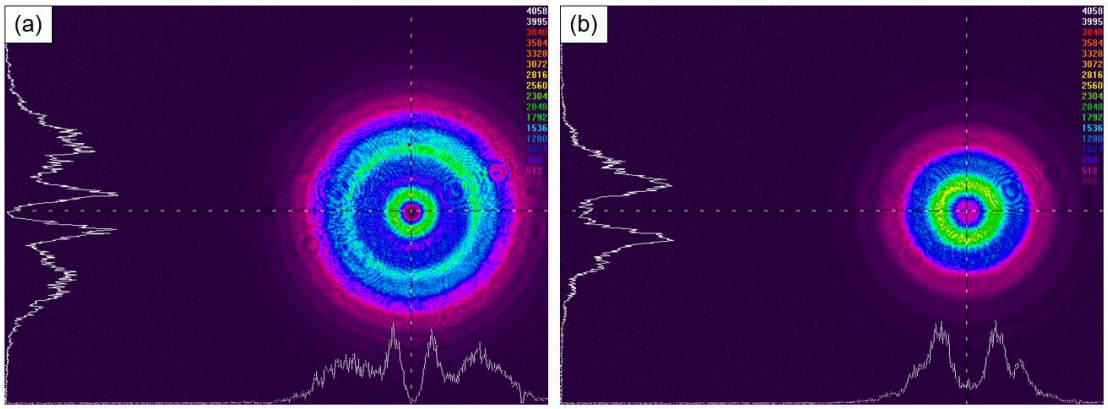

Figure 119: (a) Beam profile with 3 mm aperture after X/Y adjustment. (b) Beam profile with 2 mm aperture. Laser parameters: 150 kHz, 80 %.

Once the stage is aligned in X/Y direction, it needs to be adjusted **in angular direction**. To do so, there are two screws in the top left and right of the black pi shaper socket. (These screws are only for fine adjustments, manual angular alignment by tilting the whole stage might be necessary.) For angular alignment, a 2 mm aperture is placed on the short side of the alignment tool and 3 mm – 1 mm apertures are placed on the front for each alignment step. The beam profile should show symmetrical rings. If the profile is distorted, angular correction is necessary using the top screws, figure 120.

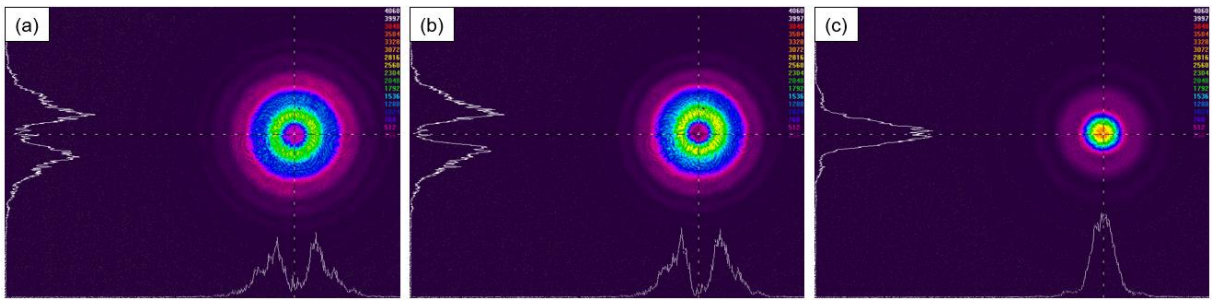

Figure 120: Beam profiles after angular alignment. (a) 2 mm aperture on the short side and 3 mm aperture on the long side of the alignment tool. (b) 2 mm apertures on both sides. (c) 2 mm aperture in the back and 1 mm aperture in the front of the alignment tool. Laser parameters: 150 kHz, 80 %.

It is important that during the angular alignment, the stage is not changed in X and Y. (It might happen that the centre of the rings is not coincidental with the crosshair.)

After completing the alignment using the alignment tool, the tool can be removed and the Spiricon set up needs to be changed.

3. Pi shaper alignment

For the next alignment step, the setup of the Spiricon is changed to create a longer beam path, figure 121.

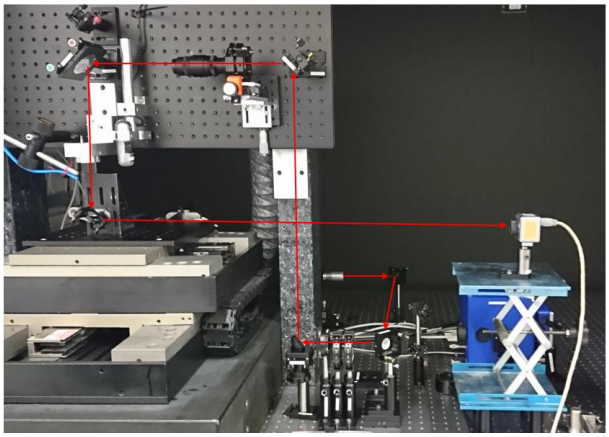

Figure 121: An additional mirror was added and positioned on the stage to create a longer beam path between the pi shaper and the Spiricon.

After adding another mirror and repositioning the Spiricon, the laser is switched on and the crosshair in the Spiricon programm is positioned to mark the centre of the raw beam, figure 122.

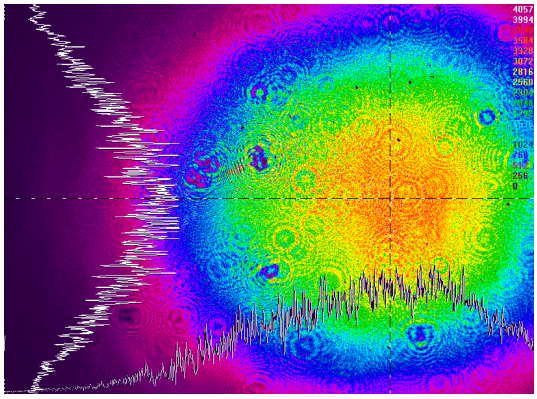

Figure 122: Raw beam in the new set up after adding another mirror. Laser parameters: 150 kHz, 80 %.

The pi shaper is then mounted on the pre-aligned stage. The beam profile will change to an airy disk distribution and the stage needs to be readjusted in **X and Y only** to create a symmetric distribution of the airy disks, figure 123.

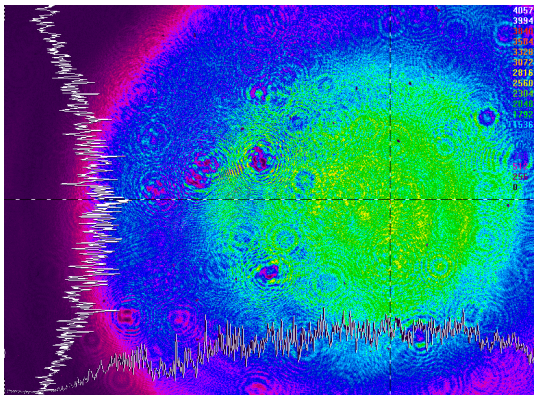

Figure 123: Beam profile after adding the pi shaper. The airy disks should be as symmetrical as possible. Laser parameters: 150 kHz, 80 %.

Next, both attenuators are added if not already done so and a 1 m focussing lens is put on the pi shaper, figure 124. The pi shaper is then focussed on the Spiricon and by turning the focusing ring the beam profiles are changed.

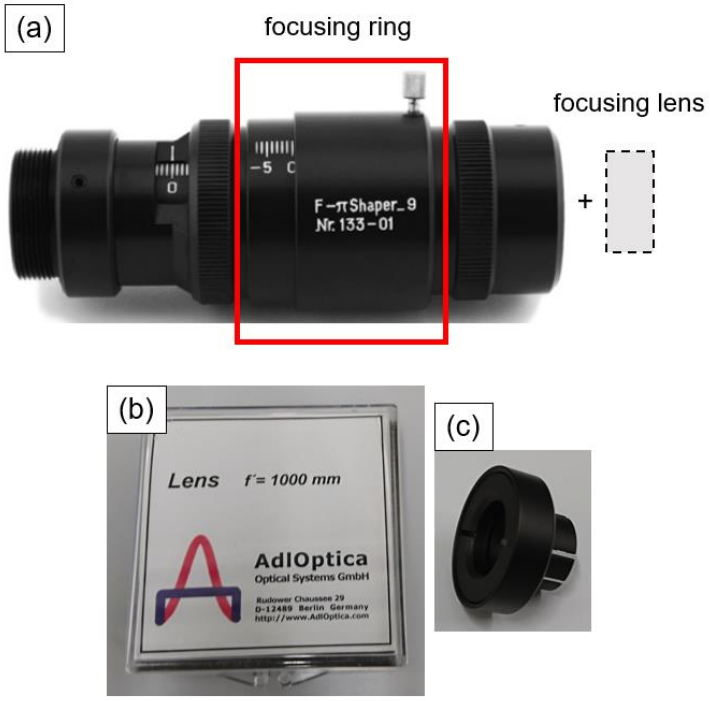

Figure 124: (a) Pi shaper. (b) 1 m focusing lens, (c) Lens holder.

When focusing the beam on the Spiricon (with 3+ neutral density filters), both attenuators need to be at maximum position and the laser parameters should be

around 100 kHz and 33 % MOD efficiency. The focal point is usually around -0.5 on the focusing ring scale and the donut shape at -1.5, figure 125.

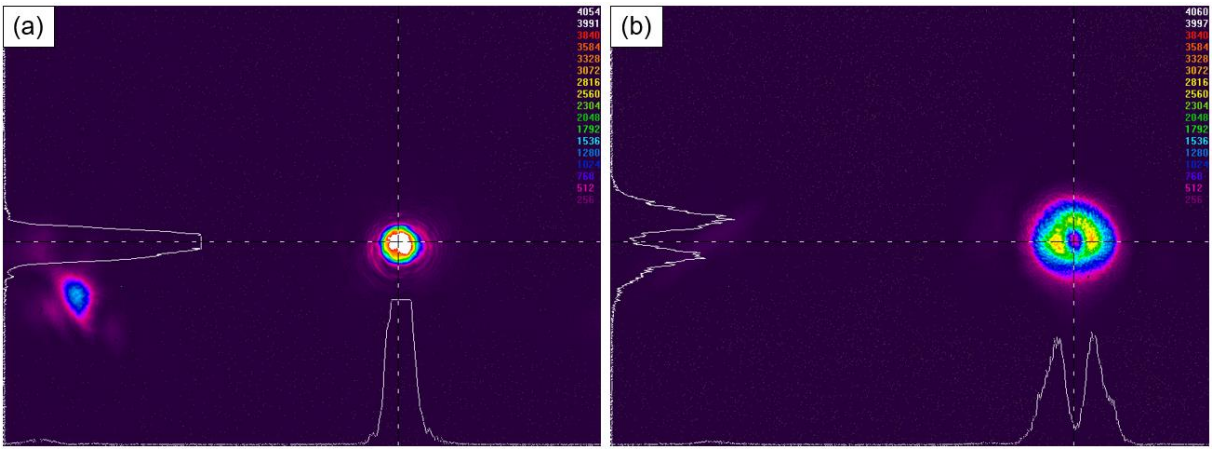

Figure 125: (a) Focal position using the focusing ring on the pi shaper. The parasite spot on the left side can be ignored and is caused by the 1 m focusing lens which does not have AR coating. (b) Donut beam shape at -1.5.

The donut shape is used for additional tip/tilt alignment. The profile should be as symmetrical as possible, figure 126.

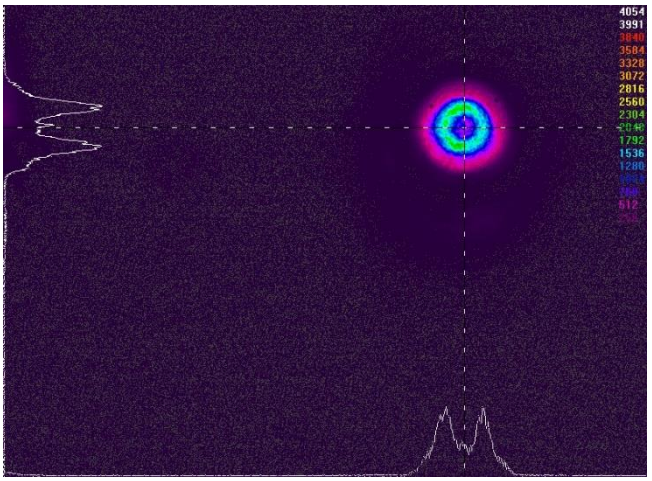

Figure 126: Donut shape after angular alignment of the pi shaper.

Finally, the pi shaper is aligned and the 1 m focusing lens can be removed.